The MOLLER Project
Measurement **O**f a **L**epton **L**epton **E**lectroweak **R**eaction

An Ultra-precise Measurement of the Weak Mixing Angle
using Møller Scattering

Conceptual Design Report

The MOLLER Collaboration

November 22, 2019 (Revised August 3, 2020)

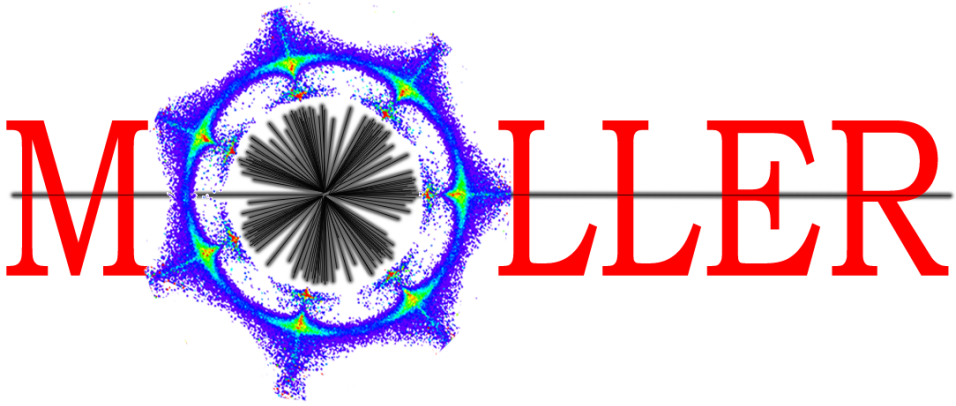

The MOLLER Collaboration

M. Abdullah Mamun, P. Adderley, E. Becker, J. Benesch, P. Brindza, J. Brock, D. Bullard, J. Butler, R.D. Carlini, J-P. Chen, E. Chudakov, S. Covrig, M.M. Dalton, P. Degtiarenko, A. Deur, A. DiPette, R. Fair, J. Fast, H. Fenker, E. Folts, D. Gaskell, A. Gavalya, P. Ghoshal, J. Grames, J. Gomez, S. Gopinath, O. Hansen, L. Harwood, W. Henry, C. Hernandez-Garcia, D.W. Higinbotham, A. Hofler, C. Hutton, D. Kashy, R. Kazimi, C. Keith, C. Keppel, P. Kessler, K. Krug, S. Malace, D. Meekins, R. Michaels, J. Miller, B. Moffit, D. Moser, M. Poelker, Y. Roblin, J. Segal, C. Soova, M. Stutzman, R. Suleiman, E. Trovatore, Y. Wang, R. Wilson, R. Wines, B. Wojtsekhowski, S. Wood, L. Zana, S. Zhang, C. Zorn
Jefferson Lab

X. Bai, G. Cates, D. Day, D. Di, K. Gnanvo, N. Liyanage, V.V. Nelyubin, H. Nguyen, C. Palatchi, K.D. Paschke, S. Premathilake, A. Zec
University of Virginia

F. Araiza-Gonzalez, K. Dehmelt, C. Clarke, A. Deshpande, C. Feldman, C. Gal, C. Ghosh, T.K. Hemmick, S. Park, R. Richards, T. Ye, J. Zhang, W. Zhang
Stony Brook University, SUNY

P. Blunden, W. Deconinck, M.T.W. Gericke, J. Mammei, C. Match, H.S. Lee, J. Pan, P. Pandey, S. Rahman, W.T.H. van Oers,
University of Manitoba

V. Bellini, V. Brio, F. Mammoliti, C. Sutera, F. Tortorici
INFN Sezione di Catania and Universita' di Catania

K. Aulenbacher, D. Becker, S. Baunack, F. Maas, V. Tioukine, M Wilfert
Johannes Gutenberg Universitaet Mainz

G. De Cataldo, R. De Leo, D. Di Bari, L. Lagamba
INFN, Sezione di Bari and Universita' di Bari

R. S. Beminiwattha, K. Johnston, N. Simicevic, S. Wells
Louisiana Tech University

D.S. Armstrong, T.D. Averett, V.F. Owen, E.W. Wertz
College of William & Mary

K.S. Kumar [Contact*], R. Miskimen, M.J. Ramsey-Musolf
University of Massachusetts, Amherst

Yu.G. Kolomensky, Y. Mei, E. Sichtermann
Lawrence Berkeley National Laboratory and University of California, Berkeley

D. Adhikari, T.A. Forest, D. McNulty
Idaho State University

J. Bessuille, E. Ihloff, J. Kelsey
Massachusetts Institute of Technology

J.A. Dunne, D. Dutta, L. El Fassi
Mississippi State University

B. Jamieson, R. Mammei, J.W. Martin
University of Winnipeg

D. Jones, J. Napolitano, D. Nikolaev
Temple University

E. King, P. Souder
Syracuse University

A. Lee, M. L. Pitt
Virginia Polytechnic Institute and State University

P.M. King, J. Roche
Ohio University

F. Meddi, G.M. Urciuoli
Dipartimento di Fisica dell'Universita' la Sapienza and INFN Sezione di Roma

E. Cisbani, F. Garibaldi
INFN Gruppo Collegato Sanita' and Istituto Superiore di Sanita'

J.C. Cornejo, B. Quinn
Carnegie Mellon University

A. Ahmidouch, S. Danagoulian
North Carolina A&T State University

O. Glamazdin, R. Pomatsalyuk
NSC Kharkov Institute of Physics and Technology

A. Aleksejevs, S. Barkanova
Memorial University, Grenfell

R. Gilman, R. Ransome
Rutgers University

T. Holmstrom
Longwood University

J. Erler
Universidad Nacional Autónoma de México

K. A. Aniol
California State U.(Los Angeles)

W.D. Ramsay
TRIUMF

E. Korkmaz
University of Northern British Columbia

D.T. Spayde
Hendrix College

F. Benmokhtar
Duquesne University

A. Del Dotto
INFN, Laboratori Nazionali di Frascati

R. Perrino
INFN Sezione di Lecce

J. Singh
NSCL and Michigan State University

C. Annasiwatta
Muskingum University

*kkumar@physics.umass.edu

Executive Summary

We present the conceptual design of the MOLLER experiment, in which we propose to measure the parity-violating asymmetry A_{PV} in polarized electron-electron (Møller) scattering. In the Standard Model, A_{PV} is due to the interference between the electromagnetic amplitude and the weak neutral current amplitude, the latter being mediated by the Z^0 boson. A_{PV} is predicted to be ≈ 33 parts per billion (ppb) at our kinematics. Our goal is to measure A_{PV} to an uncertainty of 0.8 ppb. The result would yield a measurement of the weak charge of the electron Q_W^e to a fractional uncertainty of 2.4% at an average Q^2 of 0.0056 GeV^2.

The measurement is sensitive to the interference of the electromagnetic amplitude with new neutral current amplitudes as weak as $\sim 10^{-3} \cdot G_F$ from as yet undiscovered dynamics beyond the Standard Model. Such discovery reach is unmatched by any proposed experiment measuring a flavor- and CP-conserving process over the next decade, and results in a unique window to new physics at MeV and multi-TeV scales, complementary to direct searches at high energy colliders. Within the Standard Model, the extracted Q_W^e measurement yields a determination of the weak mixing angle $\sin^2\theta_W$ with both precision and accuracy that are unmatched by any conceivable method at $Q^2 \ll M_Z^2$ in the foreseeable future, and matches the uncertainty from the single best such determination from high energy colliders.

The measurement would be carried out in Hall A at Jefferson Laboratory, where a 11 GeV longitudinally polarized electron beam would be incident on a 1.25 m liquid hydrogen target. Møller electrons (beam electrons scattering off target electrons) in the full range of the azimuth and spanning the polar angular range 5 mrad $< \theta_{\rm lab} <$ 21 mrad, would be separated from background and brought to a ring focus ~ 27 m downstream of the target by a spectrometer system consisting of a pair of toroidal magnet assemblies and precision collimators. The Møller ring would be intercepted by a system of fused silica detectors; the resulting Cherenkov light would provide a relative measure of the scattered flux.

Longitudinally polarized electrons are generated via photoemission on a GaAs photocathode by circularly polarized laser light, enabling rapid polarization (helicity) reversal and suppression of spurious systematic effects. A_{PV} would be extracted from the fractional difference in the integrated Cherenkov light response between helicity reversals. Additional systematic suppression to the sub-ppb level would be accomplished by periodically reversing the sign of the physics asymmetry by three independent methods.

Simultaneously with data collection, the fluctuations in the electron beam energy and trajectory and its potential systematic effects on A_{PV} would be precisely monitored, active feedback loops would minimize beam helicity correlations, and detector response to beam fluctuations would be continuously calibrated. Background fractions and their helicity-correlated asymmetries would be measured by dedicated auxiliary detectors. The absolute value of Q^2 would be calibrated periodically using tracking detectors. The longitudinal electron beam polarization would be measured continuously by two independent polarimeter systems.

The project team is integrated into a strong collaboration that has extensive experience in previous successful measurements using similar techniques. A comprehensive set of physics requirements has been developed and led to the conceptual design articulated in this document. The collaboration is looking forward to the engineering design, construction and deployment of the apparatus and to data collection and analysis at the completion of the project.

Contents

List of Figures

List of Tables

1 Science Motivation

1.1 Physics Context

The MOLLER experiment [1, 2] proposes to significantly expand the sensitivity reach to discover new dynamics beyond the Standard Model of electroweak interactions both at low energy scales ($\sim$ 100 MeV) as well as at high energy (multi-TeV). It is one of a small handful of projects worldwide that are designed to carry out ultra-precise measurements of electroweak observables well below the scale of electroweak symmetry breaking, and are theoretically calculable to high accuracy. Specifically, MOLLER measures the parity-violating asymmetry A_{PV} in the scattering of longitudinally polarized electrons off unpolarized electrons, using the upgraded 11 GeV beam in Hall A at Jefferson Laboratory (JLab), to an overall fractional accuracy of 2.4%. Such a result would constitute more than a factor of five improvement in fractional precision over the only other measurement of the same quantity by the E158 experiment at SLAC [3].

A_{PV} in Møller scattering is directly proportional to the weak charge of the electron Q_W^e, which is in turn proportional to the product of the electron's vector and axial-vector couplings to the Z^0 boson. The electroweak theory prediction at tree level in terms of the weak mixing angle is $Q_W^e = 1 - 4\sin^2\theta_W$; this is modified at the 1-loop level [4–6] and becomes dependent on the energy scale at which the measurement is carried out, *i.e.* $\sin^2\theta_W$ "runs". The prediction for A_{PV} for the proposed experimental design is ≈ 33 parts per billion (ppb) and the goal is to measure this quantity with an overall uncertainty of 0.8 ppb and thus achieve a 2.4% measurement of Q_W^e. Under the assumption of a SM Higgs boson mass of 126 GeV, the theoretical prediction for the MOLLER A_{PV} will be calculable to better than 0.2 ppb accuracy. The purely leptonic Møller PV asymmetry is a rare low energy observable whose theoretical uncertainties, especially due to hadronic effects, are well under control.

The electron beam energy, luminosity and stability at Jefferson Laboratory are uniquely suited to carry out such a measurement. The 11 GeV JLab beam at the upgraded facility provides a compelling new opportunity to achieve a new benchmark in sensitivity. The physics motivation has two important aspects:

1. New neutral current interactions are best parameterized model-independently at low energies by effective four-fermion interactions by the quantity Λ/g, where g characterizes the strength and Λ is the scale of the new dynamics. The proposed A_{PV} measurement is sensitive to interaction amplitudes as small as 1.5×10^{-3} times the Fermi constant, G_F, which corresponds to a sensitivity of $\Lambda/g = 7.5$ TeV. A coupling g of order one probes the TeV scale with new and unique sensitivity, while for $\Lambda \sim 100$ MeV, there is extraordinary new sensitivity approaching $10^{-3} \cdot \alpha_{QED}$. This would be *the* most sensitive probe of new flavor and CP-conserving neutral current interactions in the leptonic sector until the advent of a linear collider or a neutrino factory, and would have 5σ discovery potential in the discovery space allowed by the existing most precise low energy measurements.

2. Within the Standard Model, weak neutral current amplitudes are functions of the weak mixing angle $\sin^2\theta_W$. The two most precise independent determinations of $\sin^2\theta_W$ differ by 3σ. The world average is consistent with the theoretical prediction for the weak mixing angle assuming the 126 GeV scalar resonance observed at the LHC is the Standard Model (SM) Higgs boson. However, choosing one or the other central value ruins this consistency and implies very different new high-energy dynamics. The proposed A_{PV} measurement, which would achieve a sensitivity of $\delta(\sin^2\theta_W) = \pm 0.00028$, has the same level of precision and interpretability: the best among projected sensitivities for new measurements at low Q^2 or colliders over the next decade.

1.2 Precision Goal

The leading order Feynman diagrams relevant for Møller scattering, involving both direct and exchange diagrams that interfere with each other, are shown in Fig. 1. The parity-violating asymmetry in the scattering

of longitudinally polarized electrons on unpolarized target electrons A_{PV}, due to the interference between the photon and Z^0 boson exchange diagrams in Fig. 1, is given by [7]

$$A_{PV} = \frac{\sigma_R - \sigma_L}{\sigma_R + \sigma_L} = mE\frac{G_F}{\sqrt{2}\pi\alpha}\frac{4\sin^2\theta}{(3+\cos^2\theta)^2}Q_W^e = mE\frac{G_F}{\sqrt{2}\pi\alpha}\frac{2y(1-y)}{1+y^4+(1-y)^4}Q_W^e \quad (1)$$

where Q_W^e (proportional to the product of the electron's vector and axial-vector couplings to the Z^0 boson) is the weak charge of the electron, α is the fine structure constant, E is the incident beam energy, m is the electron mass, θ is the scattering angle in the center of mass frame, $y \equiv 1 - E'/E$ and E' is the energy of one of the scattered electrons.

The electroweak theory prediction at tree level in terms of the weak mixing angle is $Q_W^e = 1 - 4\sin^2\theta_W$; this is modified at the 1-loop level [4–6] and increases by approximately 3% compared to its value at the scale of the Z^0 boson mass, M_Z; this and other radiative corrections reduce Q_W^e to 0.0435, a $\sim 42\%$ change of its tree level value of ~ 0.075 (when evaluated at M_Z). The dominant effect comes from the "$\gamma - Z$ mixing" diagrams depicted in Fig. 2 [5]. The consequent reduction in the numerical value of Q_W^e leads to increased fractional accuracy in the determination of the weak mixing angle, $\sim 0.1\%$, matching the precision of the single best such determination from measurements of asymmetries in Z^0 decays in the e^+e^- colliders LEP and SLC.

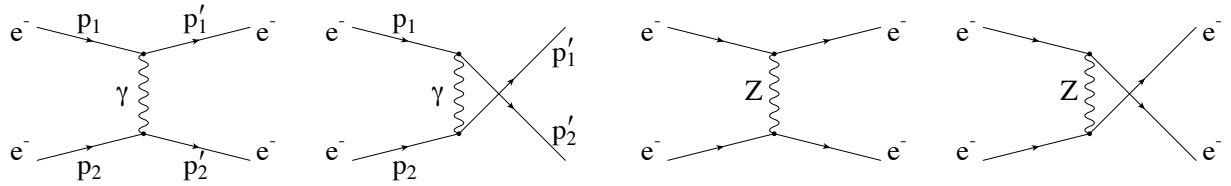

Figure 1: *Feynman diagrams for Møller scattering at tree level (reproduced from Ref. [5])*

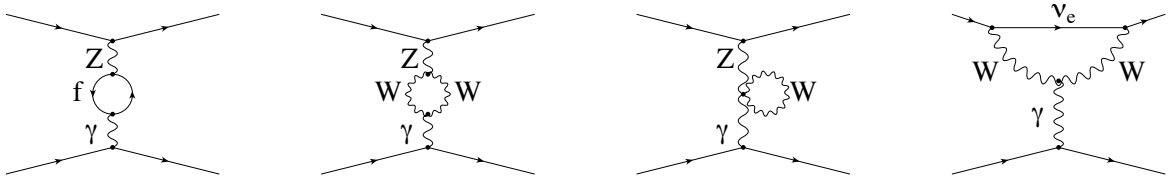

Figure 2: *Significant 1-loop radiative corrections: $\gamma - Z$ mixing diagrams and W-loop contribution to the anapole moment (reproduced from Ref. [5])*

The proposed MOLLER measurement will make a precision (2.4% relative) measurement of a suppressed Standard Model observable ($Q_W^e \sim 0.0435$) resulting in sensitivity to new neutral current amplitudes as weak as $\sim 10^{-3} \cdot G_F$ from as yet undiscovered dynamics beyond the Standard Model. The fact that the proposed measurement provides such a sensitive probe of TeV-scale dynamics beyond the SM (BSM) is a consequence of a very precise experimental goal ($\sim 10^{-3} \cdot G_F$), the energy scale of the reaction ($Q^2 \ll M_Z^2$), and the ability within the electroweak theory to provide quantitative predictions with negligible theoretical uncertainty. The proposed measurement is likely the only practical way, using a purely leptonic scattering amplitude at $Q^2 \ll M_Z^2$, to make discoveries in important regions of BSM space in the foreseeable future at any existing or planned facility worldwide.

An important point to note is that, at the proposed level of measurement accuracy of A_{PV}, the Standard Model (SM) prediction must be carried out with full treatment of one-loop radiative corrections and leading two-loop corrections. The current uncertainty associated with radiative corrections for MOLLER is estimated to be less than 0.5 ppb [13], smaller than the expected 0.8 ppb overall precision. There has been recent progress to investigate several classes of diagrams beyond one-loop [14, 15], and ongoing efforts are studying the complete set of two-loop corrections at MOLLER kinematics; such corrections are already estimated to be smaller than the statistical uncertainty goal for MOLLER. The theoretical uncertainties for the purely leptonic Møller PV are thus well under control, and the planned future work will aim to reduce the uncertainty on the A_{PV} prediction, including the effects of the apparatus, to less than 0.2 ppb.

1.3 Summary of Physics Motivation

1.3.1 Electroweak Physics

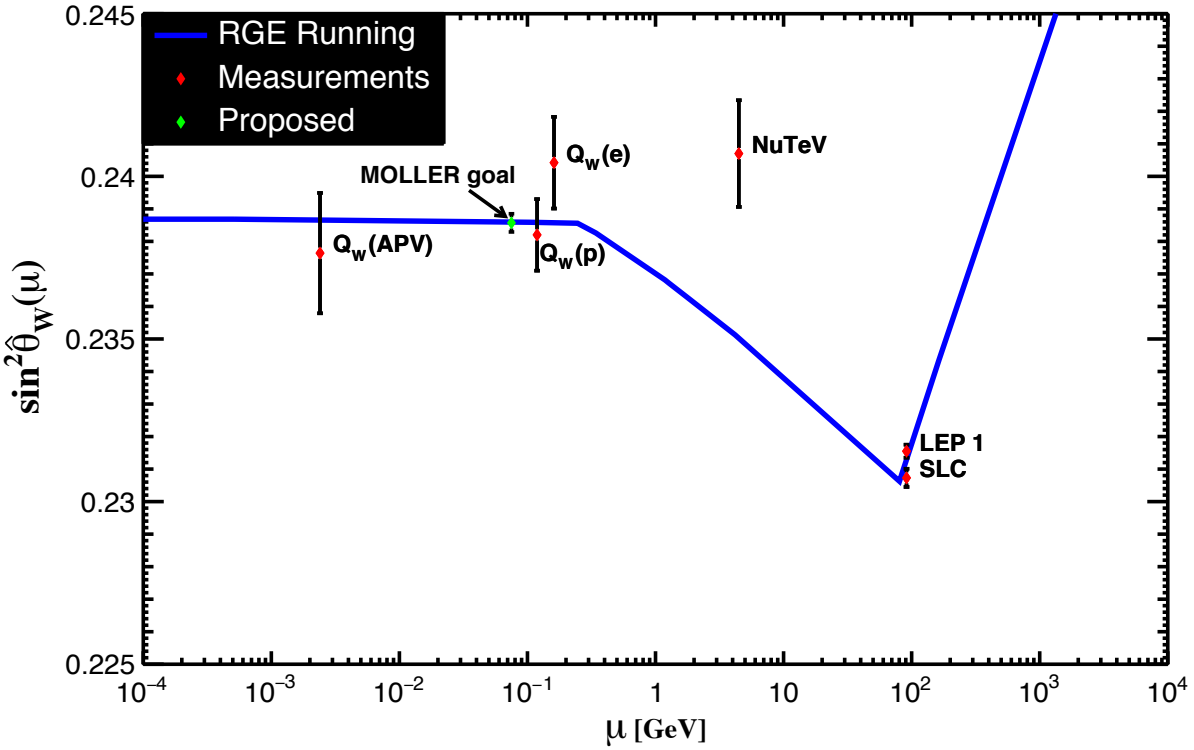

Figure 3: *The four most precise measurements of the weak mixing angle measurements vs. the energy scale μ are shown as red diamonds with error bars; the curve is reproduced from the PDG [8]. The APV point reflects the reanalysis of the original result [9] in Ref. [10]. The $Q_W(e)$ point is the E158 result [3]. The $Q_W(p)$ point is the Q_{weak} result [11]. The NuTeV point is the extracted value from the original publication result [12]. The proposed MOLLER measurement is shown at the appropriate μ value and the proposed error bar with the nominal SM prediction as the central value.*

The weak mixing angle $\sin^2\theta_W$ has played a central role in the development and validation of the electroweak theory, especially testing it at the quantum loop level, which has been the central focus of

precision electroweak physics. A key feature of MOLLER is that the A_{PV} measurement will be carried out at $Q^2 \ll M_Z^2$. Since $\sin^2\theta_W$ "runs" as a function of Q^2 due to electroweak radiative corrections, one can use $\sin^2\theta_W$ as a bookkeeping parameter to compare the consistency of the full Q^2 range of weak neutral current measurements, as shown in Fig. 3. The theory error in the low energy extrapolation is comparable to the width of the line in the figure [6]. MOLLER A_{PV} would be the first low Q^2 measurement to match the precision of the single best high energy measurement at the Z^0 resonance. The proposed MOLLER A_{PV} measurement would achieve a sensitivity of $\delta(\sin^2\theta_W) = \pm 0.00028$. That is the most precise anticipated weak mixing angle measurement currently proposed over the next decade at low or high energy.

1.3.2 New Physics Beyond the Standard Model

The MOLLER experiment measures a unique observable with a precision goal that would result in the most sensitive discovery reach for flavor- and CP- conserving scattering amplitudes in the next decade; see recent reviews that situate the measurement in broader contexts [16–18]. It is very complementary to other precision low energy experiments and the energy frontier efforts at the LHC. If the LHC continues to agree with the Standard Model with high luminosity running at the full 14 TeV energy, then MOLLER will be a significant component of a global strategy to discover signatures of a variety of physics that could escape LHC detection. Examples include hidden weak scale scenarios such as compressed supersymmetry [19], lepton number violating amplitudes such as those mediated by doubly charged scalars [20], and light MeV-scale dark matter mediators such as the "dark" Z [22, 23].

If the LHC observes an anomaly, then MOLLER will have the sensitivity to be part of a few select measurements that will provide important constraints to choose among possible beyond the Standard Model (BSM) scenarios to explain the anomaly. Examples of such BSM scenarios that have been explicitly considered for MOLLER include: new particles predicted by the Minimal Supersymmetric Standard Model observed through radiative loop effects (R-parity conserving) or tree-level interactions (R-parity violating) [24, 25] and TeV-scale Z's [26] which arise in many BSM theories.

A fairly general and model-independent way to quantify the energy scale of BSM high-energy dynamics (that MOLLER is sensitive to) is to express the resulting new amplitudes at low energies in terms of contact interactions (dimension-6 non-renormalizable operators) among leptons and quarks [27]. Specializing here to vector and axial-vector interactions between electrons and/or positrons, the interaction Lagrangian is characterized by a mass scale Λ and coupling constants g_{ij} labeled by the chirality of the leptons. For the MOLLER A_{PV} measurement with 2.4% total uncertainty (and no additional theoretical uncertainty) the resulting sensitivity to new 4-electron contact interaction amplitudes can be expressed as:

$$\frac{\Lambda}{\sqrt{|g_{RR}^2 - g_{LL}^2|}} = \frac{1}{\sqrt{\sqrt{2}G_F|\Delta Q_W^e|}} \simeq \frac{246.22\text{ GeV}}{\sqrt{0.023 Q_W^e}} = 7.5\text{ TeV}. \tag{2}$$

For example, models of lepton compositeness are characterized by strong coupling dynamics. Taking $\sqrt{|g_{RR}^2 - g_{LL}^2|} = 2\pi$ shows that mass scales as large as $\Lambda = 47$ TeV can be probed, far beyond the center of mass energies of any current or planned high energy accelerator. This allows electron substructure to be studied down to the level of 4×10^{-21} m.

The remarkable feature of the MOLLER sensitivity to four-lepton flavor-conserving contact interactions has been emphasized [28]. Not only does the contact interaction scale reach exceed those at LEP-200, the highest energy electron-positron collider to collect data, but there is unique sensitivity to a specific linear combination of left- and right-handed four electron operators to which all other collider measurements happen to be insensitive. Indeed, in the current global analysis, the E158 result [3] is used to break the degeneracy. The MOLLER measurement will allow the extension of the current limits for these operators from about 2 TeV to more than 7 TeV.

The importance of improving sensitivity over the entire multi-dimensional space of new operators is particularly important if higher sensitivity searches at the LHC yield no new discoveries. For example, in hidden weak scale scenarios such as compressed supersymmetry [19], one of the superpartner masses could be relatively light, likely if the super-partner masses are nearly degenerate. In that scenario, the LHC signatures would be very challenging to disentangle from QCD backgrounds. Another example is a lepton number violating amplitude mediated by doubly charged scalars. The MOLLER measurement is one of the rare low Q^2 observables with sensitivity to such amplitudes, which naturally arise in extended Higgs sector models containing complex triplet representations of SU(2). In a left-right symmetric model, for example, the proposed MOLLER measurement would lead to the most stringent probe of the left-handed charged scalar and its coupling to electrons, with a reach of 5.3 TeV, significantly above the LEP 2 constraint of about 3 TeV. Moreover, such sensitivity is complementary to other sensitive probes such as lepton-flavor violation and neutrinoless double-beta decay searches [20, 21].

Finally, the interesting possiblity of a light MeV-scale dark matter mediator known as the "dark" Z [22, 23] has been recently investigated. It is denoted as Z_d with mass m_{Z_d}, and it stems from a spontaneously broken $U(1)_d$ gauge symmetry associated with a secluded "dark" particle sector. The Z_d boson can couple to SM particles through a combination of kinetic and mass mixing with the photon and the Z^0-boson, with couplings ε and $\varepsilon_Z = \frac{m_{Z_d}}{m_Z}\delta$ respectively. In the presence of mass mixing ($\delta \neq 0$), a new source of "dark" parity violation arises [22] such that it has negligible effect on other precision electroweak observables at high energy, but is quite discernable at low Q^2 through a shift in the weak mixing angle [23].

In summary, the discovery reach of the proposed MOLLER experiment is unmatched by any proposed experiment measuring a flavor- and CP-conserving process over the next decade. It results in a unique window to new physics at MeV and multi-TeV scales, complementary to direct searches at high energy colliders such as the Large Hadron Collider (LHC).

2 Experiment Overview

In this section a brief overview of the MOLLER experimental design and requirements is given. The experimental design and requirements are driven by the need to measure a very small parity-violating asymmetry which requires measurement of the scattered electron flux at an unprecedentedly high rate and careful attention to a range of systematic effects. The MOLLER design is grounded on the extensive experience gained by the collaboration from other high flux integrating (as opposed to counting individual particles) parity-violation measurements such as MIT-Bates ^{12}C [31], SAMPLE [32], HAPPEX [33], SLAC E158 [3], PREX [35], and $\mathrm{Q_{weak}}$ [11].

To achieve the desired scientific impact, the experiment is designed to measure the parity-violating asymmetry in the scattering of longitudinally-polarized electrons from unpolarized target electrons to an overall fractional accuracy of 2.4%, which corresponds to an absolute accuracy of ± 0.8 ppb. The asymmetry is measured using a flux integration technique that is described in Appendix A.

2.1 Experimental Technique

The measurement will be carried out in Hall A at Jefferson Laboratory, with a 11 GeV longitudinally polarized electron beam incident on a 1.25 m liquid hydrogen target. Møller electrons (beam electrons scattering off target electrons) in the full range of the azimuth and spanning the polar angular range 5 mrad $< \theta_{lab} <$ 21 mrad, are separated from background and brought to a ring focus $\sim$ 26.5 m downstream of the target by a spectrometer system consisting of precision collimators and a pair of toroidal magnet assemblies. The Møller ring is intercepted by a system of quartz detectors; the resulting Cherenkov light provides a relative measure of the scattered flux.

The experimental techniques for producing an ultra-stable polarized electron beam, systematic control at the part per billion level and calibration techniques to control normalization errors including the degree of electron beam polarization at the $<$1% level have been continuously improved over two decades of development at Jefferson Lab. A list of the nominal parameters that describe the conceptual design of the experiment is shown in Table 1.

The minimum data needed to form an asymmetry is two adjacent data samples with opposite electron beam helicities at the planned 1.92 kHz data-taking rate. This is referred to as a pulse-pair asymmetry, and the width of this distribution (referred to as the random noise width) is what determines the statistical error on the asymmetry after averaging over all pairs. The contributions to the random noise width are shown in Table 2. The design goal is to keep all sources of random noise small compared to the counting statistics width, associated with the number of scattered electrons counted at design luminosity in the two 0.52 msec data taking samples that form a pulse pair.

The raw measured asymmetry needs to be corrected for correlations with beam fluctuations (Appendix A) and leakage from residual transverse polarization in the beam (Appendix B) resulting in the experimentally measured asymmetry A_{expt}. This then needs to be corrected for background processes (characterized by fractional dilution factors f_i^{bkgd} and asymmetries A_i^{bkgd}; see Appendix C for the complete procedure), beam polarization P_b, and an overall normalization factor R_{tot}, which contains contributions from the kinematic factor (Appendix D) and electromagnetic radiative corrections. These corrections are indicated schematically by:

$$A_{PV} = R_{tot}\frac{A_{expt}/P_b - \sum_i f_i^{bkgd} A_i^{bkgd}}{1 - \sum_i f_i^{bkgd}} \tag{3}$$

The projected systematic errors associated with these corrections for the conceptual experimental apparatus design are shown in Tab. 3.

Table 1: *Nominal parameters for the conceptual design of the MOLLER experimental apparatus.*

Parameter	Value
E [GeV]	≈ 11.0
E' [GeV]	2.0 - 9.0
θ_{cm}	50°-130°
θ_{lab}	0.26°-1.2°
$< Q^2 >$ [GeV^2]	0.0058
Maximum Current [μA]	70
Target Length (cm)	125
ρ_{tgt} [g/cm^3] (T= 20K, P = 35 psia)	0.0715
Max. Luminosity [cm^{-2} sec^{-1}]	2.4·10^{39}
σ [μBarn]	≈ 60
Møller Rate @ 65 μA [GHz]	≈ 134
Statistical Width(1.92 kHz flip) [ppm/pair]	≈ 91
Target Raster Size [mm]	5 x 5
Production running time	344 PAC-days = 8256 hours
ΔA_{raw} [ppb]	≈ 0.54
Background Fraction	≈ 0.10
P_{beam}	$\approx 90\%$
$< A_{pv} >$ [ppb]	≈ 32
$\Delta A_{stat} / < A_{expt} >$	2.1%
$\delta(\sin^2\theta_W)_{stat}$	0.00023

2.2 MOLLER Apparatus

A schematic layout of the MOLLER apparatus to be placed in Hall A at JLab is shown in Fig. 4. Here we describe very briefly the function of each subsystem following the trajectory of the beam and scattered electrons.

2.2.1 Polarized Beam

The MOLLER experiment relies on delivery of up to 70 μA of 90% longitudinally polarized, 11 GeV beam, as discussed in detail in Section 3. The polarized electron beam is generated using photoemission from circularly-polarized laser light incident on a doped gallium arsenide photocathode. The desired output was exceeded routinely at Jefferson Lab during the Q_{weak} experiment [11], where $\sim$ 180 μA of $\sim$ 89% polarized beam was routinely delivered by the polarized source. The beam quality in terms of random and helicity-correlated fluctuations must meet specified requirements to achieve the proposed statistical and systematic uncertainties. These goals should be achievable with continued development of the polarized source and accelerator setup and control procedures that worked well in previous experiments.

2.2.2 Beam Polarimetry

Precision electron beam polarimetry at the level of 0.4% is required, as discussed in detail in Section 4. A Compton polarimeter will be used for a continuous measure of the beam polarization with independent

Table 2: *Summary of projected contributions to the pulse pair asymmetry random noise width.*

Parameter	Random Noise (65 μA)
Statistical width (0.5 ms)	$\sim$ **82 ppm**
Target Density Fluctuation	30 ppm
Beam Intensity Resolution	10 ppm
Beam Position Noise	7 ppm
Detector Resolution (25%)	21 ppm (3.1%)
Electronics noise	10 ppm
Measured Width (σ_{pair})	**91 ppm**

Table 3: *Summary of projected fractional statistical and systematic errors on the parity-violating asymmetry.*

Error Source	Fractional Error (%)
Statistical	**2.1**
Absolute Norm. of the Kinematic Factor	0.5
Beam (second order)	0.4
Beam polarization	0.4
$e + p(+\gamma) \rightarrow e + X(+\gamma)$	0.4
Beam (position, angle, energy)	0.4
Beam (intensity)	0.3
$e + p(+\gamma) \rightarrow e + p(+\gamma)$	0.3
$\gamma^{(*)} + p \rightarrow (\pi, \mu, K) + X$	0.3
Transverse polarization	0.2
Neutral background (soft photons, neutrons)	0.1
Linearity	0.1
Total systematic	**1.1**

analysis of scattered photons and electrons providing a pair of measurements with a high degree of independence in systematic errors. This polarimeter will be cross-checked against periodic measurements with a Møller polarimeter using ferromagnetic foil targets. As part of global Hall A and C polarimetry upgrades, the Hall A Compton polarimeter will be upgraded with a new electron detector. Specific upgrades to the Hall A Møller polarimeter will be made to improve the acceptance and optics determination. These include installation of additional collimation and GEM-based tracking in front of the calorimeter.

2.2.3 Liquid Hydrogen and Solid Targets

To achieve the required rate of Møller scattered electrons, a liquid hydrogen target will be used, as discussed in detail in Section 5. Liquid hydrogen (LH_2) is the ideal target because it provides the largest electron thickness for the least amount of radiation length. The target will be 125 cm long and requires a cryogenic system capable of handling $\sim$ 4.0 kW. This will be the highest-power LH_2 target ever constructed, and it builds on the experience with the operation of the Q_{weak} target, which successfully operated up to 180 μA with a total power of 2.9 kW. The final design of the MOLLER target will make use of computational fluid

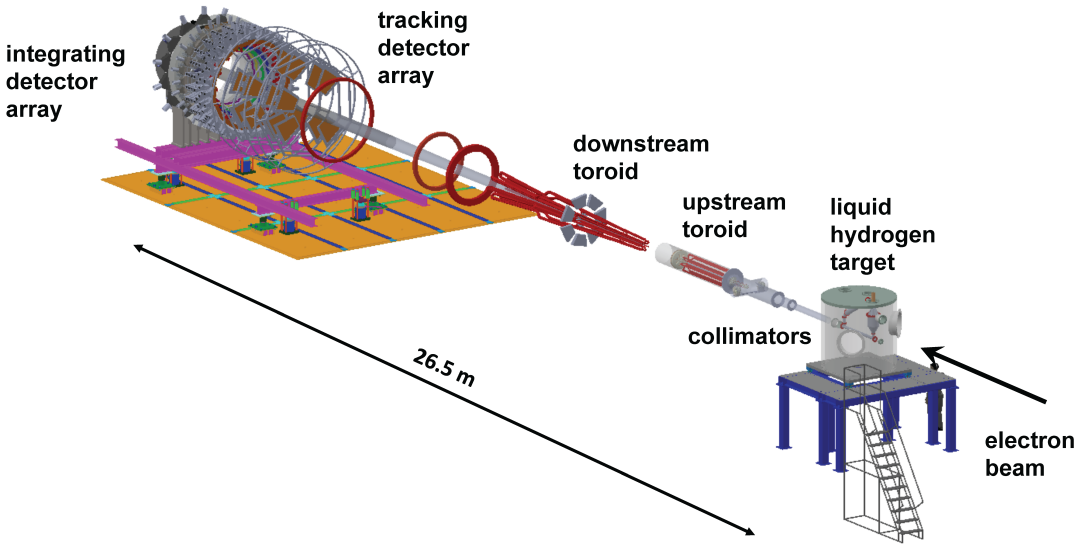

Figure 4: *MOLLER Experimental Apparatus Overview: Schematic layout of the target, spectrometer, and detectors.*

dynamics, as was done with the Q_{weak} target. A system of solid targets will be used along with the GEM tracking system in dedicated studies at lower beam currents to determine the kinematics, to study the spectrometer optics, to check the beam target alignment, to study backgrounds, and to benchmark simulations of radiative effects.

2.2.4 Spectrometer

The spectrometer defines the acceptance of the experiment, and it is optimized to maximize the signal to background, ensuring the ability to deconvolute the asymmetry of the Møller scattered electrons of interest from the background processes. It consists of a pair of 7-fold symmetry toroidal magnets and a set of collimators, discussed in detail in Section 6. The odd-fold symmetry provides $\sim 100\%$ acceptance for the identical-particle Møller scattering process. The toroidal magnets use a conventional resistive copper coil design, and they are housed in evacuated chambers to minimize scattering in the transport of the primary scattered particles through the spectrometer.

2.2.5 Tracking Detectors

The tracking system provides the diagnostic power to calibrate the primary detectors, the spectrometer optics, and the background processes over the full relevant radial and azimuthal ranges, and provides the capability of measuring the acceptance function of the primary Møller-scattered electrons, so that the absolute scale of the parity-violating Møller asymmetry can be determined to better than 0.5%. The system primarily operates at lower beam currents for individual particle counting and consists of these detectors,located downstream of the spectrometer: Gas Electron Mulitplier (GEM) detectors, trigger scintillators, pion detectors based on acrylic Cherenkov detectors, and scanner systems for monitoring the scattered beam profile at higher beam currents. This system is described in detail in Section 7.

2.2.6 Main Integrating Detectors

Downstream of the tracking detectors are the main integrating detectors, described in detail in Section 8. These detectors operate at the full beam current. The thin integrating detectors are an array of detectors based on fused silica ("quartz") as the active element. They consist of six concentric rings, with ring 5 primarily capturing the Møller electron signal, with the other rings providing measurements of background processes that can be used to correct their contribution in ring 5. The shower-max detector is an array of quartz-tungsten electromagnetic sampling calorimeters downstream of the thin quartz integrating detector array, intercepting the same scattered flux as the main Møller ring 5. It provides a supplemental, energy-weighted measurement of the Møller signal with less sensitivity to hadronic and soft backgrounds.

2.2.7 Data Acquisition and Trigger

Described in detail in Section 9, the trigger and data acquisition (DAQ) systems allow for operating the system in both the primary high beam-current integrating mode and low beam-current counting mode. The integrating mode DAQ system primarily interfaces with the integrating ADC modules to record the detector and beam monitor signals during the data-taking at high beam current. The counting mode DAQ is used for low beam-current measurements in which individual electron-scattering events can be observed.

2.2.8 Beam Diagnostics and Monitoring

The systems that MOLLER needs to measure and control the electron beam properties are described in detail in Section 10. Beam position and intensity are measured with existing beamline monitors, with improvements planned for the beam intensity measurements. A beam modulation system is used to generate controlled variations in the position, angle, and energy of the electron beam to measure the response of the detection system to those variations. Scattered beam monitors are detectors deployed to monitor potential false asymmetries in irreducible background resulting from primary scattered beam interacting in downstream collimators, beampipe, and shielding.

2.2.9 Infrastructure and Integration

The MOLLER experiment will be installed and collect data in experimental Hall A at Jefferson Lab. The infrastructure and integration considerations for the experiment are described in detail in Section 11. Infrastructure changes needed for MOLLER are in progress or planned. Upgrades to the Hall A electrical power distribution and low-conductivity water capacities are needed. To satisfy the cryogenic needs, a dedicated transfer line is planned, capable of handling the larger flow from the new End Station Refrigerator (ESR2) under construction. The MOLLER target location requires the modification of the beamline layout and utility platform and routes. Shielding is planned around the target, beamline, and electronics racks, which will require removal of some of the existing HRS magnets.

2.3 Collaboration Organization

The developments that have been described in this section for the MOLLER experiment were carried out by the collaboration during the pre-R&D phase. The collaboration operates under the guidance and oversight of the Executive Board (EB) with the following members: K. Kumar (UMass, Amherst, principal spokesperson), M. Pitt (Virginia Tech, deputy spokesperson and EB Chair), D. Armstrong (Willam and Mary), J. Fast (JLab, Project Manager), C. Keppel (JLab, Hall A/C leader), F. Maas (JGU, Mainz), J. Mammei (Manitoba), K. Paschke (Virginia), P. Souder (Syracuse).

The collaboration has also set up a Working Group (WG) structure with conveners. The current focus is on the physics requirements and subsequent focus will be on individual subsystem commissioning and performance once the construction project is completed. These working groups and conveners are:

- Polarized Source: G. Cates (Virginia) and K. Paschke (Virginia)
- Beam Instrumentation: M. Pitt (Virginia Tech)
- Hydrogen Target: S. Covrig (JLab)
- Spectrometer: J. Mammei (Manitoba)
- Integrating Detectors: M. Gericke (Manitoba) and D. McNulty (Idaho State)
- Tracking Detectors: D. Armstrong (William and Mary) and N. Liyanage (Virginia)
- Hall Integration: C. Gal (Stony Brook), D. McNulty (Idaho State) and P. Souder (Syracuse)
- Polarimetry: K. Paschke (Virginia) and J. Napolitano (Temple)
- Electronics/DAQ/Offline: P. King (Ohio) and R. Michaels (JLab)
- Simulations: R. Beminiwattha (Louisiana Tech)
- Physics Extraction: Y. Kolomensky: (UC Berkeley)

When the MOLLER project organization was developed and personnel were assigned to the various Work Breakdown Structure (WBS) elements and dependencies, key collaborators were designated as Experimental Contacts (EC's). They are listed for the various subsystems in the following:

- Target (WBS 1.02): S. Covrig
- Spectrometer (WBS 1.03): J. Mammei
- Integrating Detectors (WBS 1.04): M. Gericke
- Tracking Detectors (WBS 1.05): D. Armstrong
- Hall Infrastructure and Integration (WBS 1.06): C. Gal and D. McNulty
- DAQ/Online (WBS 1.07): P. King
- Beam Diagnostics/Monitoring (Dependency): M. Pitt
- Offline (Dependency): R. Beminiwattha
- Polarized Beam (Dependency): G. Cates
- Polarimetry (Dependency): K. Paschke

3 Polarized Beam

MOLLER will be a high precision measurement of a fractional change in the electron-electron scattering rate correlated to beam helicity, measured at high luminosity and small angle. The experimental challenge is in some ways similar to those faced by previous parity-violation experiments such as E158 at SLAC and HAPPEX-II, PREX, and Q_{weak} at JLab. Experience on those previous efforts provides the basis for estimating the performance of the polarized beam that will be required for the success of MOLLER. While similar in nature, the beam requirements are more demanding than previous experimental efforts. Even so, previous operational experience suggests that the CEBAF beam will be able to meet that standard.

Present technology, including the results of recent research and development, is expected to be capable, through an evolutionary approach, of meeting the MOLLER requirements. An essential ingredient is the injector upgrade, the centerpieces of which are a new high voltage gun and a quarter-cryomodule. The following sections outline the requirements on the performance of the polarized beam for MOLLER, compared to recent operational experience, and summarize the strategy that will lead to a successful experimental effort. The status of the injector upgrade is summarized in Section 3.5. Appendix E provides a more detailed review of the operational experience as it relates to these requirements.

3.1 Requirements for MOLLER

MOLLER is an extension of a series of high precision parity-violation experiments which typically operate at small scattering angles and measure cross-section asymmetries which are extremely small. One challenge of these experiments is that changes in the beam properties (intensity, position, profile) will change the detected scattered flux. If the changes in the beam are correlated with the electron helicity, the result can mimic the tiny parity-violating asymmetries. While changes are typically measured and corrections are applied, there is a finite precision associated with these corrections, which can be a potential source for systematic error, or a false asymmetry. Helicity-correlated beam asymmetries (HCBA) are therefore a potential systematic error, and a very high level of control of HCBA is required for the precision measurement contemplated here.

There are requirements beyond the specified run-averaged beam asymmetries. In order to achieve the necessary statistical precision, it is necessary to complete individual measurements of the scattering asymmetry very rapidly, so each measurement can occur without a significant changes in the apparatus (for example, a change in the target density). In addition, a high level of beam stability is needed during each measurement, so that an imperfect correction for a beam parameter does not introduce significant additional noise.

Rapid Helicity Flip As described in Sec. 5, the density fluctuations in the liquid hydrogen target are significant at low frequencies, but significantly reduced at frequencies of 1 kHz or above. In order to preserve the statistical power of its high counting statistics, MOLLER is designing around a helicity flip rate of 1.92 kHz. In this case, the integration period for each period of stable helicity is only 520 microseconds long. The helicity flip must be robust, completed significantly before the next integration period begins, and closely matched between the transitions to the two polarization states. In order to maintain a high duty factor, MOLLER aims to keep the "settle" time between integration periods to only 10 microseconds.

Limits on HCBA To first order, the measured asymmetry must be corrected for variations in beam parameters which include intensity, position, energy, or spot-size. The correction can be written as:

$$A_{\rm cor} = A_{\rm det} - A_Q + \alpha_E A_E + \sum \alpha_i \Delta x_i \tag{4}$$

where $A_{\rm det}$ is the asymmetry in the detected flux, A_Q is the beam charge asymmetry, A_E is the helicity correlated energy asymmetry, Δx_i are the helicity correlated position differences, and α_i are the calibration constants, which can be measured through cross correlations and linear regression, or using the beam modulation calibration, in data analysis.

The beam charge asymmetry, A_Q, is controlled using feedback during the measurement. The nonlinearity between the detectors and beam current monitors is typically controlled at the 0.5% level. Given the goal of 0.1 ppb contributed error from intensity corrections, this implies that the grand average A_I must be smaller than 10 ppb. This level of control will require active feedback to the intensity asymmetry, which is a standard technique for parity-violation experiments.

Monte Carlo simulation was used to estimate the sensitivity of the apparatus to beam motion and to energy asymmetry. With the minimum acceptance angle defined by collimators placed 5 meters downstream of the target center, the detected flux in one azimuthal segment is expected to change by approximately 17.0 ppb for a 1 nm shift in the beam centroid. This result is consistent with simple scaling arguments applied to sensitivities measured during HAPPEX-II. The approximate sensitivity to changes in the beam angle is 85 ppb/nanoradian.

The detector for the MOLLER experiment has seven segments and a high degree of azimuthal symmetry. The effect of this symmetry is estimated to be a factor of 10 reduction in sensitivity to beam trajectory; this estimate is conservative to account for detector alignment tolerances. A reasonable goal for any measurement of a small asymmetry is to keep the cumulative correction due to random or helicity-correlated beam motion, averaged over the entire data set, to be no larger than the grand statistical error. A reasonable estimate from previous experience is that position corrections can be made with a precision of better than 10%, and better than 5% for the well-measured energy uncertainty. The associated goals for HCBA are summarized in Table 4.

Spot Size Asymmetry In all the above discussion of beam-related systematic effects, it has been assumed that the dominant component in the scattered flux response to fluctuating parameters is linear. In practice, it is possible that certain second-order effects might be helicity-correlated and thus lead to systematic shifts. One common manifestation of such an effect would be a helicity-correlated difference in the beam spot-size, usually defined as as the gaussian width of the beam distribution σ. We have simulated the effect for the proposed spectrometer/collimator geometry, finding it to be at the level of (12 ppm)$\times\Delta\sigma/\sigma$. There is no technology for directly measuring spot size variation at this level. An upper limit on the helicity-correlated spot-size asymmetry will be demonstrated at the required 10^{-5} level.

Beam jitter The MOLLER goal is to keep beam-related corrections for each individual measurement to be no larger than the statistical uncertainty for that measurement. For the MOLLER 1.92 kHz flip rate, then complementary pairs are measured at 0.96 kHz, with a precision of about 90 ppm. A goal that greatly facilitates a number of diagnostic techniques is to further require that *the beam-related corrections for each of the detector's segments are no larger than twice the statistical width of that individual segment, a width that will be around 200 ppm*. As this goal does not take advantage of the azimuthal cancellation for position and angle sensitivities, it specifies a more strict requirement for beam trajectory noise than consideration of the grand averaged uncertainty.

3.2 The Polarized Electron Source

The polarized electron beam is generated using photoemission due to circularly-polarized light on a doped gallium arsenide photocathode. The polarization of incident laser light selects the polarization of the electron beam, and the rapid flip of electron beam helicity is performed with a reversal of the incident laser

Table 4: *MOLLER goals for corrections for helicity correlated electron beam asymmetries and beam noise.*

Beam Property	Assumed Sensitivity	Accuracy of Correction	Required 1 kHz random fluctuations	Required cumulative helicity-correlation	Systematic contribution
Intensity	1 ppb / ppb	$\sim$1%	< 1000 ppm	< 10 ppb	~ 0.1 ppb
Energy	-1.4 ppb / ppb	$\sim$5%	< 108 ppm	< 0.7 ppb	~ 0.05 ppb
Position	1.7 ppb / nm	$\sim$10%	< 47 μm	< 0.6 nm	~ 0.05 ppb
Angle	8.5 ppb / nrad	$\sim$10%	< 4.7 μrad	< 0.12 nrad	~ 0.05 ppb
Spot Size	0.012 ppb / ppm	-	-	< 10 ppm	~ 0.1 ppb

polarization. The laser polarization is created with an electrooptic Pockels cell, so that reversing the applied voltage flips the sense of polarization.

The voltage applied to the Pockels cell is the only change in the electron beam generation or transport that is correlated to beam helicity. The photocathode quantum efficiency has an analyzing power for linear polarized light, but is symmetric for right- or left-handed circular polarization. The photocathode response is symmetric for circularly polarized laser light, and electron beam transport is unaffected by the electron polarization. It is therefore necessary that any helicity-correlated asymmetry in the electron beam must be directly related to the voltage applied to the Pockels cell or the polarization-sensitive transport of the laser light to the photocathode.

There is significant operational experience in using the polarized electron source for parity-violation experiments at Jefferson Lab. With this experience, a detailed understanding of the sources of HCBA has emerged and led to a sophisticated protocol for systematically reducing or eliminating these effects in the laser optics of the polarized source [65–67].

While the photocathode technology is a key component for generating the polarized electron beam, it is the Pockels cell that generates the robust and rapid polarization reversal which is so critical to a precision asymmetry measurement. The polarized electron sources at SLAC, MIT-Bates, and Jefferson Lab have been using longitudinal KD*P (potassium dideuterium phosphate) Pockels cells for a long, successful operational history [65, 66]. However, most of that history has been at reversal frequencies around 30 Hz. MOLLER is designing around a flip rate of 1.92 kHz, in order to reduce the noise due to density fluctuations in the liquid hydrogen target. This implies that each integration period is only 520 microseconds long.

It is difficult to achieve a fast transition to a stable birefringent state with KD*P, such that transition periods of 60 μs or more are required, imposing an unacceptable loss of efficiency for the MOLLER experiment. The Q_{weak} experiment used a helicity-reversal rate of 960 Hz with a settling time of 70 μs. Shorter settling times were not possible with the KD*P Pockels cell, both due to charge leakage on the surface of the cell and mechanical resonances, excited by the piezoelectric property of crystal under a rapid voltage reversal, which are evident in fast and persistent oscillations in the birefringence of the cell. Pockels cells from other electro-optic materials were tested, but no commercially available Pockels cells were found that came close to the required performance.

In order to overcome this limitation, a pre-project research and development effort by the MOLLER collaboration developed a Pockels cell system capable of meeting the demanding MOLLER requirements [67]. The new system uses RTP (Rubidium Titanyl Phosphate) crystals, which show a fast response, with lower conductivity and low piezoelectric response. RTP Pockels cells operate in the so-called "transverse" configuration, with a large intrinsic birefringence that is modulated using transverse electric fields. In order to control thermal drifts of the multi-wave phase shift of the RTP crystal, Pockels cells are built using two compensating crystals. The RTP crystals are much less uniform than the KD*P crystals we have replaced,

Table 5: *Summary of comparison of MOLLER specifications on random beam property fluctuations to scaled* $\mathrm{Q}_{\mathrm{weak}}$ *measurements.*

Beam Property	MOLLER Specification	$\mathrm{Q}_{\mathrm{weak}}$ Observed
Intensity	< 1000 ppm	500 ppm
Energy	< 108 ppm	6.5 ppm
Position	< 47 μm	48 μm
Angle	< 4.7 μrad	1.4 μrad

and the additional degrees of freedom in the two-crystal transverse design add complications to achieving stable transitions with the high uniformity as required for precision measurements. This led to an innovative design that uses control over electric field gradients to counteract crystal birefringence non-uniformities and provides a method for actuating the beam position. This use of gradient-index steering allows for more precise control of position differences in the laser optics configuration, and also introduces a correction mechanism suitable for position difference feedback.

At present, the RTP Pockels cell is capable of achieving a stable transition in ~ 11 μs, with virtually none of the ringing that is observed with KD*P. This flip time is slightly longer than the intended 10 μs, which would result in only a slight increase in the experimental deadtime, for example, from 2% to 3% if a 15 μs settle period is used.

This system was installed in January 2019 and successfully used for beam operations throughout 2019. The cell was pulsed continuously since its installation, and has shown no signs of degradation in 9 continuous months of operation.

3.3 Random Beam Noise

Expectations for jitter for MOLLER running with 980 Hz pairs can be scaled from $\mathrm{Q}_{\mathrm{weak}}$ experience with 480 Hz window pairs. The summary comparison in Table 5 shows that all of the jitter requirements appear achievable. Recent experience with 11 GeV beam in Hall A suggests that the beam jitter properties for 15 Hz window pairs are similar to the 6 GeV machine.

If noise in a beam parameter is large, then the statistical convergence of beam noise is likely to lead to an average asymmetry that is outside of specification, even if there is no true helicity-correlated systematic difference in the production of the beam. In this case, feedback is required to drive the convergence faster than statistical convergence. This technique has been employed for control of charge asymmetry for every high-precision parity-violating electron scattering measurement. For MOLLER, it is likely to be needed for position difference control as well. The new RTP Pockels cell system provides a new mechanism for precision control of position differences. This system was used for automated feedback during the configuration of the PREX-2 experiment and would be available for use during MOLLER.

3.4 Beam Asymmetries for MOLLER

The so-called "standard" HCBA have traditionally been quoted as the zeroth and first moment of the asymmetry in the beam intensity profile in the experimental hall. These are measured by RF monitors, typically using cavity monitors for intensity and strip-line monitors for position. There is, at present, no monitor that isolates the second moment of asymmetry in the intensity profile, but a bound on the RMS spot size asymmetry is typically quoted using observations of the laser in the polarized source.

The most demanding requirements concern the run-averaged values for the beam asymmetry. Noise (or "jitter") in the intensity or trajectory of the beam obscures the true systematic asymmetry generated at the polarized source, with precision on small beam asymmetries achieved by integrating over periods of time. It is expected that MOLLER will use feedback techniques for both intensity and position differences that will promote faster convergence of statistical noise in the HCBA, as well as greatly reducing any systematic asymmetry.

In addition, there will be several "slow reversals" for the asymmetry measurement. These change the polarization state in the hall relative to the recorded helicity and relative to the voltage applied to the Pockels cell. Three methods will be used: an insertable half-wave plate in the laser optics of the polarized source, spin manipulation with the Wien filter and solenoids in the electron beamline in the low-energy region of the injector, and a small change in the beam energy which changes the $g-2$ spin precession between the injector and the experimental hall by a half-integer rotation. The quoted goals for the run-averaged HCBA are assumed to be averaged over data sets using the slow-reversals, which will further suppress any systematic asymmetries generated in the polarized source. This suppression is most critical for the spot-size asymmetry, which cannot be directly measured and must be bounded to provide a large margin of safety.

The requirements for these HCBA are summarized in Table 6, along with the beam parameters previously achieved in the HAPPEX-II [33] (3 GeV in 2005), $\mathrm{Q_{weak}}$ [68] (1 GeV in 2010-2012), and PREX-2 (1 GeV in 2019)experiments. The anticipated improvements that will lead to success for the MOLLER experiment are described in more detail below.

Intensity Asymmetry For previous measurements, the intensity asymmetry was controlled well within required limits. Intensity jitter has not been found to be a limiting factor. The limits for control of the intensity asymmetry will be determined by feedback efficiency and data set selection. With a greater focus on this parameter, it is expected that current technology will be able to meet the MOLLER intensity asymmetry requirement.

Position and Angle Differences In previous experiments, position and angle differences averaged to small values that approach the design values quoted for the MOLLER experiment. The MOLLER collaboration has set an ambitious goal to achieve position differences of 20 nm or less in the early injector. In addition, it is expected that cancellations via slow reversals will further suppress position differences by a factor of 10 (this is consistent with past experience). The collaboration also aims for a factor of 100 suppression of position differences from the suppression of transverse beam phase space in the relativistic boost, a process

Table 6: MOLLER beam asymmetry requirements compared to the approximate magnitude of run-averaged asymmetries achieved in previous experiments. The quoted $\mathrm{Q_{weak}}$ results are averaged over the two experimental runs. PREX-II is still under analysis; the results are preliminary, and will change in a final analysis only as the the weighting and composition of the final accepted data set changes. The uncertainties quoted for PREX-II represent a "radius of convergence" of random beam jitter, showing that the trajectory differences are consistent with convergence of random noise with zero systematic offset.

	HAPPEX-II [33] (achieved)	$\mathrm{Q_{weak}}$ [68] (achieved)	PREX-II (achieved)	MOLLER (required)
Intensity asymmetry	400 ppb	30 ppb	25 ppb	10 ppb
Energy asymmetry	0.2 ppb	0.4 ppb	1 ± 0.6 ppb	< 0.7 ppb
position differences	3.4 nm	2.5 nm	$< 2 \pm 2$ nm	0.6 nm
angle differences	0.4 nrad	0.1 nrad	$< 0.2 \pm 0.4$ nrad	0.12 nrad
size asymmetry (quoted)	–	$< 10^{-4}$	$< 10^{-5}$	$< 10^{-5}$

generally referred to as adiabatic damping. Finally, it expects to use feedback to drive faster convergence of the position noise, and this should reduce position difference an order of magnitude or more.

Taken together, these goals would imply that position/angle differences at the level of 0.002 nm (and approximately 0.0002 nrad) would be achieved. This would be a full factor of 500 better than the MOLLER goal. Due to this extremely high safety margin, the variety of suppression methods are not all required to operate simultaneously in order to achieve the MOLLER goal.

The goal of < 20 nm in the injector would about a factor of 5 better than what has been previous achieved for $\mathrm{Q_{weak}}$ and for PREX-I (before cancellation with slow reversals). The introduction of a new transverse RTP Pockels cell sytem specifically designed to meet the MOLLER requirements, and in particular the incorporation of control of the steering effects caused by electric field gradients, provide sufficient degrees of freedom to suggest that 20 nm is achievable. Furthermore, this control of voltage dependent steering is a precise mechanism for position control which will be suitable for feedback. Recent beam tests have shown that position differences of about 5 nm (at a specified beam position monitor) can be achieved in 30 minutes. Furthermore, position differences have been bounded to $<$30nm in the first 10 beam position monitors in the early injector using the new RTP Pockels cell.

$\mathrm{Q_{weak}}$ used helicity-correlated correction magnets to reduce position differences. The system was stable, so that it was only necessary to adjust the corrector set points daily. This slow update speed would not improve the speed of statistical convergence. The use of the transverse RTP Pockels cell with dynamic feedback will be a significant improvement and was employed successfully during PREX-II.

HAPPEX-II saw a reduction of position differences due to adiabatic damping from the injector to the hall of a factor between 10 and 30. This is compared to a theoretical maximum reduction (in the 3 GeV hall, compared to the 100 keV injector) of about 95, so HAPPEX-II realized 10-30% of the benefit from adiabatic damping[1]. For MOLLER at 11 GeV, it is expected that the injector will be higher energy (up to 200 keV in the injector), suggesting that the emittance should be reduced by a factor of $p/p_0 \sim 22,000$, and the position differences by about a factor of 150. Simply scaling this maximum compared to the HAPPEX-II experience suggests a factor of 15-50 improvement in position differences[2].

For MOLLER, it is reasonable to expect that the match to design optics will be much better than in the 6 GeV era. One significant factor is improvements in beam diagnostic procedures, such as the Raytrace utility for measuring beam emittance throughout the accelerator. In addition, a planned upgrade in the injector will increase the initial acceleration from 100 keV to 200 keV and reduce phase-space coupling in the injector from reorganization of injector optics and new 1/4-cryo cavity, which will together reduce the single largest source of the phase space correlations that limit the benefits of the relativistic boost. These improvements will be combined with recently developed analysis techniques that make matching more deterministic and routine, such as is used in the Optics Restoration and Finalization Procedure (ORFP) matching. It is reasonable to expect that the optics should more closely match design and the adiabatic damping should be improved relative to previous attempts. While it has not been proven that the nominal goal of a factor of 100 can be achieved, it is a reasonable target. The technical risk in not achieving it is covered by the improved source laser control, feedback and slow reversals.

As summarized in Table 6, the MOLLER requirements on beam asymmetries are reasonably close to what has been achieved in recent operational experience. Of particular note are the results from PREX-II. Though relatively brief (only about 20 beam-days), the beam asymmetries were consistent with zero

[1] $\mathrm{Q_{weak}}$ did not run with optimized design matching. The position differences in the injector were as small as had yet been achieved during JLab operations, but in the experimental hall there was no evidence of adiabatic damping, in fact, the position differences were measured to be larger than in the injector.

[2] In this discussion, the increase in emittance due to synchrotron radiation at high energy has been neglected. The helicity-correlated position differences are not affected by the addition of this stochastic noise - it is not truly the emittance of the beam that determines the reduction of the HCBA, but rather the compression of the transverse dimension of motion due to the relativistic boost. The addition of non-helicity-correlated noise (through synchrotron radiation) is not relevant in this case.

systematic asymmetry in beam trajectory. The beam asymmetry requirements for MOLLER all appear to be well within existing technology.

Spot-Size Asymmetry There has not been a method for measuring, or adjusting, the spot size asymmetry for any previous experiments. Bounds have been placed on the possible helicity correlated spot-size asymmetry through measurements of the spot-size asymmetry on the laser beam, including both the intensity and "Δ-phase" polarization profiles, with a safety margin to account for reasonable models of photocathode and vacuum window non-uniformity. The slow-reversals are also an important component of this suppression, especially the injector spin manipulation and $g-2$ reversals which will leave the configuration of the source laser optics untouched. Measurements from the configuration of the polarized source for the PREX-II experiment have bounded the possible asymmetry at the level required for MOLLER. This approach will be used again to achieve the required spot-size asymmetries for the MOLLER experiment ($< 10^{-5}$). The slow-reversals provide additional suppression beyond this, giving a safety margin.

Beyond the bound that will be achieved on the laser spot size asymmetry, there is an additional suppression of this effect for the MOLLER experiment due to the injection of stochastic noise through synchrotron radiation. This noise increases the emittance of the beam, but does so in a manner which is independent of the helicity-correlated asymmetries from the polarized source. The emittance at the high energy hall is seen to be a factor of 10 times larger than the minimum emittance observed, before significant synchrotron emission noise is added. This can be modeled as an addition of noise σ_S to the original beam size in the injector σ_I:

$$\sigma = \sqrt{\sigma_I^2 + \sigma_s^2} \tag{5}$$

The difference in the spot size in the hall is:

$$\delta\sigma = \sqrt{(\sigma_I + \delta\sigma_I)^2 + \sigma_s^2} - \sqrt{(\sigma_I - \delta\sigma_I)^2 + \sigma_s^2} \tag{6}$$

A helicity-correlated change in the spot-size has a geometric effect that scales with spot size, but the beam spot size will be fixed by the optical design. In this case, it is the spot-size asymmetry that matters. The spot size asymmetry in the hall that compares to that in the injector as

$$\frac{\delta\sigma}{\sigma} = \left(\frac{\sigma_i}{\sigma_s}\right)^2 \frac{\delta\sigma_i}{\sigma_i} \tag{7}$$

One way think of this is that the synchrotron emittance growth allows for a reduction in the optical magnification of the injector differences, while maintaining the same spot size on target. This leads to a factor of ~ 10 suppression in the spot size asymmetry at high energy, relative to the bounds achieved at lower energy. This suppression provides an additional margin of safety over the bound set in studies of the source laser optics.

Asymmetric beam halo The $\mathrm{Q}_{\mathrm{weak}}$ experiment saw a significant false asymmetry that was ascribed to a helicity-correlated change in the beam distribution on target. This is often referred to as a "halo" effect. This false asymmetry was seen in three separate detector systems: the main detectors, small angle monitors near the primary beam, and bare PMTs placed out of the signal region but near the main detectors to test for ambient backgrounds. The ratio between the false asymmetry observed in each detector system was fairly constant throughout the run. While the consistency between the detector systems allowed for sufficient correction for the $\mathrm{Q}_{\mathrm{weak}}$ result, the characteristics of the beam that led to this effect were never precisely determined. Dedicated tests were consistent with the hypothesis of a beam halo or tail consistent interacting with the beamline or collimation, but not definitive about the shape, extent, or source of the halo.

There is more than one candidate for the fundamental cause of such an asymmetric beam halo. Injector studies showed asymmetries in the longitudinal RF beam bunch profile, but it is not yet clear how to connect this to the observed asymmetric halo effects. Other models under consideration are bleed through from other halls, or fringes in the laser beam spot on the source photocathode. Monitors of small angle scattering with line of site to beam collimation and the target are essential to diagnosing such an effect. Such small-angle monitors in the existing 11 GeV beampipe will be used to search for an effect in future beam studies, most notably during the upcoming CREX experiment in 2020.

The MOLLER spectrometer by design, removes any "single bounce" path from the target or primary beam collimator to the Møller detectors, which should reduce sensitivity to similar beam effects. Similarly, the downstream beampipe and spectrometer components are well shielded from line of sight to the target by tight beam and acceptance collimation, and so the small amount of rescattering from other components will not be highly sensitive to halo. In addition, the high level of detector segmentation, with a wide range of signal rates over the azimuthal and radial distribution, would assist in diagnosing and monitoring any effect that does become manifest. While it is not yet possible to rule out a source of asymmetric halo for MOLLER, the experiment is designed to limit sensitivity while providing improved diagnostics.

3.5 Injector Upgrade

An upgrade is planned for several key components of the injector. The electron source gun currently operates at about 100 keV accelerating potential. An upgraded gun will be installed and run with a 200 keV potential. The higher electric field has been shown to increase the lifetime of the activated photocathode, which will allow for a more stable source configuration for MOLLER. In addition, the higher energy in the early injector will improve beam transport. The reduction in space charge effects in the beam will eliminate the need for an RF pre-buncher, which in present operation is a complicating element in the early injector. In conjunction with the gun update, the 1/4 cryounit accelerating cavity will be replaced. This is the first RF accelerating element, and integrates RF capture and acceleration to 10 MeV. The new cavity will reduce the significant x/y "skew" coupling relative to the existing cavity. This coupling has been a major impediment to reliably achieving a match to design optics through the injector. The Wien rotators will also be upgraded for higher fields to match the new gun voltage and more uniform optical elements. The injector upgrade will occur in two phases, with Phase 1 taking place during the long accelerator shutdown in October 2020 - May 2021, and Phase 2 planned for the next long accelerator shutdown after that.

All of these upgrades will benefit MOLLER. The higher gun voltage should better transmit the beam through apertures in the injector with less clipping, and the Wien rotator upgrade along with the removal of the pre-buncher will lead to much more efficient operation of the injector spin flip. The improved transmission and reduced skew coupling will improve the match to design optics, and so improve the benefits to HCBA suppression from adiabatic damping.

4 Beam Polarimetry

The longitudinal polarization of the 11 GeV electron beam is expected to be about 90%, with some variation depending on the specific details of the GaAs photocathode at the polarized electron source. The beam polarization may vary at the 2% level over the duration of a specific photocathode's lifetime. The polarization will be oriented to within a degree of longitudinal to avoid an azimuthal scattering asymmetry associated with transverse polarization components (see Appendix B). Since the measured parity-violating asymmetry is directly proportional to the electron beam longitudinal polarization, it is important to measure the polarization to high precision. The goal is to know the absolute polarization with robust control of systematic uncertainties to about 0.4% and to continuously monitor this polarization for significant variations. Members of the MOLLER collaboration have accumulated extensive experience [84] with two existing polarimeters in Hall A which will be used to meet these goals.

Compton polarimetry is a very promising technique for high precision polarimetry at beam energies above a few GeV. Beam interactions with a photon target are non-disruptive, so Compton polarimetry can be employed at high currents as a continuous polarization monitor. The photon target polarization can be measured and monitored with a very high precision, and the scattering between a real photon and free electron has no theoretical uncertainty, such as the atomic or nuclear effects which can complicate other measurements. Radiative corrections to the scattering process are at the level of 0.3% and are very precisely known. Compton polarimetry at JLab has previously achieved 0.6% precision on electron beam polarization and provided the basis for estimating that this technique is capable of achieving precision better than 0.4%. Several important upgrades to the Hall A Compton polarimeter will be completed by JLab before MOLLER operations begin.

The Møller polarimeter measures the scattering of beam electrons from polarized atomic electrons in a ferromagnetic foil. The use of a solid target is disruptive to the beam and limits the technique to low average beam current, but the approach provides a rapid, high statistics measurement with systematic uncertainties that are entirely independent from Compton polarimetry. The Hall A Møller polarimeter is operationally robust and commonly used by experiments with polarized scattering. An upgrade to the detection and collimation of the Møller polarimeter will be completed to support the MOLLER experiment.

The existing polarimeters and these plans for future improvements are described below. In Appendix F we more completely describe the methods that will be used to achieve high precision.

4.1 The Hall A Compton Polarimeter

As pictured in Fig. 5, the Hall A Compton polarimeter [85] is located in a chicane, about 15 meters long, which deflects the beam to insect with a laser cavity 21 cm below the primary (straight-through) beamline. After passing the electron-photon interaction point, the electron beam is bent about 2.3 degrees by the third chicane magnet to be restored to the primary beamline. Electrons scattered from the photon target are separated from the primary beam by this bend and detected using silicon microstrips just before the fourth chicane magnet. Scattered photons pass through the bore of the third chicane magnet to be detected in a calorimeter.

The photon target is a 0.85 cm long Fabry-Perot cavity crossing the electron beam at an angle of 1.4°. The laser system produces green (532 nm) light. Power levels of 10 kW have been stored in this resonant optical cavity for intersection with the electron beam, while more typical operation uses about 2 kW of stored power. The laser light can be toggled between opposite polarizations of highly circularly polarized light. The feedback loop which locks the laser to the cavity resonance can be disabled to dump the stored light and enable measurements of background from all non-Compton-scattering processes. To reduce overhead from the time required to re-lock the cavity, the transition between laser states is typically performed with a period of 1-2 minutes. The polarization of the transmitted light from the locked cavity and the reflected

light from the unlocked cavity are each monitored and can be used to characterize the laser polarization at the interaction point.

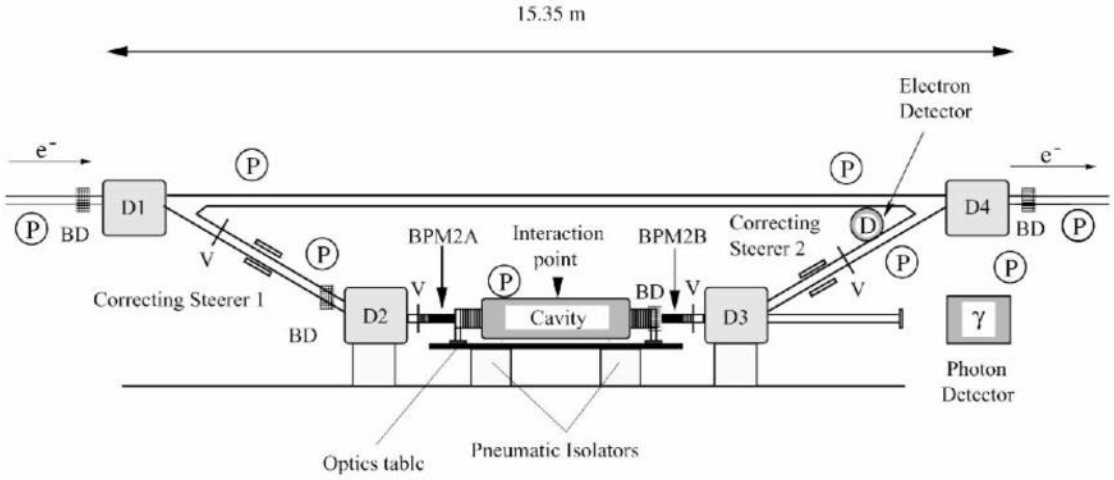

Figure 5: *Schematic of the Hall A Compton polarimeter. Figure from [85].*

At 11 GeV, with 2 kW stored laser power, the Compton-scattered rates would be approximately 1.5 kHz/μA and the asymmetry will range from 17.8% to -4% over the energy spectrum. If backgrounds remain comparable to recent operation, statistical precision of 0.4% would be possible in about 5 minutes, depending on the specific detection and analysis approach which is considered.

The vacuum in the interaction region is at the level of few $\times 10^{-8}$ torr, implying a photon background rate due to Bremsstrahlung scattering from residual gas of around 5 Hz/μA. The dominant source of background in the photon detector is thought to be tails of the beam halo distribution interacting with the apertures in the interaction region. In contrast, for the electron detector the background is thought to be dominated by energy tail or position halo of the primary beam since electrons from aperture scattering would presumably not cleanly transit the third dipole. When well-tuned, the background rates in the photon and electron detectors have been seen to be roughly similar: around $<$100 Hz/μA in recent use.

There is a long operational history for the Hall A Compton polarimeter, including measurements during the 2009-2010 runs of HAPPEX-III [86] (3 GeV) and PREX [87] (1 GeV beam energy) with precision better than 1% [88]. One significant innovation since 2010 has been the implementation of a technique for determining the laser polarization inside the resonant optical cavity with high precision [89]. A photon calorimeter matched to the higher energy was installed. Additional collimation and magnetic extensions were added to reduce the synchrotron light flux and energy into the photon calorimeter. The polarimeter has also been operated since the energy upgrade with 10.6 GeV beam during the 2016 run period and functions with expected backgrounds and sufficient control of synchrotron light.

The polarimeter will require a new electron detector to meet the precision goal for MOLLER. At present, electrons are detected in 4 planes of silicon microstrip detectors located just before the 4th dipole. Custom readout electronics pre-amplify and discriminate signals from the microstrips for readout with an FPGA DAQ module. The system is operating with low efficiency and excessive noise, and cannot provide the required uniform and efficient detection.

Plans for the Hall A polarimeter upgrade include an upgrade to install new diamond microstrip detectors. Such microstrips were successfully used for the Hall C Compton polarimeter in the $Q_{\rm weak}$ measurement [89].

Table 7: *Goals for systematic uncertainties for the Hall A Compton polarimeter at 11 GeV. Topics marked * are common systematic uncertainties between the photon and electron analyses, while the others are largely independent between the detector systems.*

Relative error (%)	electron	photon
Position asymmetries*	-	-
E_{Beam} and λ^*_{Laser}	0.03	0.03
Radiative Corrections*	0.05	0.05
Laser polarization*	0.20	0.20
Background / Deadtime / Pileup	0.20	0.20
Analyzing power Calibration / Detector Linearity	0.25	0.35
Total:	0.38	0.45

In this upgrade, the front end amplifier/discriminator boards would be remade to be optimized for the signal size and shape expected from the diamond, while the readout system would otherwise remain the same.

An alternative development for silicon pixel detectors based on HVMAP (high voltage monolithic active pixel) technology is also underway. These detectors would incorporate amplifier, discriminator, and multiplexed readout circuitry on the same radiation-hard silicon substrate as the pixel detectors. An FPGA readout of the multiplexed signal would be designed to implement tracking and geometry cuts for the 2-D readout. A prototype system is currently being developed at the University of Manitoba.

With both a functional electron detector and a photon detector, Compton scattered events can be measured with each system independently, and also using both systems together in coincidence. The potential systematic uncertainties in measurement of the asymmetry or calibration of the experimental analyzing power are quite independent between the electron and photon analyses, so the polarimeter will provide two nearly independent measurements of the electron polarization with high precision. The goals for the systematic uncertainties from the Compton polarimeter system are shown in Tab. 7.

4.2 Møller Polarimetry

Møller polarimetry provides the second arm of our two-prong approach to a precision measurement of the beam polarization. The ultimate precision goal of this polarimeter is the same as for the Compton system, but the technique is entirely different and data will be taken in short, dedicated runs at low current. Therefore, the two measurements are complementary and will provide a convincing cross check.

This approach uses polarized Møller scattering to determine the beam polarization, that is

$$\vec{e^-}_{\mathrm{Beam}} + \vec{e^-}_{\mathrm{Target}} \rightarrow e^- + e^-$$

where both final state electrons are measured in coincidence. Reaction kinematics are kept close to 90° in the center of mass, where the analyzing power for this reaction is very large (7/9) and perfectly calculable in quantum electrodynamics, including radiative corrections. In the Hall A Møller spectrometer, the electrons are momentum-analyzed in a QQQQD magnetic spectrometer, where the first two quadrupoles separate the pair in the horizontal plane, and the second two focus the pair into the dipole. Segmented calorimeters at the dipole exit detect the two electrons.

A schematic of the Møller polarimeter spectrometer is shown in Fig. 72 in Appendix F.2. This spectrometer was integral for the successful run of PREX-II in Summer 2019, which required precision in beam

Table 8: *Goals for systematic uncertainties for the Hall A Moller polarimeter at 11 GeV.*

Systematic effect	Relative error (%)
Target polarization	0.25
Analyzing power	0.20
Levchuk effect	0.10
Target heating	0.05
Background / Deadtime / Pileup	0.20
Total:	0.40

polarization at the level of 1%. It will also be a critical component of the CREX run period in 2020. These run periods, and our preparations for them, provided a wealth of information on how to optimize the spectrometer and the overall polarization measurement system.

The beam polarization $P_{\rm Beam}$ is determined by measuring the beam helicity asymmetry $A_{\rm Meas}$ in the Møller scattering reaction and using the relation

$$A_{\rm Meas} = P_{\rm Beam} P_{\rm Target} \langle A_{zz} \rangle$$

where $\langle A_{zz} \rangle$ is the analyzing power for the fundamental reaction, averaged over the spectrometer acceptance, which we determine with a thoroughly verified Monte Carlo simulation. The measured asymmetry $A_{\rm Meas}$ is determined in the same fashion as the parity violating asymmetry. This includes running long enough to obtain sufficient statistical precision, and applying corrections for various systematic effects such as beam motion, background, and deadtime.

The main challenge of precision Møller polarimetry is finding the best target for polarized electrons. Historically, this has been accomplished using thin foils of some high μ alloy, which are easily polarized to saturation with modest applied magnetic fields. Magnetic boundary conditions imply that the foil polarization is in the plane, so in these applications the foil is tilted at an angle that allows a large component in the beam direction while maintaining a practical design that allows the beam to pass through unimpeded. Precision better than a few percent, however, is not possible in this kind of arrangement. Precise knowledge of the necessary magnetization parameters for these high μ alloys is not available, and the tilted foil complicates things further, including the admission of transverse components.

Instead, we use a "brute force" polarized foil target, made of pure iron held in a > 2.5 T magnetic field, with the foil perpendicular to the beam direction [101–104]. The fundamental magnetization parameters of iron are known well enough to determine the spin polarization of the target, including corrections for orbital angular momentum and heating due to the incident electron beam. The holding field is produced by a superconducting Helmholtz coil pair, in a self contained helium supply and cryostat. Saturation magnetization is demonstrated from measurements of $A_{\rm Meas}$ as a function of the holding field.

Our knowledge of the magnetization of pure iron, based on existing data sets [100, 105–108], is shown in Fig. 71 in Appendix F.2. We are looking into ways to improve the precision further. Table 8 is a brief summary of our target systematic errors for Møller polarimetry. A more complete description is given in Appendix F.2. Of particular note is the so-called Levchuk effect [109]. Only the outer electrons in the iron atom are polarized in the presence of an external field. The upolarized inner electrons have much higher intrinsic momentum, and this has a significant effect on the outgoing scattered electron pair, which has a very small opening angle in the laboratory frame. We take an approach which attempts to focus *all* scattered electrons into the detectors, thereby minimizing the Levchuk effect. This worked well for the PREX-II and

CREX conditions at 0.95 and 2.2 GeV incident electron energies. We are currently optimizing the Møller spectrometer for 11 GeV operation with respect to this effect.

5 Liquid Hydrogen and Solid Targets

After acceleration to 11 GeV, the electron beam will impinge on a liquid hydrogen (LH_2) target. Hydrogen is the ideal source of target electrons for two reasons. First, it provides the greatest electron target thickness for the least radiation length. Secondly, the irreducible backgrounds are confined to radiative electron-proton elastic and inelastic scattering, which are relatively well-understood. Scattering off other nuclei would include radiative elastic scattering ($\propto Z^2$), breakup channels and scattering off neutrons, which would introduce significant systematic errors due to unknown and potentially large electroweak couplings.

5.1 MOLLER Target Requirements

The physics requirements for the statistical error and systematic error contribution from background processes set the target requirements. To obtain the required ~ 134 GHz rate of Møller electrons between a center of mass scattering angle of $\pm 40^\circ$ about 90° with an incident 11 GeV beam and available beam current, 9 gm/cm^2 of target thickness is required. Liquid hydrogen (LH_2) is the ideal target because it provides the largest electron thickness for the least amount of radiation length. Further, using a thick $Z > 1$ nuclear target would result in beam electrons scattering off neutrons, leading to potentially large inelastic asymmetry backgrounds with poorly known electroweak couplings. On the other hand, backgrounds from hydrogen are confined to radiative electron-proton elastic and inelastic scattering, which are relatively well understood.

The target design must also be capable of keeping the overall relative density reduction $< 1\%$ at the operating beam current to avoid count rate loss. Relative density fluctuations must be kept to <30 ppm to keep this source of random noise well below the counting statistics contribution in the random noise width. The target cell needs to be aluminum with entrance and exit windows no thicker than 0.13 mm (0.005 in) in order to achieve our systematic error goals associated with this background. The requirements on the aluminum wall thickness are looser because the incident beam and scattered particles of interest don't pass through the target cell walls but only through the end windows.

The performance requirements of the target that are driven by the statistical and systematic error goals are summarized in Table 9. The resulting nominal specifications of the proposed LH_2 target (and relevant associated beam parameters) are shown in Table 10. A description of how the proposed target will be designed and how previous target experience and Computational Fluid Dynamics will be used to assess its ability to achieve the performance requirements are provided in Appendix G.

Table 9: *Physics-driven requirements for the MOLLER target.*

Parameter	Value
Nominal Luminosity @65 μA	$2.2{\cdot}10^{39}$ cm^{-2} sec^{-1}
Relative density reduction @ 70 μA	$< 1\%$
Density fluctuations @1920 Hz	< 30 ppm
Aluminum end window thickness	≤ 0.13 mm

Table 10: *MOLLER LH_2 target and beam nominal specifications to achieve performance requirements.*

Target Parameters		Beam Parameters	
cell length	125 cm	I, E	70 μA, 11 GeV
cell thickness	8.93 g/cm^2	raster	5 mm x 5 mm
radiation length	14.6%	beam spot	100 μm
p, T	35 psia, 20 K	detected rate	134 GHz
ϕ acceptance	5 mrad (0.3°)	helicity flip rate	1920 Hz
target power	4000 W	beam power	3200 W
Al body wall thickness	< 0.25 mm		
Scatt. chamber vacuum	$< 10^{-5}$ torr		

5.2 Liquid Hydrogen Target Overview

In order to achieve the necessary rate, about 9 g/cm^2 of LH_2 is needed, making the target cell in beam 125 cm long, which in turn requires a cryogenic target system capable of handling a heat load of ~ 4 kW. This is far larger than the typical ~ 1 kW targets that are routinely in use and about 1.33 times larger than the LH_2 target for the Q_{weak} experiment.

Although the MOLLER target cell length makes it closer to the SLAC E158 LH_2 target cell, the target power budget makes it closer to the Q_{weak} LH_2 target. The SLAC E158 target was designed with a power budget of less than 1 kW to mitigate the target noise from the 120 Hz pulsed beam at SLAC. The Q_{weak} target was designed with a power budget of 2.5 kW to mitigate the target noise at 960 Hz from a CW beam. The Q_{weak} target design, engineering and commissioning are considered precursors to the MOLLER target ones. Almost the same team that delivered the Q_{weak} target will work on delivering the MOLLER target system.

A diagram of the MOLLER target system is shown in Fig. 6. A conceptual design of the target vacuum chamber is shown in Fig. 7. At the heart of the target system is the target loop. A conceptual design of the MOLLER target loop is shown in Fig. 8. During beam operations the target loop will be located inside the target vacuum chamber. The main components of the target loop are: the target cell, the LH_2 pump, the heat exchanger and the high power heater. The target loop is connected, via a gas panel inside Hall A, with a large buffer of hydrogen gas residing in the storage tanks outside Hall A. The target loop and the hydrogen storage tanks form an isocoric system designed to mitigate potential over and under-pressure events. A motion mechanism is located on the top of the target vacuum chamber, not shown in Fig. 7, provides a range of motion of about 45 cm in the vertical direction. The target lifter positions the 125 cm long LH_2 cell in beam, and provides various other positions in beam for optics and background studies targets and a position with no target on the beam line to be used for beam tuning.

The most important target design consideration is the suppression of LH_2 density fluctuation at the timescale of the helicity reversal rate. Preliminary estimates based on operational experience with the Q_{weak} target suggest that density fluctuation can be maintained at $\lesssim 30$ ppm at 1.92 kHz, corresponding to about 5% excess noise to counting statistics. In the following subsections, we discuss some of the aforementioned technical considerations. A more detailed approach is presented in Appendix G.

5.3 Target Parameters

The MOLLER experiment at 11 GeV has a 125 cm long liquid hydrogen target cell. The design beam intensity is 70 μA and the nominal beam raster size is 5 mm x 5 mm. The nominal running point for LH_2 in

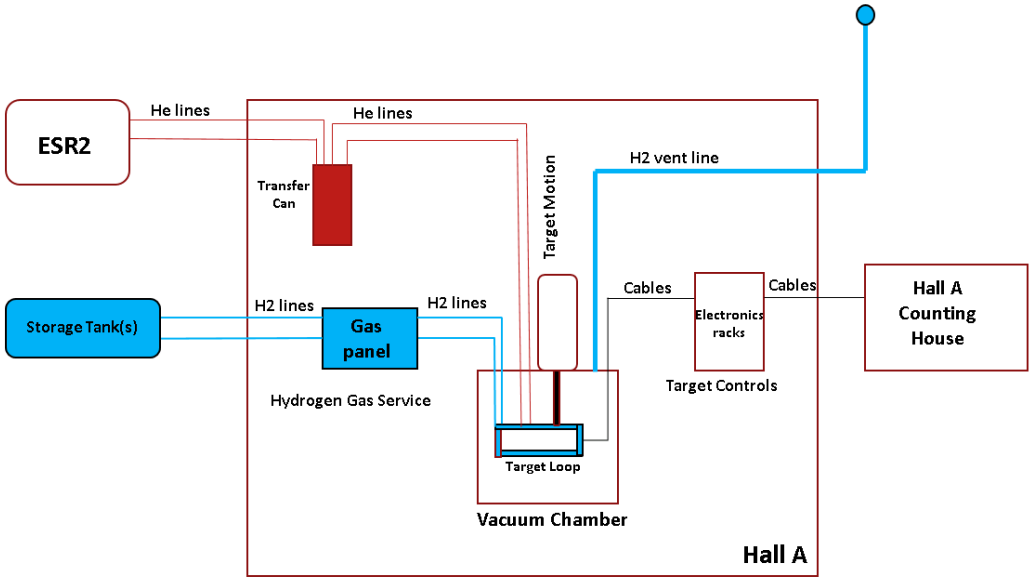

Figure 6: *A diagram of the MOLLER target system: Vacuum chamber, Hydrogen gas service, Helium gas service, Target loop, Target Motion and Target controls.*

the thermodynamic phase space (p, T) is 35 psia (2.38 atm) and 20 K. In these conditions the liquid is 3.7 K subcooled and its density is 71.5 kg/m^3. The target thickness is 9 g/cm^2 and its radiation length is 14.6%. The heating power deposited by the electron beam in the target cell is given by

$$P = I\rho L\frac{dE}{dx} \tag{8}$$

where ρL is the nominal target thickness in beam, I is the beam intensity and dE/dx is the average energy loss through collisions of one electron in unit target thickness. If $dE/dx = 4.97$ MeV/(g/cm^2) for electrons of 11 GeV in LH_2 then $P = 3.2$ kW. For an Al target cell made with beam entrance and exit windows of 0.127 mm (0.005 inches) each, the heat deposited by the beam in the windows, calculated with Eq. 8, is 6 W per window, which is about 0.25% of the target power budget. The nominal parameters of the target and beam are in Tab. 10.

In order to minimize target density variations, all high power LH_2 targets run in a closed feedback loop with the high power heater, allowing a constant heat load on the target to be maintained over time. The heater needs to account for beam heating and target power losses to the environment (such as radiative and viscous losses) and to maintain a cooling power buffer for the normal operations of the feedback loop. Based on experience with previous such targets, the losses and the buffer account for about 20% of the beam heating. Taking this into account the MOLLER target is rated for 4000 W of cooling power in nominal running conditions, which is 1.33 larger than the Q_{weak} target power rating, and by far the most powerful LH_2 target ever built and with the most stringent requirements on systematic effects. Cold helium gas from the End Station Refrigerator 2 (ESR2) will deliver the 4 kW of cooling power to the MOLLER target heat exchanger. The couterflow heat exchanger, which is part of the MOLLER target loop, will transfer the enthalpy from hydrogen to the refrigerant (helium gas) to keep the target condensed and stable. During operations the target loop fluid is kept in a state of forced convection by an immersed LH_2 pump, see Fig. 8. The pump mitigates fluid density variations in the target cell due to beam heating and ensures an efficient heat transfer

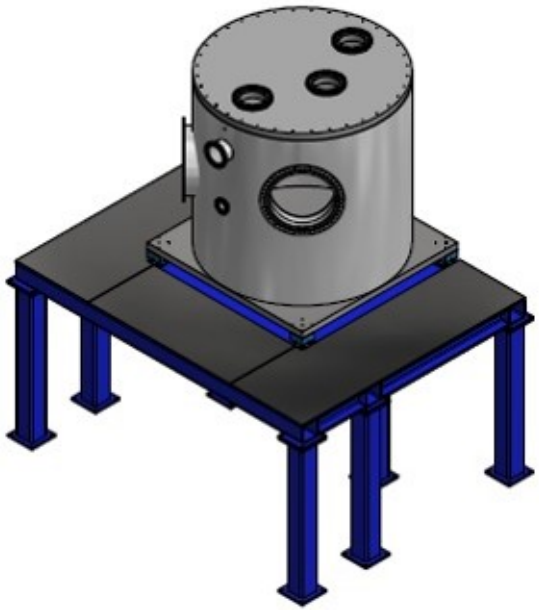

Figure 7: *CAD model of the Moller target vacuum chamber on its stand. The chamber contains the 125 cm long target cell, the target loop and the optics targets. The top plate accommodates the target motion mechanism, feedthroughs for hydrogen and helium gases and for target instrumentation.*

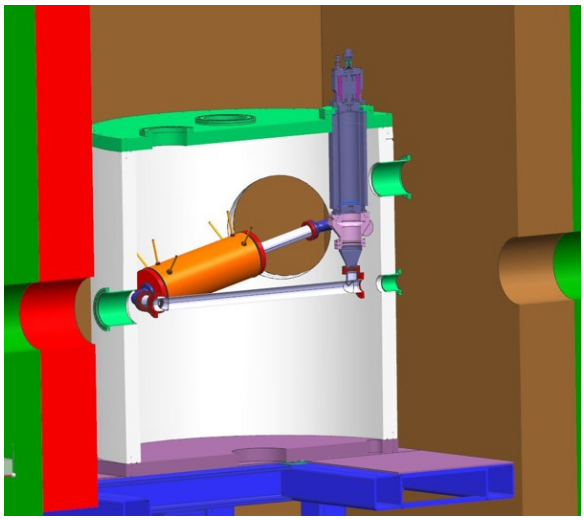

Figure 8: *A CAD conceptual design of the target loop. The loop is remotely movable in the vertical direction with a range of motion of about 45 cm by the target motion mechanism. The main components of the target loop are: cell, heat exchanger, liquid hydrogen pump and high power heater. The optics targets are coupled to the target loop (not shown in this picture).*

in the heat exchanger. If the pump stops spinning the LH_2 in the target cell reaches saturation in about 6 s with the beam on target.

5.4 LH_2 Density Effects

The MOLLER target uses LH_2 as the target material and it thus contributes two important systematic uncertainties to the physics measurement: density reduction and density fluctuation. The equation of state of the target fluid in steady-state isobaric conditions is $\rho(p,T) = \rho(T)$. The density reduction is the effect of the fluid density variation with temperature caused by the beam heating over the volume of the target cell illuminated by the beam in essentially isobaric conditions. The density fluctuation is the effect of the target fluid density variations at the time scale of the electron beam helicity period. The density reduction effect is time-independent and reduces the luminosity correspondingly. The density fluctuation effect is time-dependent and increases the width of the parity violating asymmetry distribution adding in quadrature to counting statistics [37].

5.4.1 Density Reduction

The MOLLER target is a 3.7 K sub-cooled liquid. A LH_2 temperature increase of 1 K causes a density reduction of $\Delta\rho/\rho \approx 1.5\%$ at the operating point. The LH_2 reaches saturation if its density decreases by 7.5% from the operating point. Whenever the electron beam is on target, a dynamic equilibrium is established in the interaction region, where the temperature of the fluid increases locally with respect to the beam-off condition and the fluid density decreases, resulting in a net reduction of the target thickness in beam. If the target fluid density reduction is e.g. 10%, which would be a 10% luminosity loss, then the

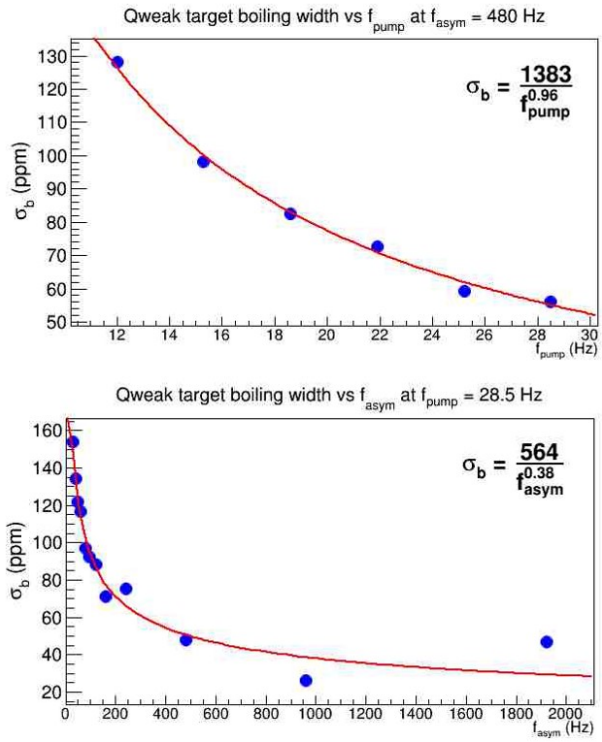

Figure 9: *Target density fluctuation noise versus LH_2 pump frequency (above) and versus beam helicity reversal frequency (below) from a* $\mathrm{Q_{weak}}$ *target data analysis. In this analysis* f_{asym} *for* $\mathrm{Q_{weak}}$ *is 480 Hz and for MOLLER is 960 Hz, which are half the beam helicity reversal frequencies respectively.*

experiment would have to run 10% longer to achieve the same statistics goal as expected from a fixed target density. This effect can be predicted with CFD and the target cell geometry can be designed to mitigate the LH_2 density loss. In nominal running conditions CFD predicted a LH_2 relative density loss of 0.8% for the $\mathrm{Q_{weak}}$ target cell geometry. The $\mathrm{Q_{weak}}$ collaboration measured a relative luminosity loss due to the target of 0.8% in nominal running conditions. The MOLLER target cell relative density reduction design value is less than 1%. As illustrated in the Appendix G, CFD predicts that Model 2 of the MOLLER target cell already exceeds this design parameter.

5.4.2 Density Fluctuation

From experience with previous LH_2 targets, the effect of density fluctuation is mitigated by optimizing both fluid conditions (flow, turbulence etc.) and beam conditions (raster size, intensity etc.). The measurements done with the G0 target [37] at a helicity reversal frequency of 30 Hz indicate a drop by a factor of 2.4 in the magnitude of LH_2 density fluctuation when the raster size was increased from 2 mm to 3 mm at constant pump rotation, and by a factor of 3.5 when the LH_2 pump pressure loss was doubled at the same raster size.

At the time when the $\mathrm{Q_{weak}}$ LH_2 target was designed it was calculated that predicting its density fluctuation effect with CFD on a state of the art computing architecture would take years. As this was unfeasible, the $\mathrm{Q_{weak}}$ team tried to estimate their target density fluctuation effect with the heuristic formula from Eq. 9. Here we use the same formula to scale the MOLLER target density fluctuation noise starting with the G0 target noise. The G0 target cell had a longitudinal flow design similar to the MOLLER target cell. The G0 target was run in the CW JLab electron beam as will be the case for the MOLLER target. We expect the

target density fluctuation to vary inversely with the raster area, linearly with the beam power and linearly with the inverse mass flow rate. These expectations have been borne out by previous target studies. We assume a linear dependence on inverse mass flow rate, which seems to be the most conservative choice.

$$\sigma_{b,M} = \sigma_{b,G_0} \frac{P_M}{P_{G_0}} \frac{A_{G_0}}{A_M} \frac{\dot{m_{G_0}}}{\dot{m_M}} \left(\frac{f_{G_0}}{f_M} \right)^{0.38} \tag{9}$$

where $\sigma_{b,G_0} = 238$ ppm, the MOLLER target power and beam raster area, P_M and A_M, were taken from Tab. 10. The dependence on the helicity reversal frequency was taken from a $\mathrm{Q_{weak}}$ target data analysis showed in Fig. 9. Considering the nominal parameters for the G0 and the MOLLER targets respectively in Eq. 9 the LH_2 density fluctuation noise of the MOLLER target is predicted to be 15 ppm, smaller than the design required 30 ppm by a factor of 2.

The dependence of target density fluctuation noise, σ_b, on helicity reversal frequency from a $\mathrm{Q_{weak}}$ target data analysis, Fig. 9, was corroborated by an empirical power law measured during $\mathrm{Q_{weak}}$ beam tests that were done in June 2008. Data were taken at helicity reversal frequencies of 30 Hz, 250 Hz, and 1000 Hz on both a carbon and a 20 cm hydrogen target (not the $\mathrm{Q_{weak}}$ target) at a range of beam currents. The hydrogen target available for the test was not one that was optimally designed for minimization of density fluctuation, but we ran at a variety of beam currents to see if our conclusions were valid over a range of "boiling" conditions. The scattered electron rate was monitored with "luminosity" monitor detectors at small scattering angles. The data from the carbon target were used to determine the parameterization of all sources of random noise other than the target density fluctuation effects in the hydrogen target. The result of the work was the target density fluctuation noise as a function of beam helicity reversal frequency determined at a variety of beam currents. A simple power law ($\sigma_b \propto f^{-0.4}$) describes the data well as a function of helicity reversal frequency f for the beam currents of 40, 60, and 80 μA, which is almost the same as the power law from Fig. 9.

The assumed scaling arguments in Eq. 9 predicted the measured density fluctuation noise for the $\mathrm{Q_{weak}}$ target within 50%. Using the available state of the art HPC today CFDFAC is working on benchmarking the $\mathrm{Q_{weak}}$ target cell density fluctuation and on expanding these technologies to the MOLLER target cell design.

5.5 Solid Targets

A system of solid targets are required for several purposes:

1. several thin targets are needed for the kinematics and spectrometer optics studies using the tracking system, in order to provide scattering events with a known origin in z,

2. a pair of thin targets with central holes will be useful for checking the alignment of the beam with the target system,

3. several relatively thick, cryogenically-cooled targets which can withstand beam currents on the order of 10's of μA are needed to provide a source of Møller-scattered electrons for commissioning studies, for benchmarking simulations of radiative effects on the event rates and distributions at the main detectors, and for studies of the backgrounds from the aluminum windows of the LH_2 target.

To allow the solid targets to be moved into the beam position, the target assembly will have a single-axis vertical motion system, with a total of between 40 and 45 cm of vertical travel. This can accommodate up to 6 solid targets, 4 of which could accept high beam power. The solid targets could be located at different z locations, eg. some could be at the z location of the upstream (entrance) window of the LH_2 target and some at the downstream (exit) window. In addition, an "optical table" will accommodate a set of (uncooled) thin

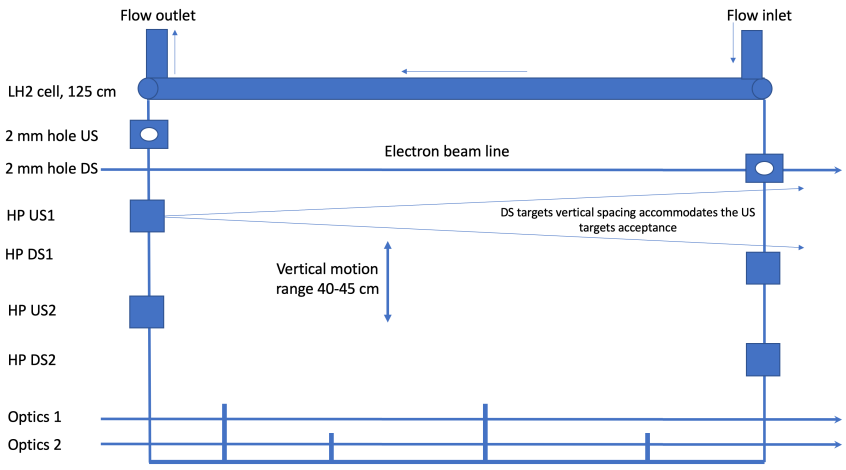

Figure 10: *Solid targets sketch. The single-axis vertical motion system can accommodate 4-5 high power (HP) solid targets, two alignment holes, one upstream (US) and one downstream (DS) and an optics foils tray. The frame of the solid targets is thermally sinked to the LH_2 cell. The solid targets will be designed with CFD to establish nominal operating conditions.*

targets for use in spectrometer optics/kinematics studies. Which of these targets are in place would again be selected by vertical motion.

A concept of the solid target configuration is provided in Fig. 10.

For the optics targets, measurements will be done with very low beam current (< 100 nA, with some measurements as low as 100 pA), dictated by the rate capability of the tracking system. Thus, the targets do not need to be high-power. Initial simulation studies of the kinematic determination procedure (see Appendix D for details) were based on using a single ^{12}C foil target located at the z of the center of the LH_2 target, however it is likely to prove useful to have optics targets at a few different z locations, providing scattered events at different scattering angles for a given sieve-collimator hole location.

The beam alignment "hole" targets will be moderately thin (1 mm) ^{12}C targets with 2-mm diameter holes. A low-current rastered beam can be brought to bear on the target. By using a raster size larger than the hole diameter, and triggering on scattered electrons, an image of the beam on the target can be made by plotting the instantaneous location of the raster beam for triggered events. This is routine practice for cryotargets used in Hall A, This provides a quick and accurate method to verify the alignment of the beam on the target ladder. We will use two such hole targets, one at the z location of the upstream window of the LH_2 target and one at the downstream window location, so that any tilts in the incident beam direction or in the target ladder can be ruled out.

For the other, high-power targets, we plan on a ^{12}C target with similar areal density as for the LH_2 target, *i.e.* 8.9 g/cm^2, this would imply a 4 cm thick target (20.7% of a radiation length, compared to the 14.6% of a radiation length for the lH_2 target). This can be used as an alternative source of Møller scattered electrons, that can be used for commissioning without need for high-power beam on the LH_2. We also will use thick ^{27}Al targets to allow us to study the distribution of scattered events on the detectors from the croytarget windows.

6 Spectrometer

The MOLLER spectrometer is a system of two toroidal magnets and a set of collimators with 7-fold symmetry that define the acceptance of the experiment (see Fig. 11). In order to achieve the stated precision on the parity-violating asymmetry (see Tab. 1), the spectrometer system must minimize both the statistical and relevant systematic uncertainties (see Tab. 3). A set of resistive, water-cooled copper coils steer and focus the scattered electrons onto the detector plane. Tungsten and copper collimators define both the scattering angle and the azimuthal acceptance and shield the experiment from radiation. The spectrometer directs the signal (electrons which Møller scatter in the target and make it into the acceptance) into a region where the contribution from backgrounds is minimized. The spectrometer provides kinematic separation between the Møller electrons and the Mott electrons (elastic and inelastic scattering from the proton) so that the contributions from each of the radiative tails of the latter to the measured asymmetry can be deconvolved. The spectrometer subsystem includes the toroidal magnets, water chiller and pumps, power supplies, collimators, magnet enclosures, beampipe and support structures as well as all the associated controls. The following sections describe the physical requirements of the spectrometer system, as well as a description of the conceptual design which will meet those requirements.

6.1 Requirements

This section describes the optics requirements of the spectrometer and the engineering constraints which place limits on its operation. The conceptual design which meets these requirements will be described in Section 6.2.

6.1.1 Optics Requirements

The spectrometer system must minimize the statistical uncertainty in the measured Møller asymmetry by maximizing the figure of merit, $FOM = A_{PV}^2 R_{ee}$, for the Møller scattered electrons(A_{PV} is the asymmetry and R_{ee} is the scattering rate). The maximum figure of merit for the Møller asymmetry occurs at a center-of-mass scattering angle $\theta_{\rm COM} = 90^\circ$ where the asymmetry is at a maximum and the cross-section is at a minimum. Møller scattering is identical-particle scattering and the electrons that are scattered to forward angles have backward-angle scattered electrons that arise from the same scattering event. The azimuthal coverage of the Møller scattering process can be maximized, even with half the azimuth being closed (blocked by the coils), by accepting both the forward- and backward-angle scattered electrons in the open sector (see drawing on the right in Fig. 12). The acceptance is defined by the primary collimator to be approximately 60° to 120° in the center-of-mass frame. The COM energy for a 11 GeV electron scattering from a target electron is 106 MeV, corresponding to extremely forward angles ($\theta_{\rm lab}$ between 5 and 21 mrad) in the laboratory frame. There is a one-to-one correspondence between $\theta_{\rm COM}$ and scattered electron energy in the lab frame, $E'_{\rm lab}$, and between $E'_{\rm lab}$ and $\theta_{\rm lab}$ (see left two plots in Fig. 12). This implies that scattered electrons in the laboratory frame in the range $3 \lesssim E' \lesssim 8$ GeV must be selected - a very large fractional momentum bite - in addition to the large range of scattered angles. This results in a very high rate of more than 140 GHz in the full azimuth.

Due to the high scattering rate, the detectors are designed to integrate the flux in each helicity window, which eliminates dead-time effects (see Section 8). The lab scattering angle and azimuthal acceptance defined by the primary collimator (see Section 6.2.3) is the same for all particles which scatter from the target. The toroidal magnets provide kinematic separation of the Møller- and Mott-scattered electrons (see Fig. 14). The largest background *rate* comes from Mott-scattered electrons that elastically scatter from protons in the target (elastics) while giving up significant energy to initial- or final-state photons (the radiative tail).

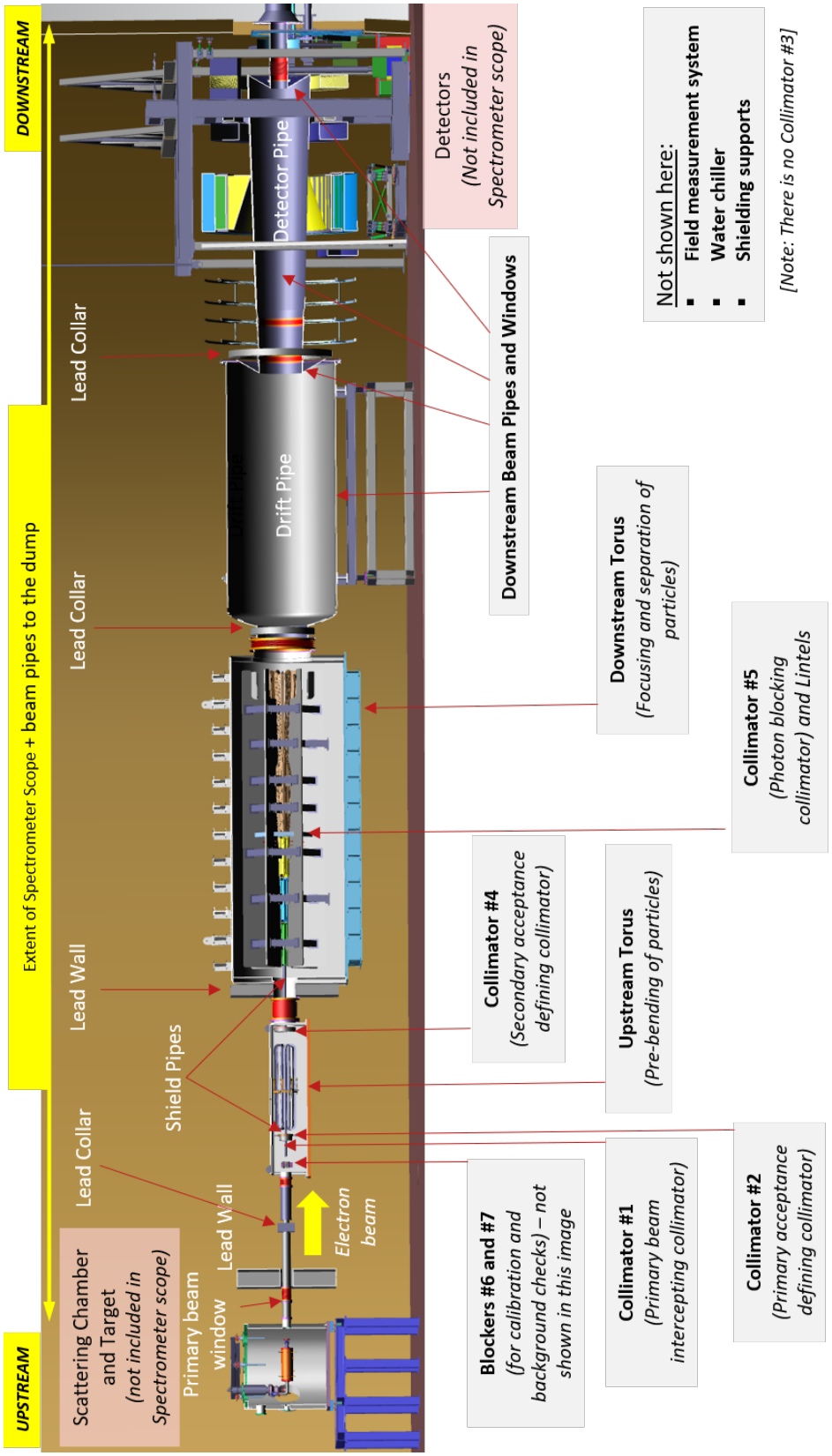

Figure 11: *Pre-conceptual Hall layout and overview of the spectrometer subsystem.*

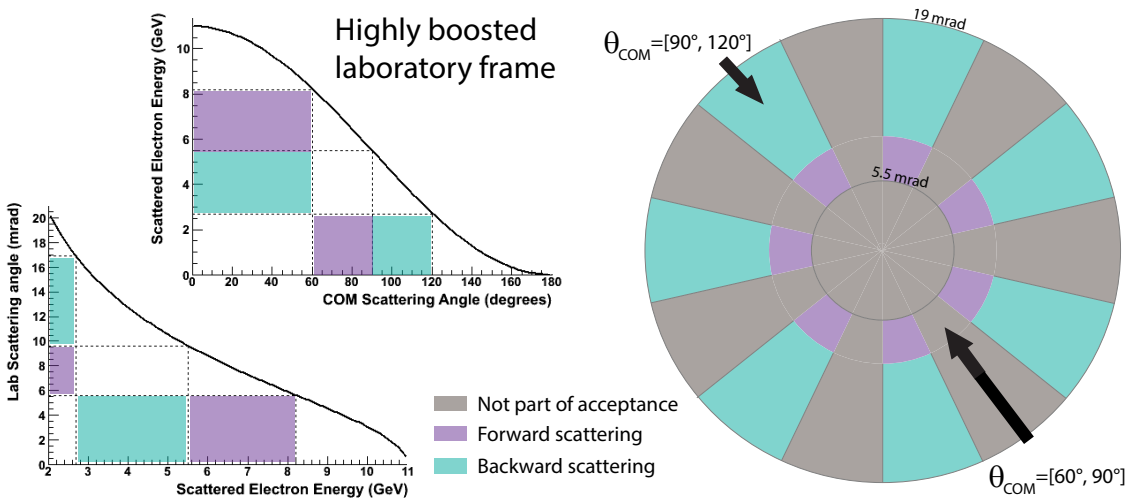

Figure 12: *The two plots on the left show the relationship between the lab and COM angles for* $E_{\rm beam} = 11$ *GeV. The colored bands in* $\theta_{\rm COM}$ *vs.* $E'_{\rm lab}$ *and* $E'_{\rm lab}$ *vs.* $\theta_{\rm lab}$ *plots indicate ranges of each quantity for the forward- and backward-scattered electrons. On the right is shown the concept for the primary acceptance collimator. By choosing an odd number of* ϕ*-sectors it is possible to achieve full azimuthal acceptance for the Møller electrons, due to the fact that the scattering involves identical particles. Information about the scattering event from forward-angle scattering in the closed sector is captured by measuring the corresponding backward-angle scatter in the open sector.*

A comparable *asymmetry* background comes from electrons that inelastically scatter from protons in the target (inelastics). There are also neutral backgrounds (soft photons and neutrons) from various sources. A summary of the rates can be found in Tab. 11. The rate of these backgrounds at the detector plane is, to first order, flat as a function of radius in the radial region where the Møller, or signal, electrons form a peak. The spectrometer must minimize the width of this "Møller peak" in order to minimize the contribution to the detector signal from these "irreducible" backgrounds.

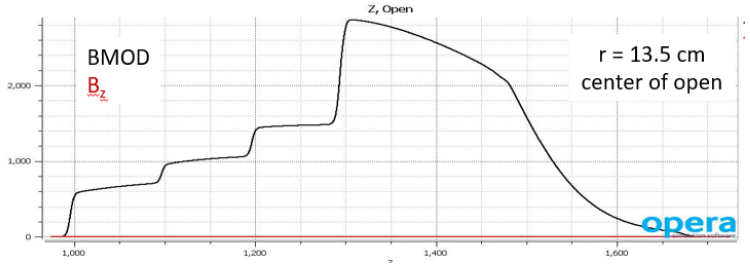

Figure 13: *Plot of the variation of the total field,* $BMOD$*, as a function of* z *for* r *= 13.5 cm at the center of an open septant (*$\phi = 0$*), where* $BMOD \sim B_\phi$ *(the radially-focussing component of the field).*

In order to achieve the desired focus and kinematic separation with the given space constraints (see Section 6.1.2), the spectrometer consists of five sections, each approximately 1 m long (except for the last two sections, which are closer to 1.5 m) with different total coil currents. This results in fields that vary along z (see Fig. 13). In addition, the two most downstream sections bend outward, away from the beam centerline. This reduces the amount of field seen by the elastic electrons. There is also a negative bend in the

Table 11: *Incident rates and asymmetries (A_i) of moller, elastic ep and inelastic ep in the Møller ring. The f_i are the fractional contributions to the total rate.*

Process	Rate (GHz)	Asymmetry A_i(ppb)	f_i (%)	$f_i A_i$
Møller	134	-31.8	90.5	-28.7
elastic ep	14	-21.4	9.3	-1.99
inelastic ep	0.37	-516	0.24	-1.28

second to last segment at large radius, in order to limit the amount of field seen by the largest angle (lowest energy) Møller electrons.

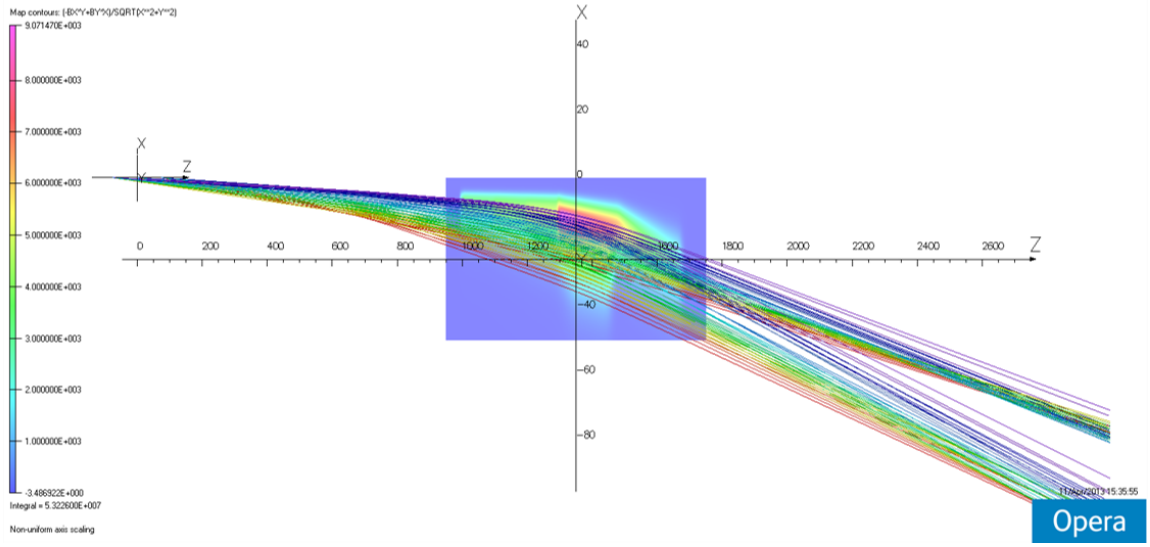

Figure 14: *Combined plot showing the radially-focussing component of the magnetic field and the moller and elastic electron tracks (colored by scattering angle) in the center of an open sector. The elastic electron peak at z=2600 cm is at a lower radius (closer to the beamline) and is well-separated from the moller peak.*

"Reducible backgrounds", including beamline and other backgrounds, can be shielded. Beamline backgrounds are photons and charged particles ($e^{\pm}$) that are produced in the target, including electrons in the primary beam that have lost a small amount of energy or which have undergone multiple scattering in the target. Due to the small stray fields from the magnets along the beamline, the charged particles can be bent away from the beamline where they may interact with material further downstream and shower, forming additional sources of backgrounds. The neutral backgrounds are minimized with a beam collimator and beam shielding tubes which form a "2-bounce system" for photons which eliminates the line of sight to the target from the detector location. The beam collimator blocks the part of the primary beam that would not be transported cleanly to the dump. This forms a single local source that can be shielded efficiently with shielding collimators and the beamline shielding tubes between collimators 2 and 4 and in the upstream portion of the downstream toroid. The target and scattering chamber will have additional shielding, which is not part of this subsystem.

In addition to maximizing the signal to background, the spectrometer system is robust against changes in beam energy, x and y positions and angles at the target which are far worse than the polarized beam conditions that have been demonstrated at the lab. The azimuthal symmetry of the spectrometer system, and indeed the whole apparatus, allows the canceling of systematic uncertainties such as the parity-conserving transverse asymmetry and detector responses to beam fluctuations. It is thus essential that any possible changes in the acceptance be independent of helicity state, and also that the angular acceptance in each open sector be the same in each of the septants. Simulations of single-coil offsets (radial, z, azimuthal, and roll, pitch and yaw about the center of mass of a coil) show that the maximum sensitivity is to radial offsets. The radial sensitivity results in a tolerance of ± 3 mm. The tolerances have been defined as an allowed "envelope" for the coils and any supports, that ensures there is no interference of the conductor (or associated supports) with the accepted particle envelope. The radial and other resulting tolerances are listed in Tab. 12).

These position tolerances are sufficient for ensuring the physics optics as well as ensuring the stated maximum radiation dose on the epoxy. In order to minimize radiation on the coils, the keep-outs include a minimum radius corresponding to $5\times$ the multiple scattering angle in the target. The tightest position constraint is on the inner radius of "trapezoidal openings" of the acceptance-defining collimator. This tolerance is relative septant to septant on a "perfect" circle. The table also includes the values of the NI (Amp-turns) necessary for the prescribed $\int \vec{B} \cdot d\vec{\ell}$ in each coil section. Systematic studies will require the ability to operate the coils at up to +10/-20% current (for short periods of time) as well as to reverse the current polarity once or twice during experiment lifetime (this can be done by manually swapping leads at the power supply end). The temporal stability of the magnet power supplies is not very stringent; the only real concern is helicity-correlated fluctuations.

6.1.2 Engineering Constraints

The Møller electrons of interest are scattered at far-forward angles, with energies between 2 and 8 GeV. The available space for drift in the experimental hall is limited as Hall A is only 87 ft in radius or 26.52 m. This requires "sculpting" the field to achieve the kinematic separation between the Møller and elastic electrons, with very little space around the azimuth to actually place conductor. Because of the high energies of the scattered electrons, the field integral must be $1T \cdot m$. The result is a long, skinny magnet with a complicated shape, as described in Section 6.2.1. The outer radius is partly limited by the need to use a bend radius no smaller than two conductor thicknesses [39].

The conductor cross-sections are quite small in order to only occupy half of the azimuth, resulting in high current densities. A review was conducted of resistive water-cooled copper magnets at JLab and at other facilities. Discussions were also held with conductor and coil vendors regarding manufacturing techniques and recommended design features. Although a conservative industry standard is 10 A/mm^2, current densities as high as 20 A/mm^2 are used successfully at various accelerators. This includes CEBAF accelerator magnets which run as high as 42 A/mm^2 when the beam is at full energy. This of course depends on the design of the water cooling system. Acceptable values for such a system are shown in Table 13.

The keep-out zones are meant to define the clearance of the coils and supports as well as the beampipe and magnet enclosures with the scattered particle envelopes. The scattered particles and primary beam should be transported to the detector plane, or dump, respectively, through a minimal thickness of material in order to minimize smearing of the Møller peak and the creation of bremsstrahlung backgrounds. The magnet enclosure will contain a vacuum on the order of 10^{-5} Torr and extend as far downstream as possible, in order to minimize the amount of air between the end of the enclosure and the detector plane, while leaving space for the GEM tracking detectors in air.

The magnet power-supply current stability affects the acceptance of the experiment by moving the scattered electron peaks relative to the detectors. However, because this is an asymmetry measurement, we are relatively insensitive to current fluctuations, as long as they are not on the timescale of the helicity flip rate

Table 12: *Engineering requirements for the magnets to achieve the necessary physics requirements. Magnet zones are defined from A-D where A is the one that extends the furthest upstream (see figure 16).*

#	Physics Requirement	Allowed Values	
		downstream	upstream
1	Envelope for an individual coil, strongback and supports, relative to the beam centerline and nominal center lines of coils	z = $\pm$ 25mm r = $\pm$3mm / $\pm$1 mm ϕ = $\pm$3 mm outer radius, $\pm$1 mm inner radius	
2	Clearance between coils, strong backs, supports and particle envelopes	1.2mm clearance at upstream ends of coils at the inner radius and 4mm everywhere else	
3	Coils must be no closer than 5x the multiple scattering radius to beam center	40 mm upstream end, 50 mm middle	30mm
4	Ampere-turns per coil per magnet	Zone A = 7752 Zone B = 10602 Zone C = 16862 Zone D = 29162	5358
5	Required variation in magnet coil currents	-20% to +10% from nominal operating current	
6	Magnetic field temporal stability	Field stability = less than 50 ppm over 8 hours; less than 100 ppm over 24 hours	
7	Magnet coil current polarity reversal	Yes - Perhaps twice during lifetime of experiment	
8	Expected Total maximum radiation dose (over 334 days at 60 μA)	3 $\times$ 10^9 Rad (30 MGy)	6 $\times$ 10^9 Rad (60 MGy)
9	Expected Total power deposition per coil (W, nominal/worst case)	2 / 5	7 / 7
10	Maximum allowable dipole field at center of magnet (i.e. beam center)	TBD	TBD

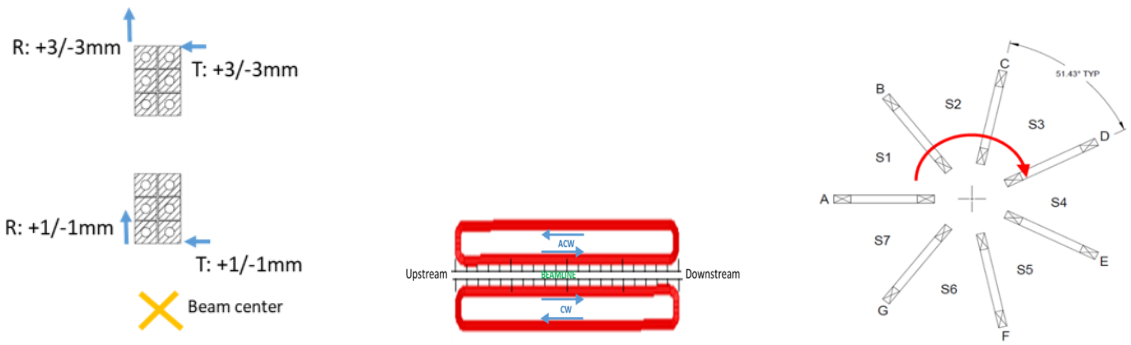

(a) (b) (c)

Figure 15: *These figures provide some clarification or additional requirements to those provided in table 12. Figure (a) shows the allowed radial and azimuthal offsets provided in line 1. Figure (b) shows the required direction of the current in the coils relative to the beam direction. In figure (c) you can see the naming scheme for the coils (A through G) and open septants (S1-S7), defined when looking downstream. The field direction is indicated as clockwise by the red arrow.*

Table 13: *Water-cooling system constraints.*

#	Parameter	Maximum Value
1	water flow rate	15 feet/sec
2	pressure drop per circuit	200 PSI
3	ΔT per circuit	35 °C
4	water out temperature	70 °C

of 1.92 KHz. Magnet power stability of 50 ppm over 8 hours and 100 ppm over 24 hours will be sufficient. We will need the ability to vary the current in the coils by +10% to -20% for short periods of time, for systematic studies. This and other requirements for the magnets to achieve the necessary optics within the given engineering constraints are summarized in Tab. 12.

6.2 Conceptual Design

This section will describe the required field configuration, the conductor layout that achieves that configuration and the collimation system that defines the acceptance. It will also provide an overview of the required services and controls for the magnets and collimators. Concepts for the equipment supports, magnet power supplies, pumping systems and a closed-loop water cooling system as well as the instrumentation and controls, testing, assembly, and installation for all of these systems will also be presented in Section 6.3.

The experiment has 7-fold symmetry, with alternating open and closed sectors. The coils are located behind the collimators in the closed sectors. The orientation is defined with a closed sector to beam left in order to shield the experiment from the synchrotron radiation in the bend in the Hall A arc. The spectrometer

must satisfy the kinematic and engineering constraints described in Sections 6.1.1 and 6.1.2. In order to achieve these requirements, a novel downstream toroid with multiple current returns was developed to fit the required current distribution within the allowed space in the hall, and will be described in Section 6.2.1. The configuration requires an upstream toroid to pre-bend the scattered electrons, which will be described in Section 6.2.2. Alternative designs for various subsystems will be described in Section 6.4.

6.2.1 Downstream Toroid

The total current (NI, in Amp-turns) in each section of the downstream toroid determines the trajectory of the scattered electrons. In order to focus such a large range of Møller energies and angles, each coil in the downstream toroid has four current-return paths, DS1-4, as shown in Fig. 16. The most upstream section of the coil (closest to the target) has the lowest total current, or NI, with increasing NI in each section. This most upstream section consists only of DS1. The fourth, most downstream part of the magnet includes all the turns (subcoils DS1-4), and thus the maximum current. The nominal current values in each section are given in Table 16. The conductors and necessary supports must not interfere with the accepted scattered electron trajectories, or tracks. The field is tailored so that the lowest angle tracks receive a set of "kicks" to radially separate the Møller and elastic e-p scattered electrons (see Fig. 14). At the upstream end of the

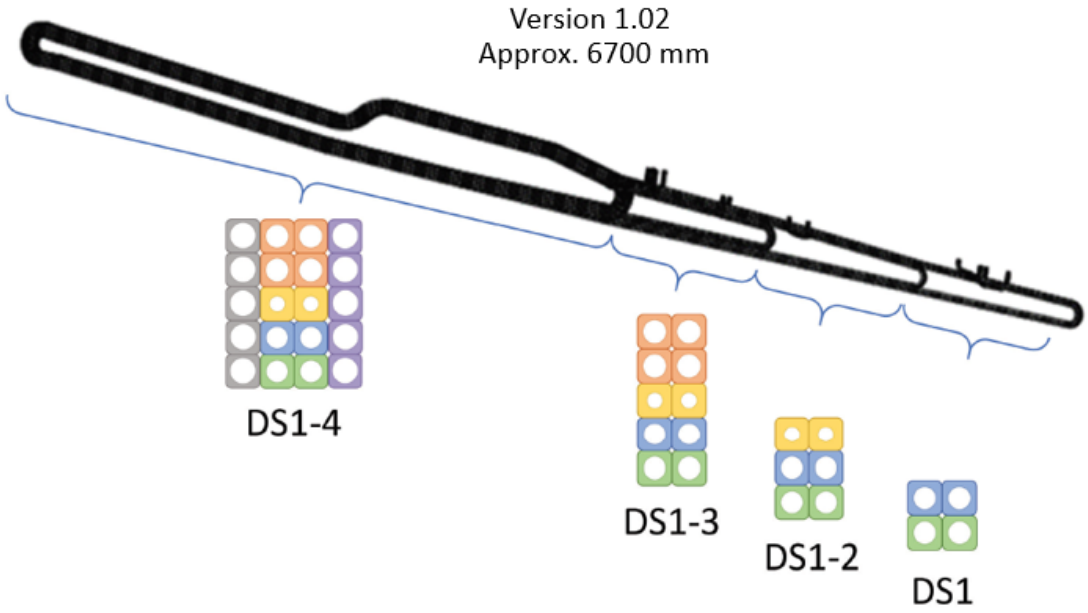

Figure 16: *Conceptual model of a single downstream coil conductor layout. Each color is a single "pancake", with each pancake being a different length. Relative sizes of conductor water-cooling holes in this figure are approximate. The different colors refer to the different cooling circuits.*

downstream magnet, the track envelopes fit between the conductor and supports in the open sectors in each septant. At a certain point, the tracks will be outside the radius of the conductors, so the conductors fill the full azimuth. Further downstream, only the Møller electrons (which have a lower momentum, and are thus pushed further out radially) see the full field in the most downstream part of the magnet due to a radial bend in the "tail" of the magnet. The higher-energy elastic ep tracks proceed at a lower radius than the outermost

part of the conductor, between the coils and supports. The largest angle (lowest momentum) Møller tracks must only experience field for a short distance in the magnet. This requires a negative curvature in the outer radius near the middle of the most downstream part of the coil.

Table 14: *The total current (NI, in Amp-turns) in each current return path in each coil of the downstream torus (DS Hybrid Coil Design Version 1.02), from the upstream end to the downstream end of the magnet. The subcoils are shown in Fig. 16 are noted.*

Subcoil	Conductor Size		No. turns	I (A/turn)	Subcoils	Total NI
	Outer (mm^2)	ID (mm)				
DS1	13x13	8.5	4	1938	DS1	7752
DS2	13x13	6	2	1425	DS1-2	10602
DS3	13x13	9	4	1565	DS1-3	16862
DS4	13x13	10	10	1230	DS1-4	29162

The conductor is readily available off-the-shelf high-conductivity oxygen-free C10200 copper (LUVATA #'s listed in Table 15). Each conductor will be wrapped with one layer of $\frac{1}{2}$-lapped glass cloth. Additional electrical insulation in the form of thin G10 shims will be used between coil pancakes where necessary. One layer of $\frac{1}{2}$-lapped glass cloth will be wrapped around each completed coil to form the ground wrap. All voids and gaps between turns will be filled with spacer material (G10 shims wrapped with glass cloth). All coil assemblies will then be Vacuum Pressure Impregnated (VPI) with radiation-tolerant CTD-403 Cyanate Ester resin (see Appendix H.4).

6.2.2 Upstream Toroid

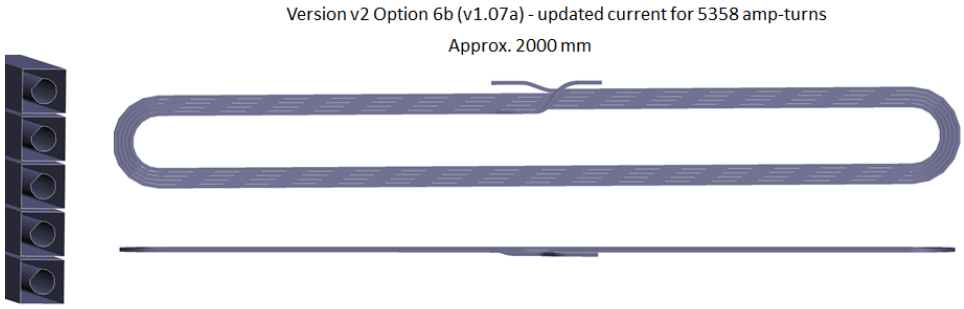

Figure 17: *Conceptual model of a single upstream coil conductor layout, which is a "single pancake" structure. Relative sizes of conductor and water-cooling holes are approximate. On the left is a cut-away view of a cross-section of the coil showing the conductors with the water-cooling holes.*

The upstream toroid consists of 7 simple single-pancake racetrack coils. The dimensions of the individual coils are shown in Fig. 17. The upstream toroid conductor is LUVATA #6842, which has an area of

9×9 mm^2 and a 5.7 mm diameter water-cooling hole. To achieve the necessary field integral, the current density in the conductor is 19.6 A/mm^2.

6.2.3 Collimation System

The collimation system includes a primary beam-collimator (collimator 1) and primary acceptance collimator (collimator 2). Collimator 1 stops the beam which would not be cleanly transported to the dump at a single location, so that it can be shielded. Collimator 2 defines the azimuthal and polar angular acceptance for scattered electrons at a unique z location. These collimators are upstream of all magnetic elements, so that differences in beam energy or magnet power fluctuations do not affect the acceptance. The relative collimator locations and their shapes can be seen in Fig. 18. There are four collimators in total - 1, 2 (see Fig. 19) which are upstream of the upstream toroid, collimator 4 which is between the upstream and downstream toroid magnets and collimator 5 which is located at about the halfway point within the downstream toroid magnet. Note that there is no collimator 3, it has been eliminated (see Section 6.4). There are also two septant blockers, 6 and 7, located between the scattering chamber and collimator 1, and a set of lead lintels located at the same z location as collimator 5, and at additional z locations upstream of the GEM detectors.

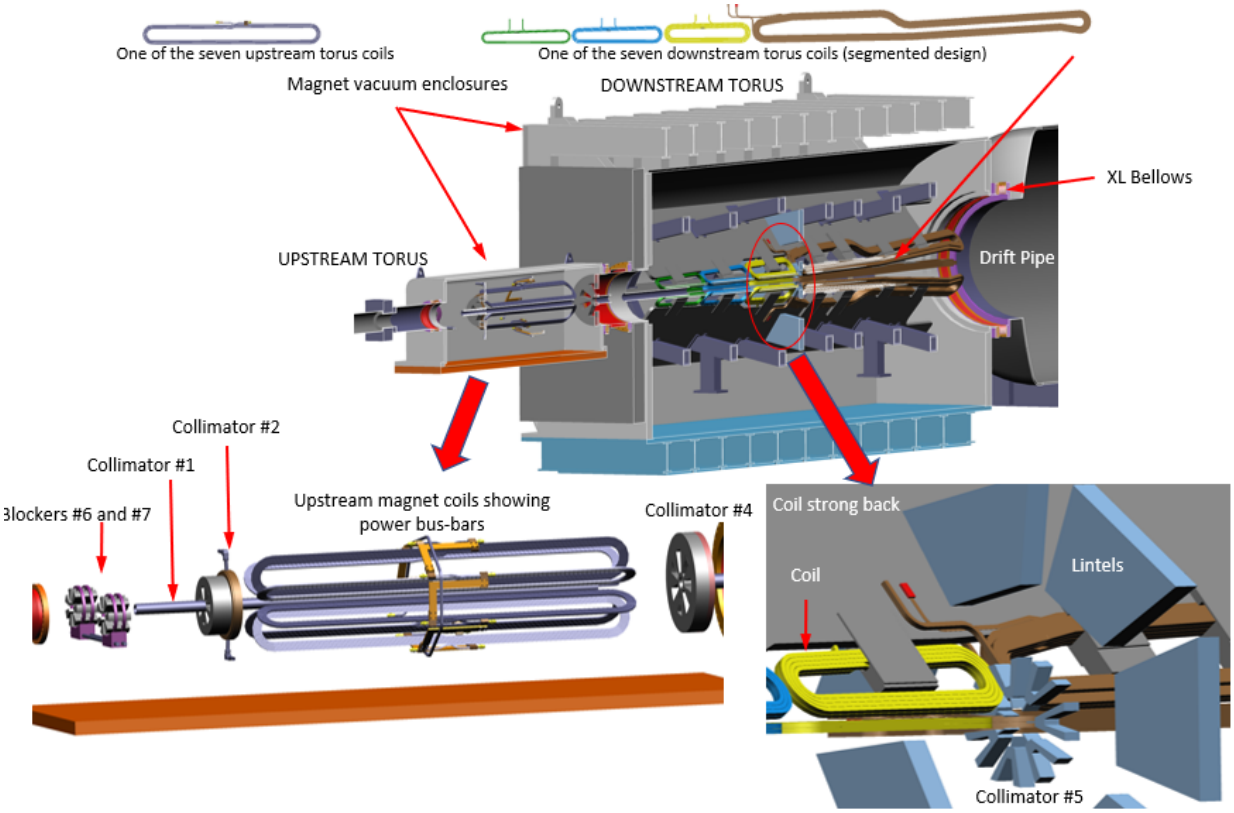

Figure 18: *Cutaway views of the upstream and downstream toroid enclosures indicating the relative locations of the magnets and collimators.*

Two "2-bounce" shielding tubes will be located between collimators 2 and 4, and at the upstream portion of the downstream toroid. The purpose of these shielding tubes is to ensure that there is no line-of-sight from the target to the detectors, and to provide some shielding for the coils. These tubes are made of tungsten and

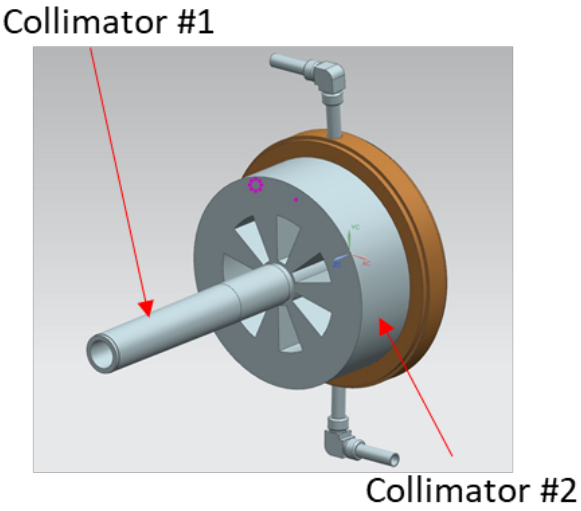

Figure 19: *CAD view of collimator 1 and 2.*

could form part of the magnet supports at the inner radius. Collimator 5 also provides photon shielding and brackets the elastic envelope.

6.3 Services, Controls and Instrumentation

Each magnet will be housed within its own aluminum vacuum chamber; each with its own separate vacuum pumping system. Each chamber will have a series of ports and feed-throughs for power, cooling water, instrumentation and vacuum pumping. All ports on the chamber will have metal seals. For the downstream toroid, due to the likelihood of heavy out-gassing during operation, there will be a provision to fit a liquid nitrogen cryogenic-panel. The cryogenic-panel will act as a cryo-pump to remove out-gassing contaminants as well as to handle any small air leaks into the chamber. Each chamber will also have adjustable legs to allow it to be aligned to the beam in the x,y and z axes. Fig. 20 illustrates a conceptual design of the instrumentation and control system, and assumes that each toroid magnet will be located within their own individual enclosure.

6.3.1 Enclosures

The pre-conceptual designs of the aluminum vacuum enclosures are shown in Fig. 21 and Fig. 22. Ports along the length of the enclosure will be used for power, water, instrumentation and pumping feedthroughs. All sealing would be accomplished using metal gaskets.

Two windows will be required to separate the magnet enclosures from the Hall environment and the accelerator region. An upstream window will isolate any potential hydrogen leak in the target from the coils, as well as separating the accelerator and magnet-enclosure vacuum regions. An exit window will be located at the downstream end of the torus enclosures. Both of these windows should be as thin as possible to limit the effect on the scattered particle envelopes and to limit the amount of background.

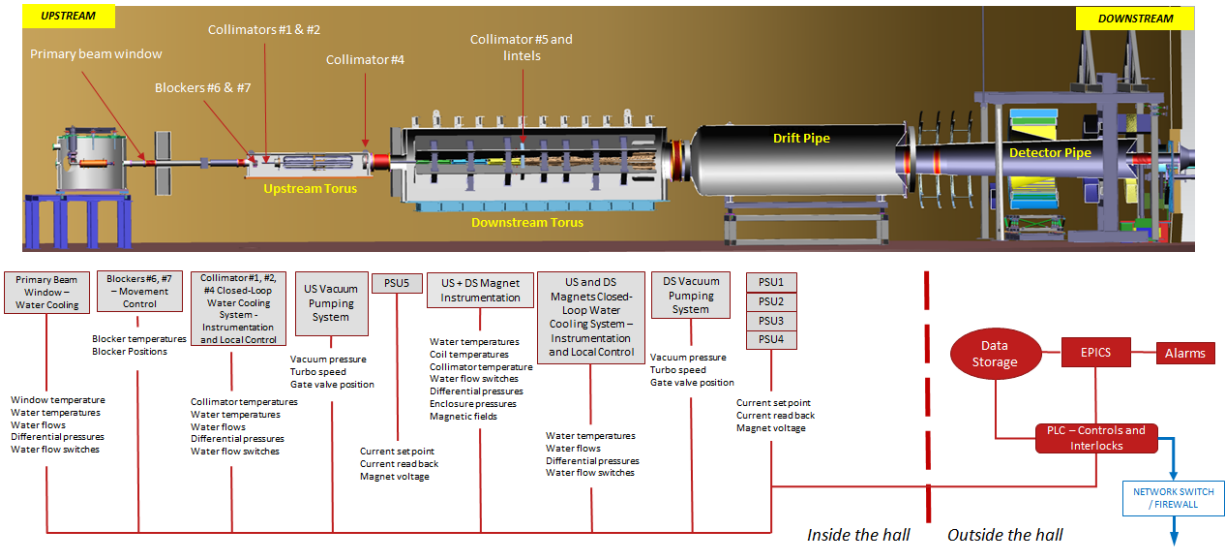

Figure 20: *Preliminary control and instrumentation layout for the spectrometer system.*

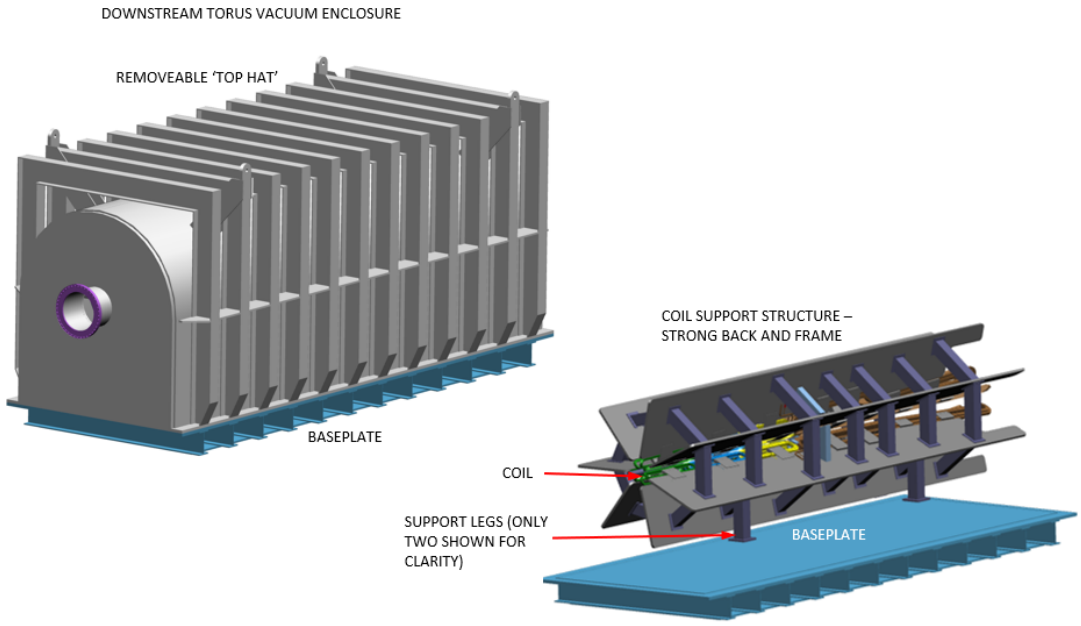

Figure 21: *CAD views of the downstream toroid enclosure.*

6.3.2 Mechanical Supports

This design consists of 7 coil assemblies – each assembly being made up of 4 separate sub-coils. The 7-coils are assembled and aligned together using an integrated strong back and frame system. The completed 7-coil assembly (on their strong back and frame mounting) would be mounted on a baseplate and aligned within the chamber itself and with the beam center line before the "top-hat" lid is lowered onto the baseplate.

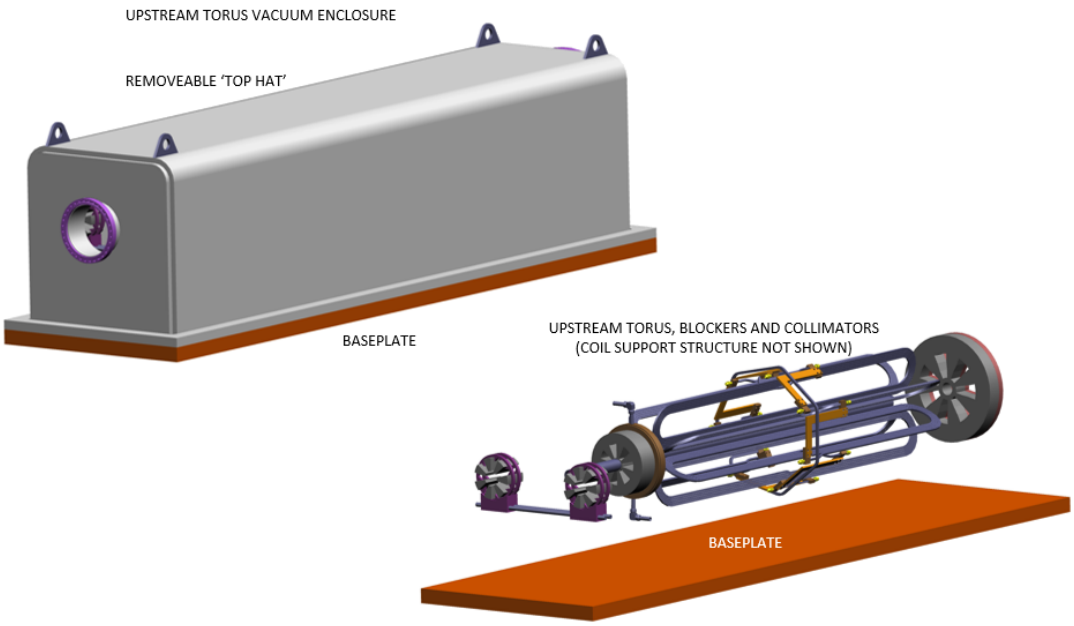

Figure 22: *CAD views of the upstream toroid enclosure.*

6.3.3 Power supplies and water cooling system

Two separate closed-loop water-cooling systems will supply the upstream and downstream magnets and will also provide cooling water for collimators 1, 2 and 4. Each magnet will have its own vacuum pumping system.

For the downstream toroid, each of the seven coil assemblies consists of four sub-coils; sub-coil 1 to 4. All sub-coil 1 coils will be connected in series, while all sub-coil 2 coils will be connected in series and so on. There will therefore be four separate electrical circuits, each requiring their own power supply. The voltage and current requirements for each of these circuits is summarized in Tab. 15. The upstream toroid will only require one power supply to drive all seven of its coils, which will be connected in series. The power bus bars for the magnet will be located radially outward from the 7-coil assembly, away from the acceptance regions, and the Go and Return bus bars will be routed together to reduce the magnetic fields from each bus bar. Electrical power fittings will be copper flags brazed to coil leads. Electrical isolation breaks (to isolate the electrical and water circuits) will use either ceramic breaks or insulating hoses suitable for use within a radiation environment. Water fittings will be 316L stainless steel VCR with copper gaskets. All fittings will be located radially outward from the coils – away from the acceptance regions.

Due to the amount of power deposited into some of the collimators, they also require water cooling. An expanded version of merged collimators 1 and 2 are shown in Fig. 23. Both collimators are fabricated from a combination of tungsten and copper, are water-cooled and share the same cooling circuit. Collimators 1 and 2 will be merged, for several reasons. The first was that merging them reduces any mis-alignment of the components. It negates the possibility of their relative alignment changing in time. This change in design also greatly simplifies the water distribution to the collimators. It also can be optimized to reduce background produced by the water distribution tubing. Calculations of the water-cooling (based on a Dynaflux R4000 Welding Chiller with 16kW capacity) for a heat load of 7 kW show that the maximum metal temperature can be kept below 60°C. This requires a water flow of 10 gpm, with a maximum velocity of

Table 15: *Water-cooling and electrical calculations for the upstream (US) and downstream DS1-4) toroid (sub-)coils (DS Hybrid Coil Design Version 1.02, and US Coil Design v2 Option 6b).*

Property by (sub-)coil	DS1	DS2	DS3	DS4	US
Conductor (LUVATA #)	10000	8449	8185	6819	6842
Current Density (A/mm^2)	17.4	10.2	15.0	13.9	19.6
Temperature Rise (C)	19.4	16.5	20.6	11.8	24.1
Water Velocity (ft/sec)	12.7	11.0	10.6	10.9	11.1
Pressure Drop (psi)	100	100	100	100	100
Flow Rate (gpm)	48.6	10.5	22.8	57.9	9.6
PS Voltage (V)	123.3	30.8	76.0	140.5	54.4
PS Current (A)	1938.0	1425.0	1565.0	1230.0	1071.5
PS Power (kW)	239.0	43.9	119.0	172.8	58.3

14 ft per second resulting in ΔP = 15 psi (plus distribution hoses). This results in a water temperature rise ΔT = 2.7°C, a temperature change of 6.8°C at the wall to transmit the heat and a temperature change of 15°C across the tungsten.

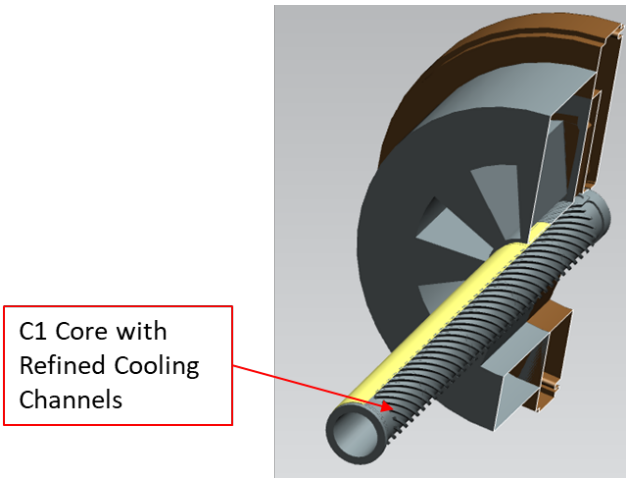

Figure 23: *CAD view of collimator 1 and 2 cooling concept.*

6.3.4 Control and Instrumentation

Each magnet and its associated sub-system will be instrumented and controlled using a PLC and EPICS-based GUI, as indicated in Fig. 20. Normal operation will consist of continuously monitoring and logging a series of key parameters (e.g. water pressure drop, coil voltages, coil and water temperatures, fields etc.).

An interlock system will be used whereby the magnets and their sub-systems can be shut down safely in the event of a fault or impending fault. Feedback from magnet shutdown will also be sent back to the accelerator control room for fast shutdown of the beam if necessary. Any gauges and pumps which are mounted on or close to the magnet chambers will be locally shielded by lead and concrete blocks.

6.4 Alternatives

Several alternatives for the downstream toroid design, including magnet technology, have been considered. A prototype downstream coil was built successfully and tested at MIT-Bates. This coil was of the "hybrid" type as presented above, and differentiated from the segmented coil as discussed in Section 6.4.2. In addition the collimation scheme has evolved, and we were required to shorten the original longitudinal extent of the experimental apparatus, to accommodate beamline elements that are needed upstream of the target. The MIT prototype coil, and other coil designs, as well as some alternatives for other aspects of the experiment will be discussed below.

6.4.1 MIT-Bates prototype coil

A prototype coil of similar design to that described above was designed, procured and tested by MIT-Bates in order to reduce or eliminate technical risks (either real or perceived) to the experiment. It was manufactured by Everson Tesla, PA in collaboration with MIT Bates Research and Engineering Lab and Stony Brook University Physics Department. The procurement of the prototype allowed us to learn about the feasibility of the fabrication of such a long, high aspect-ratio coil. The MIT-Bates engineers also performed water flow, pressure drop, current density and power tests to benchmark the water-cooling calculations. Details of these tests are available in [40].

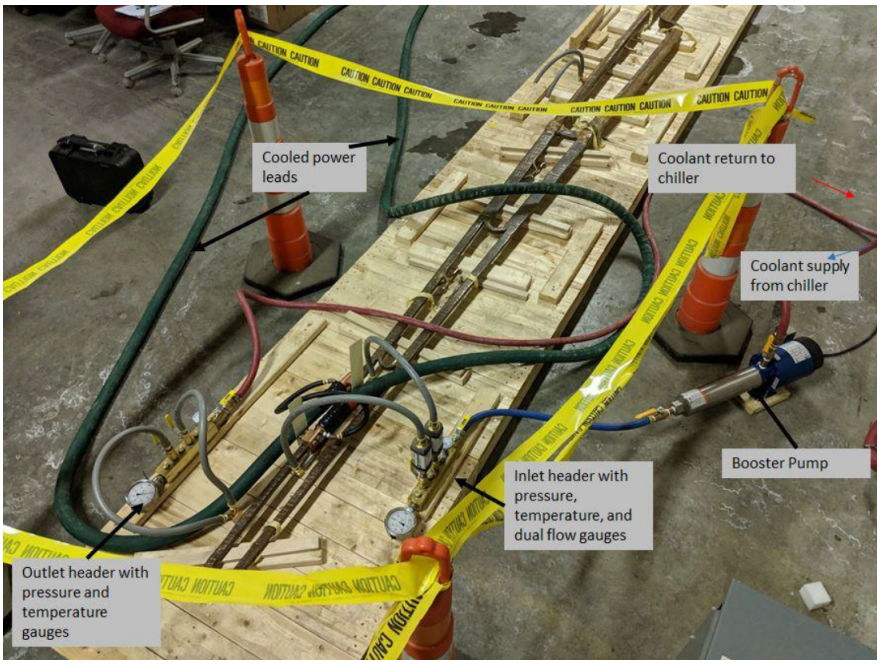

Figure 24: *Photo of the MIT prototype at MIT-Bates during testing.*

A stock sized LUVATA # 8298 conductor with VonRoll Fusa-Fab B-Stage 76003 insulation was chosen for this prototype for both cost-reduction and availability. The conductor was 11.8×10.3 mm^2 rectangular

conductor with a 6.0mm (0.235") hole. The NI in each section was similar to the required NI distribution described above for the downstream toroid. This design iteration limited the number of water connections and simplified the coil winding. Measurements of the pressure drop as a function of water flow for this prototype are shown in Fig. 25.

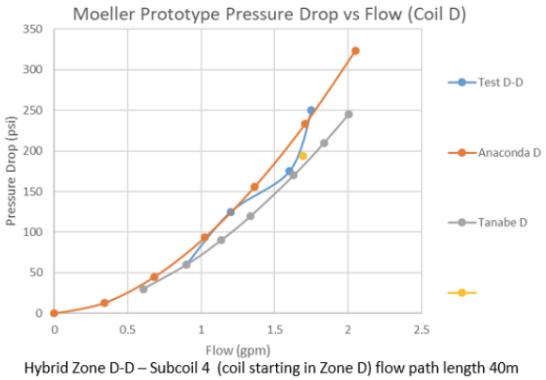

Figure 25: *Comparison of the pressure drop as a function of flow from different analytical calculations performed at JLAB with the prototype tests done at MIT-Bates. The test results are shown in blue.*

6.4.2 Downstream toroid magnet alternatives

We are evaluating two possible conceptual designs for the downstream toroid – a "hybrid" coil design and a "segmented" coil design shown in Fig. 26. The hybrid coil design consists of four sub-coils which are fabricated together to produce one interleaved coil assembly. The segmented coil design consists of four sub-coils which are fabricated separately and then assembled to produce one coil assembly. Both designs satisfy the physics optics requirements, so the down-select will purely be based upon engineering considerations, such as ease of manufacture, ease of assembly, ease of alignment, achievement of key tolerances and minimization of operational risks. We have established a set of engineering limits to guide the design of the coils including maximum allowable water flow, maximum allowable pressure drop, maximum allowable temperature rise and so on. The total currents (Amp-turns) in the four subcoils for the segmented toroid are 8915, 12192, 19391 and 33534 Amp-turns.

6.4.3 Transport medium

The choice of transport medium is closely tied with the beampipe configuration between the target and the detectors. Because the transport medium is vacuum, there is no need for a beampipe at low radius. The outer radius of the magnet enclosures can be outside the largest radius of the accepted particle envelopes. A cylindrical pipe extends the vacuum drift region to the downstream exit window, which only has to be large enough to include the Møller and elastic peaks. The beampipe from the end of the enclosure, through the detector region, and to the wall at the entry to the beam dump is designed to fit between the outer radius of the outer photon envelope and the inner radius of the elastic electron envelope.

6.4.4 Other coil designs

Several other options for the spectrometer system have been considered and rejected, such as a chicane style (as in SLAC E158), a toroidal superconducting magnet system, or placing iron in the magnets. In

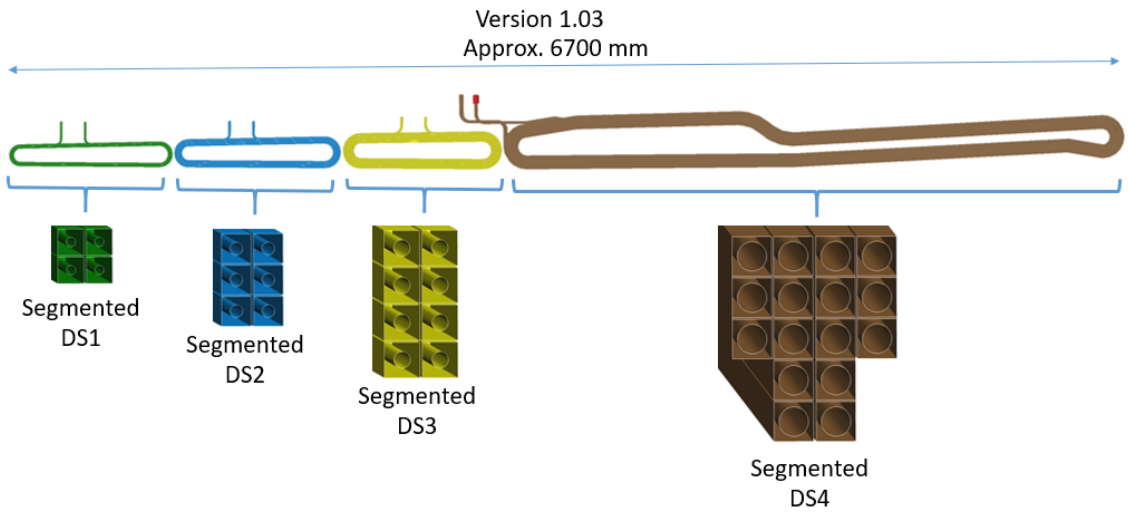

Figure 26: *Conceptual model of a single downstream coil conductor layout for the segmented design. Relative sizes of conductor water-cooling holes in this figure are approximate.*

Table 16: *The total current (NI, in Amp-turns) in each current return path in each coil of the downstream torus (DS Segmented Coil Design Version 1.03), from the upstream end to the downstream end of the magnet. The subcoils are shown in Fig. 26 are noted.*

Subcoil	Conductor Size		No. turns	I (A/turn)	Total NI
	Outer (mm^2)	ID (mm)			
DS1	12.7x12.7	4.5	4	2228.7	8915
DS2	14x14	6	6	2032.1	12192
DS3	15x15	7	8	2423.9	19391
DS4	16x16	12	16	2095.9	33534

addition, various different configurations, such as 5- or 9- fold symmetry instead of 7, and a rectangular vacuum enclosure instead of a cylindrical one have also been considered. The only options that are still being considered, in addition to the baseline design, is the segmented version of the downstream magnet coils. A brief description is written here; more information can be found in Appendix H.5.

Magnet coil technology Two coil technologies were considered – superconducting and resistive. The superconducting approach considered two types of conductor design, (a Rutherford-style cable with either copper or aluminum stabilizer, and a Cable-in-Conduit conductor with a central cooling channel with supercritical helium), while the resistive approach considered just one, a standard copper conductor with a central water-cooling channel. Consideration of the merits and demerits, of the design, fabrication, assembly and operation of the three approaches (two superconducting and one resistive), came down in favor of the water-

cooled resistive copper coil design. The associated Pugh Matrix used during the down-selection process and further discusssion of the options can be found in Appendix H.

SLAC E158 Chicane style spectrometer A chicane-style spectrometer, as was used in E158, was considered for the MOLLER experiment. However, as discussed above, in order to achieve the necessary statistical uncertainty, the chosen design achieves nearly full azimuthal acceptance by taking advantage of the identical particle scattering in the Møller process. It is not possible to achieve the same acceptance with a chicane.

Symmetry order Five-fold and 9-fold symmetries were considered for the spectrometer, instead of the 7-fold symmetry. Less than 7-fold symmetry leaves too large of an azimuth extent in the open sector and the ends of the Møller envelopes droop into the elastic peak. Nine-fold symmetry would actually be preferred from an optics perspective, but leaves even less space in the closed sector for the conductor, which results in unachievable current densities.

Iron in the magnets It is extremely undesirable to have iron anywhere in a parity-violation experiment, due to the huge asymmetry in backgrounds from electrons which scatter in the iron. Despite this, an attempt was made to implement iron in the coils in TOSCA. Due to the space constraints, however, there is no configuration with iron which will successfully increase the field.

6.4.5 Other alternatives considered

There are several other pre-conceptual designs that were considered for various aspects of the spectrometer system, such as the transport medium, overall length of the experiment, and different systems of collimators. The initially proposed length of the experiment was 28 m from target center to the detector plane (location of the Møller detectors). The collimator system has evolved from a system that included a third, "cigar-shaped", collimater between collimators 2 and 4, to one with the beam shields. Initially collimator 1 and 2 were also separated by some space, but for shielding, water-cooling and alignment improvements, a combined collimator 1 and 2 has been designed. The transport medium and magnet enclosure alternatives are discussed below.

Magnet Enclosures Irrespective of the environment in which the magnets are required to operate, (i.e. vacuum or helium), the magnets will require some type of enclosure. The design described above (see section 6.3.1) would be equally suitable for a one atmosphere helium environment with the key differences being that for the helium environment, the enclosure wall would be thinner and a central vacuum beam pipe would be necessary.

Collimator systems The collimator system has evolved to include the lintels and collars as shown in the appendix in Fig. 97, in order to shield the Møller ring from the low-energy charged particles deflected by the stray fields in the magnets. A second "beam collimator", collimator 3, has been replaced by 2-bounce shielding and with a modified collimator 1.

7 Tracking Detectors

The purposes of the tracking system are multifold: to i) verify the optical properties and acceptance of the toroidal spectrometer system, ii) verify the acceptance of the quartz detectors, iii) measure the position dependent light-output response of the quartz detectors, iv) measure the radial and azimuthal distributions of incident electrons in order to verify the fractional backgrounds from elastic and inelastic ep events in the integrating detectors, v) study neutral and "soft" backgrounds in the integrating detectors and vi) measure the background fraction and asymmetry of charged pions and their optical response in the integrating detectors. Items i) and ii) are essential for verifying the expected kinematics of the experiment, iii) will be useful for searching for radiation damage effects in the main detectors, and iv)-vi) are important for measuring and constraining background contributions.

The MOLLER tracking system consists of four layers of Gas Electron Multiplier (GEM) detectors with trigger scintillators located downstream of the spectrometer and upstream of the main integrating detectors and a pion detector system located downstream of both the main integrating detectors and shower max detectors behind a Pb absorber "donut". The pion detector consist of an azimuthally-symmetric array of acrylic Cherenkov detectors, as well as trigger scintillators and GEMs at selected azimuthal locations. Finally, sieve-hole collimators ("blockers #6 and #7" in Fig. 18) will be inserted between the upstream and downstream toroids, and will be used in conjunction with the tracking system for the kinematics verification. A discussion of the details of the kinematic verification procedure with the tracking system is provided in Appendix D.

The tracking system will primarily be used during dedicated low beam-current runs with a data taken in a "counting mode", as opposed to the standard integrating mode of data taking. The exception will be the pion detectors which will in integrating mode during the main data-taking, to measure pion asymmetries, and in low-current counting mode, to measure the pion background fraction.

7.1 Performance Requirements

The tracking requirements for the experiment include the need for full azimuthal coverage (although not in a single configuration), moderate position and angle resolution, reasonably uniform efficiency, and the ability to withstand the intense scattered electron flux and resolve individual tracks at a beam current that can be stably delivered and monitored.

1. **Rate Capability and Radiation Hardness:** The tracking system will be run when the beam current is reduced by many orders of magnitude. At the peak of the Møller distribution the electron flux is 100 MHz/cm^2 at full beam intensity, far too high for individual track reconstruction with any present technology. Previous experience (with $\mathrm{Q_{weak}}$) has shown that stable beams can be delivered with currents as low as 100 pA, The tracking system detectors will be removed from the immediate path of the scattered flux during full beam current integrating mode measurements. However their electronics must be reasonably radiation-hard, so as to not be damaged during the tracking mode data-taking, nor by the ambient radiation in their "parked" locations during full current running.

2. **Spatial Resolution:** The spatial and angular resolution requirements of the tracking system are set by their use in the kinematics verification. In this procedure (see Appendix D) we need to be able to separate events from different sieve-holes when we use a staggered-hole configuration. Simulated track reconstruction studies indicate that this can be adequately done assuming $1\ \mathrm{mm}$ spatial and $1\ \mathrm{mrad}$ angular resolution. These detector resolutions are more than adequate to "image" the individual thin quartz detectors for use in studying the position dependence of their optical response, and sufficient to generate projected radial and azimuthal rate distributions with fine enough binning for background

separation studies (eg. see Fig.30 and Fig.29). Because the tracking system will be operated in a magnetic field-free region, straight-line track fitting can be used. A four-layer tracking system is needed in order to allow for some small inefficiency, and still have at least 3-point tracks to allow a χ^2 test for valid tracks, and to suppress spurious hit combinations.

3. **Geometrical Coverage:** We must map the track distribution over the entire azimuth, and over the radial acceptance of all the integrating detectors rings (see Fig.29), to be able to identify any unexpected breakdowns of the seven-fold symmetry of the apparatus due to magnetic field or collimator imperfections beyond the expected tolerances. However, we do not require covering the full azimuth in a single measurement, so to reduce instrumentation costs, we can instrument a reduced fraction of the azimuth, and sequentially rotate the tracking detectors into different azimuthal locations. We require the ability to redundantly measure at least some azimuthal locations with different tracking detectors, in order to test our ability to "calibrate out" tracking detector inefficiencies. Coverage of a single septant requires relatively large tracking detectors ($\approx$0.5 m^2 in area). The detectors should also be low-mass, so as not to introduce additional backgrounds in the main detectors during tracking measurements; we desire $< 2\%X_0$ from the detectors.

4. **Triggering:** We need to be able to trigger tracking readout independently of the main integrating detectors, so we ensure that all incident charged particles are measured; a high-efficiency trigger ($> 99\%$) based on charged particles (used in software veto mode) will be important for studying neutral backgrounds. To reduce spurious triggers due to soft backgrounds two layers of trigger detector are planned. An "unbiased" pulser-trigger is also useful to study the trigger efficiency.

5. **Pion Identification:** The pion detector system requires the ability to suppress the Møller electrons by a factor of $> 10^3$ while retaining a significant fraction of the incident pions, so as to have the pion detectors measure the asymmetry of a roughly equal mixture of pions and Møller electrons, given the anticipated initial π^-/e^- ratio of 10^{-3}. This can be accomplished using a Pb absorber such that the total of the Shower Max detectors and the absorber corresponds to $35X_0$ in thickness.

6. **Pion Detector Angular and Radial Coverage:** There may be significant azimuthal variation in the measured pion asymmetries, due to the combination of a small transverse beam polarization, and the possibly large single-spin asymmetries in pion production Therefore we must instrument the entire azimuth for the pion asymmetry measurement. Only the pions incident on the Møller ring need to be measured, so the radial coverage of the pion detectors only needs to match their extent (roughly 85 cm - 107 cm). It is useful to subdivide the pion detectors in azimuth so as to look for pion asymmetry variation with kinematics, so we segment by 14 in ϕ, in order to have pion detectors measuring in both "open" and "closed" portions of each septant.

   In contrast, no significant azimuthal variation is expected in the pion flux, so we only need to measure the pion background fraction (in counting mode) in one septant; this requires two sets of counting mode pion detectors, one located in an "open" and one in a "closed" portion of a septant (to correlate with the pion asymmetry measurements).

7. **Pion Asymmetry statistics:** We require a measurement (azimuth-averaged) of the pion asymmetry to a 0.1 ppm statistical precision in about 10 days of data-taking, assuming the pion fraction is 10^{-3} of the Møller electron flux. We require a detector pulse-height resolution over the full pion momentum spectrum of better than 25%, so as not to significantly degrade the statistical width of the asymmetry measurement.

8. **Pion Detector Radiation Hardness** The incident charged particle flux expected on the pion detectors is $\sim 10^{-3}$ of that incident on the main integrating detectors (after the electrons are ranged-out by the

Shower Max detector and the Pb absorber), thus the pion detectors do not have the same stringent requirements for radiation hardness as do the integrating detectors. The ability to tolerate a dose of 100 kRad without degradation of the detector response is required.

7.2 Conceptual Design

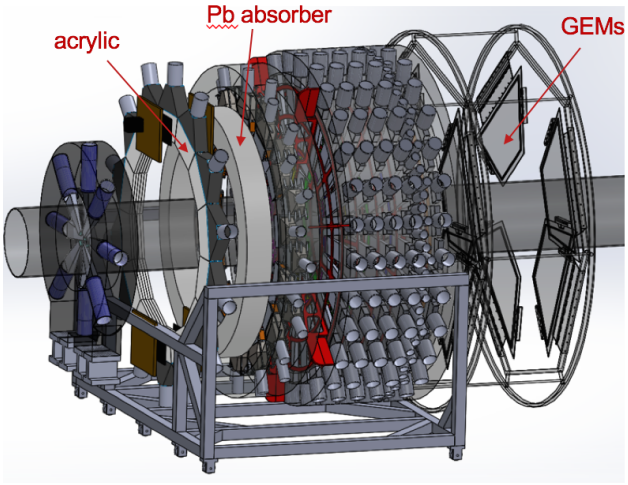

Figure 27: Location of GEM tracking system on rotating support wheels, upstream of main detectors, and the acrylic pion detector array after a Pb absorber downstream of the main detectors.

The tracking system consists of four GEM layers after the magnetic elements and immediately before the thin quartz integrating detectors, see Fig. 27. Multiple layers spaced along the beam axis provide a lever arm to reconstruct the track positions r and ϕ, but also the directions, which we will call $r' = dr/dz$ and $\phi' = d\phi/dz$. These four independent variables map from the independent variables which describe the scattered particle, the lab scattering angle $\theta_{\rm lab}$, the electron momentum p, the lab azimuthal angle $\phi_{\rm lab}$ and the reaction vertex position v_z. The GEMs will be mounted on a pair of rotating support wheels, each supporting two layers of GEM modules, with four modules per layer. The layers include trigger scintillators to provide a charged particle trigger for the counting mode data acquisition system. This assembly will be sequentially rotated to allow measurements of the full azimuthal acceptance. Some specifications for the GEM tracking system are provided in Table 17.

Table 17: *Specifications for the GEM tracker.*

Parameter	Value
Maximum rates	< 200 kHz/cm^2
Area per sector	0.5 m^2
Detection efficiency per plane	$> 90\%$
Detector thickness	$< 2\% X_0$
Position resolution	< 1 mm
Angular resolution	< 1 mrad
Radial coverage	63 cm to 120 cm

The pion detector system consists of an array of 14 acrylic Cherenkov detectors. Each detector is 3" in thickness (three 1" layers stacked together), and is trapezoidal in shape, with an inner edge 47 cm in length and an outer edge 51 cm in length, with the inner edge located at a radius of 90 cm. Each detector is read out optically by a 3" PMT, coupled to the outer edge of the acrylic via air light-guides. The Pb absorber, to range out the Møller electrons, is an annulus of inner radius 90 cm and outer radius 115 cm and 15 cm in depth, which provides (along with the Shower Max detectors) $35X_0$ of absorbing material.

In each of two of the 14 pion detector locations, corresponding to one "open" and one "closed" portion of a given septant, a plastic scintillator trigger counter and a GEM module will be inserted during counting-mode data-taking. These will be used, in conjunction with the main GEM tracker system and the Shower Max detectors, for π/e identification on a track-by-track basis, in order to determine the relative fluxes of π's and e's.

7.3 Alternatives

1. **Pion Detector Material** Parity-violating electron scattering experiments have found solid Cherenkov detectors to be an optimal detection device, for reasons discussed in Sec. 8.2.1. We considered the use of quartz as the detector medium for the pion detectors. However, as the expected radiation dose is three orders of magnitude smaller for the pion detectors than for the main integrating detectors, we opted for the cheaper and more mechanically forgiving medium of acrylic. Experience using this material for similar detectors during the first parity-violating electron scattering experiment at JLab, HAPPEX-I, was positive.

2. **Alternatives to GEMs** We considered alternate tracking technologies to GEMs. Drift chambers or straw tube chambers do not have the capability for operating at the high local particle fluxes as are required, Semiconductor trackers such as semiconductor-based pixel detectors (eg. HV-MAPS) are less mature technology than GEMs, are considerably more expensive, and introduce more multiple scattering so were rejected.

3. **Pion Detector PMT choice** We had consider larger (5" diameter) PMTs for the pion detectors, to more easily couple to the pion detector dimensions. However, optical simulations indicate that the cheaper 3" PMTs will gather more than enough light (40-50 PE's per incident charged particle), and thus it was attractive to select identical PMTs to those chosen for the thin quartz and Shower Max detectors.

4. **GEM detector segmentation** We have considered various options as to how many GEM detectors will be located in each layer. The azimuthal size of the GEM module is constrained by the dimensions of the available GEM foils, and corresponds to 27° of arc. Given dead zones due to the GEM detector frames, full azimuthal measurement capability will require at least one set of "rotations" of the GEM system. A choice of four GEM modules per layer has been selected as a balance between reduced hardware costs and the number of different rotation settings required for the tracking measurements.

7.4 Scanner Detectors

Small movable detectors that can operate at both the full beam current and at the low beam currents needed for the tracking measurements will be used at two locations in the experiment. Such scanners have been used in E158 [58], HAPPEX-II, and $\mathrm{Q_{weak}}$ [64].

The upstream scanner is located just downstream of the GEM location. It is similar to the $\mathrm{Q_{weak}}$ scanner. It consists of two small overlapping fused silica radiators (1 x 1 cm^2) coupled to air light guides and read out by photomultiplier tubes. They are instrumented to be read out either in event mode or integrating mode.

They are mounted on an xy motion stage covering one sector of the acceptance, allowing a complete scan of a sector in ~ 40 minutes. This device can be used to confirm that the rate distribution measured at low beam current by the full tracking system is not significantly different than that seen at full luminosity. It would also allow periodic rapid monitoring of the distribution during production data-taking, to ensure stability of the effective kinematics and to any changes in backgrounds.

The downstream scanner system is located downstream of the pion detectors, in the same location as the small angle monitors (SAMs). It consists of three single detectors of the type described above mounted on single axis motion stages so that the active fused silica radiator covers the radial area from 50 - 70 cm at three different azimuthal locations. With the spectrometer magnet turned off, there is a rapid change in the charged particle scattered flux in this region corresponding to the outer radius of the acceptance defining Collimator 2. This allows a precise determination of the alignment of the beam with respect to the center of Collimator 2. The downstream scanner system is not yet included in the project baseline.

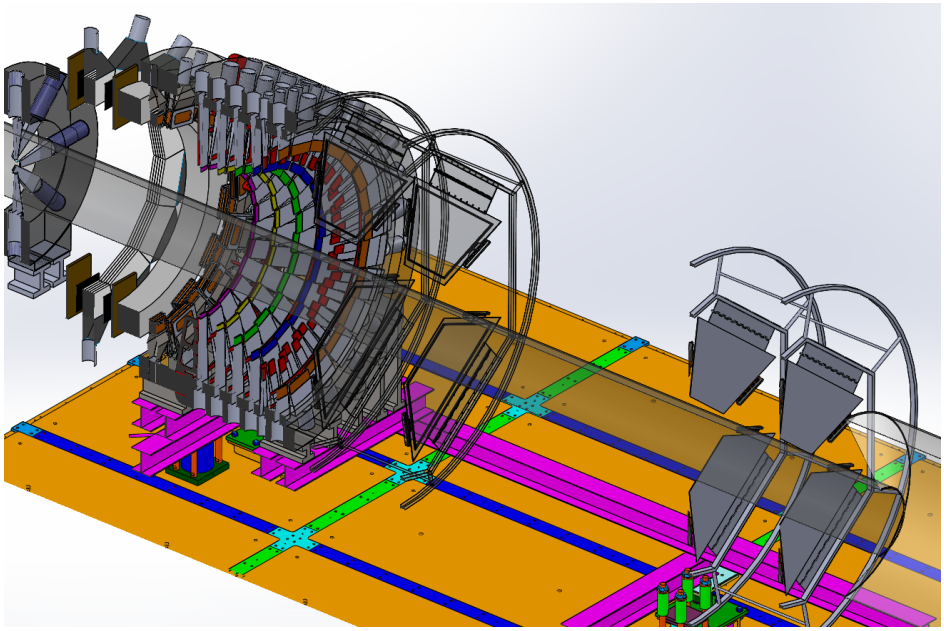

Figure 28: *A perspective view of the integrating detector assembly. The quartz tiles are shown in color, with the air-core light guides and the PMT rings in grey. Located in front of the main detector rings are the upstream GEM trackers. Located behind main detectors and a donut-shaped shield are the pion detectors and the small angle monitors.*

8 Main Integrating Detectors

The purpose of the main integrating detectors is to measure the physics asymmetries to the desired level of precision. The small size of the asymmetries and the goal for the precision of the measurement require very high statistics, meaning very high event rates in the detectors. This requires either a very high detector segmentation or a continuous integration of many overlapping pulses (integration mode). Given the precision goal for MOLLER and the high scattering rate, background susceptibility, linearity, noise behavior, and radiation hardness are major issues for the detectors. For these reasons, as described in detail below, as well as cost considerations, MOLLER adopted relatively large active surface area integration mode detector technology.

8.1 Performance Requirements

For a successful measurement, the integrating detectors have to satisfy a number of performance requirements that dictate the overall design, including the detector geometry, the choice of detector technology, materials, and readout technique. Each requirement is briefly discussed below and the corresponding design solutions are discussed in the following sections and, in more detail, in Appendices J and K.

1. **Signal yield:** To ensure that the target precision of the experiment can be reached, the detectors must maximize the detected signal yield, which means that they have to cover the full azimuth of the Møller peak region. This also means that the detector must be able to handle the high Møller event rate, which is approximately 134 GHz for the ring. This places requirements on the detector active material as well as the readout electronics and mode (integration mode).

2. **Operation mode:** The main asymmetry measurement is carried out in integration mode. However, for diagnostic, background, and momentum transfer determination, the detectors must also allow

for event or pulse mode operation at a significantly lower beam current. Pulse counting requires an active material with good photoelectron resolution and fast electronics ($\sim$ few nanosecond risetime for single pulses). A separate front-end electronics stream has to be implemented for event mode and integration mode, and the electronics must be implemented such that the detector can be switched between event mode and integrating mode measurement remotely (without manual changes). The electronics in either stream must be low noise and allow efficient data processing.

3. **Background:** In integration mode experiments, the rejection of backgrounds based on particle ID or electronic discrimination is not possible. Therefore, the experiment itself has to be designed to minimize the background in the detector region and the detectors have to be designed/chosen such that the sensitivity to the remaining background is minimized or can be determined by measurement using separate detectors. This places constraints on the detector type and material, position, geometry, shielding, and readout electronics. See also Appendices C and J.1.3.

4. **Helicity-Correlated Systematic Effects:** The detectors must be designed to help suppress helicity-correlated systematic effects as much as possible. These include possible detector signal correlation to changes in the beam current, energy, position, and angle on target. Helicity-correlated changes, for the most part, place constraints on the detector geometry, through symmetry requirements and coverage of the scattered profile, but also on the electronics. Helicity-correlated changes produce false asymmetries. The corresponding detector sensitivity measurements are made by measuring the correlation between the changes measured with the beam monitors to those measured with the detectors, which requires that the electronics chain used to process the measurements from the beam monitors is identical to that of the integrating detectors. This is particularly important in the case of the beam current monitors, since the integrating detector signal is normalized to (divided by) the current monitor signal to remove random drifts, fast fluctuations, and helicity-correlated changes in the beam current. See also Appendix K.

5. **Drifts in the detector signal:** The detector signal contains systematic drifts, both fast and slow. Non-random drifts in the detector signal can be the result of beam drifts, changes in temperature, long time-scale degradation of the detector parts, as well as electronics drifts. Almost all of these can be controlled to some degree - for example by operating the PMTs at a reasonable HV bias, in a reasonably stable temperature environment, and removed from or shielded from direct radiation exposure - but the primary way to deal with possible false asymmetries due to drifts and unwanted noise above Shot noise, due to large amplitude random drifts, is to perform each asymmetry measurement on a time scale that is short compared to the timescale of the drifts. This is achieved by running the experiment with a fast helicity reversal rate. The faster the helicity reversal rate, the more the signal variation with respect to time is well approximated as constant on the time scale of an asymmetry calculation. Variations that are faster than the helicity reversal rate are dealt with and used to advantage in the electronics chain, as described in detail in Appendix K. The choice of helicity reversal rate influences or determines almost every detail of the detector electronics design.

6. **Detector (non-)linearity:** For the purpose of this measurement, a non-linearity in the detector is defined as a change in the size of the measured asymmetry as a function of absolute signal amplitude (or offset), rather than only on the difference in the signal for different helicity states. An asymmetry from non-linearity is a multiplicative effect, meaning that it scales the real physics asymmetry. As a result, it is important to establish that the non-linearity is zero or measure it at the needed level of precision. See also Appendix J.2.

7. **Radiation hardness and shielding:** Due to the very high rate in the detector region, the Ring-5 detector elements can expect to see doses of up to 70 MRad in their active region over the lifetime of the

experiment. And although the elastic e-p overall rate is lower than the Møller rate, it is concentrated over a much smaller area producing up to 160 MRad dose on the Ring-2 detector active region. This means that the detector active material must be radiation hard enough (i.e. high purity quartz), to limit transmission loss. The other detector elements, such as photosensitive devices and electronics are somewhat removed from direct shine of the scattered electron envelope, but must still be appropriately shielded to reduce radiation damage as much as possible. All materials used in the detector construction and mounting must be radiation hard enough to maintain the structural and functional integrity of the detector system over the duration of the experiment. See also Appendix J.2.

8. **Positioning and stability:** The detector mounting structure must provide stable and reproducible positioning, with positioning accuracy at the few millimeter level. The structure must provide access to all of the vital parts of the detector and allow replacement if need be. See also Appendix J.

8.2 Conceptual Design

The toroidal spectrometer distributes the scattered electrons selected using the collimation system ≈ 26.5 m downstream of the target center in a region between a radius of 70 to 120 cm with respect to the beamline axis.Due to azimuthal defocusing in the magnets the Møller electrons populate the full range of the azimuth at the detector plane. To satisfy requirements 1, 3, and 4, this region must be populated by a series of detectors with radial and azimuthal segmentation as shown in Fig. 29. Figure 30 shows the radial segmentation of the planned detector rings superimposed with the azimuthally averaged radial distributions. The rings are numbered 1 through 6 with the Møller electrons focused onto ring 5. The elastic e-p (electron-proton) events are focused mainly on rings 2 and 3, but with a long, low rate tail into rings 4 and 5. The inelastic e-p events have a very low rate distribution extending through all rings.

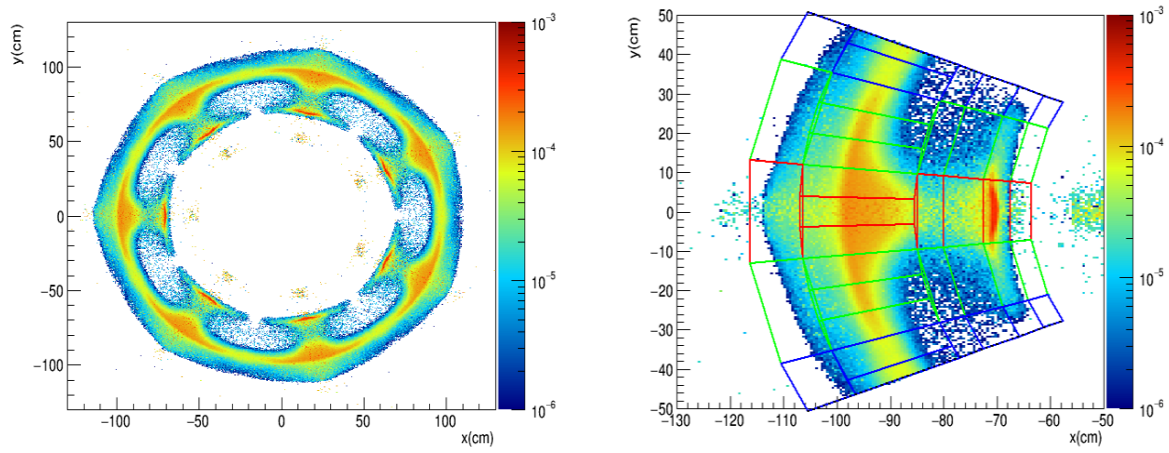

Figure 29: *Simulated, cross-section weighted, Møller and ep (elastic and inelastic) electron rates in units of* $\mathrm{GHz}/\mu\ \mathrm{A}/0.5\ \mathrm{cm}^2$. *The left plot shows the whole detector plane. The plot on the right shows superimposed azimuthal and radial bins (approximate detector locations) in one toriodal sector.*

Focusing further on requirement 3, as can be seen in Fig. 29 (left), the electron rate is highly non-uniform within a ring and mostly still focused on the individual seven sectors. The figure demonstrates that a detailed understanding of the signal, background fraction, and spectrometer optics requires a reasonably detailed

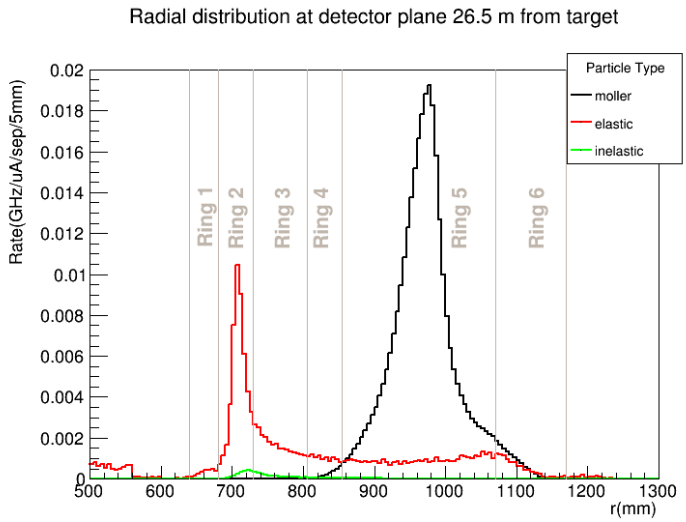

Figure 30: *Radial distribution of Møller (black), ep elastic (red), and ep inelastic electrons in the open sector detectors, 26.5 m downstream of the target. The vertical black lines delineate the proposed radial segmentation into 6 rings. The principal A_{PV} measurement is carried out in ring R5.*

detector segmentation, both in the radial and azimuthal dimensions. Azimuthal segmentation is needed, since defocusing results in a correlation between azimuthal angle and E'. Because the tail of all radiative electron-proton elastic and inelastic processes results in an important systematic correction, the detector must be able to measure these background electrons in *several* bins, so trends in yield and asymmetry can be compared to simulations. Each azimuthal sector, defined by one of the toroid sectors, is further divided into 4 sub-sectors, so that there are 28 total azimuthal channels at each radial bin. The exception to this is ring 5 (the Møller events), which is further divided into 3 additional bins, resulting in a total of 84 channels. This arrangement is illustrated in Fig. 29 (right). The detector must also minimize cross-talk between adjacent radial bins, with widely differing asymmetries, and minimize electron hit location and electron incident angle dependent biases.

The detectors that populate rings 1 through 6 are henceforth referred to as the "thin" integrating detectors. These detectors are used to carry out the main asymmetry measurement. A brief discussion of these detector is given below in Sec. 8.2.1 and the more detailed design of the detector modules is discussed in Appendix J. Additionally, a 7th detector ring, consisting of "shower-max" quartz/tungsten sandwich detectors, will provide a second, independent, measurement of the electron yield in the Møller peak ring. This detector will be less sensitive to charged hadron backgrounds and therefore provides an important background check. A brief description of the shower-max design is given in Section 8.2.2 and, with more detail, in Appendix J.

8.2.1 Thin Integrating Detectors

At the full beam current that is required to make the proposed asymmetry measurement, the detector rates vary from 10 to 100 MHz per cm^2 in the Møller and elastic e-p rings (the high rate rings, 5 and 2). At these rates, counting individual signal pulses would require highly segmented detectors with pixel sizes at the 100×100 $\mu\mathrm{m}^2$ level or better (since the rate is not uniformly distributed over a cm^2). While this is something that can perhaps be done with modern semiconductor based pixel detectors, the cost, complexity, detection efficiency, reliability, background sensitivities, and radiation hardness are major concerns.

The only other option is to integrate the signal, corresponding to a spatial integration of many events

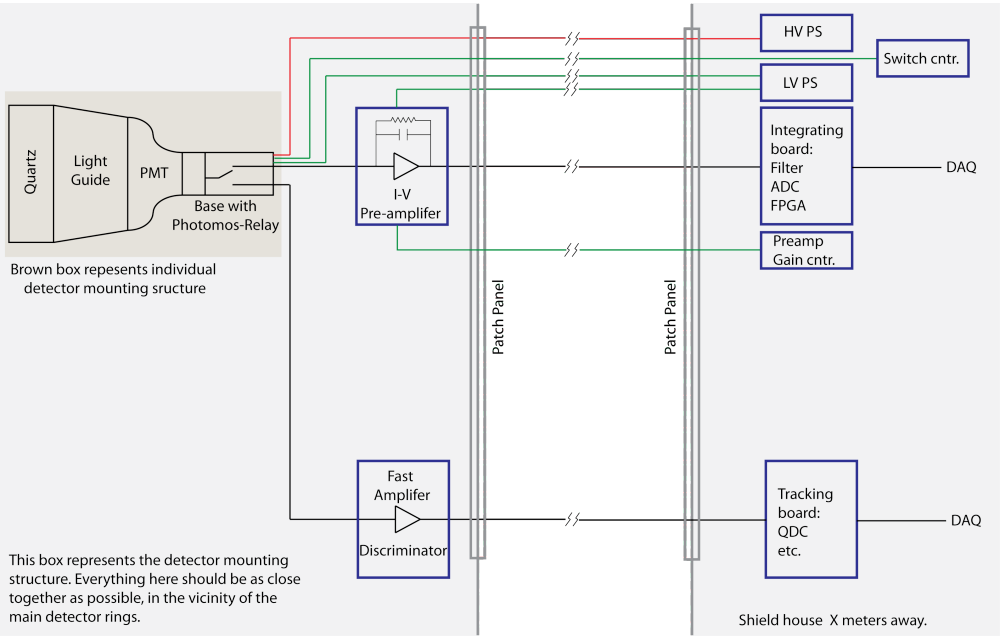

Figure 31: *Main integrating detector system layout schematic, indicating the integration mode signal chain, the tracking mode signal chain, and the PMT base control, which must be electronically switchable between the two operating modes.*

distributed over the exposed surface of a sufficiently large detector. The corresponding detector signal is a "steady state" current (for fixed beam and target properties), resulting from many overlapping individual electron pulses. In the electronics, the signal is then integrated in time, over a sample window, which must be chosen to allow a large number of individual current samples within each helicity window to reduce non-linearities and bit noise in the ADCs (see Appendix K). The samples collected within a helicity window are then effectively averaged in the DAQ software to produce a mean, RMS, and minimum and maximum values of the signal within each helicity window. The decision to operate in integration mode, with larger detectors, allows us to choose a radiation hard active material, with low background sensitivity. The ideal detector active material is artificial fused silica (henceforth "quartz"), since it is radiation-hard, and has negligible scintillation and low response to hadronic backgrounds as well as soft photon background. The best choice for the MOLLER integration running mode are therefore DIRC detectors, such that the light yield is maximized.

A high level schematic of the full main detector system concept for a single channel is shown in Fig. 31. The figure illustrates the components of each detector signal chain in both modes. The physical conceptual design of the thin detector array is shown in Figs. 32 and 33. All of the integrating detector modules will consist of three major parts: the active detection volume, made from $1\ \mathrm{cm}$ thick quartz, the light guide, consisting of an air-core channel with walls made from a high reflectivity material, and a quartz window photomultiplier tube (PMT) with high quantum efficiency and low dark current. The integrated response of the PMT to the collected light yield is the experiment's measure of the scattered electron flux. Light guides are needed to move all PMTs away from the envelope of scattered electrons and backgrounds as much as possible while, at the same time, reducing sensitivity to background (the latter resulting in the choice for the air-core, rather than a solid material).

Operation in integration mode precludes event mode cuts, based on pulse shape or amplitude discrimination, and true counting statistics is not achievable (see Appendix K). Therefore the two primary concerns

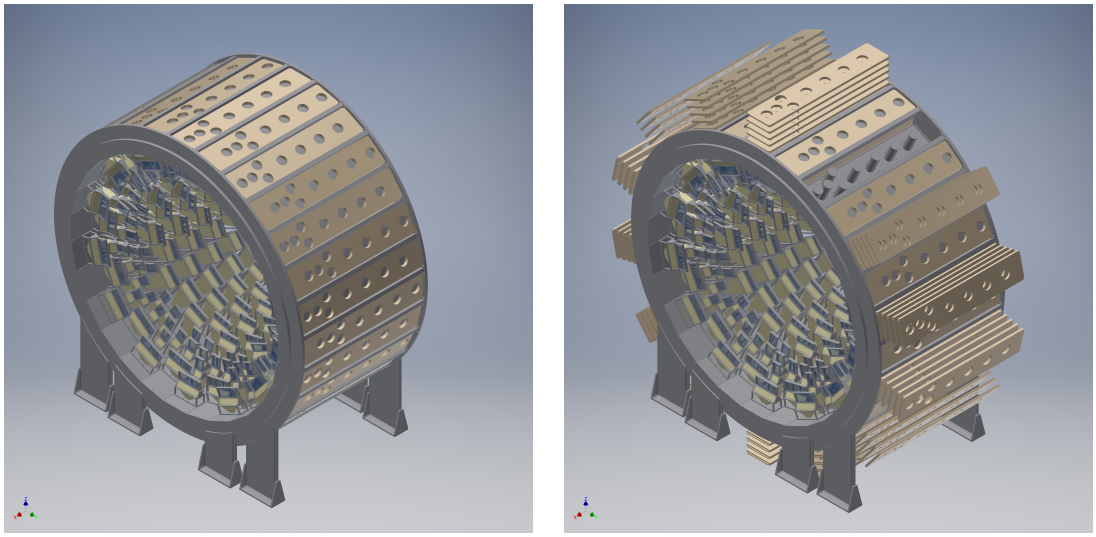

Figure 32: Conceptual design of the thin integrating detector array. The left figure shows the fully assembled array. On the right, the shielding plates have been *exploded*, to illustrate the shielding concept (stacks of shielding plates) and one set of plates has been removed to show the PMT housing. The full diameter of the router ring in this design is $3.3\ \mathrm{m}$.

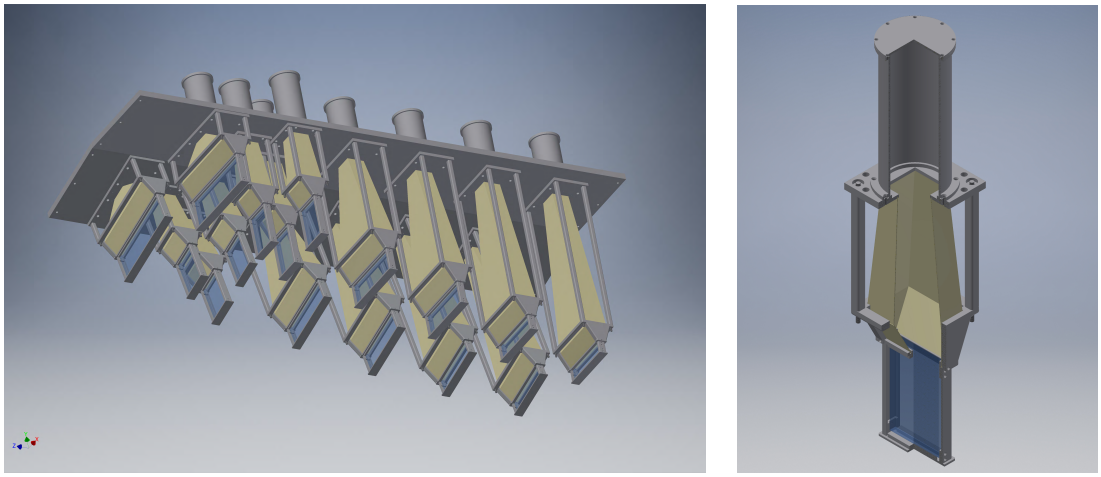

Figure 33: Conceptual design of the thin integrating detector array. The left figure shows two neighboring sections of the array, illustrating the staggered arrangement, which is done to ensure full azimuthal coverage. The right figure shows a cut-away view of the ring 5 module, including the combination of the quartz tile (blue), the light guide (yellow), and the mounting structure and PMT housing.

for the detector design are to reduce background sensitivity as much as possible and to reduce excess noise to a level that allows the detectors to operate as close to counting statistics as possible. We define excess noise as a departure from counting statistics, such that the asymmetry error for a given detector and in the i_{th} helicity pair would be

$$\sigma_{A_i} = \sqrt{1+\alpha^2}/\sqrt{2N_i}\ .$$

Where N_i is the number of primary electrons detected within the helicity window and α is the excess noise. Excess noise is a combined result of PMT noise, electronic noise, production of showers inside the quartz or light guides, general sub-optimal detector geometry, and limits in light collection efficiency. Poor design in any of these areas leads to an increase in excess noise. Shower production and light collection are intimately connected to the detector geometry, which has been optimized using bench-marked simulations. The final choice for the geometry and orientation between the quartz pieces and the light guides, as well as for the light guide material, was studied using extensive simulations and prototype testing with electron beams, as discussed in Appendix J. The thickness of the quartz was determined from simulations and prototype beam tests and is based on balancing the need for light yield (which would favor thicker quartz) with the production of showers and a corresponding increase in excess detector noise. The lateral sizes of the various quartz pieces is set by the segmentation needs discussed above.

8.2.2 Shower Max Detectors

The shower-max detector ring is an azimuthally segmented, quartz-tungsten electromagnetic sampling calorimeter located just downstream of the thin quartz integrating detector array. The shower-max intercepts the same scattered electron flux as the main Møller ring 5, as shown in Fig. 34. The purpose of the shower-max is to provide a supplemental, energy-weighted measurement of the Møller signal with less sensitivity to hadronic and soft backgrounds. As the name suggests, this detector system counts electrons by inducing an electromagnetic shower which grows to near maximum before exiting the detector. The concept uses a "stack" of high-purity tungsten plates interleaved with optically polished quartz tiles to produce the shower and Cherenkov light, respectively. Light exiting the quartz is directed to a 3 inch PMT using a mirrored-aluminum, air-core light guide.

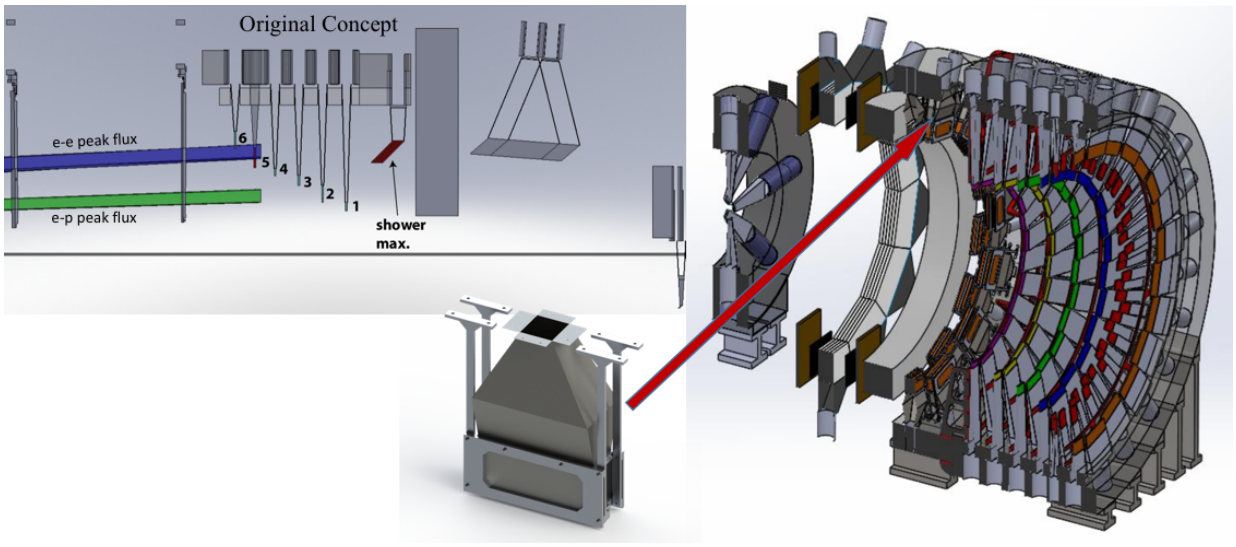

Figure 34: *(Left) Cutaway view of the original MOLLER detector package concept, showing the position of the shower-max ring relative to the thin quartz rings. (Middle) An individual shower-max detector module. (Right) The current design concept for the main integrating detector package.*

The shower-max ring consists of 28 individual detector modules completely covering the azimuth. The design requirements for each module are the same as those for the main integrating detectors (described in the previous Sec. 8.1), including the need to operate in both integrating and counting data acquisition modes. Given the radiation-hard requirements for the detector components, artificial fused silica or quartz is a natural choice for the stack's optical medium, and the interleaved, high-purity tungsten plates provide

the necessary radiation lengths in a compact size. One of the design-driving goals for the shower-max performance is to achieve better than 25% photoelectron resolution over the full range of accepted electron energies (from $\sim$ 2 - 8 GeV). The baseline design development, simulated performance studies and details of a recent shower-max beamtest at SLAC are given in Appendix L.

To guide the shower-max design process, a Geant4-based optical Monte Carlo has been developed and used to explore stack configurations and light guide geometries. Early simulation studies using 10, 6, and 4 layer stack configurations showed no significant loss in performance when using the simpler, 4-layer design. Based on these studies, and the desire to balance cost and performance, a 4-layer stack configuration was chosen for the baseline design. A set of detailed CAD renders of a single module are shown in Fig. 35. The shower-max design uses four layers of tungsten, each 8 mm thick, interleaved with four layers of quartz, each 10 mm thick; this corresponds to a total thickness of $\sim$9.5 X_o. The light guide is $\sim$25 cm long, radially (from stack to PMT), and uses an aluminum channel with a one-bounce, "funnel" mirror design to direct the Cherenkov light to a 3 inch diameter PMT. A schematic of the one-bounce design concept and simulated photoelectron (PE) distributions for the baseline design are given in Fig. 36. These results show ample PE generation with sub 20% resolution for the full range of accepted electron energies. Further R&D studies are ongoing to finalize the stack configuration and light guide geometry which optimize the PE resolution and collection uniformity. Initial prototype construction and beam testing occurred in 2018 and are detailed in Appendix L.

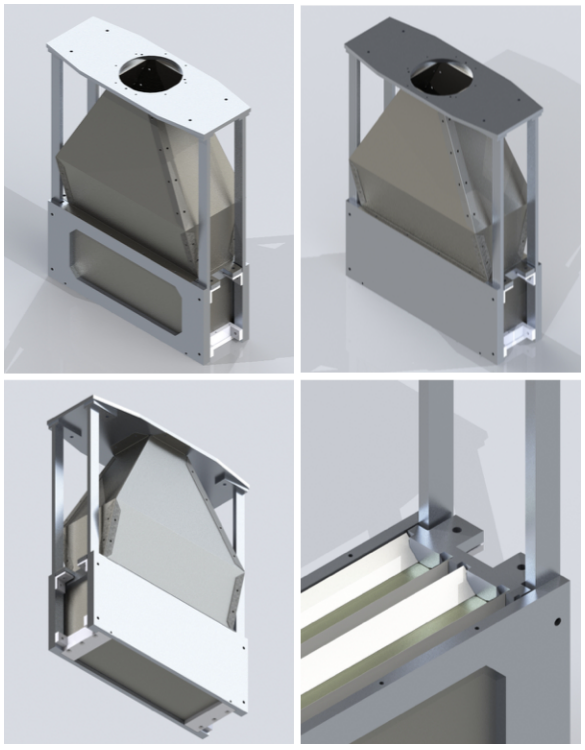

Figure 35: *CAD renders of the baseline shower-max prototype detector concept. The upper left figure shows the upstream face while the upper right shows the downstream end. The bottom right figure has the light guide removed to show the stack. All construction support materials and light guide are aluminum.*

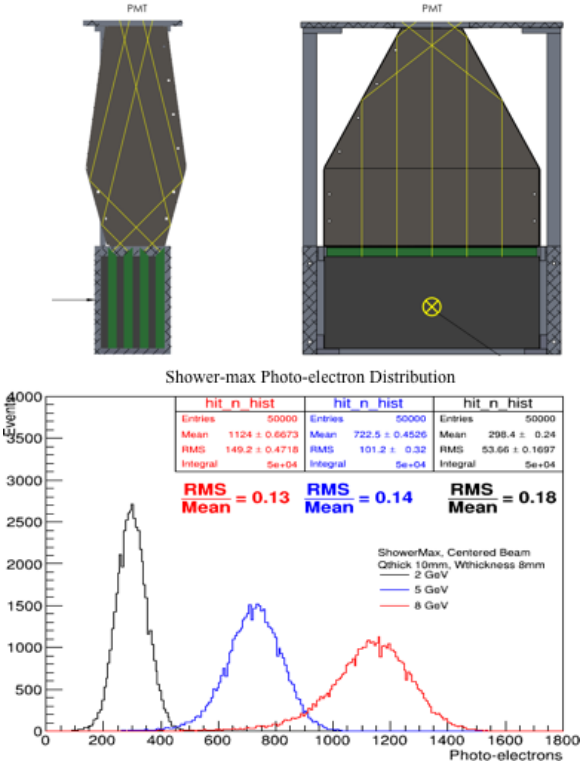

Figure 36: *CAD and G4 optical simulation results for the baseline shower-max design: top figures are CAD schematics of the detector geometry with the path of optical photons (yellow) from quartz (green) to PMT shown. Bottom plot gives simulated PE distributions for 2 GeV (black), 5 GeV (blue), and 8 GeV (red) electrons.*

8.2.3 Front-end Electronics

The front end signal chain is shown in Fig. 31. The light from the quartz is converted to a current using 3 inch quartz glass photomultiplier tubes (PMT) with a high quantum efficiency (QE) in the UV, with a peak around 280 nm. Quartz glass PMTs are necessary due to neutron backgrounds that would adversely impact performance with borosilicate PMTs and to extend the UV transmission of the window to improve the number of detected photoelectrons. For integration mode measurements, the primary concerns are that the PMTs support a high cathode and anode current over a sustained period of time and that the PMT-base combination linearity is understood at the required precision (see below). For pulse mode measurements, the PMT-base must be fast and high gain, providing a clean, single electron event, pulse. To accommodate these two very different measurement types, each mode has a separate front-end electronics chain and the PMT base is designed to be electronically switchable between integration mode and pulse (tracking) mode, implementing a low gain and high gain voltage divider, respectively. Each chain is briefly described in the paragraphs below while the details of the design and prototyping status are described in Appendix K. Both, the integration-mode, and the tracking-mode PMT parameters are summarized in Table 18.

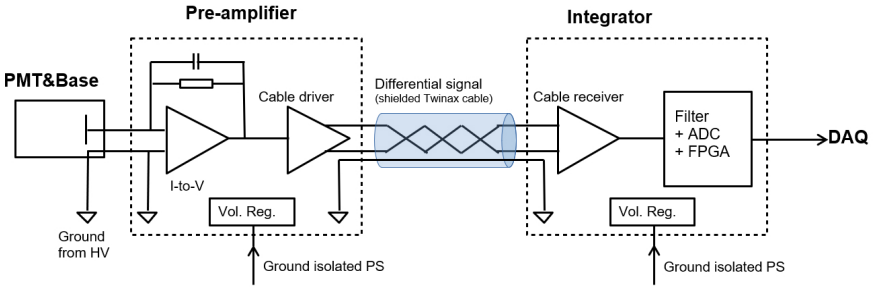

Figure 37: *Basic schematic of the frontend signal path for integration mode measurements. The PMT anode signal is converted to a voltage by a high gain trans-impedance (I-to-V) amplifier which is located close to the PMT. The amplifier implements a differential cable driver to the ADC board, which will be located about 50 meters from the detector array, in a shield bunker. The entire chain will be grounded through the PMT base high voltage ground and each module downstream from there will be powered by isolated low voltage power supplies.*

Integrating Detector Signal Chain: A more detailed schematic of the integration mode signal chain is shown in Fig. 37. In integration mode, at the maximum beam current, the event rate will vary by about an order of magnitude around the azimuth, within a given ring and by about two orders of magnitude from highest to lowest, among all of the integrating mode detectors. The highest rate in a single quartz detector will be about 5 GHz, while the lowest rate will be a few hundred MHz. To process the corresponding signal levels electronically, many of the detector channels will require variations of the base designs and the preamplifiers will have to be implemented with somewhat flexible gain. With the chosen quartz thickness, the photocathode of the PMT will conservatively produce a mean of about 20 photoelectrons per track for a detector with a light guide of average length (see prototype beam test results in Appendix J). Correspondingly, at a nominal rate of 1 GHz a mean current of roughly 3.2 μA is produced at the anode of a PMT with a gain of about 1000. For the highest rate detectors, the current is about 5 times higher. For these detectors a base gain of 400 will produce an anode current of

$$I_{\mathrm{anode}} = 5.0\ \mathrm{GHz} \times 20\ \mathrm{pe/track} \times 400 \times 1.6 \times 10^{-19} e/C = 6.4\ \mu A.$$

This is a large signal but still below the nominal 10 μA maximum usually recommended by PMT manufacturers for good long-term stability. The PMT that is currently under evaluation for both MOLLER and P2 is the 9305QKB PMT by ET Enterprises. It has a maximum anode current of 100 μA and one usually wants to stay well below that, to ensure longevity and relative long term gain stability of the PMT. The manufacturer of the 9305QKB does not specify a maximum number of Coulombs that can be drawn from the anode, but other sources [118] give a definition of PMT *end-of-life* when the anode sensitivity has dropped by a factor 2, which typically happens somewhere between 300 and 1000 Coulombs [118]. Figure 38 shows the long

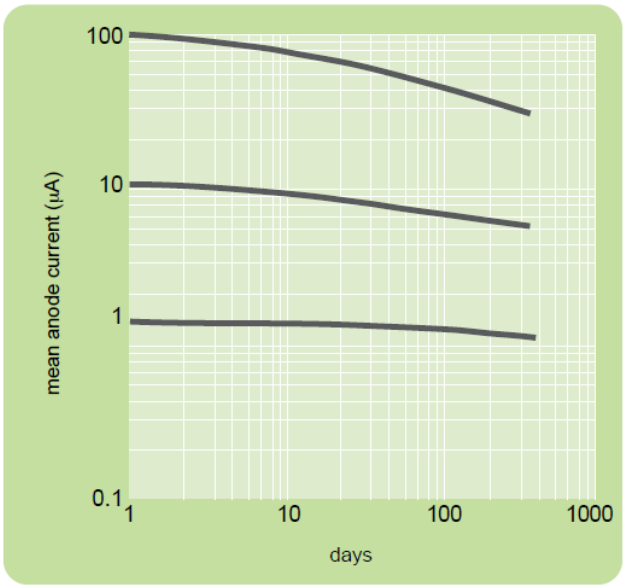

Figure 38: Plot of anode current stability under continuous illumination and constant bias voltage, taken over one year. The higher the anode current, the more pronounced is the gain drop over time. The figure was taken from [119].

term gain stability, measured by ET Enterprises (not necessarily with the 9305QKB PMT) for a few different anode currents [119]. The figure shows that, for a starting gain that produces a continuous anode current of 10 μA at the beginning, the PMT will be at its nominal *end-of-life* state after a little less than a year of running. This is roughly consistent with 300 Coulombs of charge drawn over the year. MOLLER will run for 344 full days (or 8256 hours).

In integration mode, the reduced gain can be countered by increasing the overall bias voltage over time, but for linearity and noise considerations we want to start off with a relatively high bias voltage and low number of stages to begin with and the PMT maximum voltage ratings limit the possibility for increasing the bias voltage later on. For these reasons it is prudent to keep the anode current at or below 10 μA, which means that the total PMT gain should be no more than around 1000, depending on the exact detector rate and photoelectron efficiency. Meanwhile, large dynode gain and a high photoelectron efficiency reduce excess noise. The list below summarizes the various, partially competing constraints.

1. Optimize the detector resolution, which implies maximizing n_{pe}, as long as this is not achieved while introducing shower noise or other non-Poissonian (non-cathode related) noise sources.
2. Maximize the inter-dynode gain (δ) for, at least, the first and second stages.
3. Maintain a gain that is low enough to keep the anode current at or below 10 μA.

4. Maintain reasonably linear operating conditions, which means keeping the inter-dynode and dynode to anode voltage reasonably high.

For the same PMT gain, the low rate detector anode signal would be only about 100 nA, which is too low. Therefore, the low rate detectors will need to have different PMT and preamplifier gains. The PMT that was chosen for the thin detectors has a maximum anode current of 200 μA and a maximum cathode current of 100 nA (see Appendix K).

It is known that PMTs develop significant non-linearities at low gain. A non-linearity has a multiplicative effect on the measured asymmetry, distorting the size of the asymmetry. Given the MOLLER precision goal, it is necessary to establish the linearity or measure the non-linearity of the PMTs at least at the 10^{-3} level, which has been shown to be achievable with a suitable choice of PMT and a good, low gain, base design. The goal for the integrating detectors is to keep the non-linearity for each detector at $\leq 0.5 \pm 0.1\%$. The measured asymmetry in each detector can then be corrected with the measured non-linearity.

For integration mode operation, a trans-impedance (I-to-V) preamplifier is used to convert the PMT current signal to a voltage with a high gain, and to provide the primary filtering stage for the signal. The preamplifier also implements a fully differential line driver to sustain the signal over the roughly 50 meter cable distance between the detectors and the integrating ADCs. The preamplifer is located close to the PMTs and appropriately shielded. The preamplifier voltage signal is further filtered on the ADC board and then digitized by an 18 bit, 15 Msps highly linear, commercial ADC chip. A total of 16 channels of the filter and ADC chain are implemented on a single ADC board, together with an FPGA, which queries the ADCs, collects the data and facilitates the readout. The ADC board incorporates the powerful Xilinx Zynq UltraScale FPGA, with on chip processor and embedded Linux. Together with several ports for fast fiber optic readout per board, this will allow the ADC boards to operate in fast, streaming, readout mode and act as stand-alone units that can communicate directly with the JLab trigger and DAQ system. Details about the integrating detector electronics operational criteria and design status are provided in Appendix K. The DAQ system and how the front-end electronics interfaces to it is discussed in Section 9.

Integrating Detector Pulse-Mode Signal Chain: As stated earlier in this section, for various studies, it is necessary to operate the detectors in single electron counting mode during tracking runs. In this mode, the main detectors must be able to resolve single events with fast timing, which typically requires a much higher gain than could be handled in integrating mode.

At a gain of 1×10^7, the average voltage pulse across a 50 Ω termination is

$$V_{\rm signal} = I_{\rm signal} \times R = (20{\rm pe} \times 10^7 \times 1.6 \cdot 10^{-19} C/e/10^{-8}{\rm sec}) \times \ 50\Omega = 160 \ {\rm mV}$$

which is a robust signal. Even a single photoelectron signal of 8 mV, produced for example by Compton scattering of a few MeV gamma-ray background in the radiator, could be easily observed. The PMT signal will be amplified using a high-speed shaping amplifier and sampled by a high speed $(250 \ {\rm Msps})$ flash ADC (with time resolutions of up to 4 nsec). The tracking mode ADCs and DAQ system are discussed in Sec. 9.2.2.

8.3 Alternatives

In the early stages of the detector design, various alternatives were considered, including:

1. **Position sensitive ion-chambers (PSIC):** These detectors would have been very sensitive to hadronic background and much more noisy than the Cherenkov detectors in the current design. To reduce the sensitivity to background, these detectors would have to be operated with mostly helium, but would then require both, a high pressure that would need to be maintained throughout the experiment, and

Table 18: *Parameters for the PMT signals from the quartz detector with the largest flux.*

Parameter	**Value**
Total PMTs	252 (6×28 and 1×84)
current mode:	
I_{cathode}	16 nA
gain	400
I_{anode}	6.4 μA
non-linearity (goal)	$\leq 0.5 \pm 0.1\%$
pulsed mode:	
I_{cathode}	0.24 pA at 100 KHz
gain	$1{\times}10^{7}$
I_{anode}	2.4 μA
V_{signal} (no amp.)	8 mV for 1 pe; 120 mV for 15 pe
non-linearity (goal)	$< 10^{-2}$

a pre-radiator (e.g. lead) to increase the signal level. The pre-radiator would have produced a much higher RMS width in the signal.

2. **Alternatives to quartz:** All other alternatives, such as lead-glass or lucite (or other scintillating materials) would have been either too sensitive to background, or not radiation hard enough.

3. **Alternative photosensitive devices:** Alternatives to PMTs and air core light guides, such as SiPM, or other diode based devices directly coupled to the quartz were considered, but disqualified due to the high radiation load. Since noise, linearity, and relative longevity (signal uniformity) are important in asymmetry measurements, it was considered too risky to implement such technologies.

4. **Alternative to the air-core light guide:** We also briefly considered the possibility of readout from the quartz, using fiber-optic bundles, but the geometry of the experiment is not conducive for this and, as a result, the implementation would have been difficult, more expensive, or produce more background.

9 Data Acquisition and Trigger

This subsystem consists of three major components: data acquisition, which is further divided into the integration mode DAQ and the counting mode DAQ; trigger, consisting of the electronics needed to detect particles passing through the detectors and initiate DAQ readout; and online computing, consisting of the computers, software, disks, and network to be able to record data to disk, send the data to tape, and analyze data online.

The integration mode data acquisition system primarily interfaces with the integrating ADC modules. In this mode, detector and beam monitor signals are integrated over the "helicity window" (about 0.52 ms long) at the nominal repetition frequency of 1920 Hz. Information identifying the beam helicity state, provided by the electronics in the polarized electron source, is recorded for each of these windows. The helicity state in each window is generated in 32-window-long patterns designed to cancel 60 Hz contributions to the calculated helicity-correlated asymmetries. During initial beam delivery and occasionally thereafter, the integrating ADCs are operated in a diagnostic mode in which all of the 15 Msps are recorded and reported, providing a waveform of the signals within the helicity window.

The counting mode data acquisition system is used for low-beam-current measurements in which individual electron scattering events can be observed, e.g. verification of the kinematics using the tracking system. It includes amplitude and timing measurement of all of the detector channels, digitization of a subset of the beam monitor signals, and readout of the GEM tracking detectors.

The trigger source for the integration mode is the T_stable pulse from the helicity electronics. The primary trigger for the counting mode comes from scintillators positioned to intercept electron trajectories through the GEM detectors. An important alternate counting mode trigger is the use of individual quartz detectors or combinations, to investigate signals in the quartz which are not directly related to electron trajectories.

Online computing includes both the systems involved in recording data and online analysis systems such as those providing feedback to the polarized source to control helicity-correlated beam parameters and those providing beam-parameter-corrected asymmetries for diagnostic purposes and evaluation of online data quality.

9.1 Requirements

In the integration mode DAQ, the integration windows for the detector and beam monitor signals must be synchronized with the period of stable helicity as generated by the electronics in the polarized electron source. Due to differences in signal propagation time for the detectors and beam monitors, the relative gate timing of individual integrators must be adjusted by up to several microseconds and controlled to ~ 60 ns. In production running, the integration DAQ must collect and transfer 100% of the helicity windows, without deadtime losses. The integration DAQ must support the diagnostic mode of the integration ADCs, but this mode does not require 100% throughput or deadtimeless operation.

The counting mode trigger must support trigger decisions based on input rates between 10 kHz and 300 kHz (assuming beam currents down to $\sim$ 10 pA). It must have flexibility to generate triggers from either the dedicated trigger scintillators, or from any combination of the quartz detector signals.

The networking and event building systems must support a data rate of about 130 MB/s during the production integration mode data collection to maintain 100% throughput without deadtime. Online analysis of helicity-correlated beam parameters and communication of feedback changes to the injector must occur with nearly 100% throughput and without impacting the data acquisition deadtime. Online analysis of fully-corrected detector asymmetries must occur with nearly 100% throughput and without impacting the data acquisition deadtime. Disk storage must be sufficient to hold the helicity-pattern-level asymmetry results spanning several days, to enable monitoring of changes in signal responses and correlations.

9.2 Conceptual Design

Both data acquisition systems run in the CODA (CEBAF Online Data Acquisition) framework, the Jefferson Lab DAQ toolkit in which front-end electronics readout is organized by a custom Trigger Supervisor and the event fragments are gathered via a standard TCP/IP network to a workstation where events are built, written to disk, and subsequently stored in the Mass Storage System (MSS).

Both data acquisition systems will interface with the EPICS slow-control systems to ensure that parameters important to the analysis of the data will be archived in the data files.

The integration mode and counting mode trigger systems are independent. Each DAQ system contains a Trigger Supervisor (TS) module which accepts the trigger inputs, makes a trigger decision, and initiates an accepted trigger and readout event. Connections between the TS and Trigger Interface (TI) units convey accepted triggers to the front-end electronics and ensure event synchronization. A TS module can support up to eight TI connections; for larger numbers of TI connections, Trigger Distribution (TD) modules are needed.

9.2.1 Integration-mode data acquisition and trigger

The integrating ADCs, described in Section 8.2.3 and Appendix K, are the heart of the integrating-mode DAQ. MOLLER will have approximately 500 integrating ADC channels; about 300 are used for the detector signals, about 100 for beam monitors in Hall A, and about 100 for beam monitors in the injector. Scaler modules are present in both the Hall A and injector crates. Figure 39 depicts the interconnections between the trigger supervisor, the integrators and other crates.

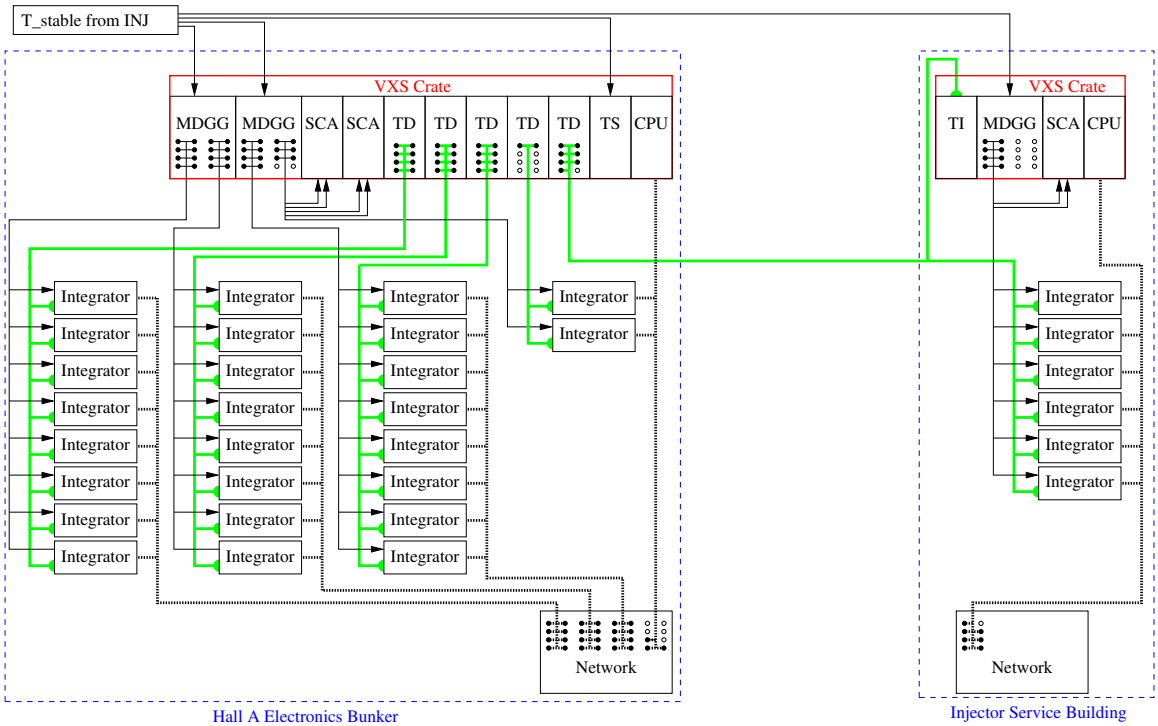

Figure 39: *Overview of the integration DAQ system. The thin black lines represent the integration start logic signals. The thick green lines represent the interface connection between the TD modules and the TI units in the integrators or VXS crate. The thick black dashed lines represent 10Gbit network connections.*

The primary integration-mode trigger is derived from the "T_stable" signal from the polarized electron source, which marks the period in which the beam helicity state is not being changed. The timing of the "T_stable" signal is adjusted by the digital delay and gate generator (MDGG) modules to form the start signal for each integration module's integration period. "T_stable" acts as the readout trigger through the integration-mode TS and then to the TI for the front-end readout modules. As the integration ADCs are not VME modules, they require special TI functionality, for which there are two alternatives. In the first, the TI functionality is built into each of the integration ADCs, and they send their data for each event directly to the event builder workstation. In the second, PCIe TI cards are used in "collector workstations" which then use point-to-point Ethernet links to pull event data from the integration ADCs, build event fragments and send them to the event builder workstation. While the first option does impact the development of the integration ADCs, it is preferred because it allows reuse of CODA event-building and network transport frameworks. The second option requires development of similar frameworks operating on the collector workstations.

9.2.2 Counting-mode data acquisition and trigger

The counting-mode DAQ consists of VME/VXS-based FADCs, VETROCs, Input/Output registers, and scalers. MOLLER will use about 300 channels of FADC and VETROC for the detector signals, with about 30 additional FADC channels used for a subset of the beam monitors. The GEM detectors are readout using sixteen MPD (Multi Purpose Digitizer) cards.

Figure 40 shows the instrumentation and trigger layout for a single quartz detector or scintillator channel. The signal passes through a NIM amplifier, from which one output goes to a JLab 250 MHz FADC module, to record signal amplitude, and another goes to a JLab discriminator/scaler module. The logic signal from the discriminator goes to a JLab VETROC (VXS-based Electron Trigger and Readout Card) module, which measures timing. Digitized data from the front-end modules is passed to the FPGA in the JLab VXS Trigger Processor (VTP) in which signal levels and coincidences are detected to form potential triggers. The VTP modules in all crates communicate with the TS to form the final accepted trigger. Triggers are prescaled within the TS to ensure deterministic deadtime calculation for rate determination. The primary trigger will be based on the trigger scintillators, but triggers based on the quartz detector signals and pulsers will also be used.

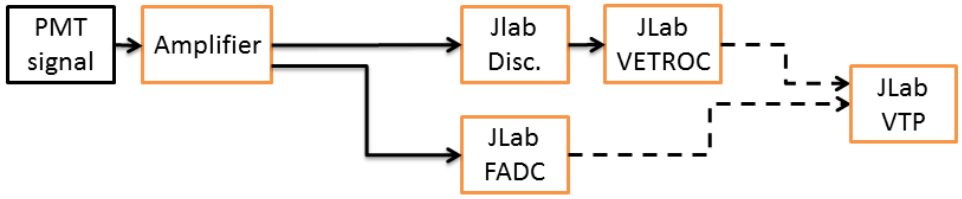

Figure 40: *Overview of the counting DAQ system for one channel as described in the text. The solid lines represent the analog or logic signals, and the dashed lines represent data transfer from the VETROC and FADC to the VTP module.*

The crate layout is diagrammed in Fig. 41. The first two VXS crates would instrument all six rings of the thin integrating quartz detectors. The third crate would instrument the shower max and pion detectors, trigger scintillators, and beam monitors. The fourth crate holds the MPD modules which readout the GEM detectors. In crates 1-3, the logic signals from the discriminators are input to the VETROC. The digitized information from the VETROC and FADC modules are collected by the VTP in each crates, and each VTP communicates potential trigger events to the TS for final trigger determination. On an accepted trigger, the

MPD cards pass the GEM data to the JLab SubSystem Processor (SSP) module for backplane and network transfer to the event builder.

Figure 41: *Crate layout for the counting DAQ system. Four VXS crates contain the instrumentation modules. Digitized information in each crate is collected by the VTP modules, then passed to the TS for the trigger decision. On an accepted trigger, the TI modules synchronize the crate readout.*

9.2.3 Online Computing

In the production integration mode running, each of the 32 integration ADC modules produces a data rate of about 4 MB/s, for a total data rate of about 130 MB/s. The network infrastructure is industry-standard 10 Gigabit Ethernet, to ensure sufficient network bandwidth to transfer the data in both data acquisition modes. Independent workstations are used for the event builder and the helicity-correlated feedback analysis. Projecting from performance in Q_{weak} and PREX-II, this is sufficient. Again projecting from the earlier experiments, a cluster of eight workstations is needed for online determination of correlations and applying corrections to the detector asymmetries based on beam parameter variation.

Parity-violation experiment analysis does not gain a large data reduction from raw data to fully-analyzed asymmetries, and prior experiments have seen an expansion of ROOT output size by as much as four times compared to the raw data. Local disk storage of about 100 TB is needed for accumulation of a few days of the online analysis outputs to monitor for drifts in responses and correlations that may indicate a problem in beam delivery.

10 Beam Diagnostics and Monitoring

The physics goal of the MOLLER experiment requires precise measurement and control of the electron beam properties. The systems in this category are needed to properly measure and correct for helicity-correlated beam properties and to characterize beam properties (such as beam halo) that could lead to potentially irreducible backgrounds from scattered beam interacting downstream of the target.

10.1 Requirements

As described in Appendix A, the scattered flux is integrated over the duration ($\sim 520\ \mu$s) of each helicity window. Equation 11 shows how one then extracts a signal proportional to the raw cross-section asymmetry by removing correlations of the scattered flux with beam properties. Uncertainties are introduced in this correction procedure due to the precision limits of measuring the beam properties and of determining the correlation coefficients of the scattered flux with beam properties. In this section, we describe the requirements to ensure that these uncertainty contributions to our random noise width (Tab. 2) and systematic errors (Tab. 3) can be achieved.

Position and intensity monitoring requirements To perform the correction procedure, relative changes (not absolute values) of the beam properties between adjacent helicity windows ("window-pairs") need to be measured with specified precision ("resolution"). The relative beam position changes need to be measured with a resolution of $\lesssim 3\ \mu$m for 960 Hz window-pairs at two locations separated by ~ 10 m (to determine projected position and angle at the target) and at a point of high (> 3 m) dispersion (to determine the beam energy). The relative beam intensity changes need to be measured with a resolution of $\lesssim 10$ ppm for 960 Hz window-pairs.

Beam modulation system A beam modulation system is needed to measure the response of the detectors to variations in beam position, angle, and energy. The successful use of the beam modulation system requires a significant phase advance between the modulation magnets and monitors used to characterize the beam motion, so that independent motions spanning the beam phase space can be observed.

Scattered beam monitors In order to monitor potential false asymmetries in irreducible background resulting from primary scattered beam interacting in downstream collimators, beampipe, and shielding, scattered beam monitors are needed: a) in locations where the primary target scattered rate is higher than the Møller rate but the expected physics asymmetry is smaller, b) in locations where the expected scattering rate from primary target interactions is small, so the majority of the signal comes from secondary interactions.

10.2 Conceptual Design

10.2.1 Beam monitoring and control

This section describes the capabilities of the existing beamline instrumentation to meet the above requirements and the improvement path where needed. It also describes the reference MOLLER beamline layout that can achieve the required phase advance.

Beam position monitor resolution The most stringent requirement on beam position monitor resolution comes from requiring that the additional random noise contribution from beam jitter (after correction for it) be no larger than 10% of the counting statistics width for a single azimuthal element of the detector. This leads to a more stringent requirement than applying the same criterion to the average over all detectors. This

is important for two reasons. It allows for high precision comparison among selected combinations of the azimuthal detector elements to study the behavior of the linear regression corrections. It also insures the precision necessary to measure the azimuthal dependence of the raw detector asymmetries for the "manual" feedback loop to control transverse polarization described in Appendix B. Applying this criterion leads to a requirement on the beam position monitor measurement resolution of 3 μm for 960 Hz window-pairs. The standard beam position monitors at JLab are referred to as thin wire "stripline" monitors [59, 63], which consist of four thin wires operating in a quarter-wavelength antenna mode. The Q_{weak} experiment has measured the beam position monitor resolution for 960 Hz quartets for these types of monitors. The study [60] was done versus beam current and the results are shown in Fig. 42. For MOLLER beam currents, typical resolutions of $\sim$ 1.3 μm are found. Taking the conservative assumption that the monitor noise is dominated by white noise, the scaling from quartets to pairs and the scaling from 480 Hz pairs to 960 Hz pairs can be estimated as two factors of $\sqrt{2}$. This results in an estimated 2.6 μm resolution for 960 Hz pairs for MOLLER, which achieves the MOLLER goal of 3 μm. It is also planned that redundant beam position measurements with a similar resolution will be performed with radio frequency microwave cavity monitors operating in the TM_{110} mode at 1497 MHz that are installed in the Hall A beamline. These have not been used extensively except during parity experiment running in Hall A where performance comparable to stripline monitors has been demonstrated.

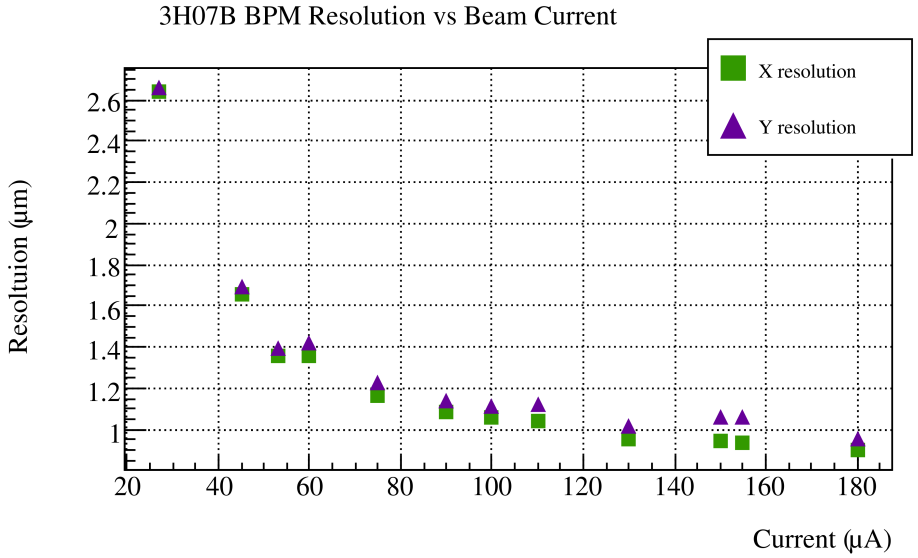

Figure 42: *Measurements of beam position monitor resolution as a function of beam current during the* Q_{weak} *experiment [60]. See text for further details.*

Beam charge monitor resolution The MOLLER requirement is 10 ppm resolution for relative beam intensity measurements for 960 Hz window-pairs. This requirement comes from the need to keep this contribution to the random noise small compared to the counting statistics contribution. Here, we report on the best values achieved to date and the work in progress by the collaboration and lab to achieve this goal. In particular, we report on the results from the Q_{weak} experiment. Q_{weak} measured beam intensity with beam current monitors (BCM) consisting of the standard JLab hardware of resonant microwave cavities operating in the TM_{010} mode. The best results were obtained with all-digital receiver electronics designed by JLab staff member John Musson [61]. The random noise in the beam charge measurement was determined by

forming the "double-difference", which is the difference between the helicity-correlated charge asymmetry for two BCMs. The RMS of this distribution determines the uncorrelated random noise of the charge measurement, referred to as the resolution. A typical value of this RMS during regular $\mathrm{Q_{weak}}$ running at a beam current of 180 μA was $\sim$ 62 ppm.

To facilitate improvements, dedicated bench tests with these digital receivers were done with a $\mathrm{Q_{weak}}$ data acquisition test stand and the beam signal replaced with a radio-frequency source signal. A more detailed description of these studies is in Appendix M, but here we discuss the main conclusions. A study versus data-taking frequency is shown in Fig. 43. The observed value at the $\mathrm{Q_{weak}}$ 240 Hz quartet frequency of 62 ppm agrees with what $\mathrm{Q_{weak}}$ observed with beam. At double that frequency, corresponding to the MOLLER data-taking frequency of 1.92 kHz, a lower value of 42 ppm was observed. That implies a resolution of 42 ppm for 960 Hz window-pairs (that comes from dividing by a factor of $\sqrt{2}$ to get to resolution and multiplying by a factor of $\sqrt{2}$ to convert from quartets to pairs under the white noise assumption). As shown below, the MOLLER beamline will be equipped with seven BCMs, so brute force averaging of those seven would lead to 42 ppm/$\sqrt{7}$ $\sim$ 16 ppm, close to the MOLLER goal. However, this limits flexibility in doing systematic studies among the monitors, so ideally the resolution of a individual monitor would be improved further.

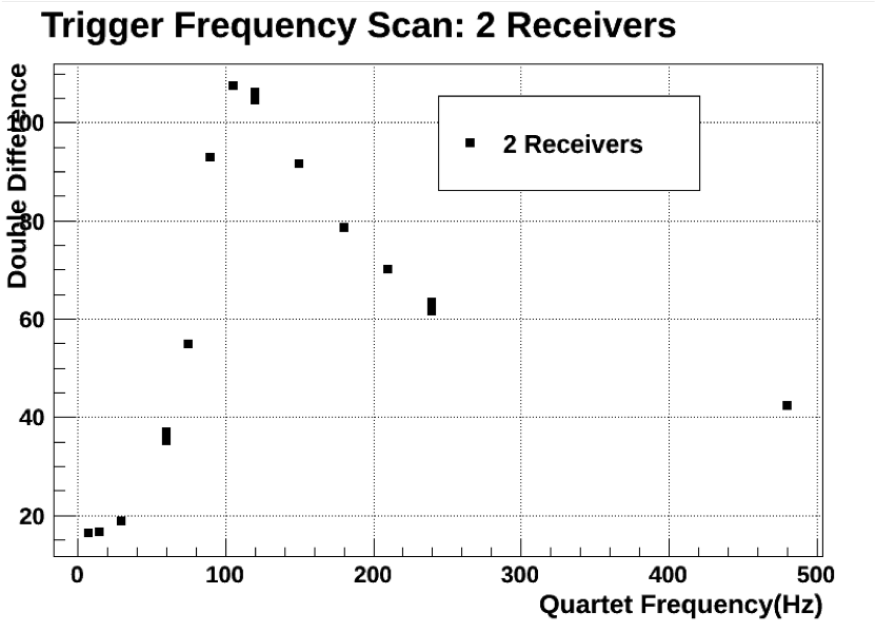

Figure 43: *Bench study of* $\mathrm{Q_{weak}}$ *digital receivers with two receivers and a common rf source to simulate the beam signal. The observed double difference versus quartet frequency is shown.*

The bench studies reported in Appendix M strongly suggest that the beam current independent noise floor observed for the digital receiver electronics is limited by phase and amplitude noise in the 1.5 GHz local oscillator that is mixed with the incoming signal in the receiver electronics. There are two potential improvement paths that the collaboration is pursuing:

- An upgraded version of the Musson digital receivers has been developed. Among various changes, a different local oscillator was employed. Initial bench tests with these receivers for $\mathrm{Q_{weak}}$ running parameters gave a factor of two smaller double difference of 32 ppm. That would bring the brute-force averaged result quoted above down below the MOLLER goal of 10 ppm. These digital receivers will be further tested during the PREX-II and CREX runs.

- A completely new approach of an all digital beam processor is being pursued by collaborators at UC Berkeley led by Yury Kolomensky. This development makes use of high sampling rate ($\gtrsim 3$ Gsps) and high dynamic range (> 10 bits) ADCs that are capable of direct RF sampling, thus eliminating the need for the local oscillator. Initial bench studies of this type of receiver gave ~ 10 ppm resolution for 960 Hz window-pairs. Studies of this receiver type during the upcoming CREX run are being planned.

Beam modulation system A beam modulation system is used to measure the response of the detectors to variations in beam position, angle, and energy. Such a system is currently being used in Hall A for the PREX-II and CREX experiments. For position and angle, the system consists of air core copper coils installed in the Hall A arc. The coils are driven by a waveform generator and power amplifier to allow small displacements of the beam from the nominal trajectory with a desired time dependent pattern. Modulations in beam energy are accomplished in the same fashion using the same driving electronics to vary the input voltage to one of the superconducting radiofrequency accelerating cavities in the south linac of the accelerator. Appropriate software controls the modulation cycles using the EPICS control framework and interfaces to the data acquisition system.

MOLLER beamline A reference design for the MOLLER beamline in Hall A has been developed by Jay Benesch [62]. It largely uses existing instrumentation with modifications to the beam line needed to satisfy the MOLLER requirements. The layout is shown in Fig. 44. Complete details of the design can be found in the tech note, but we summarize some of the highlights here. A major feature of this design is that the six Møller polarimeter magnets are completely degaussed so they act as a beam drift during normal beam transport. The fast raster is thus downstream of the last focussing element, in contrast to the current Hall A situation where it is upstream of six active quadrupoles. This removes many of the optics design constraints of the current beamline.

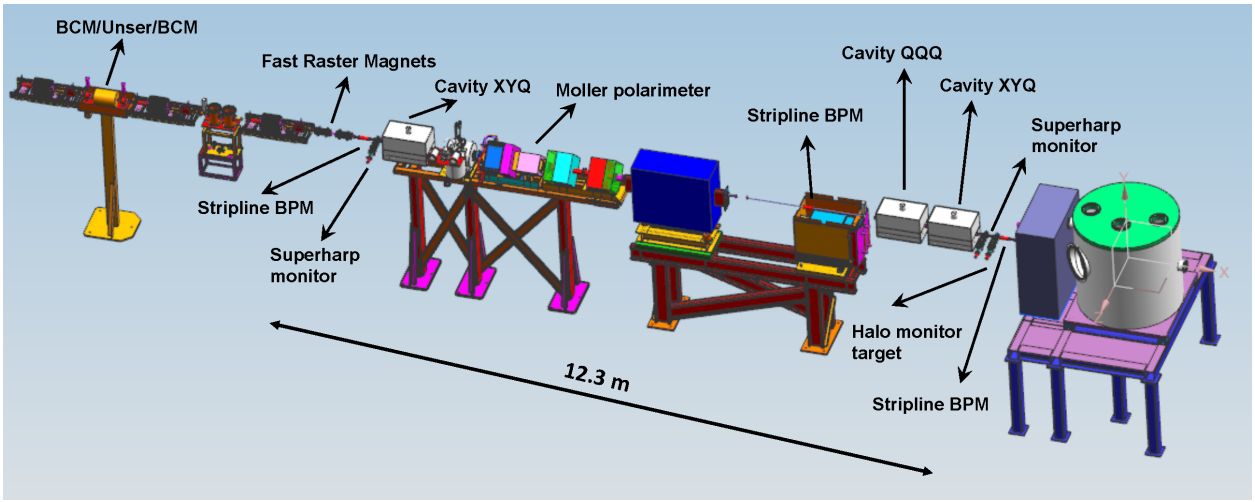

Figure 44: *Reference design of the MOLLER beam line.*

Major elements of this option, from upstream to downstream in Fig. 44 include:

- Quadrupole and corrector magnets, for position lock at both the Møller polarimeter and MOLLER experiment targets

- Existing BCM/Unser/BCM combination, moved ~ 4 m upstream of its current location
- Quadrupole and corrector magnets, for position lock at both the Møller polarimeter and MOLLER experiment targets
- Fast raster, moved ~ 3 m downstream of its current location, with only two of the coils used
- A short 1.6 meter diagnostic girder, with a stripline beam position monitors (BPMs), microwave cavity XYQ box, and a superharp beam profile monitor
- Møller polarimeter, unmoved from its current location, but with fully degaussed quadrupoles and dipole during production running
- A 4 meter diagnostic girder including a stripline BPM, a microwave cavity XYQ box, a microwave cavity QQQ box (three BCMs), a superharp beam profile monitor, and a superharp drive with a halo hole target in it that can be used to monitor beam halo with simple downstream lucite based counters (as was done during $\mathrm{Q_{weak}}$)
- The MOLLER target.

In terms of the critical instrumentation for measuring MOLLER beam properties, this design has redundant position and angle measurements with stripline and microwave cavity beam position monitors (BPMs) separated by > 10 m to ensure good angular resolution. It also has a total of seven BCMs, with two upstream of the fast raster and five downstream. The OptiMX code was used to determine the beam optical properties of this configuration [62]. Figure 45 shows the beam size in X and Y along the beamline. The intrinsic spot size sigma at the MOLLER target is ~ 150 μm in both dimensions. The largest spot size sigma is ~ 340 μm, and it occurs in a region with a 22 mm ID beam pipe. Figure 46 shows the raster response, with the desired half-size of 2.5 cm at the MOLLER target. In contrast to the existing Hall A beamline, the behavior is symmetric in X and Y. Finally, Fig. 47 shows that the phase advance between the beam modulation coils and the beam position monitors is adequate ($> \pi/6$) to ensure that the full phase space of position and angle motions can be probed. This is an improvement over the existing situation in Hall A where the phase advance in the vertical between the BPMs is typically not adequate.

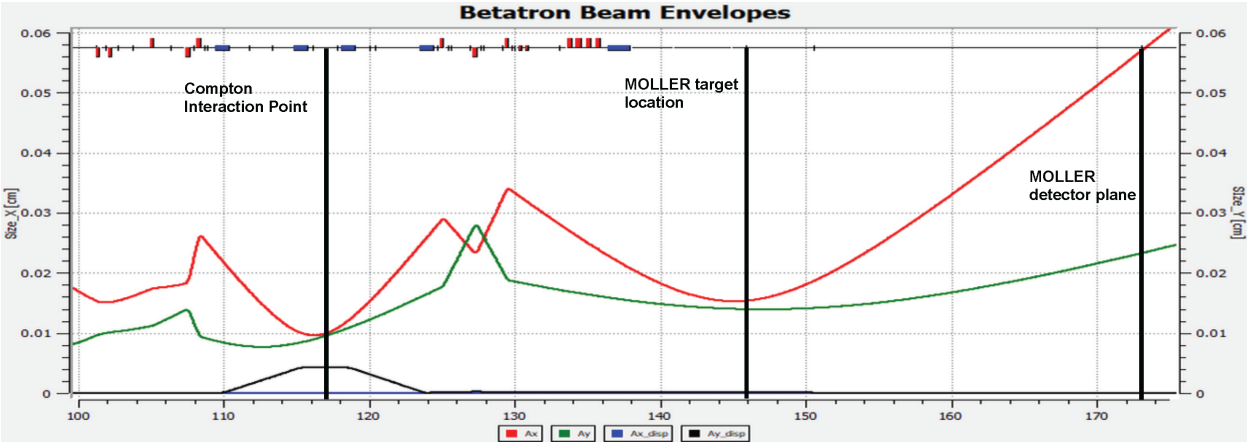

Figure 45: *Reference design betatron envelopes. The red trace is X and the green trace is Y. The x axis is location along the beamline in meters. The location of the MOLLER target and detector plane are indicated by vertical lines.*

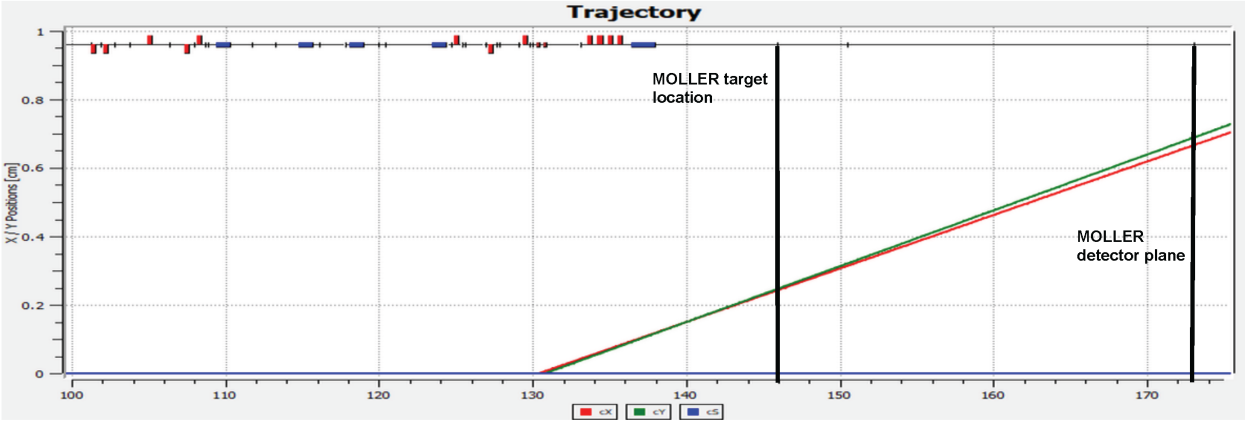

Figure 46: *Reference design raster response. The x axis is location along the beamline in meters. The y axis is the half-size of the rastered beam. The location of the MOLLER target and detector plane are indicated by vertical lines.*

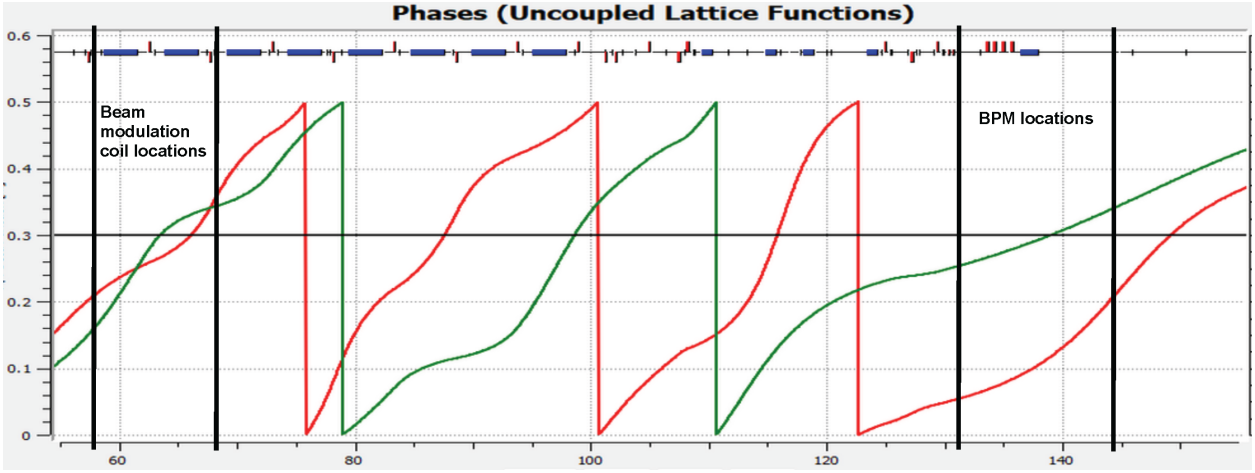

Figure 47: *Reference design phase advance. The units of the left axis are 1.0 = 2π. The two vertical lines on the left represent the location of air core correctors in the beam modulation system, with an XY pair at each location. The two vertical lines at the right show the locations of beam position monitors. The red trace is X and the green trace is Y. The phase advance between the modulation coils and the beam position monitors for both X and Y is adequate ($> \pi/6$) to ensure that the full phase space of position and angle motions can be probed.*

10.2.2 Scattered beam monitors

A set of detectors, referred to as scattered beam monitors (SBM) will be installed at various locations to monitor potential false asymmetries in irreducible background that results from the primary scattered beam interacting in downstream collimators, beampipes, and shielding. Small and large angle scattered beam monitors (SAM and LAM) - also referred to as luminosity monitors - will be located in regions where the scattered rate is estimated to be larger than the main Møller rate, but the physics asymmetry is expected to be smaller. These detectors will consist of quartz Cherenkov radiators and air light guides to transport the light to photomultiplier tubes. Diffuse scattered beam monitors (DBM) will be deployed in locations

where the expected scattering rate from primary target interactions is small, so the majority of the signal would come from secondary interactions. These detectors will be similar to the luminosity monitors, but they will also consist of detectors with only PMT and light guide or only PMT to better characterize how the background interacts with the typical detector components. Detectors of this type proved very useful in the $\mathrm{Q}_{\mathrm{weak}}$ experiment [11] to correct for an observed beamline background asymmetry, which was a false asymmetry caused by secondary events scattered from the beamline and the tungsten beam collimator.

The planned location for the SAMs is shown at the left edge of Fig. 28. These SAMs, consisting of quartz detectors that will detect the charged particle flux at extreme forward angles, have two purposes. Since they have higher statistics than the primary Møller flux, they serve as a sensitive diagnostic of target density fluctuations, beam fluctuations and electronics noise. The small scattering angle also implies that they should have a much smaller parity-violating asymmetry, so that they can also serve as a "null asymmetry monitor".

In the current spectrometer design, we have determined that the forward angle charged particle flux in the θ_{lab} range between 2 and 2.5 mrad should not feel any fields. We therefore plan to instrument the region between 6.0 and 7.5 cm thirty meters downstream of the target with eight of the SAMs. This arrangement is very similar to the geometry of the $\mathrm{Q}_{\mathrm{weak}}$ downstream luminosity monitors [64]. The scattered electron rate into the full azimuth at this location (coming equally from Møller and elastic e-p scattered electrons) is about 950 GHz. This will yield a rate of $\sim$ 75 GHz per detector, very similar to the $\mathrm{Q}_{\mathrm{weak}}$ case. Assuming 10 photoelectrons per event, we would expect a photocathode current of 120 nA. Given the similarities to $\mathrm{Q}_{\mathrm{weak}}$, we could employ a similar photomultiplier arrangement. A multi-alkali photocathode is used and the dynodes are tied together to run it in "unity-gain" mode. The output is fed into a TRIUMF current-to-voltage preamplifier with a transimpedance of 25 MΩ to yield a voltage of 3.0 V. The photomultiplier tubes would be shielded by (or encased in) a lead ring. SAMs operating under very similar conditions are being used in the ongoing PREX-II and CREX experiments, and the experienced gained there will be used to further refine the design.

The total rate in the eight detectors will be $\sim$5 times higher than the main detector, implying a two times smaller statistical error per pulse pair. Assuming the Møller and elastic e-p processes are the largest contributors to the signal in this detector, the expected physics asymmetry is $\sim$3 ppb, an order of magnitude smaller than the asymmetry in the main detector. So this would serve as a "null-asymmetry" monitor at that level and a sensitive check for any false asymmetries from backgrounds.

One technical concern with these detectors is the high radiation dose that will be received by the artificial fused silica over the course of the run. It is about 8 Grad per detector. The similar size and material $\mathrm{Q}_{\mathrm{weak}}$ downstream luminosity monitors showed no evidence of radiation damage up to $\sim$ 2 Grad. There is no reason to believe that there will be any degradation as one goes beyond 2 Grad, but if there were, the materials in these detectors are inexpensive enough that periodic replacements are feasible.

11 Infrastructure and Integration

The high luminosity of the MOLLER experiment will lead to high secondary particle production inside the experimental hall. To allow electronics to operate without interruptions and timely personnel access, shielding is required to minimize the radiation field inside and outside of the hall. Integrating these components into Hall A requires careful consideration in order to allow for efficient installation while at the same time providing flexibility to maintain and service components during experimental data taking. In addition to the above considerations, significant modifications to the existing hall beam line and components are required in order to fit the MOLLER apparatus within the Hall. Additionally, the cryogenic cooling capacity, as well as the electrical and chilled water cooling capacities need to be upgraded to support MOLLER and other upcoming experimental programs. The following subsections will describe each issue listed above.

11.1 Infrastructure

MOLLER will be installed and collect data in experimental Hall A at JLab. This subsection will describe the basic utilities required to efficiently run the experiment.

11.1.1 Electrical power

The installed electrical capacity of Hall A is slightly above 1 MVA. The MOLLER downstream toroid magnet alone is expected to consume 0.6 - 1.0 MVA leaving marginal capacity to power the remaining hall and MOLLER experiment equipment. To increase the electrical power in the hall, an upgrade of an additional 2 MVA will be conducted in May-Dec 2020 well in advance of MOLLER data taking. Additional routing circuitry will be installed going to the electronics enclosure (see Section 11.2.1) to power the racks and the low voltage power supplies for the MOLLER tracking detectors.

11.1.2 Water cooling capacity

The MOLLER water cooling requirements are expected to be slightly above 1 MW which is about the limit of the present water cooling capacity of Hall A with a flow of 250 GPM. Increasing the water flow to Hall A to 500 GPM to double the cooling capacity requires some changes to the feed pipes coming into the hall as well as control changes to the pumping system circulating the Low Conductivity Water (LCW) to Halls A and C. The Super BigBite Spectrometer (SBS) program, which will start data taking in Fall of 2020, also requires an upgraded LCW system. Consequently, this requirement will be met before MOLLER running.

An isolated Low Conductivity Water (LCW) circuit to cool the two toroidal magnets and collimators is needed for MOLLER. Refer to sub-section 6.3.3 for a discussion of this detail.

11.1.3 Cryogenic cooling capacity

The high-power LH_2 cryogenic target requires cooling above what the existing End Station Refrigerator (ESR) and Hall A cryogenic distribution transfer lines can deliver. For MOLLER, a dedicated transfer line capable of handling the larger flow is needed between the cryogenic target and a new End Station Refrigerator (ESR 2) currently under construction. This requirement is met by the ESR 2 construction budget and should also be completed by 2023, in advance of MOLLER data taking.

Table 19: Power deposition along beam line for 65μA electron beam and a 1.25 m target length.

Beam line element	**Power deposition [W]**
Target	4000
Collimator 1	4000
Collimator 2	700
Collimator 4	70
Collimator 5 and lintel	40

11.1.4 Air conditioning

The existing air conditioning available in Hall A is sufficient for the experiment with the exception of the electronics enclosure (see 11.2.1). Additional air conditioning to ensure reliable operations of the electronics racks inside the enclosure are included in the project plan.

11.2 Particle shielding

Particle shielding is necessary in order to protect sensitive electronics in the experimental hall and personnel both inside the hall and on the JLab site. Due to the high rate of scattering from the 1.25 m long target a large radiation field is expected inside the experimental hall during data collection. In addition, this high radiation field can increase the background rate in the main detector leading to decreased sensitivities.

The power supplies and electronics used to collect the data can be temporarily disabled or permanently damaged by radiation. Temporary damage occurs through Single Event Upsets (such as a bit flip in a memory chip) and will decrease the data collection efficiency. This type of damage most often is precipitated by either high energy hadrons (E>10 MeV) or low energy (thermal) neutrons. Long term damage occurs at different levels for different materials, but for most uses inside the hall we focus on the damage to silicon-based chips. This type of damage takes into account interactions from electrons, positrons, pions, protons and neutrons from a few 10^{-13} to 10 GeV with the resulting impact typically expressed by the displacement damage equivalent or total non-ionizing dose. Once a certain damage level has been reached the component will need to be replaced, again decreasing data taking efficiency.

Personnel will require access inside the hall during experimental data taking in order to inspect and maintain the equipment in good working order. The radiation field will activate different components which may have a cool-down period of weeks. In order to allow for timely access to the hall the shielding has been designed around the areas which will intercept the largest amount of radiation. Additionally, we aim to limit the radiation escaping the hall to under the lab-mandated limit for public air-dose of 10 mrem/year.

Figure 48 shows the different components along the beam line from the target to the end of the downstream torus. The shielding of each area is directly proportional to the beam power absorbed by the different elements. Table 19 lists the power deposition along the beam line. The shielding is focused mostly around the target chamber and collimator 1 and 2. It is made out of concrete and is approximately 1.4 m in thickness on all sides. The shield huts will be constructed from individual concrete blocks. The target enclosure will be engineered to allow access during the experiment and provide feedthroughs for the target cooling and motion mechanisms. It will contain approximately 600 tons of concrete, 50 tons of lead and 10 tons of steel for the supports and frame. The shielding around collimator 1 and 2 will be approximately 264 tons of concrete with additional steel needed for the frame. The shielding around collimator 4 is expected to be approximately 2.5 tons. Collimator 4, 5, the lead wall behind collimator 4 and the lintels are needed to prevent secondaries from reaching the detector plane.

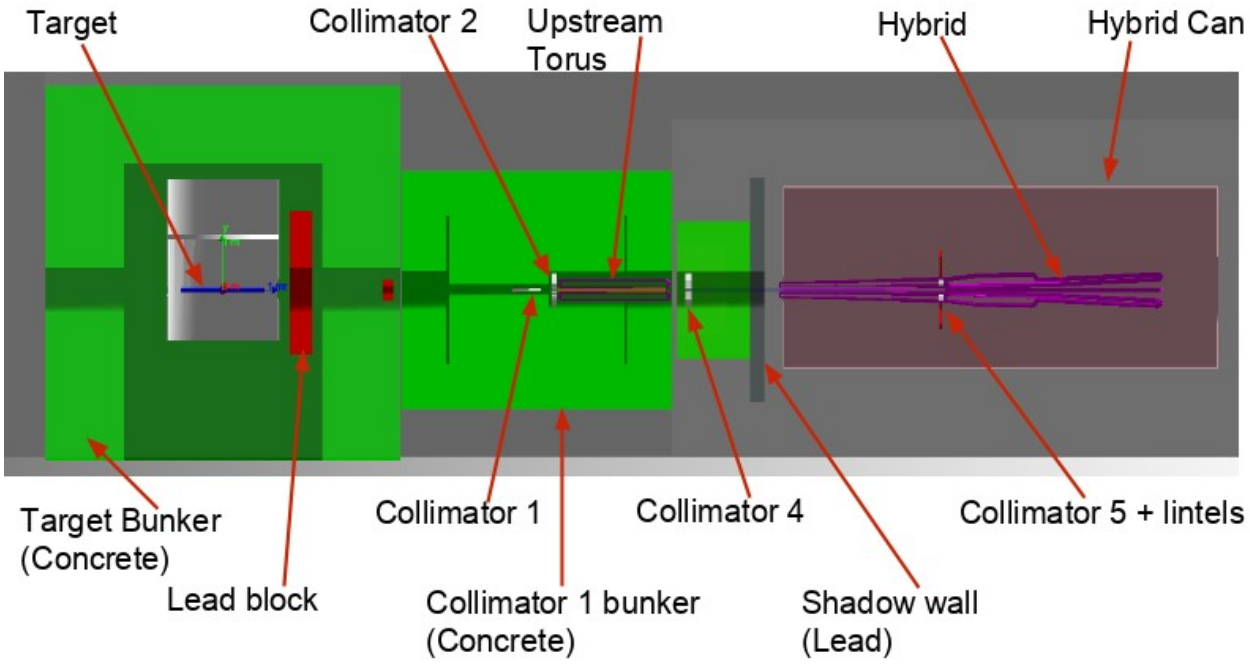

Figure 48: Simulation design of the shielding used for the MOLLER experiment. Components represent reasonable material budget but not realistic design.

11.2.1 Electronics racks and shielding enclosure

The GEM tracking detectors require approximately 512 signals together with pre-amplifiers and low voltage power supplies. This all fits in 8 standard electronics racks. They will be located approximately 10 m from the GEM front-end boards. In order to protect them from harmful radiation a shielding enclose will be constructed that will be approximately 3 m wide, 2.2 m deep and 2.5 m in height. The walls are expected to be made out of 1 m thick concrete. The side facing the hall wall will be open to allow for access and air circulation. Cooling of the racks will be done through an 8 Ton air conditioning unit. This design allows flexibility to increase the rack number if needed with little added cost.

11.3 Hall A integration

Figure 49 provides an overview of the changes needed to the experimental hall in order to accommodate MOLLER. Changes to both High Resolution Spectrometers (HRS) will be needed in order to allow for sufficient shielding around the target and collimator 1 and 2. Depending on the final design of the shielding, the pivot, HRS links as well as the first two quadrupoles in both arms will need to be removed or reconfigured. MOLLER will use a shielded enclosure that will be built in 2020 for the SBS suite of experiments to house patch panels, low voltage and high voltage power supplies for the magnets needed for the experiments.

11.3.1 Beam line modifications

In order to allow for the large extent of the MOLLER apparatus and to the precision required modifications to the beam line upstream of the target will be required. A reconfiguration of the existing quadrupoles and addition of correctors is needed in order to allow for position locks in front of both the Møller polarimeter and the MOLLER experiment. The beam current monitor box as well as the fast raster are moved upstream

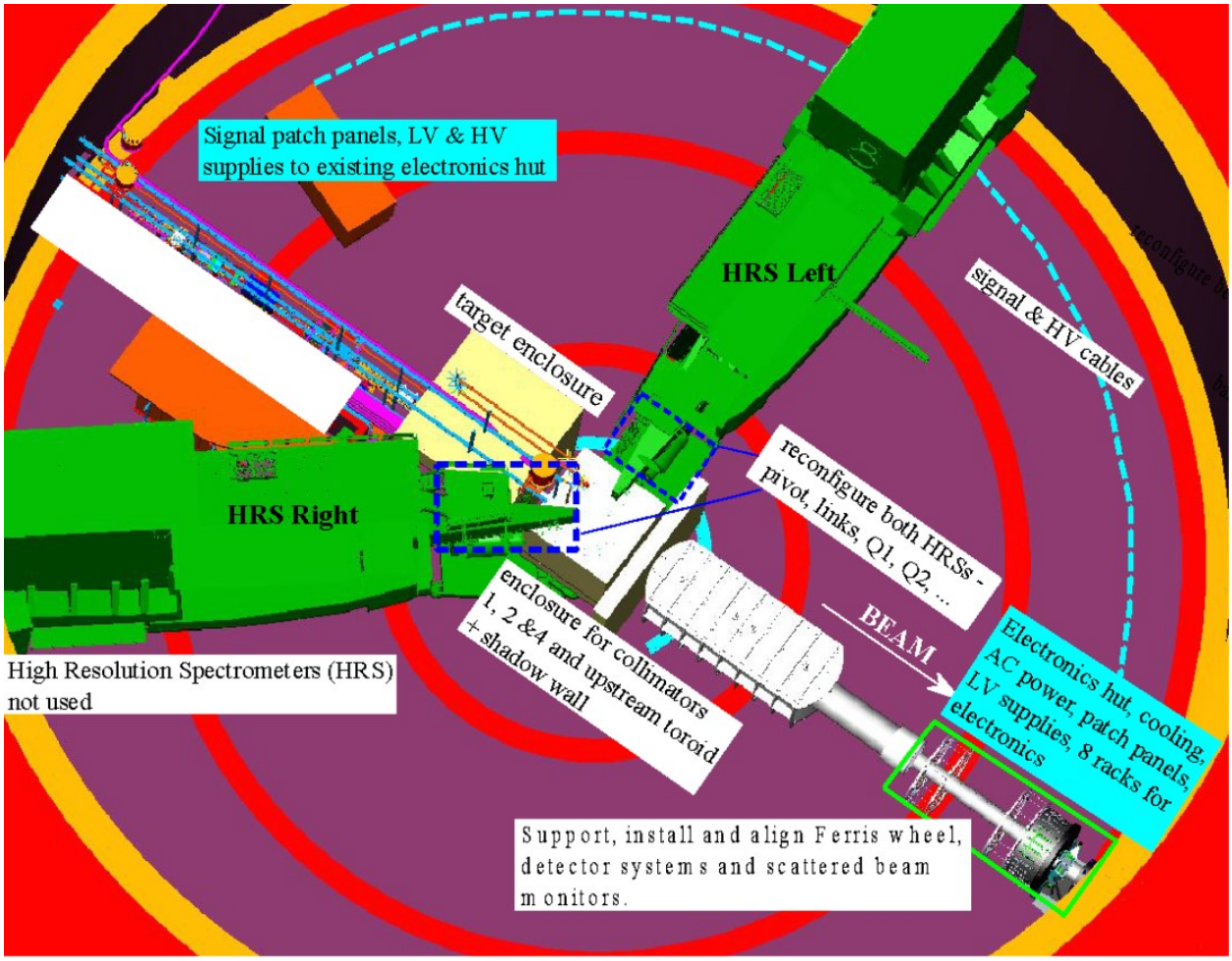

Figure 49: Overview of the changes needed to Hall A to accommodate the MOLLER experiment.

and downstream, respectively. Additional diagnostics will be added to increase the level of beam characterization possible: 2 super-harps to provide beam profile measurements, 1 additional cavity beam current monitor, and a reconfiguration of existing position cavity monitors. All of these diagnostics will be in pairs that will be separated by approximately 13 m to allow for high position and angle sensitivity. To see a more detailed discussion see Section 10. The Møller polarimeter will remain in place to reduce cost, but will undergo a reconfiguration of the detector shielding to allow for some of the new beam line elements. The existing balcony that provides utilities to the current pivot/target area will need to be modified to allow these utilities to reach the MOLLER target which will be located 4.6 m upstream of the current Hall A target location.

11.3.2 Signal and power cables

For the signal path MOLLER expects to have about 400 runs of RG58 and RG108A/U 78 Ω BNC Twinax cable. Each run consists of 4 cables: 60” to pre-amplifiers, 600” to patch panels, 320” to an additional patch panel and 600” to the ADC. The high voltage will be carried by approximately 385 SHV 600” RG8A/U cables. The cables will use standard cable trays to traverse the distance between the different components.

11.3.3 Detector support structures

The weight of the detector system has been taken into account and floor plates will be employed in order to allow for an even distribution of weight. The support structure for the tracking detectors will allow for them to be retracted during high current data collection. Additionally, the support structure will allow the GEM planes to be rotated into different sectors, thus reducing the need to cover the entire acceptance.

The support structures for the main integrating detectors will allow the sub-systems to be split along a vertical plane and inserted and retracted from the beamline to provide access to the beam pipe flanges and for detector maintenance.

A Flux Integration

The integrated response of the Cherenkov light from electrons that traverse the detector is linearly proportional to the scattered flux. The parity-violating asymmetry is measured by averaging the fractional difference in the response of the detectors F over many window-pairs:

$$A_i \equiv \left(\frac{F_R - F_L}{F_R + F_L}\right)_i \simeq \left(\frac{\Delta F}{2F}\right)_i; \quad A_{raw} = \langle A_i \rangle; \quad \delta(A_{raw}) = \sigma(A_i)/\sqrt{N}. \tag{10}$$

Here, A_i is the asymmetry in the ith window-pair, made from nearby (in the time domain) windows of opposite helicity. There are several aspects of the electronics and data acquisition (DAQ) specific to parity-violation experiments that we discuss briefly in the following. The collaboration has extensive experience in these aspects of the experimental technique.

Second generation parity violation experiments at JLab such as HAPPEX-II used a helicity reversal frequency of 30 Hz, which had the benefit of largely canceling beam jitter and electronics noise related to 60 Hz line noise. PREX ran successfully with 240 Hz helicity-reversal, while $Q_{\rm weak}$ used 960 Hz reversal. It will be necessary for MOLLER to flip the helicity even more quickly. One reason is that target density fluctuations are only expected to contribute at frequencies below a few hundred Hz.

Perhaps of equal importance is that, at the MOLLER event rate of ~ 150 GHz, suppression of electronics white noise at the required level is a severe challenge. At a helicity flip rate of 60 Hz, the variance $\sigma(A_i)$ would be 28 ppm. A pedestal noise level below 3×10^{-6} would be required in order to ensure negligible contribution from white noise to $\sigma(A_i)$. We are designing around a flip rate of 1.92 kHz, such that $\sigma(A_i)$ would be 80 ppm. This requires a pedestal noise floor of 1×10^{-5}, which appears feasible. It also implies that each helicity state is held for $\sim 500\mu$s. In order to avoid excess noise from 60 Hz line variations, a scheme for selecting helicity states will be required which will force complementary pairs at corresponding phases in the 60 Hz cycle.

The main scattered electronic flux detectors are not the only parameters that must be integrated over each helicity window. Even with perfect electronics, $\sigma(A_i)$ in Eqn. 10 would be dominated by fluctuations in electron beam parameters due to window-to-window fluctuations in intensity, position, angle and energy. To exploit the full available statistics one must remove the correlations of F to beam intensity, position, angle and energy, thus extracting the measured raw asymmetry as follows:

$$A_i = \left(\frac{\Delta F}{2F} - \frac{\Delta I}{2I}\right)_i - \sum \left(\alpha_j (\Delta X_j)_i\right). \tag{11}$$

Here, I is the time-averaged beam intensity over the duration of a helicity window, X_j are corresponding average beam trajectory parameters derived from judiciously placed beam position monitors and $\alpha_j \equiv \partial F/\partial X_j$ are coefficients that depend on the kinematics of Møller scattering as well as the detailed spectrometer and detector geometry of the given experiment. The parameters I and X_j will be derived from monitor signals in much the same way as the relative flux F, by feeding voltage outputs that are proportional to beam parameters into the same ADCs. It is critical to maintain close synchronization between the integration cycles of all the ADCs.

B Transverse Beam Polarization

If there is any transverse polarization component to the beam on target, the apparent A_{PV} as a function of the azimuthal angle would show a modulation due to the beam-normal single-spin analyzing power A_T in Møller scattering, a QED effect involving the interference between the tree-level amplitudes and the two-photon exchange amplitudes. The relevant parameter for A_T is the energy of each electron in COM frame, which is 53 MeV; the electron's boost factor is therefore rather modest. The magnitude of A_T is such that even a few percent transverse polarization can result in an azimuthal modulation of the measured polarization asymmetry that is an order of magnitude larger than A_{PV}. While this effect should cancel if one averages data over the full range of the azimuth, imperfect cancellation could lead to a significant systematic error.

Some interesting features of A_T facilitate a strategy that would allow us to keep this potential systematic error under control. If one looks at A_T as a function of the COM scattering angle, or equivalently $y \equiv 1 - E'/E$, one finds that A_T must vanish at $y = 1/2$, which corresponds to 90° scattering in the COM frame, due to CP symmetry. Thus, the maximum A_T is around 15 ppm, and occurs at $|y - 0.5| \approx 0.2$, at the very edges of the momentum acceptance and more importantly, A_T is of opposite sign at these two extremes. This leads to an order of magnitude suppression in the effective A_T averaged over all detectors. Figure 50 illustrates these points by showing A_T as a function of E' at a beam energy of 11 GeV.

It is possible by passive setup procedures to limit the transverse component of the beam polarization at the target to be less than 1°. One can measure the ϕ modulation to very high precision during production data collection within the first few hours, by studying the azimuthal dependence of the raw detector asymmetry, since different azimuthal detectors have very different acceptances as a function of y. This is illustrated in Figure 51, which shows the simulated average transverse asymmetry for the different types of azimuthal detectors. Thus, it should be possible to devise a "manual" feedback loop that would make small tweaks to the launch angle of the electron beam polarization at the low energy end of the machine based on the measured A_T's. This technique is designed to converge to zero transverse polarization. In practice, the suppression should go like $1/N$, where N is the number of adjustments. In principle, we should gain a factor of about 25 below the setup accuracy of 1° in a week. We will assume this factor for the duration of the entire data collection period for the estimate of the systematic error.

If one now further conservatively assumes only a factor of 10 suppression in the grand average of A_{PV} over the full range of detectors, then the total systematic error from the correction to A_{PV} is less than 0.07 ppb. If this level of suppression is difficult to achieve in practice, some of it can be recovered by a slightly different reweighting of the data from the various different azimuthal detectors with only a small loss in the statistical error in the extracted A_{PV}.

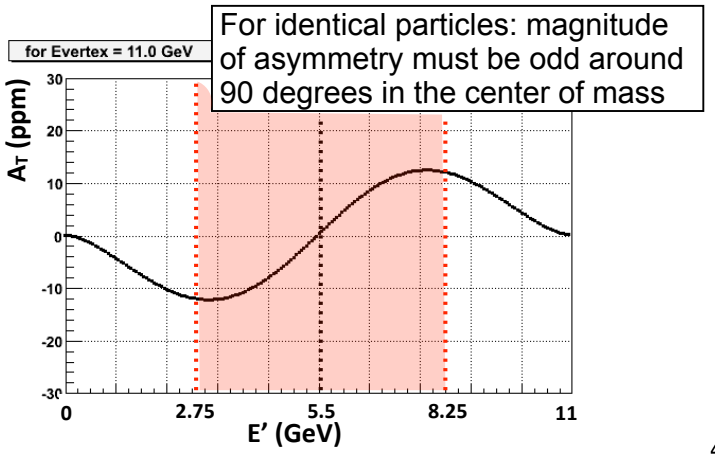

Figure 50: *QED prediction for the beam-normal single-spin analyzing power A_T in Møller scattering as a function of E' at 11 GeV beam energy, with the approximate acceptance range for the MOLLER experiment shown in the shaded region.*

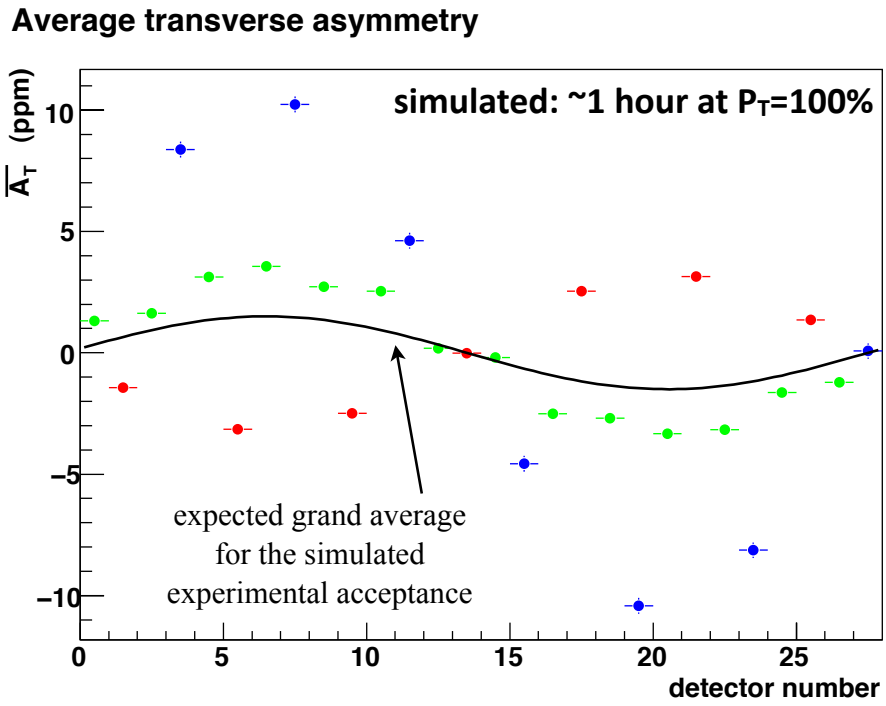

Figure 51: *Simulated values of the transverse asymmetries for 100% transverse polarization for the three different types of azimuthal detectors in the Møller ring - open (red), transition (green), and closed (blue). See Figures 141 and 142 for the definitions of these azimuthal detector types and their kinematic coverages. Even with the expected production transverse polarization of $< 1-2\%$, the expected transverse modulation is large enough that it can be measured within a few hours of production running, allowing for a "manual" feedback technique to minimize the transverse beam polarization.*

C Backgrounds

This appendix describes the backgrounds anticipated in the MOLLER experiment, the approach taken in the design of the apparatus to reduce backgrounds and maintain the ability to make small and robust corrections, and our analysis approach to measure the principal components of the irreducible electron background. The MOLLER apparatus is designed to direct the collimated Møller electrons to a region otherwise free of background so that the scattered flux can be integrated to measure the parity-violating asymmetry. As shown in Figure 30, the Møller signal is fashioned into a "peak" in the radial direction by the spectrometer at the detector plane approximately 27 m downstream of the target. The primary Møller detectors must measure the flux that traverses a relatively thin annular ring (width ~ 5 cm) of approximately 95 cm radius. A ring of 84 quartz tiles covering this ring form the primary Møller detectors. The Cherenkov light from the quartz is directed radially outwards by air lightguides onto photomultiplier tubes (PMTs) that are enclosed in shielding in an annulus that is approximately 1.5 m in radius. The background at the PMTs can be broken into three broad categories:

1. Irredudicible electrons that originate from beam electrons (and associated bremßtrahlung) scattering off target material other than target electrons: specifically protons and Al nuclei in the target windows

2. Cherenkov light generated by other charged and neutral particles impinging on the detector quartz

3. Light and charged particles generated in the lightguides by electrons and other background radiation.

The dominant background components are from the first category and are discussed in this section. As discussed in Appendix J, pre-R&D and simulations are under way to improve our estimates and systematic errors from the subdominant second and third categories as well.

The MOLLER apparatus is designed to unfold the various background components and facilitate a robust background subtraction. The key design constraint that enables this is instrumenting a sufficiently wide annulus at the detector plane, with significant radial and azimuthal segmentation, to measure variations of fluxes as well as parity-violating asymmetries. In particular, the poorly known and difficult to calculate behaviour of the inelastic electron-proton weak neutral current vector coupling as a function of inelasticity will be directly measured in auxiliary quartz detectors adjacent to the main Møller ring.

The parity-violating asymmetries in the scattered electron flux will be monitored in 18 different categories of tiles depending on their relative placement at the detector plane as a function of the radial distance from the beamline, and their azimuthal orientation with respect to the mid-planes of the spectrometer azimuthal sectors. There are large variations in the rates and parity-violating asymmetries in these tiles depending on the relative contributions from Møller, elastic e-p, inelastic e-p and elastic e-Al scattering. This enables our approach, described in detail below in Section C.6, to extract both the signal and background asymmetries. First, we subtract out asymmetry and dilution components which are smaller or comparable to the ultimate statistical error i.e. of the order of 3% or less. These will include all subdominant components (second and third background categories in the PMTs described above). Then we carry out a simultaneous fit of the remaining components using dilutions determined from Monte Carlo simulations and extract independent parity-violating couplings for the chosen $e - X$ scattering processes. This procedure results in acceptably small systematic errors associated with correcting for the irreducible electron background asymmetries.

In the sections below, we provide brief summaries of the principal backgrounds followed by a description of the simultaneous fit procedure and its results. A more complete description of all these topics can be found in the backgrounds report [71] prepared by the collaboration in response to a recommendation from the DOE 2014 Science Review of MOLLER [72].

C.1 Elastic ep Scattering

The principal irreducible background under the Møller "peak" (see Fig. 30) is radiative elastic electron-proton (ep) scattering, which constitutes 8.9% of the signal. The background can be easily modeled and then verified explicitly with auxiliary tracking measurements of the radial profile of the scattered flux. The theoretical prediction for the parity-violating asymmetry is also well known for this process. Recently, the $\gamma - Z$ box radiative correction was calculated at 11 GeV [69]; this significantly impacts the effective value of Q_W but does not add significantly to the projected error in the correction. In addition, the Qweak measurement of the weak charge of the proton Q_W^p can be used to directly cross-check the predicted background asymmetry. After the modeling has been fine-tuned with calibration data, the Q^2 distribution of the background under the Møller peak can be estimated from the Monte Carlo simulation. The average Q^2 is 0.004 GeV^2.

C.2 Inelastic ep Scattering

A more challenging background correction is due to the smaller dilution from inelastic ep scattering, as well as that same process from the Al target windows. Even though the contribution from the background to the detected rate is expected to be small, $\lesssim 0.5\%$, the asymmetry correction can be significantly larger due to the fact that the estimated coupling to the Z boson is more than an order of magnitude larger than Q_W^e. There are only a few data points on the asymmetries for Δ and resonance region production, and none at higher W ([73–75]). Cross sections are also less well known than for the elastic processes.

Experiment	Q^2 (GeV^2)	W (GeV)	A/Q^2 (ppm)
G0 [73]	0.24	1.18	-98 ± 22
PVDIS [74]	0.95	1.26	-72 ± 10
"	0.83	1.59	-89 ± 9
"	0.76	1.86	-82 ± 7
"	1.47	1.98	-81 ± 12
" [75]	1.28	2.03	-61 ± 19
"	1.08	2.07	-84 ± 4
"	1.91	2.33	-84 ± 4

Table 20: *World data on parity-violating asymmetries in inelastic scattering from the nucleon.*

The world data on parity-violating asymmetries in inelastic scattering from the nucleon are summarized in Table 20. Note that the data are consistent with a simple scaling: $A_{\rm inel} = -85$ ppm$/({\rm GeV})^2 \times {\rm Q}^2$, without radical W-dependence. One additional datum is from E158 [3], where they extracted the asymmetry from a combination of proton elastic and inelastic scattering, and obtained a result consistent with the standard model proton weak charge and the above scaling at about 20% accuracy. The W-dependence is key for us: the range of accepted Ws for the experiment spans 1 to 5 GeV, and the inelastic background underneath the Møller signal in the main Møller detector ring represents a different mix of W's than the inelastic events measured in the other detector rings. Therefore, if there is a significant variation of the asymmetry with W, then we will need to extract asymmetries for the appropriate regions in W from the simultaneous fit.

Theory does give us some guidance here. Several groups have provided calculations of the inelastic ep asymmetries. These have been mainly motivated by the desire to benchmark calculations of the γZ box diagram contributions for Qweak [80]. Results from Matsui, Sato and Lee [76], Gorchtein, Horowitz and

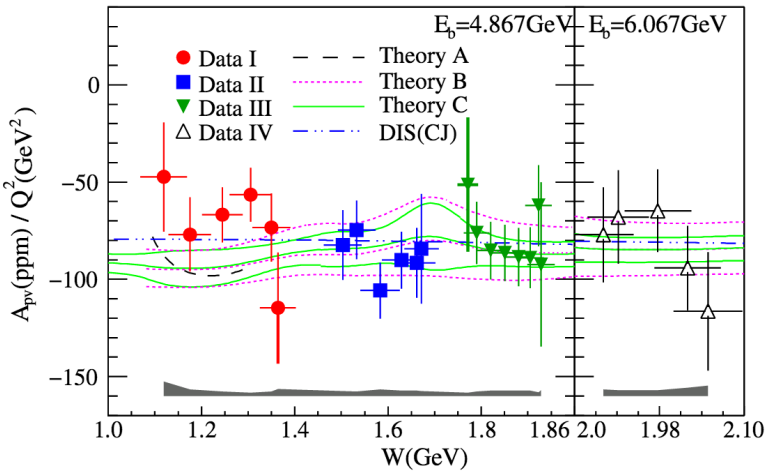

Figure 52: *Inelastic asymmetry from the 6 GeV PVDIS experiment [74] compared to model calculations: Theory A: Matsui* et al. *[76], Theory B: Gorchtein* et al. *[77], Theory C: AJM group [78], as well as a duality-based prediction, DIS(CJ).*

Ramsey-Musolf [77], and the Adelaide-JLab-Manitoba (AJM) collaboration [78] are compared with the 6 GeV PVDIS data in Fig. 52. All the calculations are in good agreement with the data, and suggest at most a modest W evolution in the resonance region. Indeed, the models are in good agreement with the simple $A_{\rm inel} = -85\ {\rm ppm}/({\rm GeV})^2 \times {\rm Q}^2$ scaling in this W region, at the 20% level.

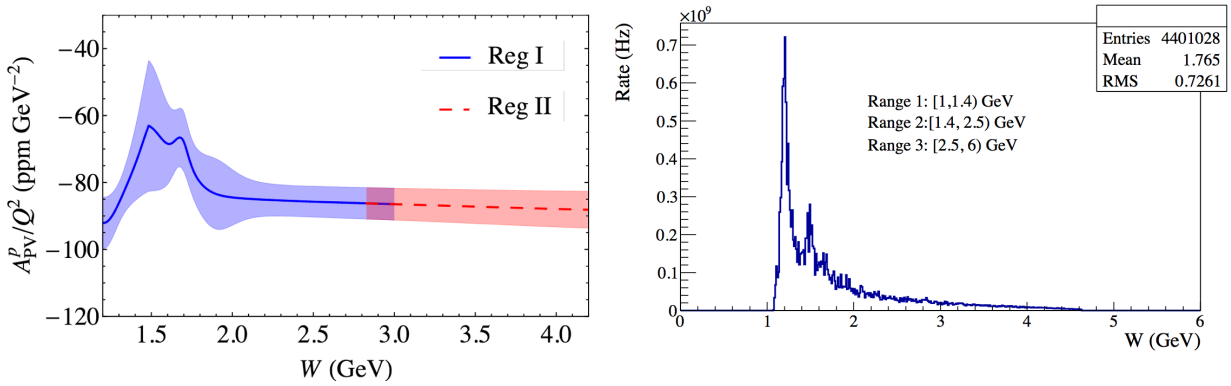

Figure 53: *Left: AJM collaboration [69] calculation of ep inelastic asymmetry for MOLLER kinematics, with theoretical uncertainty band indicated. Right: Simulated rate from ep inelastic scattering vs. W. The ranges for the three bins in W for our asymmetry ansatz are indicated.*

The AJM group have extended their calculation to the MOLLER kinematic range [69] ($Q^2 \sim 0.004\,{\rm GeV}^2$). The results are shown in Fig. 53. In a more recent publication [79], they have further explored the dependence of the asymmetry on the scale at which they match the high-Q^2 and low-Q^2 region. Assuming a very conservative (100%) uncertainty on the key parameter (the continuum $\gamma - \gamma$ to $\gamma - Z$ rotation parameter) for all $Q^2 < 1\ {\rm GeV}^2$, the relative uncertainty in their Region I kinematics increases from $\sim 8.6\%$ (as shown in Fig. 53) to $\sim 12\%$.

The modest W-dependence shown motivates our ansatz for treating the inelastic asymmetry: we break the kinematics for inelastics into three bins in W: (i) the Δ region, $1 < W < 1.4$ GeV (ii) the "resonance region", $1.4 < W < 2.5$ GeV, and the "continuum" $2.5 < W < 6$ GeV. We use the Christy-Bosted global fit [81] for the cross sections. Figure 53 shows the simulated rate as a function of W in our acceptance. We then model the inelastic asymmetry in these three bins using $A_{\rm inel} = Kf(W)Q^2$ where K contains electroweak couplings, and $f(W)$ is assumed to be constant in each of the three bins in W. We then treat the three $f(W)$ as free parameters to be extracted from our data via the simultaneous fit to the asymmetries in all bins in (radius, ϕ) described in Section C.6. We thus minimize uncertainty due to theoretical input on the inelastic asymmetries; we rely *on our data* to extract the inelastic contributions.

C.3 Aluminum Target Windows

The 150 cm long MOLLER hydrogen target will have $\sim$ 100 μm thick entrance and exit windows made of aluminum. The dilution and asymmetry from electron scattering off Al nuclei represents one of the irreducible background corrections. The aluminum end window correction in the Qweak experiment [11] led to a $\sim$28% correction to the parity-violating e-p asymmetry that Qweak measured. The correction for the MOLLER experiment will be much smaller (about 1.5%). Below, we briefly describe the Qweak correction and provide a simplified estimate of why it will be significantly smaller in MOLLER before moving on to the detailed simulations in Section C.6.

For the kinematics of the Qweak experiment (E = 1155 MeV, $\theta_{lab} \sim 7.9^\circ$, $Q^2 = 0.025$ (Gev/c)^2), the contribution of the aluminum windows to the rate is about $\sim$ 3.2% (about 76% of which is e-Al elastic nuclear scattering). A detailed calculation of the e-^{27}Al parity-violating asymmetry has been performed by Horowitz [82]. At the average momentum transfer of the Qweak experiment, the asymmetry is $\sim$2200 ppb, significantly larger than the e-p asymmetry of ~ -240 ppb. So, despite the relatively small rate contribution of 3.2%, the $2200/240 = 9$ times larger asymmetry leads to a 28% contribution to the measured asymmetry in the Qweak experiment. Qweak ultimately estimated this correction to better than 10% of itself.

This contribution will be significantly smaller in the MOLLER experiment for two main reasons. The ratio of aluminum to hydrogen is about a factor of four ($35/150$, the ratio of hydrogen target lengths) smaller in the MOLLER experiment. Most importantly, in Qweak the full elastic e-Al peak was detected along with the e-p elastic peak. In contrast, for MOLLER, the e-Al elastic peak is well separated spatially from the main Møller peak (see Fig.54 in Section C.6). It is only its radiative tail (about 12% of the peak rate) that gets detected.

Including some other less significant factors leads to the conclusion that the correction is about 0.5 ppb, which is 1.5% of the anticipated Møller asymmetry of $\sim$34 ppb. The other contributions from scattering on aluminum are smaller. Thus we do an estimate of their asymmetry and a direct subtraction prior to the simultaneous fit described in Section C.6. These processes include quasi-elastic scattering, inelastic excitations of the aluminum nucleus, and scattering off of impurities in the alloy planned for the target windows. More details of how these processes are treated are available in the full backgrounds report [71].

C.4 Hadrons and Muons

There is the possibility of negatively charged pions, heavier mesons and muons to contribute at a small level to the signal in the Møller detectors. The dilution from such a background is likely to be negligibly small, but the parity-violating asymmetry of this background will depend on the processes that create them. The dominant source is from pions produced by real and virtual photoproduction off protons in the target. We have run Monte Carlo simulations with representations of the MOLLER magnetic fields and collimation using a pion generator based on the Wiser parameterization [70] for direct photoproduction and using the equivalent photon approximation for electroproduction. We find the rate in the Møller ring to be of the order

of 0.06%. The parity-violating asymmetry in real photoproduction should be of the order of the hadronic parity-violation parameter f_π, which is experimentally known to be less than 10^{-7}.

We estimate that the rate above is 60% of the total pion rate, with the rest coming from electroproduction. We estimate that the average Q^2 for the latter process is 0.04 GeV^2 and that therefore the parity-violating asymmetry for these pions will be of the order of 4 ppm. Combining all these factors, one can see that the correction in the Møller ring will be of the order of 1 ppb or about 3%. This is the basis for the pion contributions assumed in Table 21 of Section C.6.

For comparison, this background was studied for the E158 configuration and the dilution factor was explicitly measured to be 0.12% in the Møller detector. The parity-violating asymmetry, measured in dedicated pion detectors sensitive to the hadronic leakage behind the Møller detector and shielding, was found to be ~ 0.5 ppm.

Decays of hyperons produced in the hydrogen target require special treatment. Estimates show that the acceptance in the Møller ring is a fractional rate below 10^{-9}. Nevertheless, the analyzing power (polarization transfer from the primary beam electron) could be very significant, and we are in the process of carrying out more careful calculations. More importantly, this is the primary reason why we plan to directly measure the pion asymmetry during physics data collection by monitoring the flux of charged particles downstream of the Møller ring and shielding.

We have a preliminary concept to accomplish this with dedicated "pion" detectors described in Sec. 7.2. Using realistic assumptions for the efficiency of measuring the parity-violating asymmetry by integrating the detector response over the full duration of data-taking, the projected statistical error is ~ 105 ppb. This projects to a systematic error of the order of 0.14 ppb on the correction to the Møller A_{PV} in the thin quartz detectors or about 0.5%. The correction and thus the systematic error will be smaller by a factor of 3 for the "shower-max" quartz/tungsten sandwich detectors. Given the redundancy and the different weights to the corrections in the two kinds of detectors, we assign a systematic error of 0.3%. Additional Monte Carlo studies of the kinematic acceptances of pions from weak decays are being planned as input to further refine the conceptual design of the "pion" detectors.

C.5 Photons and Neutrons

In a forward spectrometer of the type being discussed, it is very challenging to suppress neutral background from soft photons and neutrons. We will follow a strategy similar to E158, where neutron background was heavily suppressed by burying the photodetectors in a lead shield and we will follow a similar strategy here. As described in Section 6.2.3, a collimation system has been designed to achieve a near-perfect "two-bounce" collimation system. There will be at most one or two edges from which photons could reach one of the primary detectors after undergoing only one bounce from the target. The flux at these edges will be rather modest compared to the signal flux.

Further suppression will be achieved for the auxiliary Møller detector made of alternating plates of quartz and tungsten i.e. a "shower max" detector. Based on previous experience and simulation, we anticipate suppressing this background at the level of a fraction of a percent and expect to make the correction with an error less than 0.1%. These backgrounds can be measured with special runs, such as by "blinding" the Cherenkov photodetectors and looking for the residual beam-correlated response, as well as runs with the spectrometer magnets turned off. Such backgrounds are not expected to have any polarization asymmetry.

C.6 Simultaneous Fit Strategy and Results

Here we describe our strategy for making use of the radial and azimuthal segmentation of the detector to do a simultaneous fit to separate the signal and background components. Electron distributions at the detector plane are shown in Fig. 54 from a full GEANT 4 [83] simulation of interactions in the long liquid

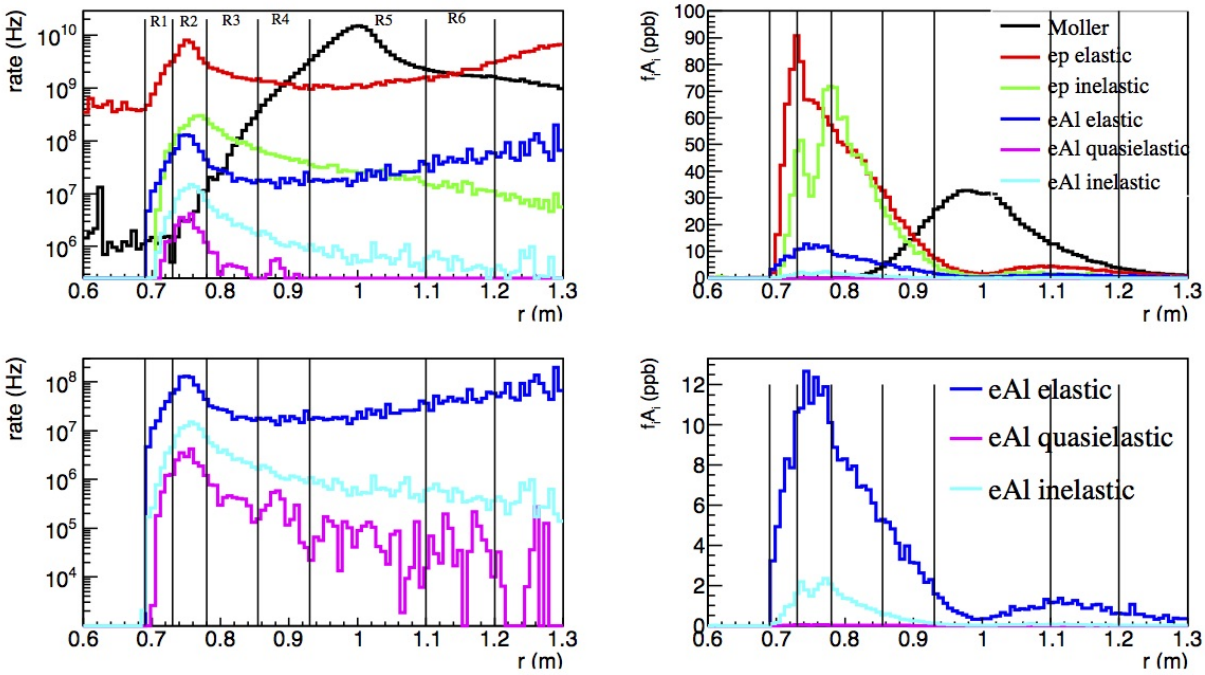

Figure 54: *Simulated signal and background vs. radial location of detected electron at the MOLLER detector ring. In all figures: the Moller electron signal is in black, background from elastic scattering on the proton is red, inelastic scattering from the proton in green, and elastic, quasielastic, and inelastic scattering from the Al target windows in blue, magenta and cyan, respectively. Upper left: rates, in Hz. Lower left: rates for just the Al contributions. Upper right: contribution to the total measured asymmetry, in ppb, for all processes ($f_i A_i$, where f_i is the dilution for the individual process). Lower right: as above, for Al contributions only. Note: the figures on the left have a log scale, while those on the right are linear scale. The boundaries of the 6 detector rings are indicated by vertical black lines.*

hydrogen target with the approriate collimation and 3-D magnetic field map for the two toroid assemblies. Events were generated in the target from Møller scattering from electrons in hydrogen, elastic and inelastic scattering from protons in hydrogen, and elastic, quasielastic, and inelastic scattering from the Al entrance and exit windows of the target, using appropriate cross sections and material thicknesses. The plots show the detected electron rates *vs.* radial location at the z-location of the MOLLER detector, as well as the dilution-weighted asymmetries $f_i A_i$. The dilution for a given process is defined as

$$f_i = \frac{N_i}{\sum_j N_j},$$

where N_i is the rate of detected events from process i. The rates and asymmetries shown are summed over the full detected azimuth ϕ, and correspond to the maximum beam current of 85 μA and beam polarization of 80%.

These distributions represent what the experiment will see, after we have subtracted out the small backgrounds from particles other than scattered electrons which generate light in the quartz detectors. These small asymmetry and dilution components (the second and third background categories listed in the introduction to this section) are each smaller or comparable to our statistical error *i.e.* of the order of 3% or less, and are not discussed further here.

These plots make our strategy clear for dealing with the remaining irreducible backgrounds (*i.e.* from scattered electrons in the detectors from processes other than the Moller-scattering signal). The division of the detector into six radial rings will allow us to measure the asymmetries in rings where the signal completely dominates, *i.e.* ring 5 (0.92 to 1.1 m), where the signal will be about 85% of the measured asymmetry, but also to measure the asymmetries in rings where the various different backgrounds contribute differing fractions to the asymmetry. A simultaneous fit to all these asymmetries, constrained by the various dilution factors for each process, will allow us to extract the Møller asymmetry with high precision, and, along the way, determine the asymmetries of the various background processes as by-products.

Note that these figures actually hide an additional degree of freedom that will be very useful in the fitting process: the azimuthal (ϕ) dependence of the various dilutions and asymmetries. Each detector ring is divided into three ϕ sectors (see Fig. 29). Due to the spectrometer optics, the different ϕ sectors of a given ring will accept a different kinematic range and so each will see different fractions of the various backgrounds. This gives us additional leverage to extract each asymmetry contribution independently, as discussed below.

For this fitting process we clearly need to know (1) the cross sections and kinematics (and thus the dilution f_i) in each detector bin (radius,ϕ) for each process and (2) a model for how the asymmetry A_i varies with kinematics (Q^2 and W) over the detector acceptance (radius,ϕ) bin.

Knowledge of the f_i is not problematic; the relevant form factors and differential cross sections are well-known, so in combination with simulation of the well-determined spectrometer optics we will have the f_i available for each detector element. We can validate these using high-granularity measurements of the total detected electron rates as a function of (radius,ϕ) using our tracking system, which will also extract the central kinematics of the experiment. We might even envision using the rate distributions from the tracking system as an additional input constraint to the fitting method.

Table 21 shows the total predicted asymmetry in each radial ring, A_m, and its statistical precision σ_A/A along with the fractional contributions to the measured asymmetries from each relevant process. One can see from this table the strategy of the simultaneous fit. Ring 5 is dominated by the Moller signal. Rings 1 and 2 have very different contributes from ep-elastics and ep-inelastics, allowing these asymmetries to be disentangled. Ring 6 has a large relative contribution from e-Al elastics compared to other rings, *etc.*. Note also that the background fraction from Al elastic scattering in ring 5 is 1.47%, in agreement with the 1.5% scaling estimate from Qweak given above in Section C.3. The azimuthal ϕ degree of freedom also has some striking differences in the variation of the processes which are useful; more details can be found in the full backgrounds report [71].

ring #	$\frac{\sigma_A}{A}$ (%)	A_m (ppb)	Møller	e-p elastic	e-p inelastic	e-Al elastic	e-Al quasielastic	e-Al inelastic	pions
			$f_iA_i(\%)$	$f_iA_i(\%)$	$f_iA_i(\%)$	$f_iA_i(\%)$	$f_iA_i(\%)$	$f_iA_i(\%)$	$f_iA_i(\%)$
1	3.05	-78.69	0	79.9	28.6	-9.66	0	1.12	0
2	1.09	-103.1	0	65.3	44.1	-11.3	0	1.83	0.05
3	1.68	-91.15	1.12	50.3	54.3	-8.25	0	1.34	1.13
4	3.06	-44.73	33.5	37.8	28.3	-7.33	0	0.63	7.04
5	1.61	-34.26	88.2	6.61	3.56	-1.47	0	0.09	2.98
6	7.24	-13.28	57.5	25.3	8.40	-7.47	0	0.30	15.9

Table 21: *Asymmetries from various contributions for the 6 rings. A contribution of less than* 0.05% *is listed as* 0.

Simultaneous Fit Results: The 18 asymmetries (6 radial rings, each with 3 ϕ sectors) produced in the

full simulation, with statistics corresponding to the full beam time request of 344 days, were simultaneously fitted. The fit had 6 free parameters: the asymmetries for Møller, ep-elastic, e-Al elastic and e-p inelastic (3 W bins) scattering with appropriate Q^2 evolution for each. The f_i dilutions were taken from the simulation. The small contributions from quasielastic scattering and inelastic scattering from the Al windows were subtracted before the simultaneous fit.

Processes	Expected A (ppb)	σ_A (ppb)	$\frac{\sigma_A}{\lvert A\rvert}$ (%)
Moller	-35.20	0.64	1.8
ep-elastic	-19.67	1.82	9.2
ep-inelastic (1)	-439.94	80.6	18.3
ep-inelastic (2)	-433.96	38.3	8.8
ep-inelastic (3)	-384.59	91.5	23.8
eAl-elastic	297.27	83.01	27.9

Table 22: *Results of the simultaneous fit to the 18 quartz tile asymmetries. The asymmetries (A_i) in ring 5 and their fitting errors in ppb and in % are shown.*

The results of the fit are shown in Table 22. We see that the desired precision (1.8%) in the Moller asymmetry is achieved. Very similar results are found with a 4-parameter fit (where the ep-inelastics were assumed to have single asymmetry that scales as Q^2, independent of W), with again a 1.8% precision on the Møller asymmetry. The extracted uncertainties are degraded in all the background couplings in the 6-parameter fit due to correlations. We choose this fit as our final result as a very conservative estimate of the systematic errors due to Al and inelastic backgrounds. Table 23 shows the size of each correction as well as systematic error (due to the statistical uncertainties including correlations in the extracted couplings from the fit in Table 22).

Process	Correction (%)	Systematic Error (%)
e-p elastic	-6.61	0.38*
e-p inelastic ($W < 1.4$ GeV)	-1.03	0.22
e-p inelastic ($1.4 < W < 2.5$ GeV)	-1.22	0.13
e-p inelastic ($W > 2.5$ GeV)	-1.31	0.36
e-Al elastic	+1.47	0.15*
e-Al other	< 0.10	< 0.10

Table 23: *The fractional correction to the Møller asymmetry in Ring 5 and the associated systematic errors due to the extracted fit uncertainties shown in Table 22 are listed. The statistical error in the Møller asymmetry is 1.88%. The rows marked with a * are assumed to have additional external input. The systematic error on the e-p elastic contribution is assigned a fractional error of 5%. The systematic error on the e-Al elastic contribution is assigned as a fractional error of* 10% *as discussed in the full backgrounds report [71]. The "e-Al other" contributions include quasi-elastic scattering and inelastic scattering from discrete nuclear excited states and the giant dipole resonance.*

The important takeaway message is this: **the radial and azimuthal segmentation of the detector, combined with the toroidal spectrometer optics and the kinematics of the various background processes, will allow us to untangle the Moller asymmetry from those of the dominant background processes, without recourse to other data or theoretical predictions for those background asymmetries**. All that

we require are the cross sections and simple expectations on the leading Q^2 (and, for inelastics, W) dependence of the asymmetries.

Given the individual systematic errors in each correction in Table 23, we have done a preliminary exploration of the correlations between the corrections. We find that the systematic error on the sum of the corrections from the error matrix is of the order of 0.3%, significantly smaller than several of the individual systematic errors. This essentially indicates that the linear combinations of the various components in the corrections in Ring 5 (the main Møller signal) are well constrained in other tiles. Since this requires further study, we just state here that the total systematic error from the corrections due to inelastic scattering are bounded at 0.7% (linear sum of the three components), but that they are likely to be reduced by about a factor of two after further study.

In summary, a simultaneous fit of measured asymmetries making use of the radial and azimuthal segmentation of the detector determines the background asymmetry contributions to the needed precision. It also provides asymmetry measurements for these additional processes.

D Absolute Normalization of the Kinematic Factor

For low energy scattering with a fixed beam energy, $E \ll M_Z$, A_{PV} at tree level is dependent on a single variable, e.g. scattering angle or final energy. For Møller scattering, there is an additional kinematic dependence on both the scattering angle and accepted energy range of scattered electrons in the effective value of the kinematic factor $\mathcal{A}$, where $\mathcal{A} \equiv A_{PV}/Q_W^e$ from Eqn. 1 in Sec. 1.2, which is dependent on the beam energy E and the center-of-mass scattering angle θ

$$\mathcal{A} \equiv \frac{mG_F}{\sqrt{2}\pi\alpha} \frac{4E\sin^2\theta}{(3+\cos^2\theta)^2}. \tag{12}$$

The uncertainty in the overall kinematic factor therefore contributes directly to the ultimate uncertainty on Q_W^e. Our goal is to determine the overall kinematic factor for our apparatus to a fractional accuracy of 0.5%. We will rely on the extensive experience that was developed to measure Q^2 for Qweak. Also, sub-1% accuracy has been achieved in the HAPPEX measurements.

The average kinematic factor can be determined from data using comparisons to a detailed Monte Carlo which includes the full radiative treatment of the Møller process. By taking measurements at fixed angle and energy points and the known radiative $e+e \to e+e$ cross section, the acceptance function can be accurately reconstructed. In the approximation where radiation in the target is neglected, the kinematic factor can be largely determined from surveyed, precisely-machined collimator apertures and the absolute beam energy calibration tools in the Hall A beam line. Additionally, the use of a moveable sieve is planned, allowing for the reconstruction of fixed angles to be calibrated with a set of carbon target foils (to suppress radiative effects and fix vertex position) at several beam energies, as discussed below.

With the beam going through a 10.5 gm/cm^2 target however, the distribution of trajectories and energies are significantly modified. This requires not only a detailed Monte Carlo simulation but also validation by direct measurement of individual tracks in calibration runs at low current. This is one of the primary motivations for the tracking system. The large amount of multiple scattering, dE/dx and radiative losses due to the thick target, coupled with the large kinematic acceptance, and the rapid variation of the asymmetry with scattering angle, means that the Monte Carlo simulation of the effective kinematic factor seen by each detector segment needs to be validated carefully.

Additionally, a reweighting of the kinematic factor would be required due to any variation in the analog response of the integrating detectors. The tracking system can evaluate this effect by measuring the variation in response as a function of position in the quartz using single Møller electron tracks at low beam currents. If the integrating quartz detectors cover the full acceptance of the events passing through the collimators, a precise survey of the collimators would in principle provide an accurate measurement of the kinematic factor.

The contributions from positioning uncertainties by the target, collimator, or magnetic field are all negligible compared to the upstream collimator inner radius, which is defined by a machining tolerance. Given a tolerance of 200 μm on machining and an 1 mm tolerance on uncorrelated positioning between systems, this gives a systematic uncertainty of no more than 0.03 ppb, or 0.1% in the measured asymmetry. The acceptance at fixed angles can be determined with a sieve allowing events at fixed angles and normalizing to the relative cross section. Based on acceptance fitting discussed below, systematic control on the average analyzing power of less than 0.5% can be achieved through several methods such as a simple 6-point spline interpolation.

D.1 Kinematics Validation Approach

To measure the acceptance of the apparatus, a model of the magnetic transport optics must first be obtained. Calibration of the optics over a relatively broad range can be performed by mapping out specific and iden-

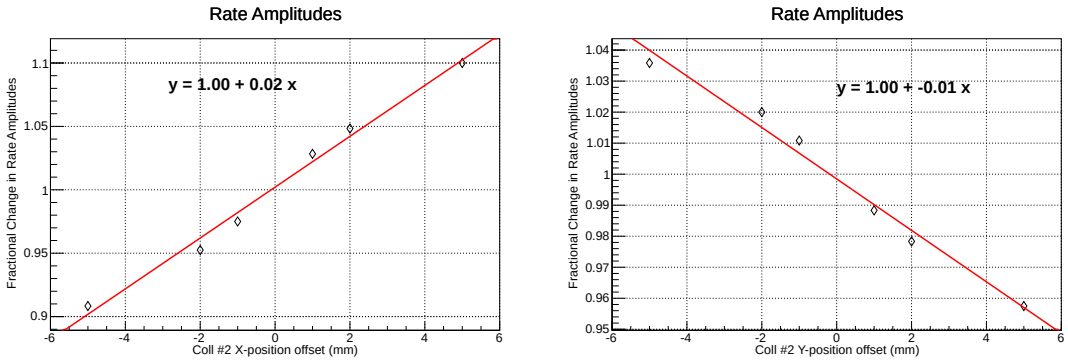

Figure 55: *A misplacement of the acceptance-defining collimator transverse to the beam produces a small azimuthal modulation in rate of about 2-3%/mm.*

tifiable points with defined polar and azimuthal angles, momentum, and target position. Using a nuclear elastic or Møller interaction with a well defined beam energy correlates the momentum and polar angle.

With the use of foil target and a removable sieve before the magnetic elements, the remaining variables can be constrained. The sieve must be at least $\sim 40\ X_0$ to be able to sufficiently stop the highest energy electrons. As this sieve must be tied to the acceptance-defining collimator, absolute positioning can be done both by survey and cross-checked by measuring and then minimizing the azimuthal modulation of rates resulting from a small transverse displacement of the acceptance defining collimator.

Figure 55 shows the amplitude of the rate modulation as a function of the collimator displacement. An array of scintillator pairs immediately behind the quartz will allow for counting mode operation with well-defined relative azimuthal efficiency. Assuming a modulation amplitude measurement to an accuracy of 2% of the average rate per sector, the positioning of the collimator can be determined to an accuracy ~ 1 mm. The impact of the residual uncertainty of 1 mm on the transverse position of the acceptance-defining collimator will be less than 1% on the average analyzing power variable $\langle \mathcal{A} \rangle$, and thus negligible. Nevertheless, knowing the value of this shift is important for constraining other systematics, such as parity conserving asymmetries and helicity-correlated beam trajectory differences which which could produce their own azimuthal modulations in the observed detector asymmetries.

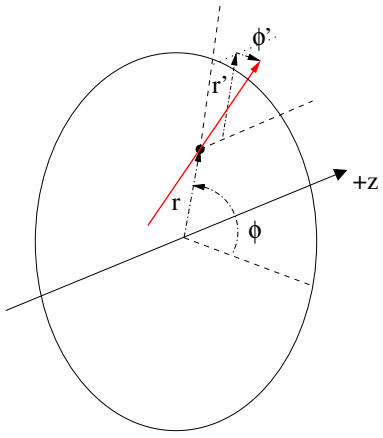

Figure 56: *Tracking coordinates system. Note that r' and ϕ' must be taken with infinitesimal change in z.*

The GEM tracking system will reconstruct not only the positions, which we will denote with cylindrical coordinates r and ϕ, but also the directions, which we will call $r' = dr/dz$ and $\phi' = d\phi/dz$. , shown in Fig. 56. These four independent variables map from the independent variables which describe the scattered particle, the lab scattering angle $\theta_{\rm lab}$, the electron momentum p, the lab azimuthal angle $\phi_{\rm lab}$ and the reaction vertex position v_z (we neglect the v_x and v_y coordinates as these are known event-by-event from the raster current and represent small perturbations in the map).

By having a map of ($\theta_{\rm lab}$, p, $\phi_{\rm lab}$, v_z) $\rightarrow$ (r, ϕ, r', ϕ') at specific points and if this map is one-to-one, the problem of optics reduces to interpolating between these points. The propagated uncertainty on $\langle \mathcal{A} \rangle$ is then dependent on the number of calibration points and the functional form of the acceptance used. The form of the acceptance must rely upon simulations and perturbations on various positioning and magnetic fields which can then be used for a maximum likelihood fit. This is also critical to take into account higher order effects such as beam raster, multiple scattering, and radiative effects.

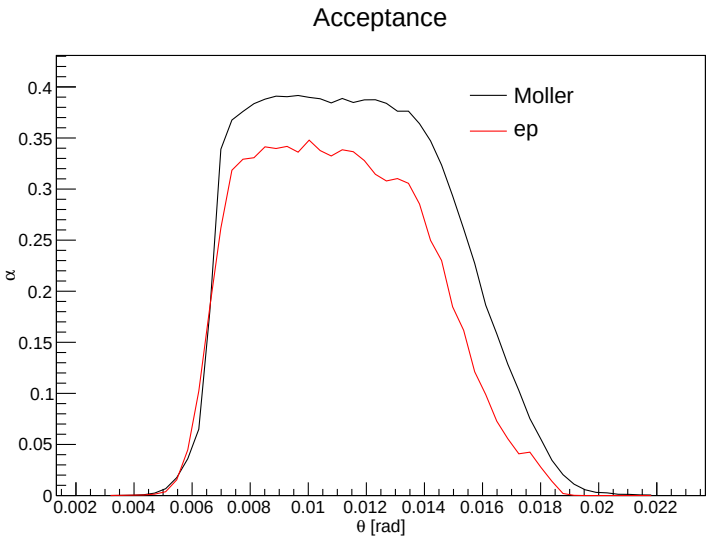

Figure 57: *Acceptance of Møller and ep elastic events, scaled arbitrarily, and ignoring radiative effects.*

While direct measurement of the Møller acceptance over the full region of phase space will be possible, this may prove to be unnecessary. There is a natural kinematic relation between the Møller-scattered, and elastic $e-p$ scattered events; see Fig. 57. By comparing the form of the $e-p$ elastic events to various simulation position and field scenarios, in addition to directly measured acceptance points and the Møller optics, additional confidence can be built in the acceptance function. Based on Monte Carlo simulations using simple models of the acceptance, such as splines which contain no actual physics or geometrical information, differences between the average analyzing power variable through various methods and the "true" value were found to be $\lesssim 0.5\%$.

To obtain the relative Møller acceptance at individual points in $\theta_{\rm lab}$, which is directly related to the free variable θ in Eqn. 12, the first step is to measure judiciously chosen narrow angle bites of Møller-scattered events at the 11 GeV beam energy. A fixed sieve where each of six sectors samples a pair of different angles is proposed, which relies on the symmetry of the magnetic field sectors. One sector will be covered by the sum of all 12 slits as a check of the symmetry. To maximize ϕ coverage (which is desirable to see edge effects of the phi acceptance), fixed ϕ coordinates can be obtained by blocking small sections through constant θ "slots".

Calibration runs at special incident beam energies of 4.4, 6.6 and 8.8 GeV will help to map out variations

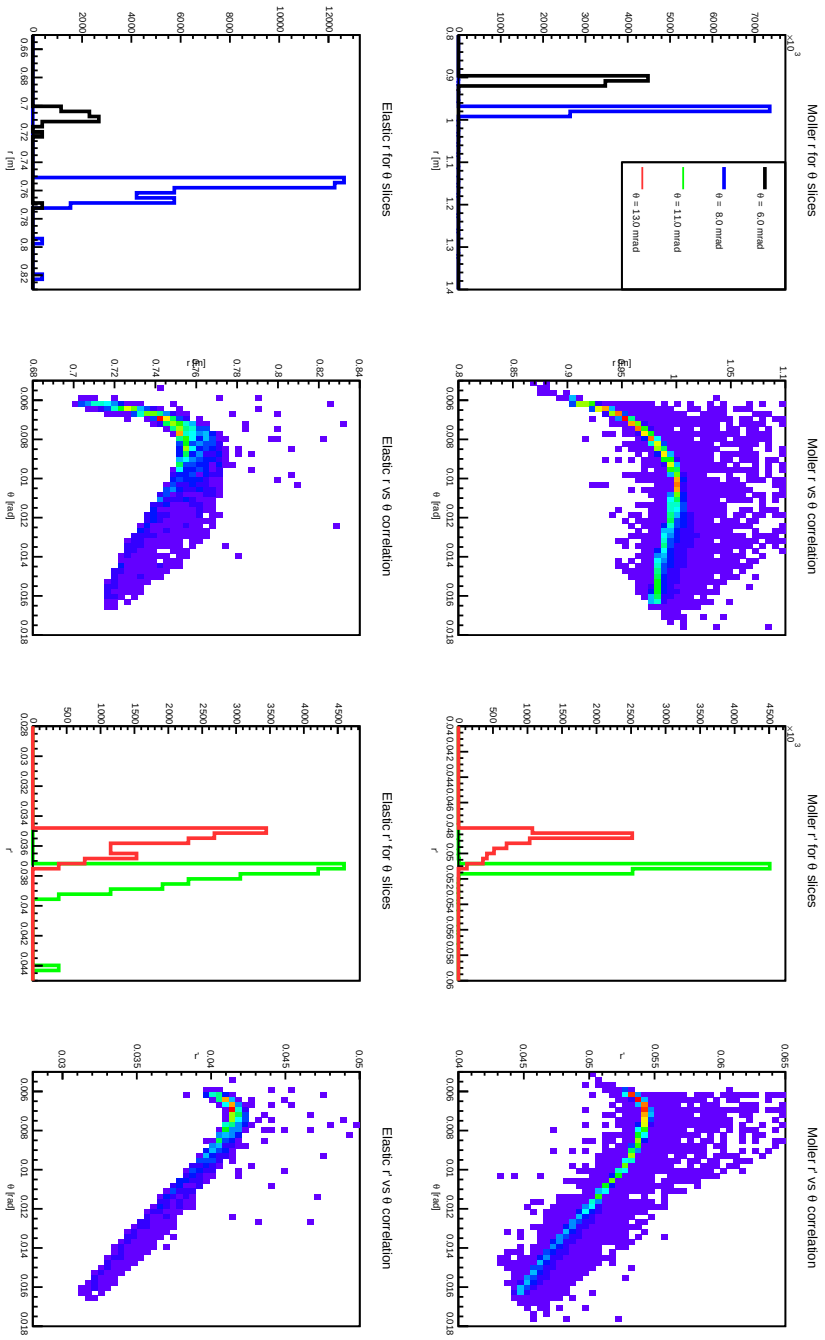

Figure 58: *The general properties of the optics reconstruction. Shown in the 1D histograms are the radius r and tangent $r' = dr/dz$ for Moller (top row) and elastic (bottom row) events for two 0.2 mrad slices in θ each. Raster effects are suppressed and only thin foil target is considered. The separation between Moller events, as well as the elastic events, is clear at the* mrad *level. Small angles ($\theta_{\rm lab} < 10$ mrad) may be reconstructed with the variable r while for larger angles, r' can be used and is practically linear. There is a small ϕ dependence and a sector dependence which has been averaged over for simplicity.*

in the momentum acceptance which must be folded in to account for radiative effects. To make relative relationships between different energies, the angles must be placed where 11 GeV Møller-scattered momenta would coincide with nuclear-elastically scattered (equivalently, the incident beam) momenta i.e. $\theta \sim 12$ and $8\ \mathrm{mrad}$ respectively for 4.4 and $6.6\ \mathrm{GeV}$.

A separation between the top row points in Fig 58 is all that is required by the GEMs for this task, meaning a few mm resolution in position with a GEM spacing of a few meters (to guarantee a resolution of $r' \sim 10^{-3}$). Kinematically at these angles, elastic scattering from even light nuclear targets do not have large recoil energies, providing scattered electrons which are practically mono-energetic. This is fortunate, because as Z increases, the nuclear cross section increases as Z^2, whereas the Møller cross section increases as Z (the bound number of electrons). A set of light target foils, such as ^{12}C, will be used for the calibration runs.

The present design of a GEM chamber introduces roughly a 0.5% radiation length for electrons incident normal to the plane. Using the standard multiple scattering formula for the central 98% of the scattered distribution of ultra-relativistic particles, for the lowest momentum electrons of interest ($\sim$ 2 GeV), and $x/X_0 = 2 \times 0.5\%$ for the two upstream chambers, this corresponds to $\delta\theta$ of about $0.4\ \mathrm{mrad}$. This is the limiting factor on the angular resolution in the GEMs, but is still sufficient to separate the staggered peaks in the acceptance calibration.

E Meeting the Polarized Beam Requirements

The polarized electron beam is created using a technology first developed at SLAC to enable the original parity-violating electron scattering experiment [110]: laser-induced photoemission from a GaAs wafer. The circular polarization of the laser light, controlled by the polarity of the voltage across a Pockels cell determines the sign of the longitudinal polarization of the emitted electron bunch, thus facilitating rapid helicity reversal of the electron beam. Time "windows" are generated in the electron bunch train at a frequency of 1.92 kHz, with the sign of the beam's longitudinal polarization following a pattern over 32 windows, optimized to eliminate both 60 Hz noise and rapid fluctuations in a differential comparison between the two helicity states. The polarity of these 32-window patterns are selected psuedo-randomly, to avoid any possible systematic from random noise that is coherent with this differential pattern.

The time-averaged responses of beam position monitors characterize the beam trajectory and energy for each window. In order to maintain the statistical power of MOLLER, the random beam variations over these complementary windows must not contribute significant noise over the counting statistics of the detected scattered electron flux. It is useful to consider just neighboring windows of opposite helicity, with these window-pairs occurring at a frequency of about 1 kHz. The differential measurement of cross-section over a window-pair will have a statistical precision of about one part in 10^5. In order to avoid introducing significant noise at that level, the beam position centroid fluctuation must be stable to $\sim$10's of microns, and this variations measured with precision at the level of a few microns, over these window-pairs.

Averaged over the entire data collection period, the beam trajectory must remain unchanged with respect to the sign of the electron beam polarization at the sub-nanometer level in order to keep beam-related false asymmetry corrections at the 1 ppb level. In addition to the rapid helicity-reversal, other techniques will reverse the polarity of the beam polarization on target while otherwise keeping the experimental configuration fixed. Such a mechanism is referred to as a "slow reversal" of beam helicity, and the use of several complementary slow reversals will further cancel systematic errors to the 0.1 ppb level, from sources such as residual electronics cross-talk or asymmetries in the unmeasured moments of the beam distribution (*e.g.* a "spot size" asymmetry).

E.1 The Polarized Electron Source

Laser light illuminates a semiconducting photocathode, the surface of which has been chemically treated to produce a negative work function, referred to as a negative electron affinity (NEA) surface. The laser light wavelength is tuned to promote electrons from a specific valence band to the conduction band of the semi-conductor. The photocathode is held at a negative potential, so as the electrons from the conduction band exit the cathode they are accelerated into the injector beamline.

Through doping or other stress applied to the photocathode, the degeneracy in the spin-orbit states of the specific valence band are split, as shown in Fig. 59. For circularly polarized light, the spin-1 photon is restricted to exclusively promote electrons to a single spin state. This process produces an electron beam polarization of nearly 100%, however, some depolarization occurs in the diffusion of the liberated electrons to the photoconductor surface. The CEBAF polarized source now routinely provides close to $\sim 90\%$ polarization with nearly 200 μA beam current. Since the electron polarization is fully determined by the circular polarization of the incident laser light, it is possible to rapidly flip the helicity of the electron beam by changing the laser polarization. A reversal of the applied voltage on the Pockels cell reverses the circular polarization of the laser light, and thus the helicity of the electron beam. A schematic diagram of the experimental configuration is shown in Fig. 60.

The RTP Pockels cell (pictured in Fig. 61) developed by the MOLLER collaboration replaced the KD*P Pockels cell in the JLab polarized source in January 2019. It was successfully used for beam operations throughout 2019.

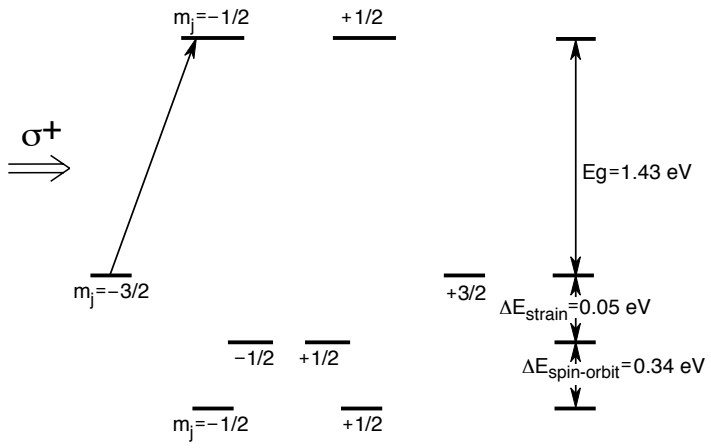

Figure 59: *Band structure of GaAs, showing how circularly polarized laser light produces polarized electrons.*

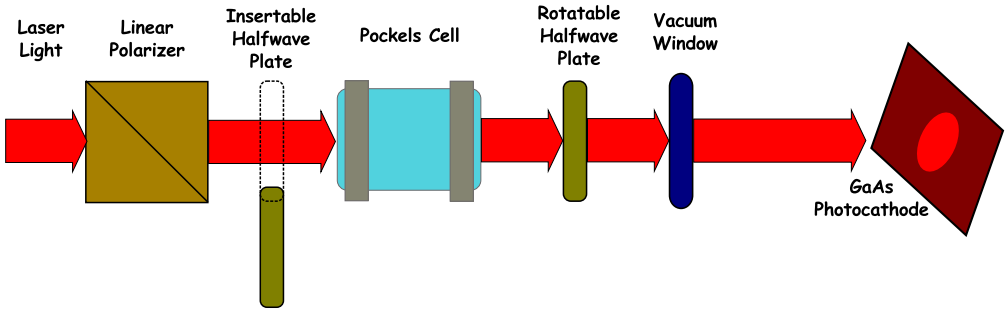

Figure 60: *Schematic of the laser transport line that allows for rapid reversal of the electron beam polarization.*

The sections below refer to results from experiments that have made use of this technology, including the HAPPEX-II measurements (2004-2005), Q_{weak} (2010-2012), and PREX-2 (2019). The HAPPEX and PREX measurements took place in Hall A and Q_{weak} in Hall C. These earlier experiments used the KD*P Pockels cell, while the very demanding PREX-2 experiment ran in the summer of 2019 with the new RTP Pockels cell system.

E.2 Rapid Helicity Flip

The Q_{weak} experiment used a helicity-reversal rate of 960 Hz, with a settling time of 70 μs. Shorter settling times were not possible with the KD*P Pockels cell, both due to charge leakage on the surface of the cell and mechanical resonances, excited by the piezoelectric property of crystal under a rapid voltage reversal, which are evident in fast and persistent oscillations in the birefringence of the cell.

At present ,the RTP Pockels cell is capable of achieving a stable transition in $\sim$ 11 μs, with virtually none of the ringing that is observed with KD*P (see Fig. 62). The cell was pulsed continuously since its installation in January, and the quality of the transition has shown no signs of degradation.

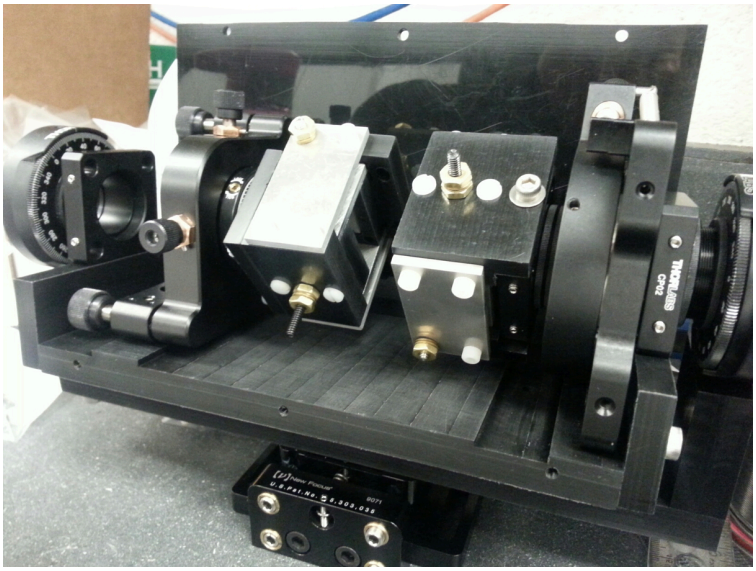

Figure 61: *The RTP Pockels cell developed to support 2 kHz flipping and precise control of beam asymmetries for MOLLER.*

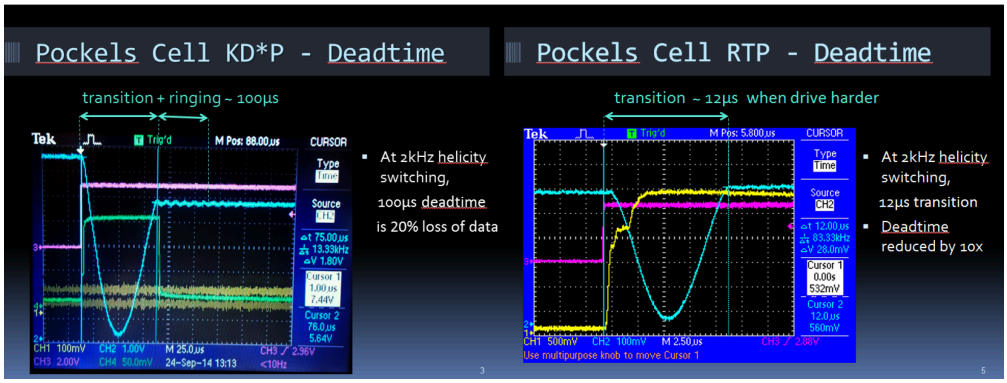

Figure 62: *Transition Time: These measurements were performed by driving the Pockels Cells near quarter-wave voltage and examining the transmission through an analyzer oriented along the birefringence axis. KD*P optomechanical ringing has a* $\sim 10\mu s$ *period. Left: blue trace is transmission through KD*P cell, pink trace is helicity trigger, green trace is the LED pulse detected by a photodiode. Right: blue trace is transmission through RTP cell, pink trace is helicity trigger, yellow trace is the LED pulse detected by a photodiode.*

E.3 Helicity-Correlated Beam Asymmetries

There is significant operational experience in using the polarized electron source for parity-violation experiments at Jefferson Lab. With this experience, and detailed understanding of the sources of HCBA in the laser optics of the polarized source have led to a sophisticated protocol for systematically reducing or eliminating these effects [65, 66]. The HAPPEX-II experiment made use of this improved understanding to achieve run-averaged helicity-correlated position differences, measured in the experimental hall, which were consistent with zero systematic offset within the beam jitter convergence radius of < 2 nm and 0.2 nanoradian

in angle. Further refinements of the configuration technique [112] let to a configuration of the laser optics of the polarized source that provided position differences in the injector that were smaller than those during HAPPEX-2 by about a factor of two. While Q_{weak} did not take advantage of adiabatic damping, it utilized a slow feedback technique to meet its goals for control of beam position differences [111].

PREX-2 ran using the new RTP Pockels cell system. This innovative system utilized electric field gradients to counteract crystal non-uniformities to optimize the beam trajectory differences [67]. Figure 63 shows position differences measured at various beam position monitors through the injector during the source optimization studies. This tight control of position differences at the low-energy front-end of the machine represent the best control yet achieved at JLab. As with HAPPEX-II, the beam parameter difference measured in the hall during this relatively short experiment (about 20 beam-days) were consistent with zero within the radius of convergence of beam noise, < 2 nm in position, < 0.4 nrad in angle, and $< 1.5\sigma$ from zero on the dispersive position monitor.

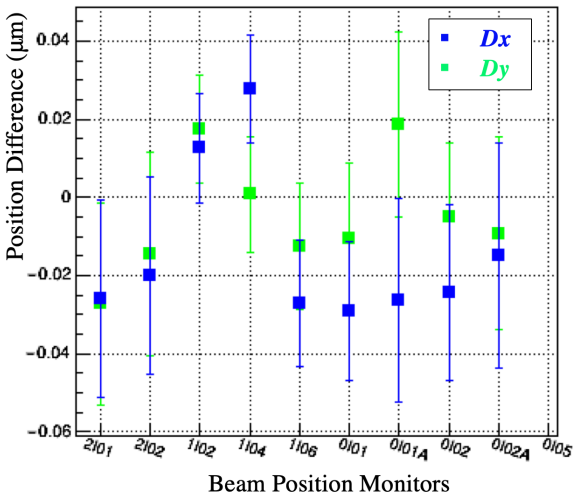

Figure 63: *Position differences in nanometers (vertical axis) measured at various beam position monitors in the injector (horizontal axis) during beam studies leading up to source configuration for the PREX-2 experiment in 2019.*

Table 6 shows results from previous experiments at Jefferson Lab. The tight bounds on beam parameter differences result from careful configuration of the polarized source, electron beam transport that takes advantage of adiabatic damping of trajectory differences, and slow helicity reversals.

E.4 Slow Helicity Reversal Techniques

The technique of "slow helicity reversal" generally refers to the introduction of an additional helicity flip, which changes the sign of the helicity relative to some sources of HCBA. An example would be the introduction of an additional half-cycle $g-2$ rotation, which would reverse the electron beam helicity with respect to the helicity of the beam created in the polarized source. The statistical consistency of data sets taken in different states of the reversal can be used to demonstrate the absence of large, unknown systematic errors, and the combination of data sets (appropriately sign-corrected) provides a method for further canceling possible unmeasured or poorly-corrected HCBA effects.

Until quite recently, only one slow-reversal has been commonly employed at CEBAF. A half-wave plate is inserted into the laser path to reverse the sign of laser polarization, relative to the voltage applied to the

Pockels cell (see Fig. 60). This slow-reversal is particularly effective for cancelling two types of effects. First, any false asymmetries related to electronic signals, either from the logic or Pockels cell high voltage, will be completely unaffected by the insertion of a half-wave plate. Thus, such false asymmetries will not change sign while the physics asymmetry does change sign. Second, a Pockels cell can steer or even focus the beam in a fully helicity-correlated fashion that is unrelated to polarization effects, due the gradients in the applied electric field [67]. Such steering and focusing will be unaffected by the half-wave plate, again insuring the false asymmetries will not change sign when the physics asymmetry does. Many HCBA's, however, are explicitly related to helicity-dependent residual linear polarization. Most of these effects will change sign with the insertion of the half-wave plate just at the physics asymmetry does, and hence are not cancelled. For this reason, other methods of slow-helicity reversal are desirable.

At 11 GeV, the total number of $g-2$ spin rotations will be large, on the order of 120π. It will be possible to change the orientation of spin, while maintaining very similar beam optics properties, by changing the energy of the accelerator by about 100 MeV. This interval is small enough to not require invasive reconfiguration of the experiment: backgrounds, spectrometer optics, etc. should remain very similar. This would be a very effective slow reversal, in that all HCBAs from the source should influence the final measurement with the opposite sign. Since this is disruptive to other halls, this method would be used a few times over the duration of the entire run.

A similarly effective slow reversal that can be used much more often can be created using spin manipulation in the injector. Spin manipulation (using a "Wien rotator") is necessary in the CEBAF injector to align the electron polarization into the horizontal plane, and then to set the in-plane launch angle to optimize longitudinal polarization at the experimental target. In principle, it is possible to apply a half-cycle spin rotation using a single Wien rotator, however, in practice this is complicated by large differences in the focusing effects of the Wien at the different setpoints. For this reason, additional spin manipulation hardware has been added to the CEBAF injector to provide more dynamic range. The "Double-Wien" rotator (shown schematically in Fig. 64) uses a second Wien rotator and a solenoid to provide a full 180° spin precession through the injector. This system was commissioned prior to the original PREX run in 2010, and it was used routinely during both the $\mathrm{Q_{weak}}$ and PREX-2 experiments. The operation during PREX-2 produced a slow spin flip spin flip with negligible changes to the trajectory in the injector, as demonstrated in Figure 65. MOLLER intends to use this reversal weekly.

E.5 Adiabatic Damping

The impact of helicity-correlated spatial variation in the beam can be greatly reduced in the accelerated beam impinging on the target due to the process of adiabatic damping. A simple consequence of relativistic mechanics is that the available phase space for a beam which has been adiabatically accelerated to a momentum p from a momentum p_0 is reduced by a factor of $\sqrt{p/p_0}$. For example, HAPPEX-II ran with a 3 GeV beam energy, which should correspond to a reduction in beam motion in each dimension by a factor of ~ 95, compared to motion of the 100 keV injector beam.

The benefits of this effect are typically not fully realized. While the damping of transverse motion is a simple consequence of the relativistic boost, an optics tune that deviates from design can produce significant correlations in phase space which can magnify helicity-correlated differences in the beam trajectory. Getting close to the theoretical limit requires detailed diagnostics and careful configuration of the beam optics to maintain a match with the design parameters. The collaboration typically works closely with accelerator physicists to produce the best results and maintain them over the duration of data collection. The best performance from the HAPPEX-II experiment suggested that helicity-correlated variations were suppressed by factors up to ~ 30.

The importance of focussing effort on adiabatic damping is illustrated in Figure 66, which illustrates the recent experience of the $\mathrm{Q_{weak}}$ experiment. The position differences in the injector where the best

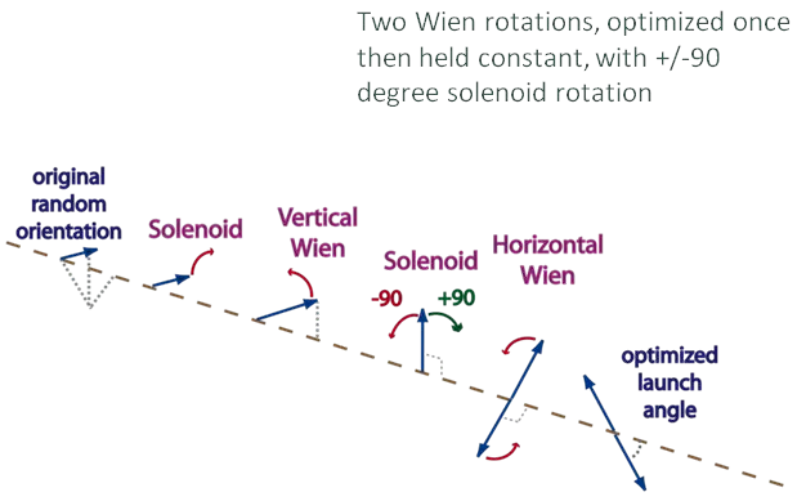

Figure 64: *Schematic of the concept of the "Double-Wien" filter, which allows a full "slow" flip of the electron beam polarization with minimal disruption to the front end electron beam trajectory. The flip is accomplished by adjusting the second solenoid, without changing the settings of the two Wien rotators.*

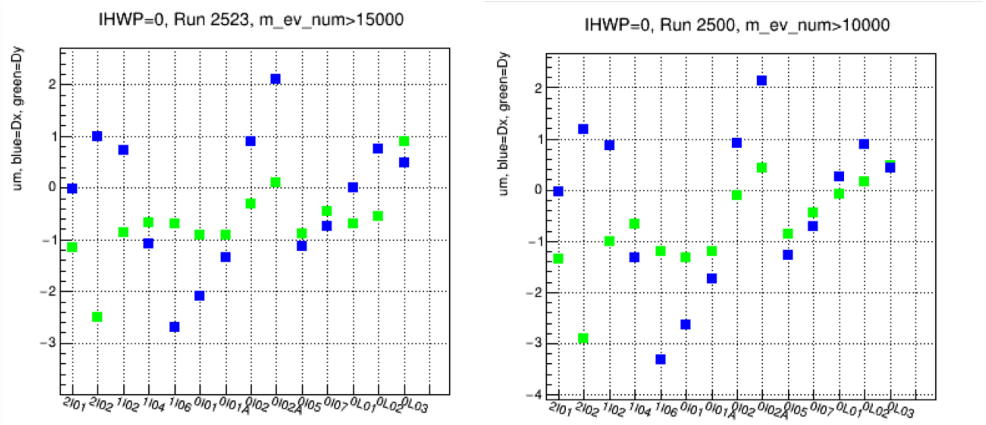

Figure 65: *Measurements through the injector of large position differences induced for this calibration by RTP setpoints. Left and right panels compare the "FlipLeft" and "FlipRight" configurations of the double-Wien rotator during configuration studies for PREX-2. The excellent comparison demonstrates that the beam trajectory remains the same even under this* 180° *spin precession.*

achieved to that point, < 50 nm in the 100 keV injector region. However, adequate time was not spent to properly match the accelerator tune resulting in a lack of adiabatic damping. The result as position differences in the experimental hall of ~ 100 nm, actually greater than in the polarized injector region. This apparent expansion of position difference suggests that correlations magnify the trajectory differences from the injector in the course of beam transport to the experimental hall.

Despite the benefits of adiabatic damping realized during HAPPEX-II, it has proven difficult to demonstrate a robust damping factor for position differences during other experiments. Due to improvements in the polarized source configuration, damping has not always been required to achieve experimental goals. In

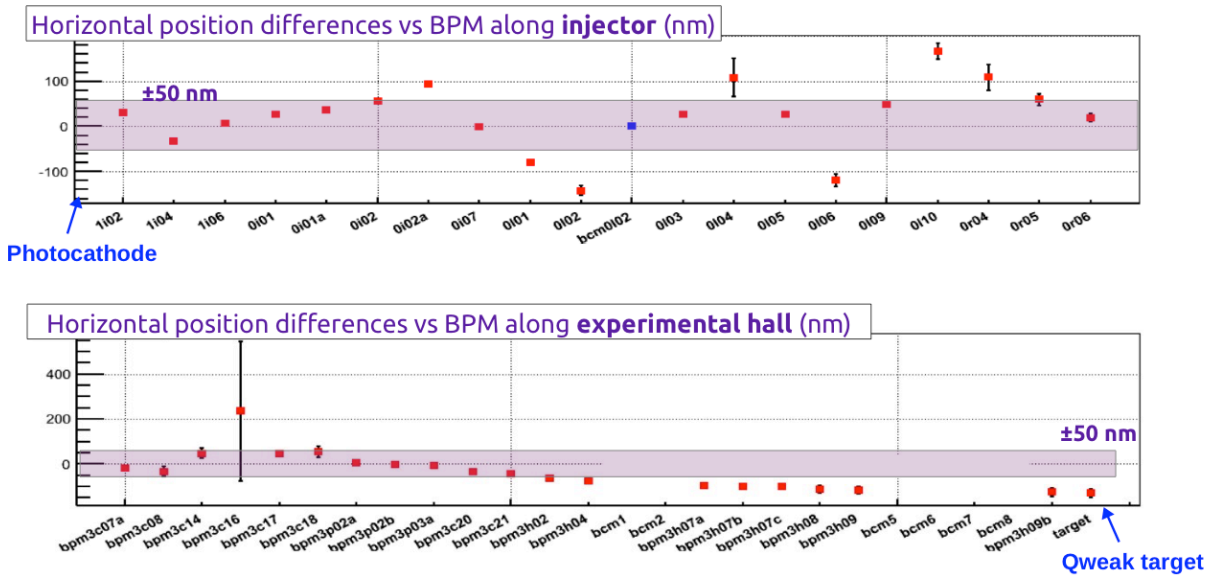

Figure 66: *Helicity-correlated position differences in the horizontal direction at various places in the beamline during* Q_{weak}. *The pink band in each figure represents* ± 50 *nm about zero. The upper figure shows the position differences in the polarized injector region, where careful laser optics setup resulted in position differences* < 50 *nm in the 100 keV region. The accelerator tune was not well matched, resulting in a lack of adiabatic damping that led to increased position differences* ~ 100 *nm in the experimental hall.*

particular, it appears difficult to measure and control the beam optics in the injector, especially the 100 keV region, in a manner that would allow the full benefit of damping. Improved tools for maintaining a match to design optics have been employed at JLab, but as yet there has been insufficient experience to demonstrate large benefits for control of HCBA.

E.6 Beam Halo: Beyond the usual PQB

The Q_{weak} experiment saw a significant false asymmetry that was ascribed to a helicity-correlated change in the beam distribution on target. This is often referred to as a "halo" effect. It should be noted that there is not clear evidence to tie this effect to a specific technical definition of "halo".

Three separate detector systems observed this false asymmetry. The main detectors for the experiment were one of these. Another was the "lumi" monitors, which measured slightly lower angle scattered particles than the main detector but in line-of-sight of the target and with no magnetic field to sweep away low energy Møller scatters. The so-called "auxiliary" detectors, composed of portions of a detector (such as a bare PMT, or a PMT with just the light guide) which were placed out of the elastic stripe near the main detectors, also saw the asymmetry. The ratio between the false asymmetry observed in each detector system was fairly constant throughout the run.

While the consistency between the detector systems allowed for sufficient correction for the Q_{weak} result, the characteristics of the beam that led to this effect were never precisely determined. Measurements taken while blocking the spectrometer aperture for some octants were able to demonstrate an asymmetry background signal that corresponded to the observed background asymmetries during production running. This asymmetry of this component could be changed with quad settings in the beam line (presumably changing the beta function at the target to enhance or suppress the effect of an asymmetric halo), or by changing the

laser phase relative to the master phase. These observations are consistent with some beam halo interacting with the beamline or collimation, but not definitive about the shape, extent, or source of the halo.

There is more than one candidate for the fundamental cause of such an asymmetric beam halo. Injector studies showed asymmetries in the longitudinal RF beam bunch profile, but it is not yet clear how to connect this to the observed asymmetric halo effects. Other models under consideration are bleed through from other halls, or fringes in the laser beam spot on the source photocathode producing asymmetric halo distributions well off of the central electron trajectory.

Studies using the Hall A SAMs One intriguing aspect was that each of the $\mathrm{Q}_{\mathrm{weak}}$ detector systems that observed these "halo" asymmetries was seen to be significantly non-linear with the measured beam current. This non-linearity was not constant in time, with large variations in magnitude and even at some some points changing sign. The effect was different in magnitude for each detector system, but these varied together, so a larger-than-average non-linearity observed in the lumi monitors would predict a larger-than-average non-linearity in the main detectors.

To explain these observations, a model was proposed in which the beam was asymmetric in some halo region, which was less likely to produce signal in the detectors (presumably due to geometric acceptance effects). The beam current monitor is not very position sensitive, so it would accurately measure the average current fluctuation even while a spatial distribution to the intensity asymmetry would change the average asymmetry in any given detector. The largest false asymmetries are seen at times when the non-linearity over the charge noise is seen to be greatest.

This provides some hope for a convenient diagnostic tool. In Hall A, Small Angle Monitors (SAMS, formerly known as "LUMI" monitors) in the beamline between the target and the dump provide high-rate monitoring of small-angle scatters from production targets. They have extremely well-understood linearity and noise characteristics. When used at high beam currents with a moderately thick target they can provide a high precision test of the non-linearity of detector relative to the intensity jitter of the beam. In addition, at these small scattering angles the parity-violating asymmetry is expected to be very small. These detectors were installed for the PREX-2 and CREX experiments, and are to be used in investigations of both non-linearity of their response to beam intensity noise, and in the measurement of systematic "false" asymmetries that could be caused by halo. In addition, the "halo" monitor which can be used to investigate the intensity of a position halo or tail will be available for beam studies in Hall A.

Summary of plans for MOLLER As described above, during the PREX/CREX run period we will attempt to use the non-linearity of small-angle monitors over the measured beam intensity noise as a tool for studying this asymmetry halo. It is hoped that this can establish a diagnostic technique, which can correlate an observed effect with other diagnostics in the injector or accelerator. The results of those studies will also help inform planning for continuing these studies opportunistically during subsequent 11 GeV running.

Clearly more information is needed to demonstrate that this possible effect is fully controlled for MOLLER, but existing hardware and technology appear to provide the necessary tools for testing the effect in advance of the MOLLER production runs.

F Electron Beam Polarimetry

In the following sections, we describe details of the implementations of these polarimeters in Hall A, the methods that will be used to achieve high precision, and modifications to existing hardware that will be required.

F.1 The Hall A Compton Polarimeter

The Hall A Compton polarimeter is described in Sec. 4.1. A more detailed description of the laser system and photon calorimeter is provided below, along with a detailed discussion of analysis techniques that will enable high precision polarimetry.

F.1.1 Laser System

As described above, the laser system stores up to 10 kW power in a resonant cavity for intersection with the electron beam. The system consists of a 1064 nm ND:YAG seed laser coupled to a Ytterbium-doped fiber amplifier to produce about 5 W power. This is converted to 1-2 W of 532 nm light using a Periodically-Poled Lithium Niobate (PPLN) doubling crystal. The light is prepared in a suitable polarization state with a combination of quarter-wave and half-wave birefringent optics, then transported through mode-matching optics and directed through a vacuum window and and onto the cavity mirror. Resonance is maintained with a Pound-Drever-Hall (PDH) lock using retro-reflected light analyzed at the polarization preparation station, with feedback and modulation sidebands through the 1064 nm seed laser. This system was first used for the PREX-I experiment in 2010 and has been operated since that time, typically configured for a factor of 2000 in cavity gain providing power levels of about 2 kW.

One challenge is the precise determination of the inter-cavity polarization, which cannot be directly measured with the cavity in resonance. This challenge is complicated by the birefringence of the vacuum windows, which is in part stress-induced and changes significantly under vacuum load. The polarization of light arriving at the cavity entrance can be inferred from light reflected back from the cavity and analyzed with the same apparatus used to create the initial polarization state, measuring a single power level [90]. This technique was employed in Hall C during the $Q_{\rm weak}$ experiment to maximize the circular polarization of light injected in the cavity and to monitor the polarization during the run. It was verified to work by two methods. In the first, with the cavity under vacuum in running conditions, a scan over a broad range of initial polarization states was performed, and the recorded analyzed reflected power was shown to be well described by the simple hypothesis of optical reversibility. A more direct verification was made with the cavity opened, directly measuring the polarization of the injected light in the cavity and correlating this with the analysis of the reflected light. The correlation is shown over the full range of the scan, and zoomed in for measurements at maximum circular polarization, in Fig. 67. In operation, the Hall C Compton polarimeter ran with the reflected light very near minimum, with an implied uncertainty on the circular polarization within the cavity of 0.1%.

The technique has been implemented and further studied in the Hall A polarimeter, which makes use of a significantly higher cavity gain compared to the system in Hall C. It was found that intrinsic birefringence in this cavity was a significant effect, which significantly complicates this approach. The cavity birefringence must be characterized and incorporated into this scheme, as was done for the 2019 PREX-2 and CREX experimental runs. The stability of this determination can be cross-checked using the polarization analysis station in the transmitted beamline. While this process requires significantly more calibration and preparation to control for cavity birefringence, it is expected that it will be capable of determining and monitoring the circular polarization in the cavity to the level of 0.2%.

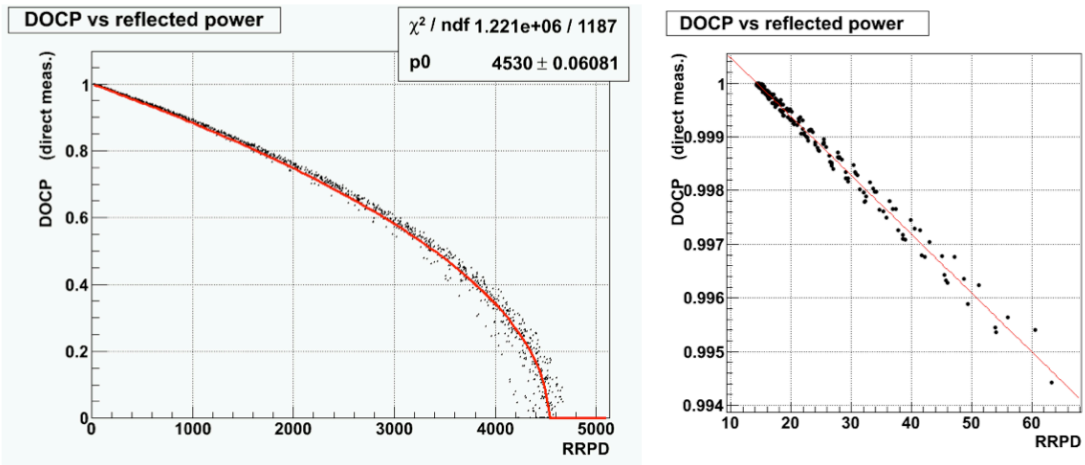

Figure 67: *Measured degree of circular polarization in the Hall C Compton laser cavity vs. the polarization-analyzed reflected light, measured over a broad scan of initial polarization states. The figure on the right is zoomed in the region of maximum circular polarization.*

F.1.2 Electron Detector

Presently, electrons are detected in a set of 4 planes of silicon microstrip detectors located just before the 4th dipole. Each microstrip plane instruments 192 strips with a pitch of 240 μm, with strips running in the horizontal direction so as to provide resolution in the vertical (dispersive) direction. Custom readout electronics pre-amplify and discriminate signals from the microstrips, implement a simple tracking algorithm to reduce non-directional backgrounds, and count hits in each strip over specified integration gates corresponding to the helicity pattern of the electron beam. Presently, this system is operating at low efficiency with poor signal size for a minimum ionizing track compared to environmental noise on individual strips. In addition, the active area of these planes is smaller than ideal for high precision measurements, when used with 532 nm light at 11 GeV.

An upgrade for this detector system is required. Plans for the HIPPOL capital improvement project include an upgrade to diamond microstrip detectors. Such microstrips were successfully used for the Hall C Compton polarimeter in the Q_{weak} measurement [89]. Diamond microstrips are more radiation hard and less susceptible to low-energy photon backgrounds. They are more difficult to procure than silicon strips, but a recent SBIR has led to a new commercial availability. In this upgrade, the front end amplifier/discriminator boards would be remade to be optimized for the signal size and shape expected from the diamond, while the readout system would otherwise remain the same.

An alternative development for silicon pixel detectors based on HVMAP technology is also underway. These detectors would incorporate amplifier, discriminator, and multiplexed readout circuitry on the same radiation-hard silicon substrate as the pixel detectors. An FPGA readout of the multiplexed signal would be designed to implement tracking, and geometry cuts for the 2-D readout. A prototype system is currently being developed at Manitoba, in research funded by NSERC.

F.1.3 Photon Detector

The calorimeter for detecting scattered photons lies about 7 meters downstream of the interaction point. The strong forward boost of scattered photons leads to a tightly collimated photon beam (< 1 mrad for $> 1\%$ of the Compton edge), so the primary consideration for calorimeter size is energy resolution through shower

loss. The photon detector is composed of an array of four $PbWO_4$ crystals, with a total transverse size of 6×6 cm^2 and length 20 cm, instrumented with a single photomultiplier tube. The $PbWO_4$ materials is ideal for its high density and fast response, and the light yield provides sufficient resolution for the high energy photons (up to 3.1 GeV at 11 GeV beam energy) that will dominate the measurement. The PMT signal is split between two parallel data acquisitions: one with a fast-counting, buffered ADC self-triggered on pulses from the photon detector, and the other utilizing a 250MHz flash ADC (fADC) to integrate the total signal over periods corresponding to the helicity pattern of the electron beam. The fADC system can also record a very low rate of individual pulses for calibration. Each of these dual readouts can be analyzed independently. The fast counting ADC readout and the sample pulses in the fADC system can both be triggered using the electron detector, providing an electron-photon coincidence spectrum for calibration.

At 11 GeV, synchrotron radiation from the dipole magnets threatens be a significant background in the photon detector, potentially overwhelming the Compton scattered signal by a factor of 10. This radiation is reduced using a lead shield in front of the photon detector, but it is desirable to keep this shield thin to minimize the effect of the measured Compton spectrum. For this reason, the synchrotron light is suppressed using a modification of the chicane magnets, and a remote-adjustable vertical collimator is installed to cut much of the remaining synchrotron radiation.

In order to reduce the synchrotron radiation in the region of acceptance for Compton scattered electrons, the fringe fields at the edges of the chicane dipoles were modified with magnetic "shims" to soften the bend into and out of the interaction region. Figure 68 shows the energy spectrum of synchrotron light attenuated by lead shielding between 1–5 mm thick, depending on the beam energy. On the left, the spectrum for 11 GeV with unmodified magnets is compared to calculations for the recent runs of HAPPEX-III (3 GeV) and PV-DIS (6 GeV). On the right, the energy spectrum ("Fringe 2") is shown when iron extensions, 15 cm in length, are added to the dipole magnets in order to provide an extended region of reduced field. This reduced magnetic field produces synchrotron light with lower energy range and with reduced intensity, for the portion of the electron beam trajectory that projects to the photon detector. With this modification, the bending strength of the magnet remains the same but the synchrotron light radiated into the detector is reduced by a factor of 10^4. The magnetic field extensions were modeled using TOSCA. They have been installed and used in 2016 with 11 GeV operation of the polarimeter.

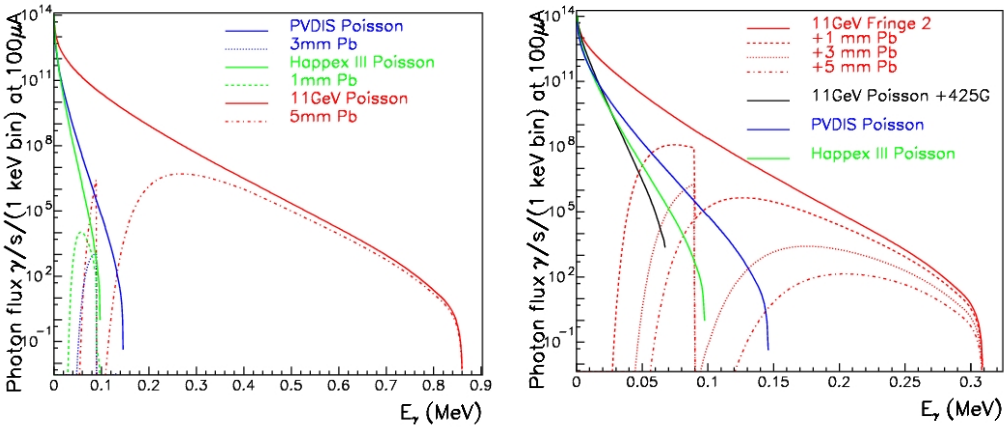

Figure 68: *Energy spectrum of synchrotron radiation penetrating lead shielding of thickness listed. Plot on left shows unmodified chicane magnets, plot on right shows energy spectrum when using magnetic shims which reduce the field for the bend radiating into the Compton photon detector acceptance. Note the different horizontal scales between the plots.*

A vertical collimator was developed to further cut the synchrotron radiation level. These provide a horizontal slit just in front of the photon detector, with the vertical size of the slit precisely controlled with a remote actuator. The collimator can be positioned to block the vertical stripe of synchrotron radiation, below the Compton photons due to the second chicane dipole and above the Compton photons due to the third chicane dipole. Very near the Compton photon acceptance, the synchrotron radiation is significantly reduced by the magnetic shims. Together, the shims and vertical "jaw" collimator have been seen to provide excellent suppression of synchrotron radiation.

F.1.4 Systematic Uncertainties in the Compton Polarimeter

The Hall A Compton polarimeter described above should assure operability and sufficient precision at 11 GeV. Although all of the challenges that will be encountered on the path to 0.4% precision cannot be predicted, it is useful to review the techniques and understandings that lead to the conclusion that this will be within reach. Table 7 summarizes the goals for various contributions to systematic uncertainty, based on the collaboration's experience with Compton polarimeter from high-precision experiments such as PREX and Q_{weak}. The first four rows list sources of uncertainty which are highly or completely correlated between the electron and photon analyses. The other tabulated uncertainties arise in detector readout or calibration and are mostly or entirely decorrelated between the analyses. Each of these separate categories of potential systematic uncertainty: correlated, electron-only, and photon-only, will be discussed in the following sections.

Sources of Correlated Error Any error associated with the Compton scattering process will be a common source of systematic error between the electron- and photon-detector analyses. One example lies in the energy normalization of the scattering process. The analyzing power is a function of both electron energy and photon energy, so these must be precisely determined. The photon wavelength will be determined to better than 0.1 nm and the electron energy to 0.05%, which leads to an uncertainty at the level of 0.03%. A similarly small uncertainty will come from radiative corrections, which are calculable [91] with high precision and will contribute at the level of $< 10^{-3}$.

Helicity-correlated changes in luminosity of the laser/electron interaction point can introduce a false asymmetry. Various causes of luminosity variation must be considered, such as electron beam intensity, beam motion or spot-size variation. The control of helicity-correlated beam asymmetries is now a standard technology at Jefferson Lab, and typically achievable results (few part per million intensity, 10's of nanometers beam motion, $<10^{-3}$ spot size changes) will suitably constrain the electron-photon crossing luminosity variations. Another possible source of false asymmetry would be electronics pickup of the helicity signal, which could potentially impact an integrating photon analysis. However, the demands of the primary experiment for isolation of the helicity signal exceed those for polarimetry by several orders of magnitude. In addition, the laser polarization reversal provides an additional cancellation for asymmetries correlated to the electron beam helicity. For these reasons, beam asymmetries are expected to be a negligible source of uncertainty in this measurement.

A more significant potential source of error comes from the uncertainty in the photon polarization. As described above, the determination of photon polarization will require calibration of the intrinsic birefringence of the cavity and will utilize the analysis of light reflected from the cavity input mirror and transmitted through the cavity. Together, these will provide robust and precise control and measurement of the polarization state in the cavity with a precision of 0.2%.

Systematic Errors for the Electron Detector The electron detector is composed of 4 planes of microstrips normal to the electron beam trajectory and positioned on the low-energy side of the beam trajectory in the dispersive chicane. Electrons which have given up energy to a scattering process are separated from

the primary beam by the third chicane dipole, and the energy of a detected electron is implied by the distance of the track from the primary beam with a dispersion of about 0.45% of the beam energy per millimeter. Models of the chicane magnets are used to calculate the electron energy as a function of position in the detector. The absolute normalization of the energy of the electron detected in each strip is sensitive to details of the magnetic chicane and beam position, and is the key challenge in normalizing the observed asymmetry spectrum.

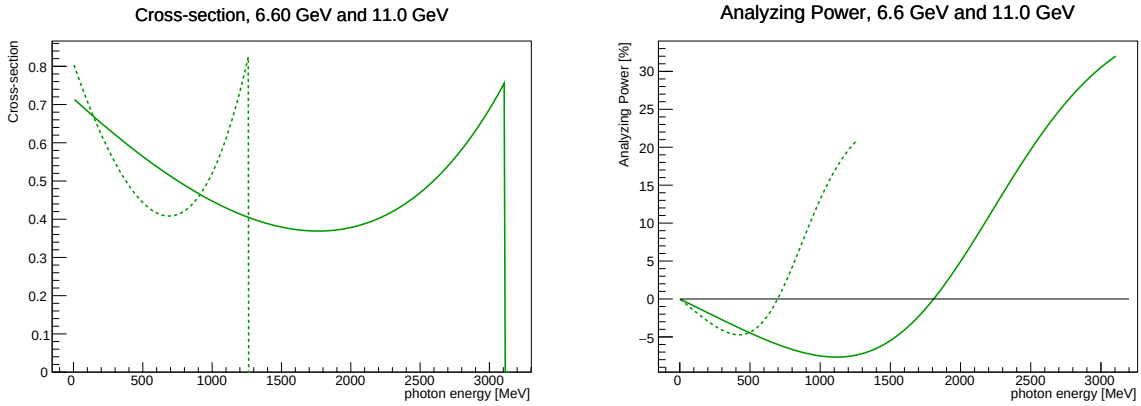

Figure 69: *The cross-section and asymmetry plotted versus Compton scattered photon energy for the Hall A polarimeter at 11 GeV (solid line) and at 6.6 GeV (dotted line) with 532 nm light.*

The cross-section and asymmetry as a function of Compton scattered photon energy is plotted in Figure 69 for an 11 GeV and 6.6 GeV electron beam. The Compton edge (the kinematic endpoint of the Compton energy spectrum) is observed in the electron detector and used to calibrate the distance of the detector from the primary beam. In addition, the asymmetry as a function of photon energy k exhibits a zero crossing. Determining the location of this asymmetry zero crossing (0xing) provides a second absolute energy calibration point, so together the Compton edge and 0xing can be used to calibrate two parameters: the detector location relative to the beam and the strength of the magnetic field in dipole 3. In this way, survey results and magnetic field maps serve as a cross-check to a beam-based self-calibration of the Compton energy spectrum. The precision of this calibration is limited by delta-ray production in the microstrips, which distorts the measured spectrum, and efficiency variations between the microstrips.

The recent analysis of the Hall C Compton polarimeter for the $\mathrm{Q_{weak}}$ experiment provides the best example of the potential of this technique [89]. The chicane had been optimized to low energies, and with a large bend angle and 532 nm light, the 0xing was 8.5 mm from the primary beam for the 1 GeV beam energy. At this distance, backgrounds were reasonably low, and the diamond microstrip detector could be positioned close enough to the primary beam to accept well beyond the zero-crossing. While the microstrip detector exhibited significant efficiency variations from between strips, the asymmetry distribution was not distorted by this effect. The rate and asymmetry distribution are shown in Fig. 70. The shape of the asymmetry spectrum over microstrip position, which is slightly non-linear in electron momentum, was calculated in Monte Carlo simulation of the Compton spectrometer using magnetic models of the chicane magnets. This shape template was fit to the asymmetry distribution, returning a scale factor corresponding to the spectrometer dispersion, the location of the Compton edge, and the polarization of the electron beam. The fit results were stable and robust, with no observable, systematic deviations in the residuals of the fit to the asymmetry spectrum shape. Simulation was used to demonstrate that the results were very insensitive to a broad range of possible systematic errors, including uncertainties in magnet Bdl or field map, detector noise, detector alignment, or the effect of triggering algorithms. Delta-ray production from the electron interacting in the

detector was also seen to be important, so that results from the later detector planes had to be significantly corrected due to distortions in the asymmetry spectrum from the multiple tracks; the correction in the first plane of the detector was negligible. The most significant systematic error contributions, about 0.4%, were a result of dead-time in the fast-triggering DAQ algorithms, which could be complicated by noisy or inefficient strips. Over the run, the electron detector normalization in this analysis was estimated to be known to 0.56%. It was also clear that improvements in the DAQ algorithms would be able to further improve on this precision.

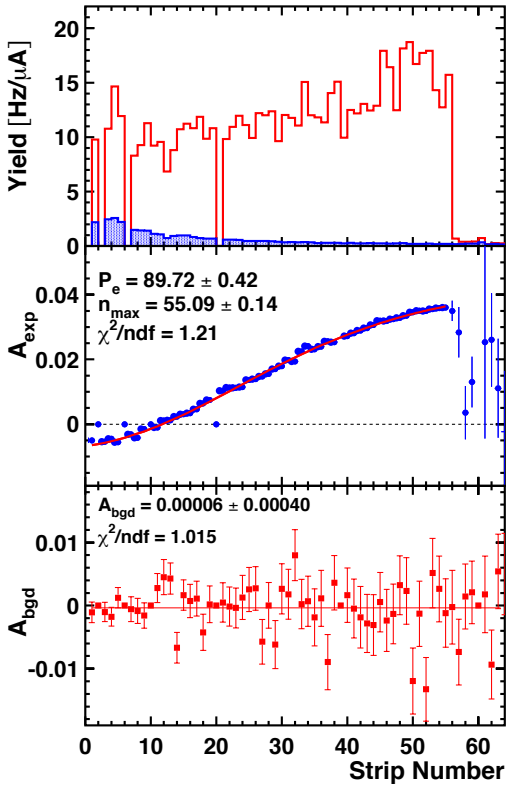

Figure 70: *The measured rate and asymmetry spectrum in the Hall C Compton polarimeter measured in the first plane of the electron detector, as a function of microstrip number from the detector edge which is about 6 mm from the primary beam. top: measured rate with laser on (red) and off (blue); middle: background-subtracted asymmetry spectrum, fit to expected shape with free parameters for spectrometer calibration and polarization; bottom: measured background asymmetry, uniform and consistent with zero.*

In the Hall A system at 11 GeV, the 0xing will be around 33 mm from the primary beam, which should allow for robust operation. Improvements in the DAQ system suggested by the Hall C experience should lead to a reduction of the rate-dependent DAQ inefficiencies that were the largest source of systematic uncertainty. The high statistical power of the measurement will also be important; for example, high precision studies can be performed to benchmark models of the readout system against changes in the laser power or the parameters of the triggering (preamp levels, logical gate lengths, coincidence levels, etc). Based on the Q_{weak} experience at the 1 GeV beam energy, it is expected that the electron detector analysis at high energy will be normalizable to a level significantly better than 0.4%.

The large statistical power also enables alternative analyses with significantly different systematic un-

certainties. Using only the last, single silicon strip at the Compton edge will be capable of 0.4% statistical precision on time-scales of around one hour. The rate of change of the asymmetry in this region is only 0.5% / mm. locating this strip, relative to Compton edge, to a little better than half its own width should provide a robust accuracy on the analyzing power better than 0.4%. This technique would be sensitive to determination of the location of the Compton edge, but otherwise very insensitive to other calibration parameters.

Similarly, the asymmetry minimum, which lies about 19 mm from the 11 GeV primary beam, could be used. The statistical power is much lower in this region, with a single strip requiring 30 hours to achieve 0.4% statistical precision on the polarization (assuming signal-noise ratio of 10:1). However, here the asymmetry is not changing with position, so there is minimal calibration error in selecting a strip in this minimum. Beam position and angle may vary the location of the asymmetry minimum on the detector over hundreds of microns during this time span, but such changes can be tracked using beam position monitors or the Compton edge. The analyzing power varies by only about 0.4% of itself over a range of ± 1.6 mm, suggesting minimal corrections will be necessary .

Regardless of the analysis, contributions from deadtime and pileup will need to be understood. The fast-counting DAQ can take very high rates with low deadtime, and deterministic deadtime intervals are enforced in readout and acquisition electronics stages. The segmentation will keep rates in individual microstrips to < 2 kHz. The high statistical power of the measurement is of significant use here; high precision studies can be performed to benchmark models of the readout system against changes in the laser power or the parameters of the triggering (preamp levels, logical gate lengths, coincidence levels, etc).

Backgrounds are also a potential but small source of systematic uncertainty. Backgrounds are studied with the laser cavity unlocked, allowing both the background level and asymmetry to be well determined. However, high backgrounds could impact the systematic error due to deadtime or pile-up corrections. There is also the possibility of backgrounds from Compton-scattered electrons, which can produce delta rays when scattering in the detector or in its shielding. These tracks can themselves be sufficiently forward-going to pass the trigger, thus changing the analyzing power as a function of energy. Simulation will be used to study these contributions, and empirical studies of track distribution and electron-tagged photon energy spectra can be used to identify such effects in the data.

Systematic Errors for the Photon Detector The precise determination of the analyzing power as a function of energy is more difficult for the photon calorimeter than for the electron detector due to the width and shape of the detector response function. In order to fit the asymmetry as a function of detected photon energy, the analyzing power must be calculated as a convolution of the response function with the theoretical analyzing power curve. In general, determining the effect of a low-energy threshold on the analyzing power depends sensitively on the shape of the response function; at low energies this is a major source of uncertainty. At high energies, the improved resolution and consistency of the response function shape over the range of interest should significantly reduce this problem. The response function shape and energy calibration can be simulated, and studied using the photon tagging through coincidence triggers with the electron detector. Characterization of the phototube response as a function of both pulse-size (to correctly check the analyzing power determination) and rate (to correctly measure the asymmetry) will also be important.

The pulse-counting analysis in the photon detector is also sensitive to pile-up and deadtime effects, which distort the asymmetry distribution. Background and rate distributions will serve as inputs to simulation for corrections to the analyzing power. In the current Hall A analysis, pile-up corrections are estimated at the level of 1%, and the effect can be controlled at a level better than 10% of itself.

Uncertainties related to the threshold, response function shape, absolute energy calibration, deadtime and pile-up can also be eliminated by integrating the photon calorimeter signal, without threshold [88]. These previous problems are then replaced with a requirement on the linearity of the average response to

the photon energy. Because the analyzing power integral is energy-weighted, the statistical figure-of-merit is not badly degraded by the negative asymmetry region at low photon energies.

The PREX experiment, with a beam energy near 1 GeV, relied on the integrating photon method for polarimetry at the level of 1% precision. Simulations of the photon response function were sufficient to control the analyzing power uncertainties for those measurements. The dominant uncertainty in the asymmetry measurement arises from variation in the photomultiplier response with changes in average rate which introduces a systematic error through background subtraction.

At high energies, with the ability to study response function with the electron-detector-tagged photon beam over a large fraction of the energy range, the photon detector analyzing power normalization uncertainty in the range of 0.3% should be achievable.

Summary of Compton Polarimetry The prospects for 0.4% Compton polarimetry are excellent. This ambitious goal will require vigorous and dedicated efforts to reduce sources of systematic uncertainty. At lower beam energies, precision has reached 1% (PREX at 1 GeV), 0.8% (HAPPEX-3 at 3 GeV) and, most recently, 0.7% ($\mathrm{Q_{weak}}$ at 1 GeV). It is worth noting that, in each case, the systematic uncertainty of polarimetry was significantly better than required for the experiment. These measurements all used lower beam energies, with a reduced energy range of the Compton-scattered spectrum and smaller scattering asymmetries. At the higher energies employed for SoLID, the kinematics are favorable for an improvement in precision.

A dominant systematic uncertainty in the previous Hall A measurements was the determination of the laser polarization in the optical cavity. Techniques, first developed during the $\mathrm{Q_{weak}}$ experiment and since further refined in Hall A, will provide control on laser polarization to 0.2% or better.

In the case of the electron detector, the "self-calibration" technique (using the shape of the analyzing power between the Compton edge and zero crossing) was successfully employed with the Hall C Compton polarimeter at 1 GeV for the $\mathrm{Q_{weak}}$ measurement. The fit to the shape of the asymmetry spectrum proved to be remarkably resilient to calibration errors, with an estimated uncertainty in the analyzing power normalization of 0.56%. With the increase in the scattered energy spectrum at the higher 11 GeV beam energy, it is expected that the electron detector analysis will be precise at a level much better than 0.4%.

For the photon detector, the integration readout method has been successfully used in the HAPPEX-3 and PREX experiments, with the primary limitation being the characterization of the phototube response over the range of signal levels. At 11 GeV, coincidence measurements between the photon and electron detectors will also provide a significant cross-check to the response function and energy calibrations, enabling a counting measurement which is far more precise than what has been possible in previous runs at low beam energies.

It is expected that some significant fraction of data production time wil be used for studies of the Compton polarimeter system which are not disruptive to the experiment, for example, scans of detector positions, laser power and polarization, and data acquisition parameters. The scattering asymmetry at 11 GeV is relatively large which, for some analysis approaches, will provide statistical precision at the level of $\sim$0.5% in about five minutes of data collection. This rapid access to high statistical power, which is so powerful for cross-checking potential sources of systematic uncertainty, has never before been available for Compton polarimetry at JLab. Given this high statistical power, beam-based studies will be an effective method for constraining many of the possible experimental systematic uncertainties.

As described above, recent experience with analysis techniques, laser polarization measurements, and the favorable kinematics of the higher electron beam energy have opened the door to robust 0.4% precision Compton polarimetry for the SoLID program.

F.2 Moller Polarimetry

Møller polarimetry is complementary to Compton polarimetry, both providing the same level of precision on the electron beam polarization, but with completely different systematic uncertainties. The systems are

also complementary because the Møller polarimeter makes measurements in short, dedicated runs, while the Compton polarimeter takes data continuously as the experiment runs in production mode.

Each technique is designed to achieve $\sim 0.4\%$ precision on the beam polarization. Their agreement will be a key ingredient in minimizing the uncertainty in this parameter.

During PREX and CREX data taking in 2019 and 2020, we have gained much experience with the new Hall A system, albeit mainly at lower energies. Much of this experience has led to new procedures for understanding many systematic effects, and minimizing their contributions to the ultimate precision.

F.2.1 Principles of Møller Polarimetry

Møller polarimeters exploit the helicity dependence of polarized Møller scattering, namely

$$\vec{e}^{\,-} + \vec{e}^{\,-} \rightarrow e^- + e^-,$$

to extract the beam polarization by using a polarized electron target of known polarization. This reaction has several attractive features for measuring beam polarization. First, Møller scattering has a very high analyzing power, with a maximum of 7/9 for scattering at $\theta_{\rm CM} = 90^\circ$, that can be precisely calculated in QED. Secondly, the cross section is very large for GeV incident energies, providing an ample count rate. Third, the two electrons emerge symmetrically, making coincident detection relatively straightforward. Polarimeters based on this reaction have been in use for more than three decades and many potential systematic effects are now controlled at a level below 1%. Many Møller polarimeters utilize a magnetic spectrometer system to momentum-select the outgoing electron pair, which are typically detected in coincidence to reduce backgrounds and control systematic uncertainties. Various types of magnetic systems have been employed over the years. The Møller polarimeter in Hall A uses an iron foil magnetized with a set of superconducting Helmholz coils, followed next by a set of four quadrupole magnets to focus the events of interest and finally a dipole to momentum-select the outgoing electron pair as can be seen in Fig. 72. We will continue to use the existing Hall A Møller spectrometer system, with some upgrades to meet precision criteria necessary for MOLLER.

One of the main challenges is to identify an appropriate target of polarized electrons. Tilted ferromagnetic foils with high purity have been used in the past, but are not able to reach the required precision in target polarization. For MOLLER, we will use a pure iron foil, polarized perpendicular to the foil plane in a ~ 4 T applied field. The magnetic saturation properties of iron are known well enough so that we can reach the required precision.

In the end, we extract the beam polarization P_B from the equation

$$A_{\rm meas} = P_B P_T \langle A_{zz} \rangle$$

where $A_{\rm meas}$ is the measured spin asymmetry in Møller scattering, P_T is the target spin polarization, and $\langle A_{zz} \rangle$ is the analyzing power averaged over the spectrometer acceptance. These quantities clearly need to be determined to high precision in order to meet our goal. For example, sensitivity of $A_{\rm meas}$ to all manner of beam motion and intensity need to be known, magnetization and spin-orbit effects in iron must be well understood in order to extract P_T, and accurate spectrometer simulations are needed to find $\langle A_{zz} \rangle$, including accounting for kinematic variations between inner (unpolarized) atomic electrons and polarized outer electrons, also known as the Levchuk Effect.

We are fortunate to have the experience from having completed PREX and expect to finish CREX in the 2019/2020 CEBAF run cycle, each of which require $\sim$ 1% precision on the beam polarization. A greater understanding of the system has allowed for the development of optical setup procedures that greatly reduce sensitivity to precise knowledge of the quadrupole and dipole fields and allows tuning of the Levchuk correction to nearly negligible levels. The experience and insight gained from these experiments has greatly shaped our thinking as we prepare for precision polarimetry for MOLLER.

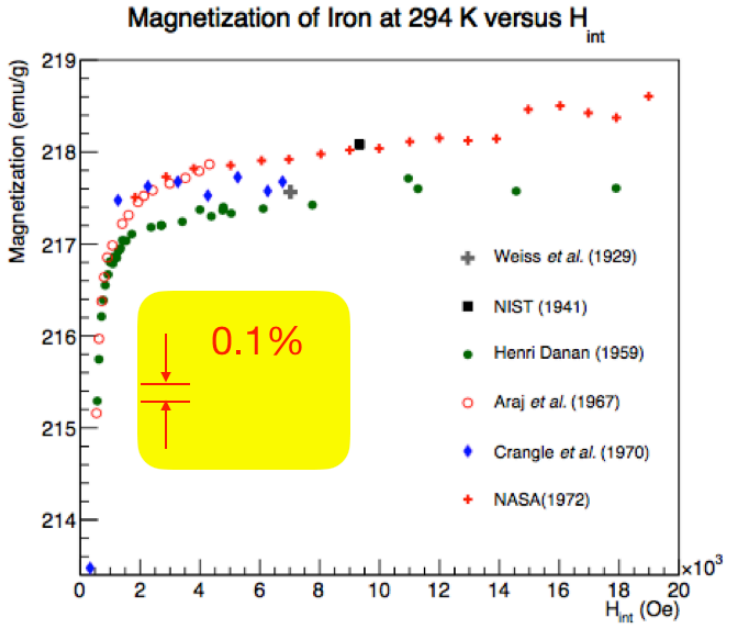

Figure 71: *Magnetization data for pure iron, from a number of experiments. Iron "saturates" at an applied field near 10 kOe (i.e. 1 Tesla), but displays a slow increase at very high fields due to paramagnetism. Measurements are generally in good agreement, at level of a few tenths of a percent.*

F.2.2 Iron Foils as Targets for Precision Møller Polarimetry

Nearly all high energy Møller polarimeters operated to date [93–100] make use of tilted ferromagnetic foil targets. High permeability alloys coupled with ∼few hundred Gauss magnetic fields preferentially polarize in the plane of the foil, so tilting the foil at a moderate angle gives a substantial longitudinal target polarization. Calculating the effective polarization, however, is typically the limiting systematic error, and such devices cannot ultimately do better than several percent precision. A different approach [101–103] using a high magnetic field perpendicular to the foil plane is now used for the polarimeter in Hall A.

The first step in determining the target electron polarization is to understand the magnetization of iron, that is, the magnetic dipole moment per unit volume. Figure 71 shows magnetization data for pure iron, taken from a variety of published measurements over a wide range of applied magnetic fields, in the region of saturation. The measurements are in agreement at the level of $\pm 0.15\%$.

In order to get the electron spin polarization from this magnetization, it is also necessary to correct for the contribution from orbital motion. For this, one needs to rely on the so-called gyromagnetic ratio $g' \approx 1.9$ in iron; see G. G. Scott and H. W. Sturner, Phys. Rev. 184, 490 (1969). The resulting $\sim$5% correction contributes to the uncertainty in target polarization at a level similar in size to the magnetization. Although the precision claimed by the G. G. Scott published result is $\pm 0.1\%$, our independent review of world data suggests this uncertainty should be conservatively increased by a factor of 2 making it the dominant uncertainty in the target polarization at 0.22%. A simulation of the heat deposition using computational fluid dynamics showed the foil temperature would increase by about 19 degrees Celcius under a 1 μA current load which translates into a 0.4% correction for temperature on an iron foil. Conservatively allowing 25% error on this translates into a $\sim$0.1% error. Estimates of error on target angle suggest that if the target angle can be controlled at the $\pm 2^\circ$ level, the uncertainty in the target polarization from this effect will be limited to $\sim 0.1\%$. Studies are ongoing at Jefferson Lab using a Kerr apparatus to measure and limit the systematic effect of target angle. Combining these four target polarization effects (angle, temperature, magnetization and orbital correction) gives a total uncertainty in target polarization of $\pm 0.3\%$. This level of uncertainty is not expected to improve significantly and depends on successfully limiting the sensitivity to target angle as expected.

F.2.3 The Hall A Møller Spectrometer

The existing Hall A Møller polarimeter spectrometer [93, 94] will be used for MOLLER. This QQQQD system, for which Levchuk corrections are minimized to be $\sim 2\%$ [93] will meet our needs with some minor upgrades. Originally a QQQD magnetic array, a fourth quadrupole has been added to optimize operation up to 11 GeV, and data has already been taken at this energy. One of the key uncertainties in the system we have observed is the difference between the predicted (simulated) and measured Møller rates as a function of current in the various quadrupoles. Recent insights from the PREX experience have revealed the flexibility of this system to reduce sensitivity to precise knowledge of the quadrupole optics by tuning the quadrupole currents relative to a feature in the rate versus current scan rather than an absolute value. Furthermore, experience has shown that by setting up the optics plus detector combination such that the detector defines the momentum acceptance allows one to "tune" the Levchuk correction to a small value that is also insensitive to the precise current in the quadrupoles. Systematic tests planned for the CREX data-taking period will allow further precision testing of these key insights. An asymmetry versus quadrupole current scan taken during PREX including a region of increased Levchuk sensitivity was consistent between data and simulation. A similar planned precision scan with a 3-fold increased sensitivity to Levchuk at the CREX optics will allow us to determine the accuracy of our current Levchuk model. Recent simulations have suggested that with the current hardware we can tune the Levchuk correction at MOLLER energies to significantly less than the 1% level. A conservative 50% error on this makes the Levchuk correction a leading systematic error for Møller. However, with more optical simulation studies, upgrades to the existing system along with precision benchmarks of the Levchuk model from CREX we expect to be able to substantially reduce both the size and relative uncertainty of this correction. We believe a total uncertainty of 0.2% or better on the Levchuk correction is achievable.

The acceptance-averaged polarization analyzing power of the target $\langle A_{zz} \rangle$ comes from simulation and depends on several factors. What is measured is the effective analyzing power which combines radiative effects, multiple scattering, Levchuk effects and detector/spectrometer acceptance. Although these are physically distinct effects they are difficult to distinguish except in simulation. As previously mentioned, the strategy for dealing with the Levchuk effect will be to tune the optics to minimize this correction to as low a value as possible as well as comparing the simulation over a region of phase space where the Levchuk is predicted to dominate by a factor of a few allowing a precision test of this effect in simulation. The prescription for dealing with radiative corrections is well known and this correction can be precisely calculated. Effects from multiple scattering can also be rather precisely simulated if the target foil thickness is known and are not expected to be a significant source of uncertainty. Finally, as previously mentioned, the strategy for dealing with uncertainties in spectrometer acceptance is to tune the quadrupoles + dipole into a region of relative insensitivity to the precise details of the magnetic fields. This strategy has been utilized successfully in the PREX-2 experiment and is currently being implemented into CREX. Given these strategies a 0.2% uncertainty for the acceptance-averaged analyzing power (excluding the Levchuk correction) is believed to be achievable.

Measurement of DAQ deadtime is accomplished by taking dedicated and injecting a known rate of LED light pulses into the detector. The difference between the injected rate and the measured rate of LED pulses as a function of beam current provides a measure of the deadtime. The relative deadtime measured during PREX-2 on a 10 micron thick foil at 1 muA was 0.35%. Deadtime during MOLLER is not expected to be significantly different from this. Although deadtime is accurately measured, a conservative 0.1% error has been assigned to this for MOLLER.

In the current configuration accidental coincidences are measured and subtracted by measuring the apparent coincidences in a window that is time delayed by 100 ns. The time was chosen to be close enough to accurately measured the beam conditions as close to the Møller coincidence window as possible to avoid time dependence intrinsic to the accelerator but far enough to not overlap with truly correlated Møller events.

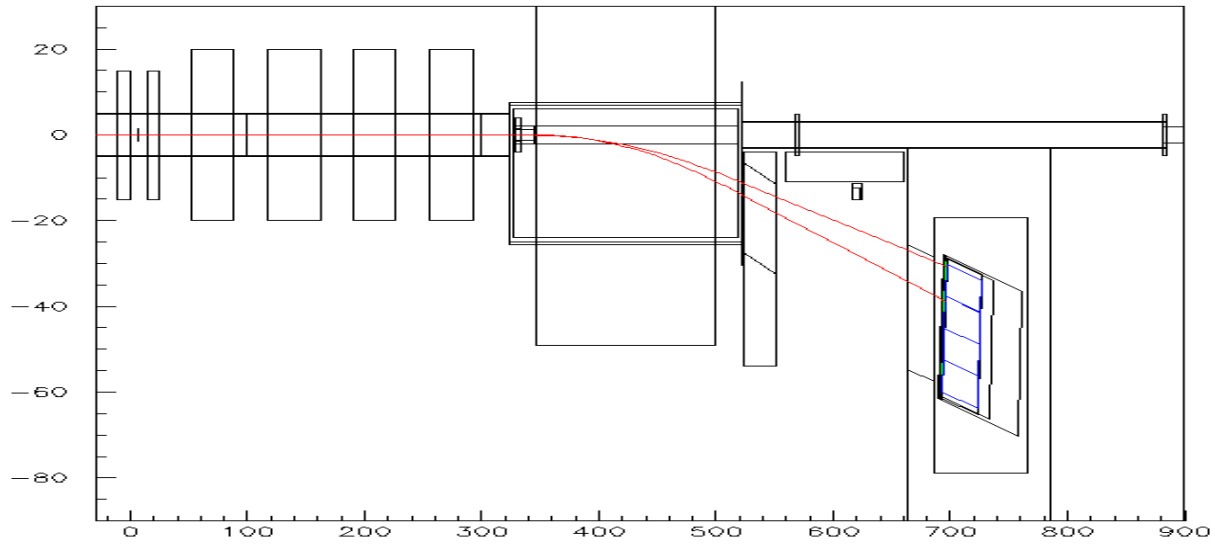

Figure 72: *Elevation view of the Hall A Møller polarimeter spectrometer, including a simulated pair of electrons from Møller scattering near* 90° *in the center of mass. The Fe target is shown near z=0 surrounded by the super-conducting Helmholtz coils. The four rectangles between z=60 and z=300 are the quadrupoles followed by the large dipole extending from z=340 to 500.*

Current procedures call for maintaining an accidental rate below 1%. Measurements of accidental-corrected asymmetry versus accidental rates far exceeding the percent level taken during PREX-2 showed no dependence on the accidental rate. Given these considerations, a 0.1% conservative upper limit for the accidental correction has been assigned.

Figure 72 shows the layout of the spectrometer in elevation view. The first two quadrupoles defocus in the horizontal plane, and the second two focus the ~ 5.5 GeV electrons so that they enter the dipole on parallel trajectories. They are bent downward into the detector array.

Upgrades for MOLLER. Two upgrades to the spectrometer are included in the MOLLER project that are expected to help reach the precision goals. One is to include a **GEM Tracking System** that allows us to accurately measure trajectories through the spectrometer. The GEMs will provide a precision knowledge of the position and angle distributions. These parameters depend on the spectrometer optics, radiative corrections, the Levchuk effect and multiple scattering and will provide a simulation calibration/benchmark that will allow us to reach and justify the precision goals for determining $\langle A_{zz} \rangle$. The second upgrade is to build and install a new **Scattered Electron Collimator** to define the acceptance rather than downstream elements such as the dipole faces and shielding that are not precisely known or well determined. Restricting the phase space, mainly in center of mass scattering angle, is also used to get a more precise determination of $\langle A_{zz} \rangle$ from simulation. Another upgrade that is currently underway, but not specified in the MOLLER project is a new FADC data acquisition system. This could be used with the current calorimeter detector to provide among other things, information on the energy of the electrons. Triggering readout in concert with GEMS would give electron energy, angle and position providing in principle a complete picture of the spectrometer optics that can be used to further reduce the uncertainty in $\langle A_{zz} \rangle$.

F.2.4 Systematic Uncertainties and Expected Performance

Table 24 shows the current and projected list of systematic errors for Møller polarimeters at Jefferson Lab.

Variable	Hall C	Hall A	
		Tilted	High Field
Target polarization*	0.25%	1.50%	0.27%
Target angle	‡	0.50%	0.10%
Analyzing power	0.24%	0.30%	0.20%
Levchuk effect	0.30%	0.20%	0.20%
Target temperature	0.05%	‡	0.10%
Dead time	‡	0.30%	0.10%
Background	‡	0.30%	0.10%
Others	0.10%	0.50%	0.10%
Total	0.47%	1.8%	0.45%

‡: Not Estimated

*includes magnetization and $g\prime$ contributions

Table 24: Systematic error summary for Møller polarimeters at JLab, including expected uncertainties for the Hall A High Field system to be used with MOLLER. The Hall C polarimeter [101] uses a high field pure iron target [102, 103] with a simple two-quadrupole spectrometer. The existing Hall A device [93] uses a tilted ferromagnetic alloy target, and a spectrometer with a dipole magnet following three quadrupoles. A high-field pure iron target upgrade is underway, with an additional quadrupole in the spectrometer for high energy operation.

The uncertainties for the Hall C Møller polarimeter are taken from [104]. The corresponding columns for Hall A are anticipated, based on previous experience with the Hall C system and anticipated performance of the apparatus. In summary, the target foil polarization systematics are unlikely to be reduced and depend upon ongoing research efforts that are expected to limit foil alignment uncertainties to the 0.1% level. Efforts going forward will be concentrated in understanding how to minimize sensitivity to $\langle A_{zz} \rangle$ including the Levchuk effect. Insights from PREX-2 provide confidence that this is achievable. The precision goals listed for each systematic explicitly listed in Table 24 including an extra 0.1% for those not explicitly included appear to be within reach.

G Target

Prototyping the MOLLER target cell is part of the scope of a DOE Early Career grant awarded in 2012 to Silviu Covrig Dusa. Silviu has setup a CFD Facility (CFDFAC) at Jefferson Lab. CFDFAC uses ANSYS-CFD on high performance computing (HPC). CFDFAC develops new technologies to design low noise targets for scattering experiments. CFDFAC has made low noise, high performance designs for the standard LH_2 targets in Halls A and C up to 30 cm in length. One such target design has been used by the DVCS/Gmp experiments that ran in Hall A after the 12 GeV upgrade of the CEBAF machine. The DVCS/Gmp target density reduction was almost an order of magnitude better than similar targets that ran during the 6 GeV era at Jefferson Lab. CFDFAC has driven the designs of the APEX and PREX2/CREX targets in Hall A. CFDFAC has been tasked to perform the thermal assessments for all current and future targets in Halls A and C, like the tritium target for MARATHON, the ^{40}Ar target and the ^{3}He polarized target.

G.1 Comparable Targets

Unpolarized LH_2 targets with internal heat dissipation of up to 1 kW have been successfully and safely run in the SAMPLE, HAPPEX, PVA4, G0 and SLAC E158 experiments. The LH_2 target for the Q_{weak} experiment is the first target in the world that has significantly exceeded 1 kW in internal heating.

Although these targets could not be more different in geometry and experimental conditions, they all have as a central part a cryogenic closed re-circulation loop, made of a thin-windowed cell traversed by the beam, a heat exchanger, an in-line pump and a high power heater. The central part of the cryogenic loop is the target cell as it is the region where the interaction between the target fluid and the electron beam takes place. The rest of the loop is designed around the cell to satisfy the requirements for cooling power and fluid flow. A summary of design parameters and target systematic effects for previous LH_2 targets used in parity

Table 25: *Liquid hydrogen targets for parity violation experiments. Summary of design parameters and operational experience where available. It puts in perspective the design parameters of the MOLLER target and its performance requirements.*

	p/T/$\dot{m}$	L	P/I	E	beam spot	$\Delta\rho/\rho$	$\delta\rho/\rho$
	psia/K/kg/s	cm	W/μA	GeV	mm	%	ppm
SAMPLE	25/20/0.6	40	700/40	0.2	2	1	<1000@60Ha
HAPPEX	26/19/0.1	25	1000/100	3.48	5x5		<100@30Hz
PVA4	25/17/0.13	10	250/20	0.854	0.1	0.1	392@50Hz
E158	21/20/1.8	150	700/11-12	45/48	1	1.5	<65@120Hz
G0	25/19/0.3	20	500/40-60	3	2x2	1.5	<238@30Hz
Q_{weak}	35/19/1	35	2500/180	1.165	4x4	0.8	<50@960Hz
MOLLER	35/20/1.8	125	4000/70	11	5x5	< 1	<30@1920Hz

violation experiments is presented in Table 25 for comparison. The quoted systematic effects for targets that have run before are the measured ones, where available, for the MOLLER target they are the design ones. The last two columns in Table 25 correspond to LH_2 density reduction and density fluctuation effects respectively.

In this respect the MOLLER target will have the same conceptual components as previous LH_2 targets. The target design will have to satisfy the detector acceptance requirements, and, more stringently for such a high luminosity and high precision experiment, the target density fluctuation that affect the physics measurement will have to be minimized.

G.2 Cell Design

There are three boiling regimes that can contribute to the target density fluctuation effect: nucleate, bubble and film boiling. Nucleate boiling could happen in sub-cooled liquids at low heat flux into the liquid, micro-bubbles could form, usually at boundaries, and recondensate as there is not enough heat to sustain bubble growth. If the heat flux into the liquid increases the liquid reaches saturation and bubble boiling is possible. Bubble boiling starts usually at boundaries, but in forced convection flow, bubbles could break from boundaries and the flow becomes 2-phase flow. If the heat flux into the liquid increases further then neighboring bubbles on a boundary can connect with each other forming a continuous film of vapor on that boundary, called film boiling.

The target density fluctuation effect is usually dominated by the target cell windows region. The heat density deposited by the electron beam in the thin Al windows is typically one order of magnitude higher than the heat density deposited in LH_2. The heat deposited by the beam in the window material is dissipated through conduction in the window material and convection on only one side of the window, the LH_2 side, as the other side is exposed to vacuum. The target liquid boils at a window with high probability if two partially correlated effects happen simultaneously: surpassing the critical heat flux and a temperature excursion between the window and the bulk liquid greater than a few tens of degrees. Typically for these targets the heat flux from the window to LH_2 is much higher than the critical heat flux for boiling. The critical heat flux for LH_2 at a wall is on the order of 10 W/cm^2 [36]. The total heat flux at the windows in nominal conditions is 43 W/cm^2 for the G0, 78 W/cm^2 for the Q_{weak} and 24 W/cm^2 for the MOLLER targets respectively. CFD simulations revealed that over the beam raster area the convective part of the total heat flux is 18 W/cm^2 for the G0 target and 33 W/cm^2 for the Q_{weak} target. The temperature excursions determined with CFD for the G0 and the Q_{weak} targets at the windows are on the order 30-50 K. The G0 and the Q_{weak} targets seem likely to develop liquid boiling at the windows. Of these three targets the MOLLER target has the lowest total heat flux at the windows and careful CFD design could decrease the convective part of the total heat flux below the boiling threshold.

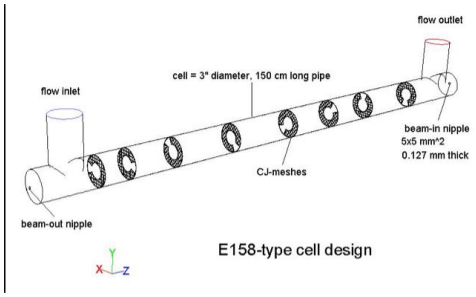

Figure 73: *CAD model of the original E158 target cell with meshes inside.*

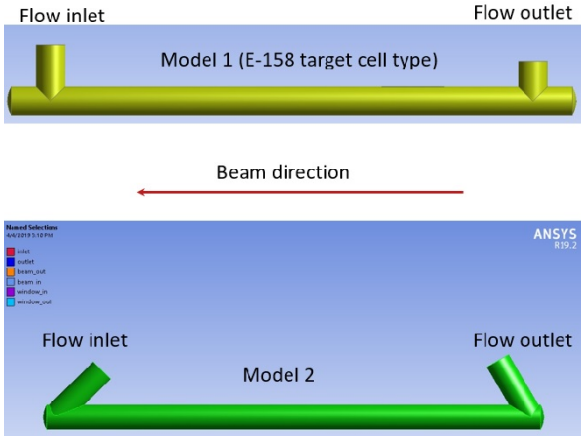

Figure 74: *CAD models for the MOLLER target cell that have been simulated with CFD.*

A 150 cm long cell was used in the 55 liter LH_2 target for the E158 Møller scattering experiment at

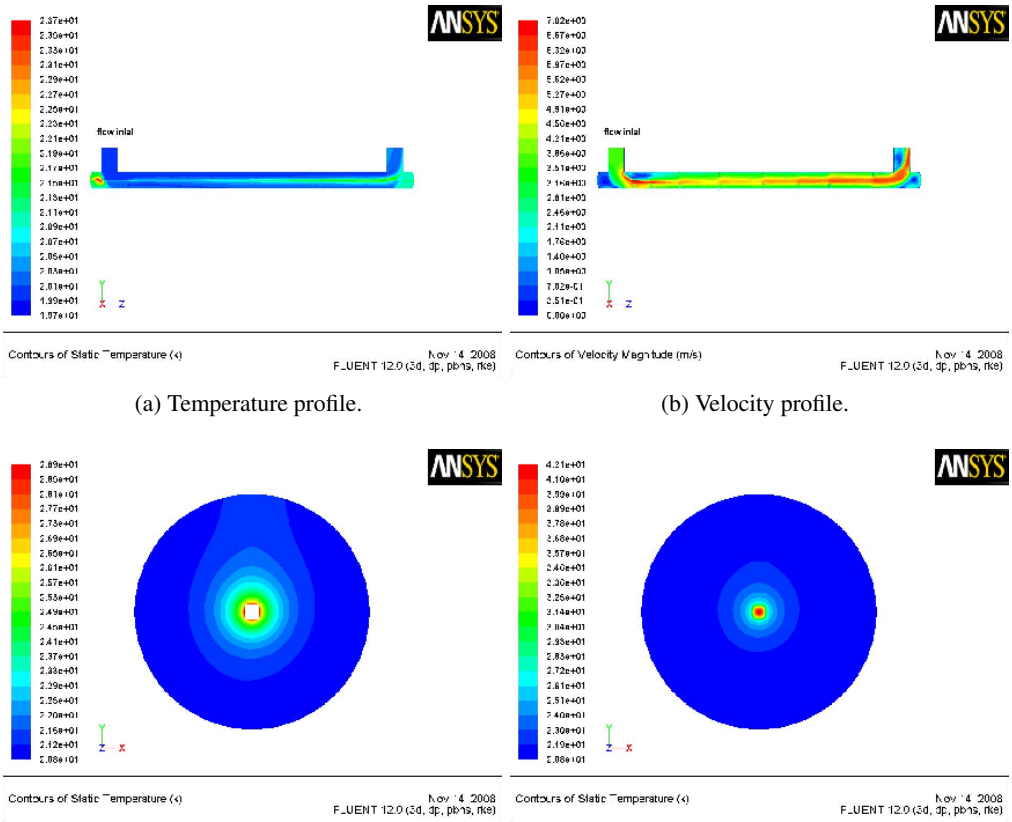

(a) Temperature profile.

(b) Velocity profile.

(c) Beam-out window without the 5x5 mm^2 electron beam envelope.

(d) Beam-out window with rastered beam envelope.

Figure 75: *CFD simulations of a E158-type cell in nominal MOLLER conditions.*

SLAC at 45 GeV and 48 GeV electron beam energies. The E158 target was rated for 700 W beam heating removal and 1000 W cooling power. The E158 target density fluctuation contributed 65 ppm [38] to a Møller detector asymmetry width of 200 ppm at a repetition rate of 120 Hz or about 5% of the detector asymmetry width. A drawing of the target cell for the E158 experiment is in Fig. 73. The cell is made of 3" ID pipe with a 3" inlet and outlet that are connected to the rest of the vertical cryogenic loop. Inside the target cell there are 8 wire mesh rings with a 45^o cut-out and 1.5" diameter clearance in the middle. The rings were meant to increase fluid turbulence and mixing in the cell. This cell geometry is a natural first candidate for a target cell for the MOLLER experiment. This type of cell with meshes and without meshes inside it was simulated with CFD in the MOLLER nominal conditions and it was found that the meshes have no effect on the LH_2 density reduction. Subsequently the E158 type cell geometry was considered without meshes inside it in designing the MOLLER target cell. Fig. 74 shows two MOLLER cell geometries that have been simulated with CFD. Model 1 is a E158 type cell without meshes inside it and Model 2 is a similar geometry that aims to eliminate the potential dead flow space between the cell beam windows and its flow inlet and outlet respectively. In the CFD simulations the heating from the electron beam was implemented as a uniform power deposition in the volume of the cell illuminated by the rastered beam. The cell walls are made of Al and the beam heating in the windows was implemented also as a uniform power deposition in them. Hydrogen properties were implemented as functions of temperature in isobaric conditions from the freezing point to 300 K. The boiling model used in CFD simulations was evaporation-condensation, which accounts for the phase transition at saturation with the appropriate latent heat parameter.

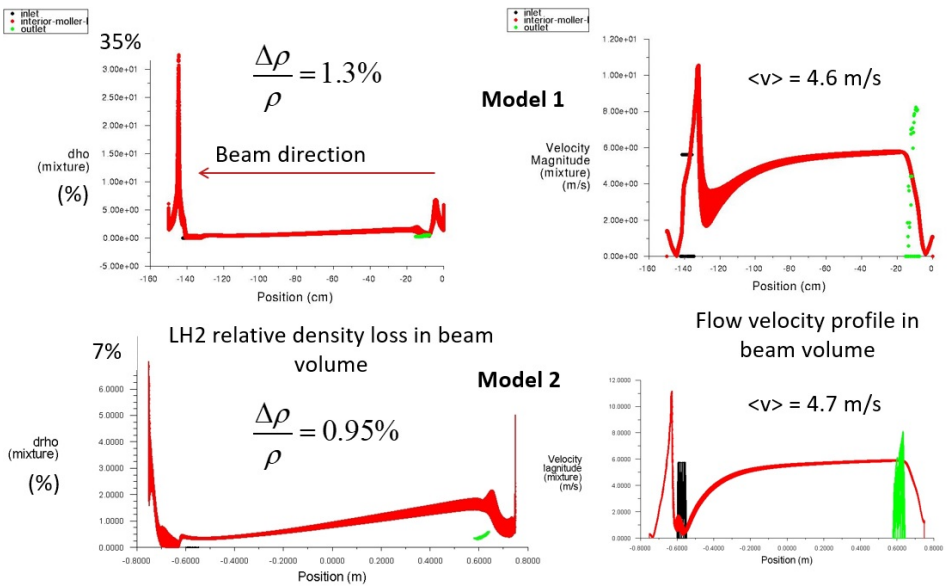

Figure 76: *Models 1 and 2 profiles of LH_2 density loss and flow velocity in the cell along the electron beam direction predicted with CFD. Values from the beam illuminated volume in the models are in red, in black and green are values from the LH_2 flow inlet and outlet respectively to the models, as shown in fig. 74.*

The results from figs. 75a-75d are for the E158 type cell with internal meshes. The global temperature increase of the LH_2 between the inlet and the outlet to the cell is 0.37 K but the average over the beam volume is 1.23 K, which yields a LH_2 density reduction of 2% for a LH_2 flow rate of 1.1 kg/s (the Q_{weak} target flow rate). The temperature averaged over the cell windows' beam nipples is 30.1 K for the beam-in window and 34.8 K for the beam-out window. The convective heat flux, predicted with CFD, from the window nipples to LH_2 is 4 W/cm^2 for beam-in and 8 W/cm^2 for beam-out respectively, which are both less then the critical heat flux for LH_2 boiling [36]. Although the cell geometry is symmetrical between the inlet and outlet the flow near the end caps of the cell is not. The cap at the inlet (with the beam-out window) experiences a large vortex with very little flow in the middle, where the liquid is boiling. This cell design has been refined to get rid of the bulk liquid boiling, yielding Model 2.

A comparison between Models 1 and 2 is shown in fig. 76, assuming the nominal MOLLER LH_2 flow rate of 1.8 kg/s. The potential LH_2 boiling regions in the endcaps of Model 1 have been eliminated in Model 2, though the flow velocity profile in the beam illuminated volume in both models is essentially the same. While Model 1 (E158 type cell without meshes) has a predicted density reduction 30% above the design value, Model 2 is predicted to be below the design value of 1%.

G.3 Summary of Q_{weak} Target Performance

The Q_{weak} target is considered to be the precursor for the MOLLER target design. This section reviews what has been learned from the Q_{weak} target experience. The Q_{weak} target was the first one designed with CFD at Jefferson Lab. The CFD software engine used was `FLUENT` developed by Fluent Inc. (now part of ANSYS, Inc). The 35 cm long Q_{weak} target was commissioned in 2010 and the measured performance indicates that its design goals have been met. The target has been successfully operated with 3 kW of cooling power. It has been run at beam currents between 150 and 180 μA. The target density fluctuation contribution to the asymmetry width has been measured using several techniques. Fig. 77 shows the measured target density fluctuation noise versus beam current at a smaller than nominal beam raster area. In nominal running

conditions, 180 μA beam current, 30 Hz LH_2 pump rotation, 4x4 mm^2 beam rastered spot on the target cell and 960 Hz helicity frequency, the measured target density fluctuation was 46 ppm and its design value was bound at 50 ppm. The counting statistics for the Q_{weak} asymmetry in quartets of beam helicity states was measured to be 200 ppm. In nominal running conditions the target noise increased the asymmetry width by less than 3%. The bulk LH_2 density reduction has also been bounded to 0.8% at 180 μA, which is the same as the CFD predicted one. This should be compared with the performance of the standard pivot 15 cm machined LH_2 cells during the 6 GeV era at JLAB, for which the density reduction at 100 μA has been measured to be at the level of 20%. Although the design raster size for the Q_{weak} target was 4x4 mm^2, the target's performance was so good that it was operated routinely at 150 μA with a raster size of only 3.0x3.0 mm^2. The data accumulated with the Q_{weak} target will be used to benchmark the CFD simulations for the MOLLER target, thus reducing technical risk.

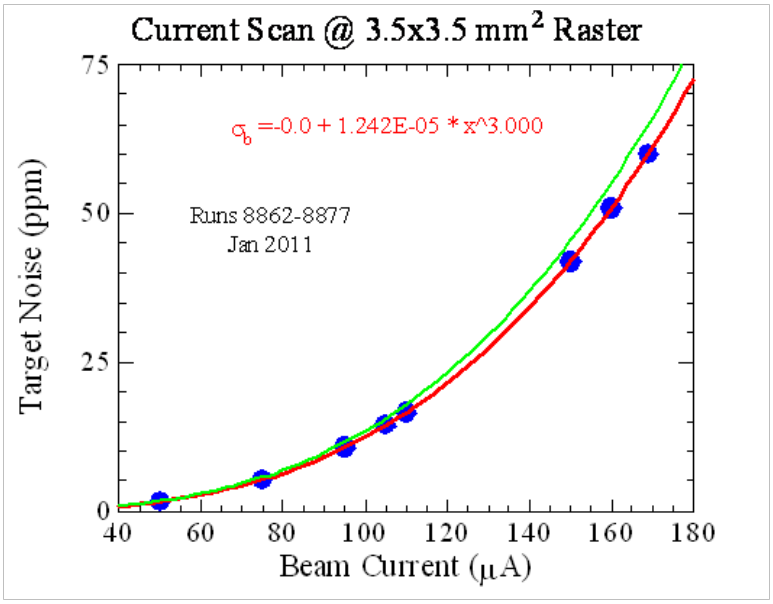

Figure 77: Q_{weak} *target performance: density fluctuation width versus beam current from* Q_{weak} *measurements. The blue points are measured data. The red curve is a fit to the data. The green curve is another fit, providing a measure of the uncertainties.*

CFD was used in almost all aspects of the design of the Q_{weak} target. It was used to tailor the cell fluid space in order to optimize the flow, temperature and density profiles across the beam axis in the hydrogen volume as well as at the cell windows. These simulations were used to fix the mass flow required of the target, one of the most crucial design parameters. The pressure head represented by the complicated cell shape was derived by CFD. Analytic calculations for the Q_{weak} target's heater and some aspects of the heat exchanger were checked with CFD simulations. CFD simulations fixed the raster size required for the target and helped us design strategies for various off-normal events. In many respects the novel design which emerged was considered a bit of a gamble, given that CFD was not a proven tool for target design at the time. The fact that the Q_{weak} target has achieved all of its design goals validates the use of CFD as a design tool for targets.

The matrix of 24 solid targets that are part of the Q_{weak} experiment were also designed with CFD. The relationship between temperatures at the center of each target to thermometry scattered around the solid target frame was studied with CFD. Knowing how high these thermometers can safely go, by virtue of the CFD calculations, has made it possible to put more beam current on our solid targets than has ever been

done before at JLAB. The $\mathrm{Q}_{\mathrm{weak}}$ target performance also shows that its heat exchanger design process was correct. Note that the $\mathrm{Q}_{\mathrm{weak}}$ heat exchanger is a completely novel design which combines a 4 K and a 15 K heat exchanger using overlapping heat exchanger coils in the same shell. It also shows that the high power heater design and fabrication process was correct. The 3 kW heater performance was unmatched. When beam trips occur, or beam is restored to full current, the typical temperature excursions in the target loop are less than 0.1 K.

The pressure head predicted for the $\mathrm{Q}_{\mathrm{weak}}$ target at the design mass flow of 1.1 kg/s was 1.2 psi. The head measured with the $\mathrm{Q}_{\mathrm{weak}}$ target at this massflow is 1.1 psi, in amazingly good agreement with the prediction considering how very difficult it is to calculate this parameter. The fact that the required massflow and pressure head were achieved for the $\mathrm{Q}_{\mathrm{weak}}$ target also validates the pump design and commissioning process before beam. Problems have been encountered with the $\mathrm{Q}_{\mathrm{weak}}$ pump bearings early into the first run. After repairs were done the pump worked flawlessly over two years. The basic deliverables of the pump (head and massflow) have been achieved at the required values.

$\mathrm{Q}_{\mathrm{weak}}$ initiated the use of faster helicity reversal as a tool to mitigate the effects of target noise on the experiment. Fast Fourier transforms acquired under a wide variety of conditions during the $\mathrm{Q}_{\mathrm{weak}}$ experiment's commissioning phase show that this is an important and effective tool for reaching the goals of the experiment, and its effectiveness for the MOLLER experiment is now also validated.

To summarize: the $\mathrm{Q}_{\mathrm{weak}}$ target employed a large number of novel and highly unusual ideas to meet its goals and every single one of these new ideas has worked. This greatly reduces the risk associated with the extensions needed for the MOLLER target. The expected performance in terms of the density fluctuation should meet the MOLLER requirements. The cooling power needed for the target will be delivered by the ESR2, which is part of JLab's upgrade of its cooling capacity infrastructure in the 12 GeV era for the experimental halls.

H Spectrometer

This appendix contains additional information about the spectrometer system, including descriptions of a phase space study, the effect of stray fields in the magnets, and the sensitivity study from which the position tolerances for the magnets are derived. It also includes information about additional magnet properties, including magnetic force calculations, 50 G limits, the effect of power leads, dose calculations, and additional plots for alternatives discussed in the main text. There is an example Pugh matrix, which is a tool used by the spectrometer group to assist in choosing between alternative designs. Appendix I has more information about tolerances and alignment, including the collimators and magnets.

H.1 Phase space study

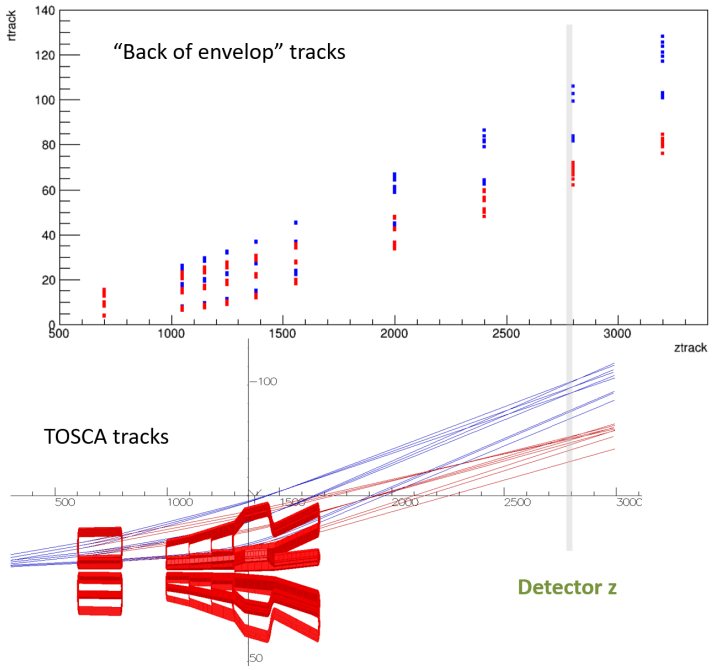

Figure 78: *Comparison of the phase space study (back of the envelope, top) and the tracks from TOSCA.*

The phase space for the design of the spectrometer system is large. In order to explore the phase space in an efficient manner, a "back of the envelope" calculation was performed. The optics can be approximated rather well (see Fg. 78) by calculating the change in the bend angle (kick) given to the particles at the central z location of each section, given by

$$\alpha[\mathrm{rad}] = \frac{\int \vec{B} \cdot d\vec{\ell}[\mathrm{Tm}]}{3.33E[\mathrm{GeV}]} \tag{13}$$

using the $B = B_\phi$ component of the field at the center of an open section in each of the magnet sections. The kicks from each of the magnet sections are combined and the radius of particles of different energies at the detector plane is calculated. The RMS of the radii of the correct range of energies for both moller and elastic electrons serves as a proxy for their foci and the separation is the difference in the radius of the lowest moller and highest elastic electron. The moller and elastic focii should be minimized; the separation between the respective peaks should be maximized. The results of the phase space study show that we are

not at the optimal optics of this magnet system because we are limited by the maximum current density in the coils, the length of the hall, and the need to leave half the azimuth completely open to maximize the azimuthal acceptance (see Section 6.1.2).

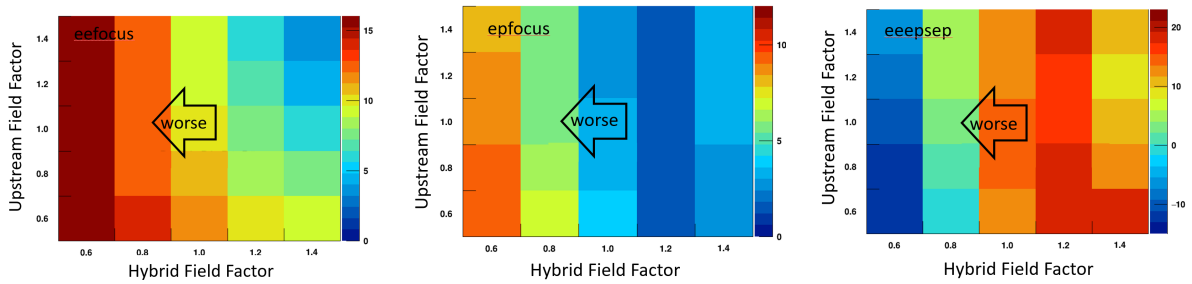

Figure 79: *Results of the phase space study for different factors on the the total current in the upstream and downstream ("hybrid") magnets. These plots are for the variation of the "focii" of the mollers (a) and elastics (b). The separation "eeepsep" is also shown (c).*

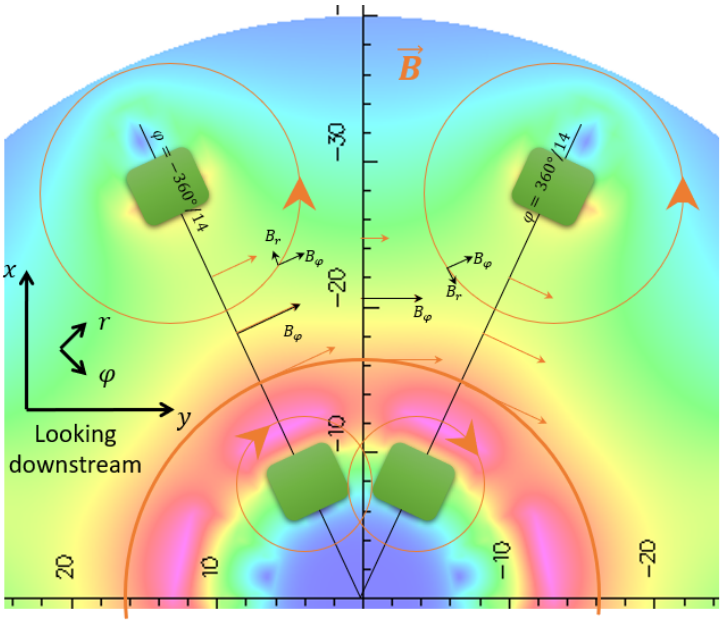

Figure 80: *Fields in open septant. The cross-section of the adjacent coils is shown as green blocks. The contour plot shows the relative strength of the radially focusing component of the field, B_ϕ.*

At the very center of the septant the field is all in the azimuthal (ϕ) direction, but is a lower value than in the center of the closed section. For an ideal torus, the ϕ component of the field would be constant as a function of ϕ, the fields would depend only on radius. For a real toroid, the fields vary as a function of r, z and ϕ throughout the septant as shown in Fig. 80. The radial component of the field, B_r results in the ϕ de-focusing seen in the Møller envelopes (see Fig. 29). This de-focussing occurs when the electrons pass between the outer radius part of the coils, and actually helps to reduce the rate per unit area on the individual quartz detectors. Between the inner radius part of the coils, the electrons are focused, due to the

sign reversal of B_r. This focusing is necessary for the electron envelopes to fit between the inner radius part of the upstream end of the downstream torus.

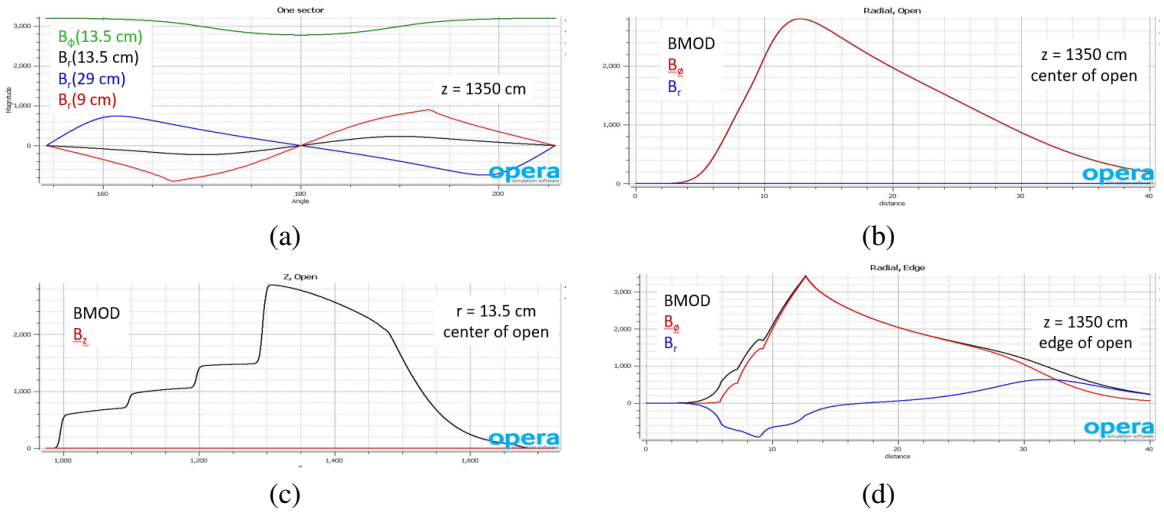

Figure 81: *Plots of the variation of the field components for selected* $r = 13.5cm, z = 1350cm$ *and* $\phi = 0$*, unless otherwise noted. The plot of* B_ϕ *as a function of* ϕ *is shown in green, with the* B_r *for several radii (a). The total field, BMOD, and the* r *and* ϕ *components are shown in (b). The* z*-component is shown in (c). BMOD,* r *and* ϕ *components at the edge of an open sector are shown in (d).*

The calculations described as part of the phase space study include only the radially-focusing component of the field, B_ϕ, at the center of an open septant, $\phi = 0$ at discrete z values. Representative plots of the field variations from a TOSCA model with a "blocky model" of a realistic conductor layout are shown in Fig. 81. The plot of B_ϕ as a function of ϕ for z=1350cm (near the middle of the downstream torus) and a radius of 13.5 cm (just outside the radius of the inner radius part of the coils) is shown in the upper left plot of Fig. 81. It is possible to see the decrease in field in the center of the septant. The ϕ de-focusing component of the field, B_r for several radii (same z) is also shown; the reversal of the sign from inner to outer radius can be seen. Plots of BMOD as functions of r and z at the center of an open section ($\phi = 0$ are shown in (b) and (c) respectively, and of BMOD, B_r and B_ϕ at the edge of an open septant in (d). From these plots you can see the characteristic toroidal dependence of the field on radius, which increases to a maximum where all of the current is contained within that radius, and then drops off. The variation of the field with z is due to the optimized fields as a function of z, and the four different current return paths as described in Section 6.2.1.

H.2 Stray Fields

In order to ensure "2-bounces" are necessary for target photons to get to the detectors, the beam shielding tubes must be placed inside the coils between collimators 2 and 4 and at the upstream end of the downstream coil. Fig. 82 shows the result of the "2-bounce" code for the configuration without the beam shielding tubes in place. The detectors are able to "see" surfaces that have direct line-of-sight to the target. The green on the detectors is eliminated when the tubes are in place.

It is necessary to ensure that the spectrometer enclosures and supports and the beampipes do not intersect the scattered electrons (moller or elastic) or the inner and outer photon envelopes. To define the "keep-out" zones, a set of envelopes is created using the GEANT4 simulation and provided to the engineers in a format that they can import directly into their CAD models (see Fig. 83). In this figure the tube at the outer radius

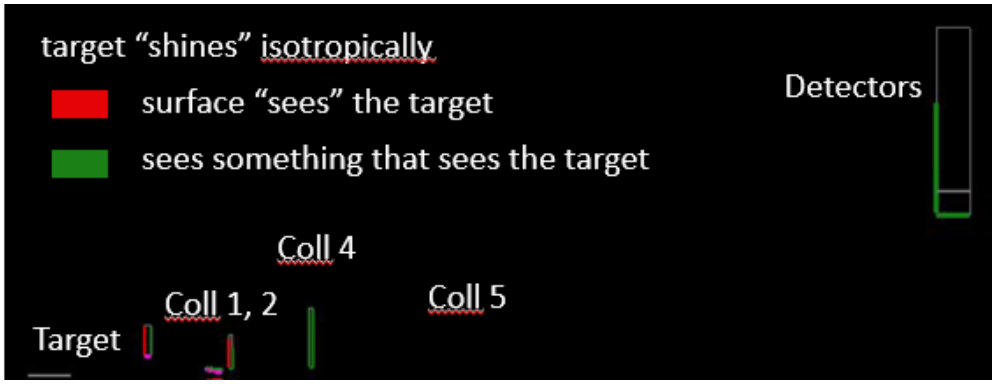

Figure 82: *Results of "2-bounce" code with no beam shielding tubes. In this code the target shines isotropically, and anything that sees the target is indicated in red. Surfaces that see red areas are indicated in green. In this case the detectors are seeing surfaces with direct line-of-sight to the target.*

is interfering with the moller envelope, and was subsequently changed. In the vacuum configuration there is no inner beampipe like the one shown between the inner and outer photon envelopes. The vacuum enclosure would have a radius to be larger than the outer radius of the moller envelope. Downstream of the enclosure, in the detector region, the beam pipe would easily fit outside the outer photon envelop and inside the elastic peak (not shown). However, in the helium case, that inner beampipe is necessary, and must fit between the inner and outer photon envelopes.

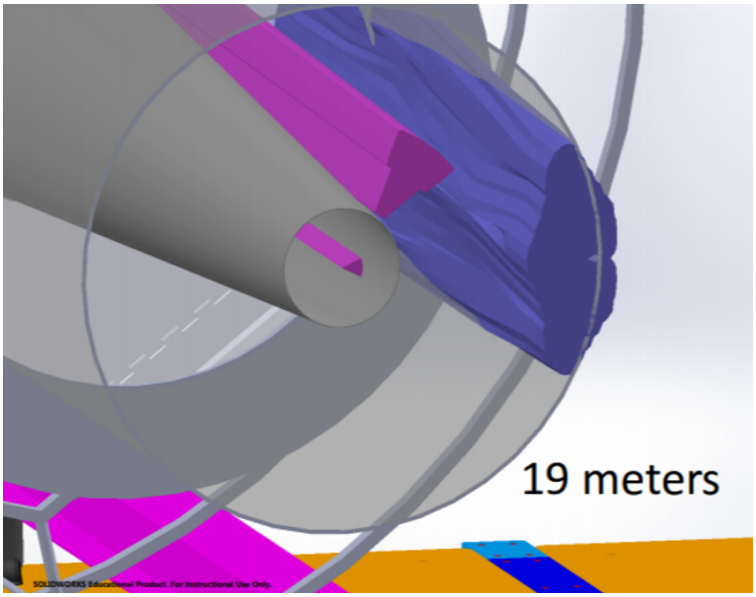

Figure 83: *Example showing the inner and outer photon envelopes (magenta) and the moller envelope (indigo) in single septants (not the same septant) at the end of the hybrid torus.*

In the helium configuration, even with no interference with the photon envelopes, there is significant background created all along the inner beampipe. Charged particles which lose a small amount of energy and/or multiple scatter in the target and which would otherwise be transported cleanly to the dump can be deflected by the stray fields in the magnets. These stray fields exist even in the case of symmetric coils (see

Fig. 84). These fields are small, and don't have much effect on the highest energy electrons, or electrons with very small angles (see top plot in Fig. 86). However, at larger angles even medium energy tracks can start to be deflected by these stray fields. The lowest energy tracks are swept completely away into the beam shielding tubes. The beam shielding tubes will be optimized to shield more of the tracks with medium energy and larger angles. In the vacuum case this will be very effective; the background from these types of events is already low. In the helium case, because of the central beampipe, it would be necessary to shield that whole inner beampipe.

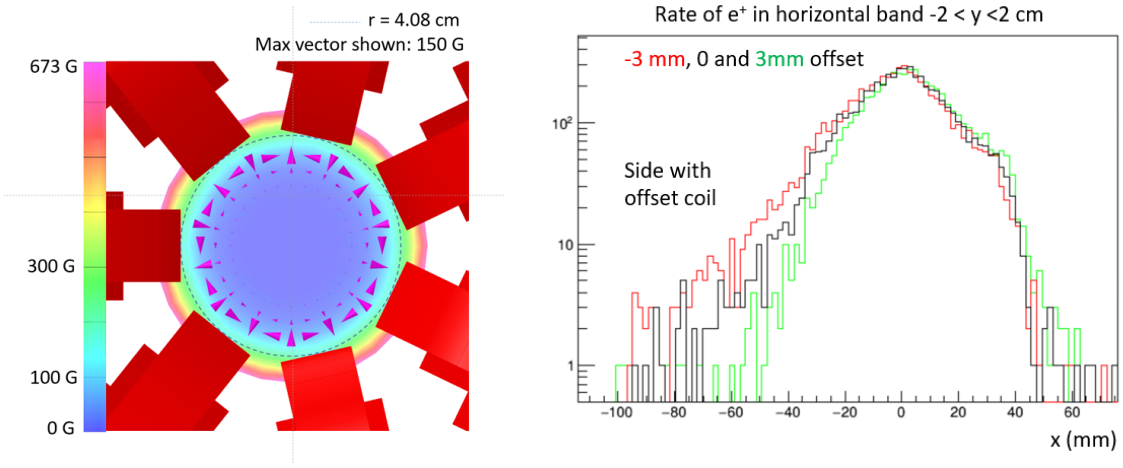

(a) (b)

Figure 84: *(a) Vector and contour plots of the total field in the center of the downstream torus, for symmetric coils. (b) Distortion in the positron distribution in a horizontal band at the end of the hall when the horizontal coil is offset radially ± 3mm, or the stated radial offset tolerance for the coil based on sensitivity studies.*

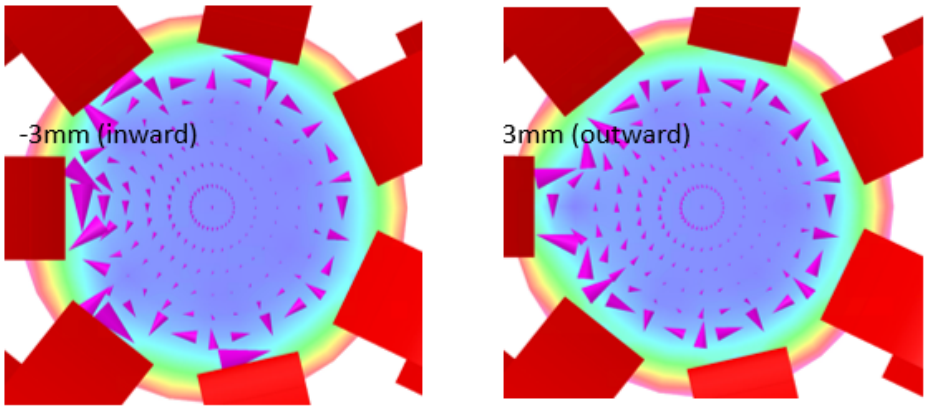

Figure 85: *Vector and contour plots of the total field in the center of the downstream torus for the case with the horizontal coil offset by 3 mm inward (left) and 3 mm outward (right).*

The effect of coil offsets on the stray fields was studied for the vacuum case. The fields for coils with the horizontal coil offset radially by ± 3 mm are shown in Fig. 85. The effect of offsetting this coil is very small.

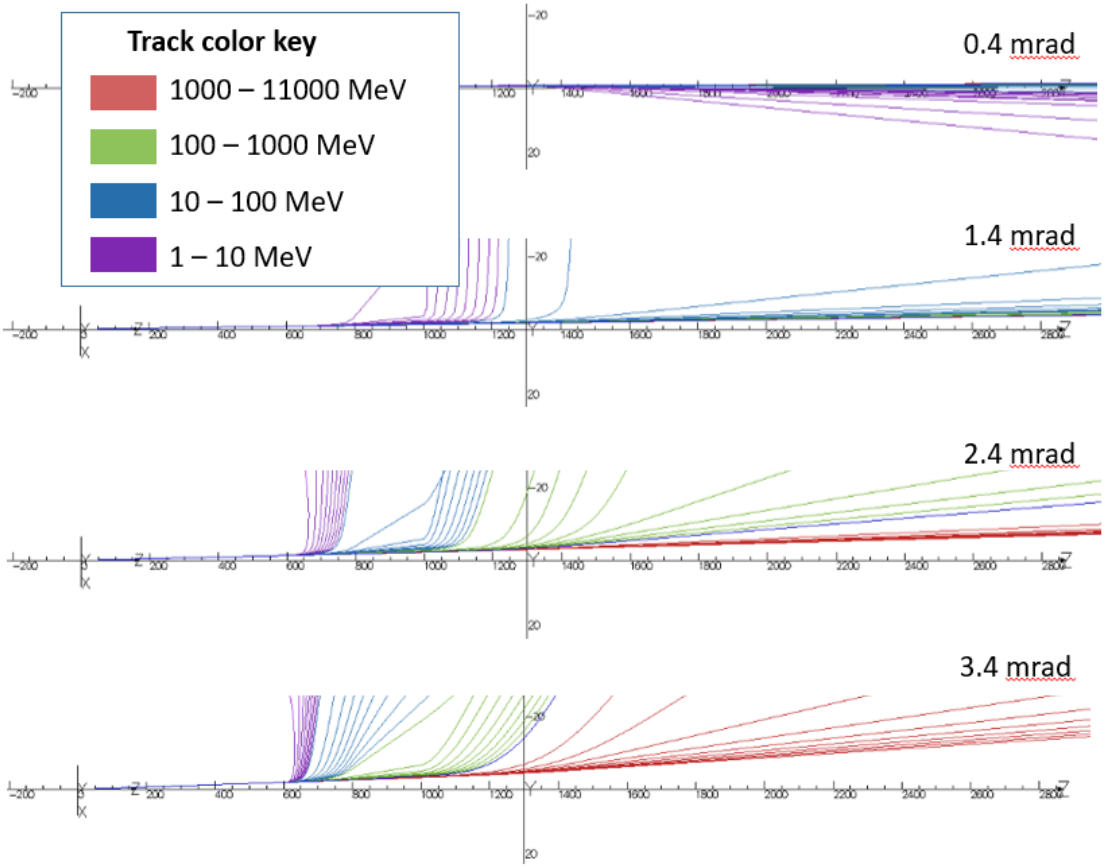

Figure 86: Electron tracks for different energy ranges and scattering angles in TOSCA. These angles are for particles that would otherwise be transported cleanly to the dump.

It was most clearly seen in the case of the horizontal deflection of positrons, which is shown in the right of Fig. 84. The additional deflection resulting from the coil being offset is still small, and mostly affects the tails. It is estimated to be $\mp$ 2 cm at the entrance to the dump. This can be taken into account by leaving appropriate clearances when optimizing the beamline and shielding in the vacuum case.

H.3 Sensitivity studies

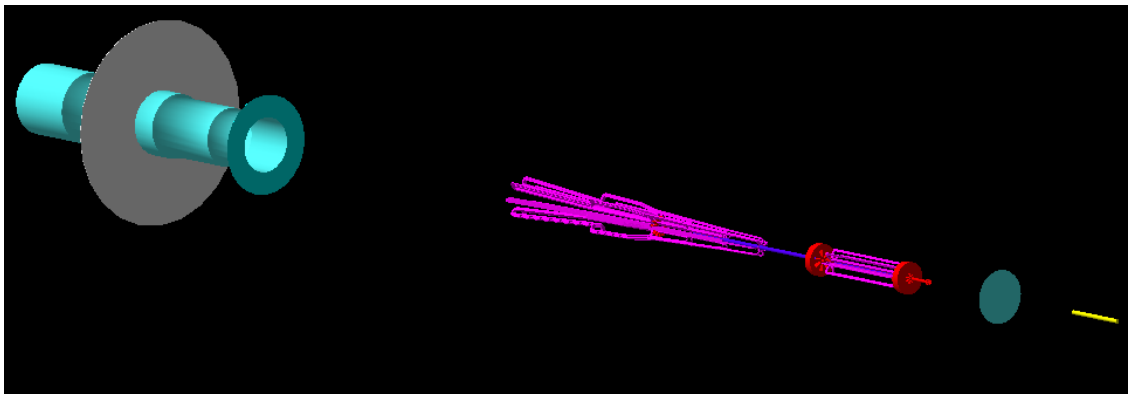

Figure 87: *The simulation geometry in the GEANT4 GDML, with the shielding and enclosures hidden so one can see the collimators and coils. Aluminum windows and beampipe are shown in cyan and the hydrogen is shown as yellow. The collimators (CuW alloy) are red, blue is W beam-shield, and the copper of the magnet coils is shown in magenta.*

In order to determine the position tolerances, the sensitivity to offsets of a single coil in six directions are simulated in GEANT4 (see Fig. 87). Field maps corresponding to a single coil being offset radially, along the beamline, or rotated azimuthally (r, z, and θ, respectively) and for rotations about the center of mass of the coil in roll, pitch and yaw (see Fig. 88) were produced. Each offset type had 11 steps, 5 below and 5 above the nominal, symmetric positions and orientations, resulting in a total of 66 total field maps. These field maps were imported into the GEANT4 simulation. Møller tracks are generated for each step of each offset, and the distributions of the peak at the detector plane are compared. The tolerances are determined by multiplying the inverse of the slope of the mean asymmetry vs. offset step value (determined without optimizing the detector definitions) by the allowed uncertainty in the asymmetry, $\delta A \sim 0.1\mathrm{ppb}$, or

$$\Delta(x_i) = \delta A \left(\frac{\partial A}{\partial x_i} \right)^{-1} \tag{14}$$

The tolerances determined in the study are summarized in table 26. It should be noted that if we know about an offset and can include it in our simulation then we are actually insensitive to position and orientation offsets to first order. The sensitivity comes in is if there is a completely unknown offset which is not properly accounted for in the simulation. This will affect our ability to de-convolute the asymmetries of the backgrounds and the Møller signal. The sensitivity of the downstream magnet can be improved by adjusting the relative position of the inner radial edges of the quartz in the moller ring.

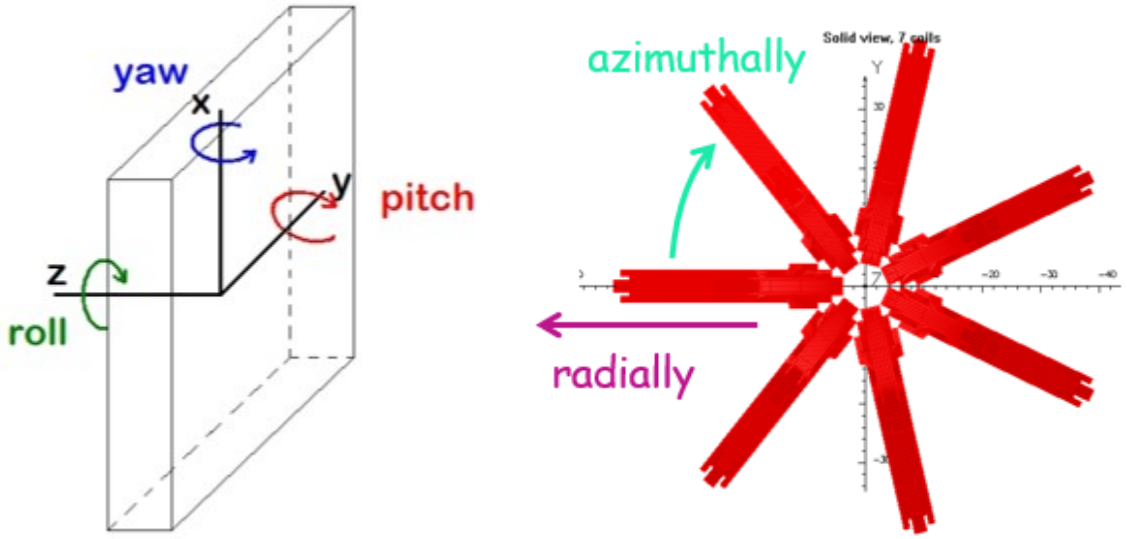

(a) (b)

Figure 88: *Sensitivity study coordinates: (a) Diagram showing the definition of the rotations. (b)View of the downstream toroid, looking downstream, with the ratial and azimuthal offsets indicated; z offsets would be into or out of the page.*

Table 26: *Summary of the tolerances for coil offsets as determined in the single coil offset sensitivity study. Note that 0.3 degrees over a rotation in azimuth of a coil results in an offset of about 2 mm of the outer radius of the coil.*

Direction	Tolerance (mm or degrees)	
	US magnet	DS magnet
r	20	2
z	130	54
θ	6.5	0.4
roll	2.0	0.8
pitch	1.9	0.3
yaw	8.8	0.7

Table 27: *Results of the magnetic force study. The forces shown are those on the horizontal coil, or on the positive x axis.*

Configuration	Part of Coil	F_x (lbs)	F_y (lbs)	F_z (lbs)
symmetric	Inner	-4111	0	120
	Returns	2013	0	-31
	Outer	214	0	-98
	Total	-1884	0	-9
horizontal coil off	Inner	-3304	-711	98
	Returns	1723	-237	-28
	Outer	182	-63	-80
	Total	-1399	-1011	-10

H.4 Additional magnet properties

In addition to the studies described above, estimates of the magnetic forces on different parts of the coil, the field extent (reported as 50 G limits), the effect of power leads on the field and doses on the coils have been estimated.

H.4.1 Magnetic forces

The magnetic forces on the coils of a symmetric toroidal magnet tend to pull the individual coils into a circular shape, and to pull the coils toward the center of the torus ("centering force"). The magnetic forces for symmetric coils have been modeled in TOSCA, and a summary of the results for the forces on the horizontal coil (where x is the same as the radial direction) is given in Table 27. The centering force is evident in the large force (-4111 lbs) in the negative x direction on the inner radius part of the coil, and the much smaller force (214 lbs) in the positive x direction on the outer radius part of the coil. These forces also tend to pull the coil into a circular shape. For the symmetric coils, there was no force in the y (or azimuthal direction). In the case of non-symmetric coils, an additional force tends to collapse the coils in the azimuthal y direction. The forces for this case have been bound by looking at an extreme case where the current density in the horizontal coil was set to zero (see bottom portion of Table 27). This will not actually be possible in reality because the subcoils are connected in seriess. These values serve as an extreme upper bound on the possible magnetic forces. In order to calculate the net forces in the summary table, the force per unit length on each segment of the downstream torus was calculated in TOSCA. These values have been provided to the engineers to be included in their FEA studies of the coil deflections.

H.4.2 Extent of the fields

The field outside of the downstream magnet could adversely affect the optics of the experiment and present a potential hazard if too high. An upper limit for the extent of the high field region was estimated by drawing

the 50 G limits for a single downstream coil (see Fig. 89). The field drops below 50 G within about 25 cm of the perimeter of the coil, which is inside the radius of the strongbacks and the enclosure.

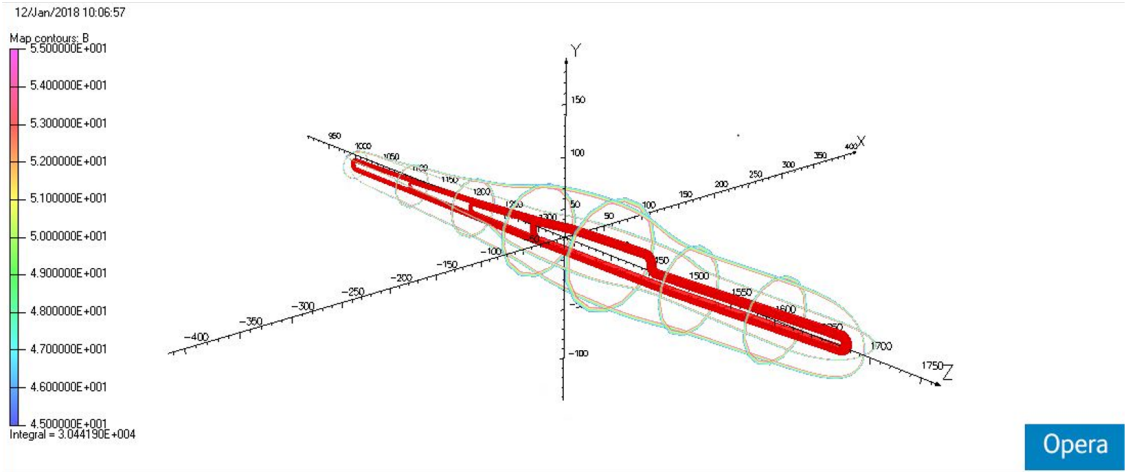

Figure 89: *Single coil 50 G limits, indicated by contour plots for 45-55 G.*

H.4.3 Effect of Power Leads

The effect of the power leads was bound by simulating solenoids without counter-winding (see Fig. 90). These solenoids had the same conductor cross-section and current for each section of the magnets (including the upstream magnet). There was essentially no effect on the scattered electron envelopes. In addition, these power leads will actually be counter-wound in order to cancel the fields.

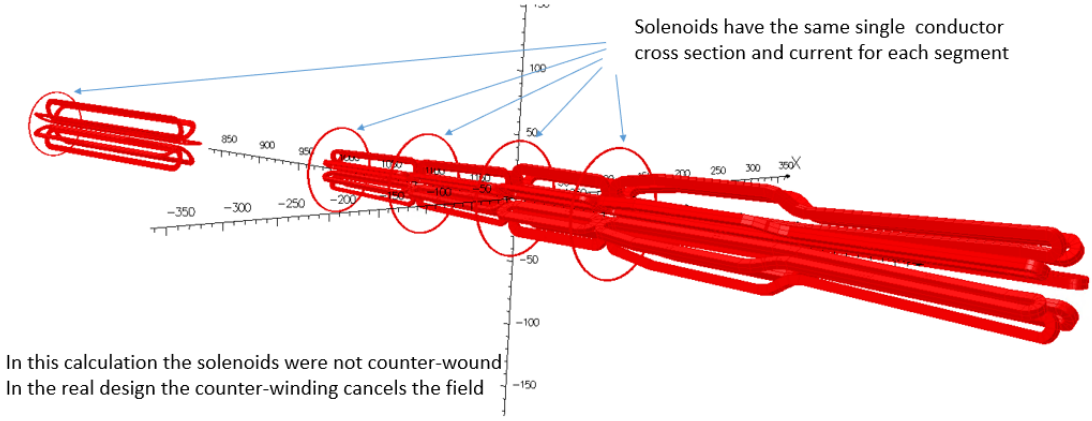

Figure 90: *Configuration used to estimate the worst-case effect of the power leads on the magnetic fields.*

H.4.4 Dose on coils

The power on the coils is important due to the effects on the water-cooling estimates, as well as the rad-hardness of the epoxy and other materials in the coil package. The incident power on the torus coils has

been determined as a function of radius and z in 1 cm^2 pixels (see Fig. 91). These values are the total over all 7 coils and around the azimuth; this can be translated to a power per volume by dividing by 7$\times$ the coil thickness. These values provided an upper limit on the power deposited in the coils, which can be included in the water-cooling calculations. It is also used to estimate the dose on the epoxy. The estimated dose on the hot spot on upstream torus coils (86 mW/cm^2), assuming 334 days at 60 μA is 61 MGy. The dose for most of the rest of the coils is 20 MGy. For the downstream torus coils (0.86 mW/cm^2) there is a smaller dose of 0.61 MGy. Note that this incident power is significantly higher in the helium configuration, due to the presence of the central beampipe.

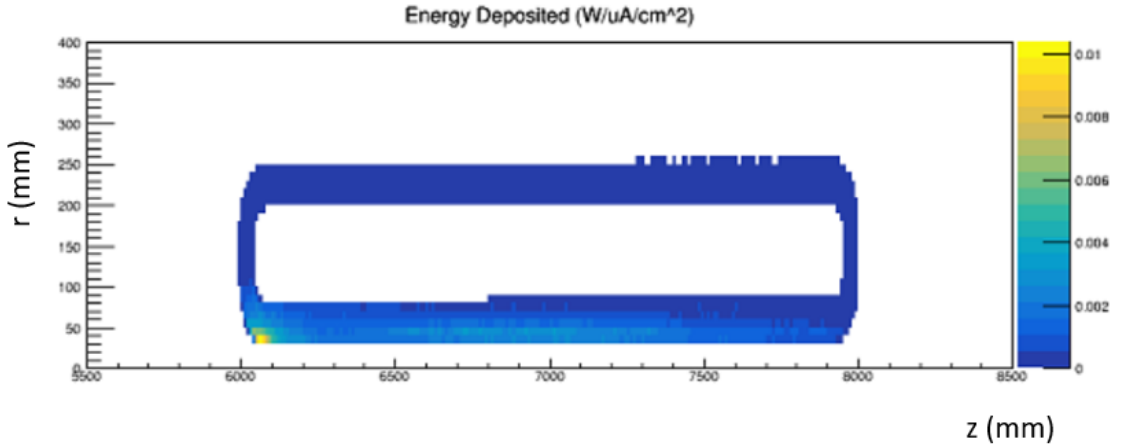

(a)

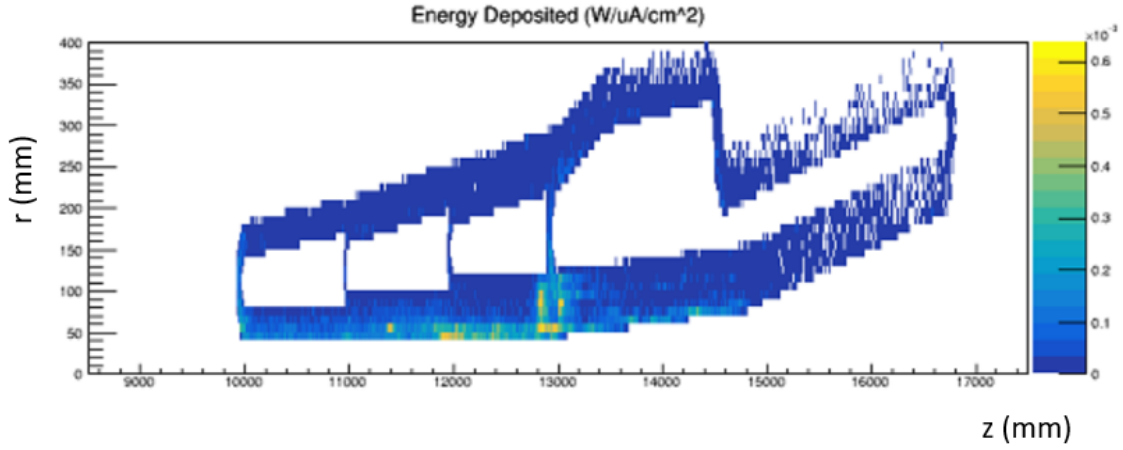

(b)

Figure 91: *Total incident power per μA on the upstream (a) and downstream (b) coils in 1 cm^2 pixels. The maximum incident power in the upstream torus is 0.01 $W/\mu A/cm^2$, and 0.007 $W/\mu A/cm^2$ on the downstream torus.*

The dose estimates are being refined with a more sophisticated coil model in GEANT4 which includes layers of epoxy and copper. However, given the above values as an upper limit, and taking into account the effect on the shear strength, an appropriate epoxy, CTD-403 has been selected (see Fig. 92). The approximate doses for the hot spots of the upstream and downstream toroids is shown on the plot. The chosen epoxy has a high shear strength, and shows less than approximately 15% reduction for the estimated upper

limit of the dose on the upstream toroid. Although the shear strength data shown in Fig. 92 were obtained at 77 K, it is very likely that this is still the most suitable impregnation resin to use for the magnet coils, as the strength appears to drop only by about 15%.

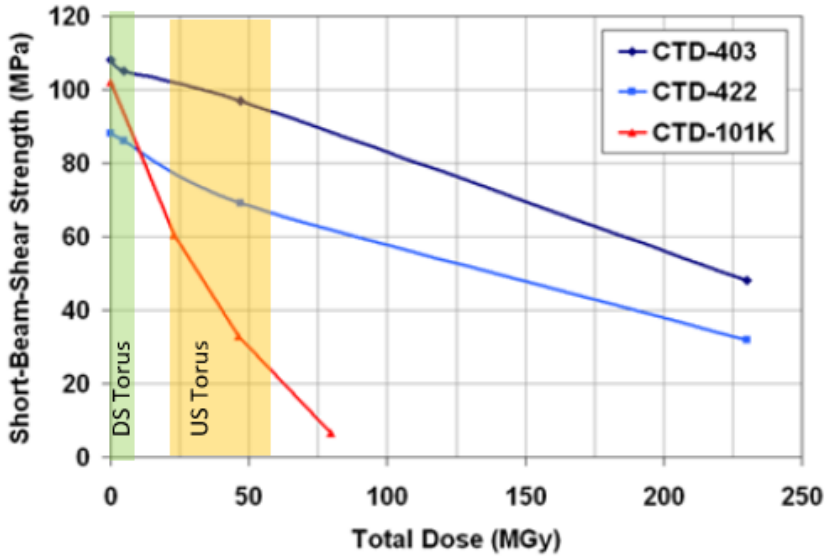

Figure 92: *Plot of the change in shear stress for integrated dose for three different epoxy resins. The ranges of estimated dose for the upstream and downstream toroid are shaded (yellow and green, respectively). Figure modified, original is from [41].*

H.5 Additional information on alternatives

Alternative designs for the coils in the downstream toroid, as well as the supports and enclosures were discussed in the main text. Some additional information is provided here in the form of plots and CAD pictures.

H.5.1 MIT prototype

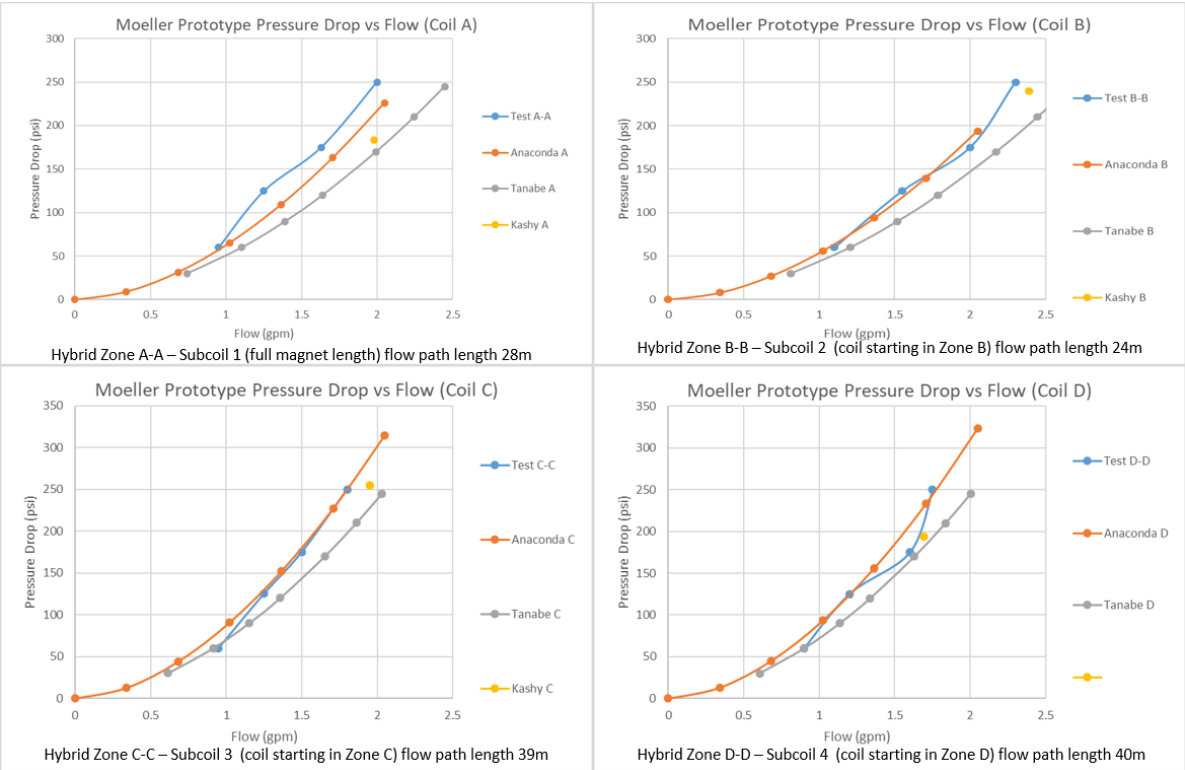

Figure 93: *Comparison of the pressure drop as a function of flow from different analytical calculations performed at JLAB with the prototype tests done at MIT-Bates. The test results are shown in blue.*

H.5.2 Hybrid vs. segmented downstream toroid coils

Similar optics can be achieved with segmented coils in the downstream toroid. The segmented sub-coil 4 design is presently being iterated to reduce the required drive voltage requirements. All other engineering constraints have been met.

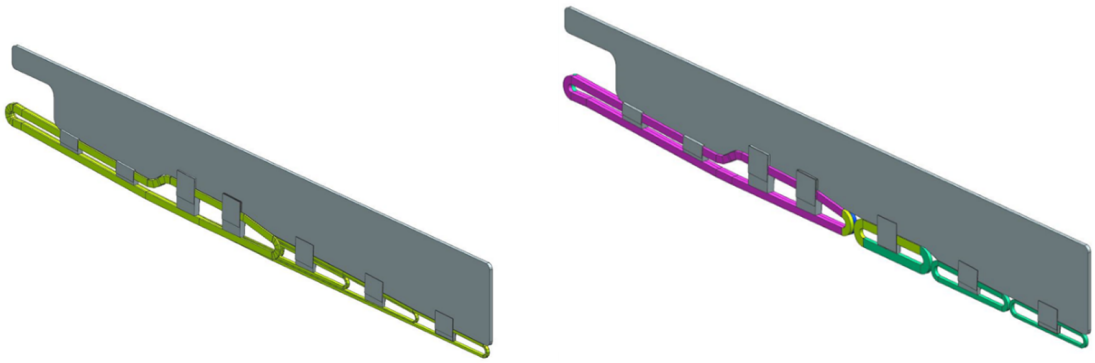

(a) (b)

Figure 94: *Strongback concept for the (a) "hybrid" and (b) "segmented" version of a single downstream toroid coil. The segmented coils would be assembled into coil packs similar to the hybrid coils.*

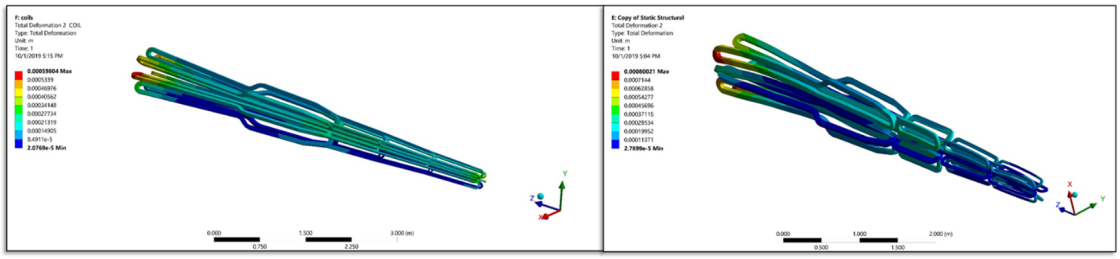

Figure 95: *Comparison of the FEA of the deflection in the "hybrid" (left) and "segmented" (right) versions of the downstream toroid coils. Deformation of the magnet coils at full operating current and gravity load. Exaggerated in image (more for segmented than hybrid); maximum deformations are 0.6 mm for the hybrid and 0.8 mm for the segmented.*

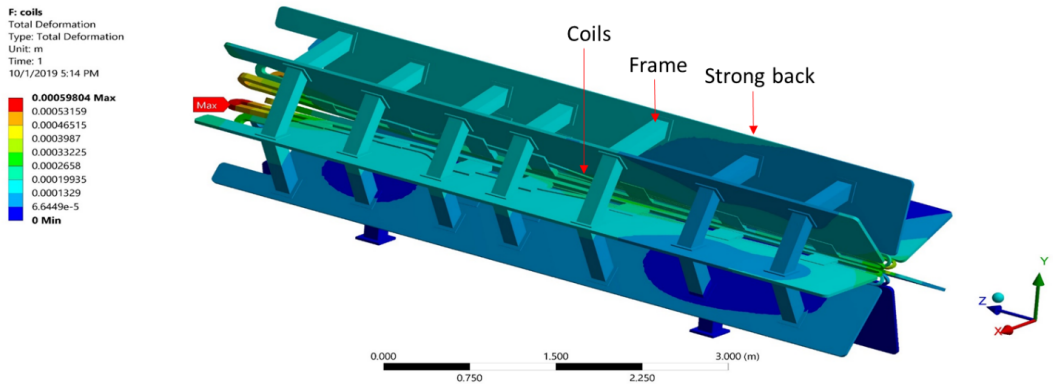

Figure 96: *FEA of the deflection of the downstream toroid including the strongbacks and support frame. Coil packs in both cases are very similar.*

H.5.3 Transport medium and enclosures

In the case of a helium transport medium, a central beampipe is required (indicated in orange in the figure). This beampipe must fit between the outer radius of the inner photon envelope (IPE) and the inner radius of the outer photon envelope (OPE) in order to minimize the backgrounds caused by these high rate photon envelopes. However, due to stray fields in the center of the magnets, these beampipes at low radius become significant sources of background. This is not an issue in the vacuum case because the radius of the beampipe is much larger.

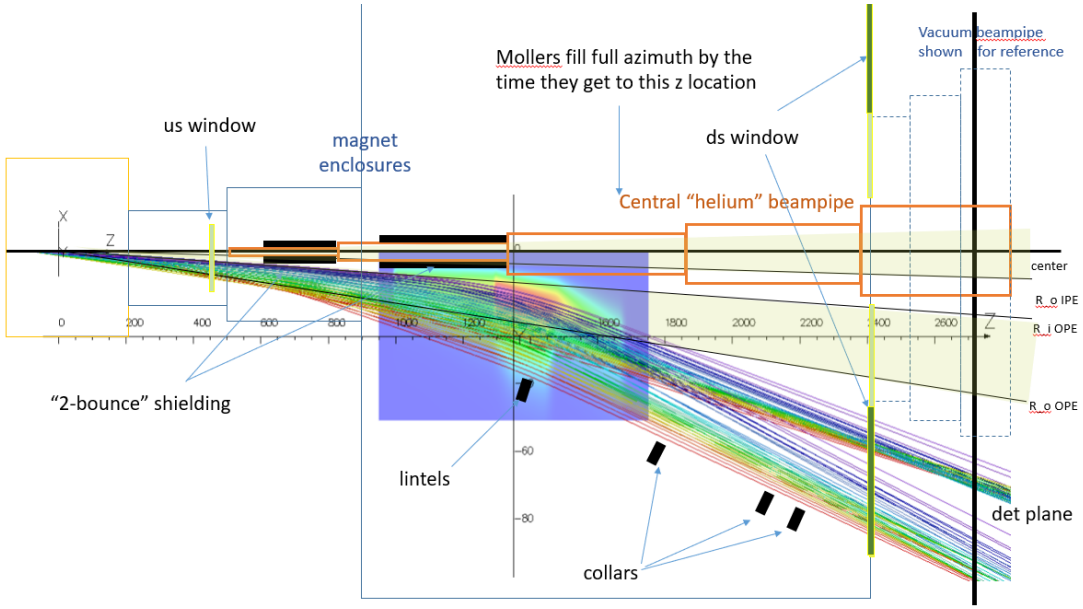

Figure 97: *Pre-conceptual cartoon showing the difference between the beamlines in the case of vacuum and helium transport media. The moller and elastic trackes are shown, colored by theta. Two yellow-ish regions indicate the extent of the inner photon envelope (IPE) and the outer photon envelope (OPE). The beampipe is designed so that it doesn't interfere with any of these envelopes. The magnet enclosures are very similar in either case, but the helium case requires a central beampipe (shown in orange) that becomes a significant source of background which is not an issue in the vacuum case.*

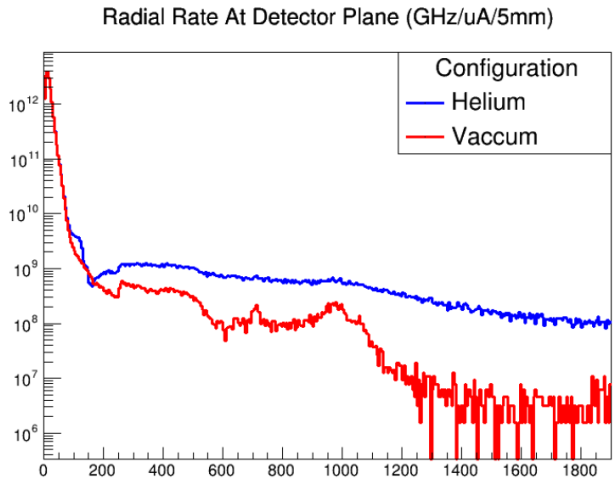

Figure 98: *Comparison between vacuum and helium choices: radial distribution of the rate of all particles with energy greater than 1 MeV at the detector plane, 26.5 me downstream of the target center. The inner photon envelope extends to around 150 cm. The outer photon envelope extends from approximately 200 cm to 580 cm. The elastic peak is around 700 cm, and the Møller peak is around 1000 cm.*

H.5.4 Superconducting concept

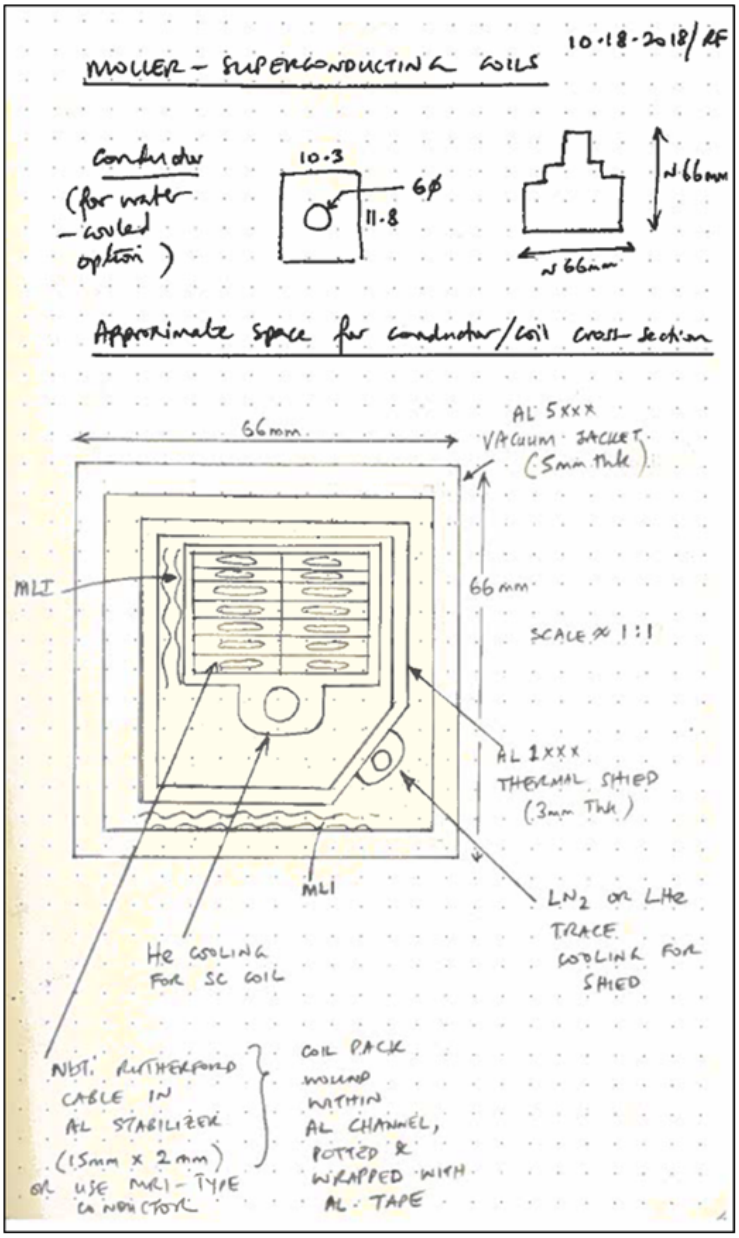

Figure 99: *Conduction-cooled superconducting Rutherford cable concept with thermal radiation shield and vacuum jacket.*

Pugh Decision Matrix

Project	**MOLLER - HYBRID TORUS**
Sub-System	**Coil Technology**
Version No.	10.00 - assume Helium environment option, so SC coils will require a separate vacuum jacket and the complexity that that will entail.
Date	4.12.2019
Engineers	R. Fair / P. Ghoshal

Notes
(a) Use the 'SC - RUTHERFORD' option as the **BASELINE OPTION** to compare against.
(b) SC - RUTHERFORD assumes a Rutherford-style cable soldered into a copper C-channel
(c) SC - CICC assumes a Cable-In-Conduit Conductor with a central cooling channel with supercritical Helium
(d) RESISTIVE WATER-COOLED assumes copper coils with a central cooling channel with water

	Criteria (Critical to Quality)	Criteria Rating or Weight (1 - 10)	SC - RUTHERFORD (BASELINE)	ALTERNATIVE OPTIONS: RESISTIVE WATER-COOLED	ALTERNATIVE OPTIONS: SC - CICC	JUSTIFICATION FOR SCORE COMPARED TO BASELINE
1	Ability to realign magnet coils after installation	5	0	0	0	Difficult to gauge exact location of the current-carrying portions of the conductor for all options
2	Ease of installation	4	0	1	0	Resistive coils will be easier to handle and assemble. No thermal shields and vacuum jackets to distort. No MLI to fit. Note: the magnet vacuum chamber will likely only be at about 0.1 Torr - the SC coils will require at least 1E-5 Torr
3	Ease of maintenance	4	0	1	0	No cryogenic-related equipment and sub-assemblies to maintain for resistive coils, just electrical, vacuum and water connections
4	Low operating cost	4	0	-1	0	Using supercritical Helium - Potential savings of up to $1M on electrical power over a period of 3 years (assuming experiment runs for 6 months per year over 3 years at $0.12/kWhr)
5	Largest Physics acceptance	10	0	0	1	Use of CICC should minimize the coil cross-section, even after allowing for the presence of a thermal shield, MLI and vacuum jacket. We may not require the thermal shield...we can operate the magnet at even 7K.
6	Minimal background sources	3	0	0	0	Equally same for either case
7	Sufficient cooling power to handle coil heating due to beam, particles, radiation	6	0	1	0	Although the average heating due to radiation effects is of the order of a few watts, transient (*unknown*) events can produce higher energy spikes causing the SC coils to quench.
8	Minimal material in the beamline and acceptance regions	8	0	0	1	Use of CICC should minimize the coil cross-section, even after allowing for the presence of a thermal shield, MLI and vacuum jacket
9	High Ampere-Turns in the coils	8	0	0	1	Should be able to obtain even higher current densities with CICC when compared to the SC-Rutherford option and cetainly higher than that achievable with resistive coils
10	Ease of penetrating environmental enclosure - for services (cooling, power, instrumentation, mechanical linkages)	2	0	1	0	Easier to penetrate just a vacuum chamber for resistive coils - no thermal shield and MLI to penetrate.
11	Minimal movement due to thermal expansion/contraction of coils	2	0	0	0	This is always the case for either magnet type - either warming up for resistive magnets or cooling fos SC magnets
12	Minimal technical complexity of coil design	5	0	1	0	The CICC option should be simpler than the Rutherford option. Resistive coils will be easier to manufacture also. However, if a Helium environment is now being used, then any SC coils will require a separate vacuum jacket, (perhaps a thermal shield) and MLI which increases the technical complexity of the design.
13	Minimal complexity of protection system	5	0	1	0	Should be easier to protect resistive coils. The CICC option may be more difficult to protect especially due to potential pressure spikes within the He channel during a quench
14	Minimal technical complexity of control and instrumentation systems	3	0	1	0	Control and Instrumentation for resistive coils should be more straightforward - no need to monitor and control cryogenic valves, no need for ice-management systems etc.
15	Minimal technical complexity of vacuum pumping system	2	0	1	0	Vacuum environments always add complexity. If we opt for a Helium environment, then the resistive coils will score higher as a simpler pumping system can be used.
16	Minimal forces between coils during normal operation and.or during fault conditions	2	0	0	0	No difference between options
17	Low conductor cost	4	0	1	0	Resistive coils should have the lowest conductor cost. CICC cable is potentially more expensive. JLab still has surplus Rutherford cable which may need to be soldered into a copper c-channel.
18	Low cost coil winding and fabrication tooling	4	0	1	0	Resistive coils will only require minimal tooling for winding. SC coils will need additional jigs to form the thermal shield and coil vacuum jacket.
19	Minimal welding	1	0	1	0	No welding of coil vacuum jackets necessary for resistive coils
20	Low cost current leads	3	0	1	0	No vapor-cooled leads required for resistive coils - just high-current electrical feedthroughs and water-cooled leads.
21	Minimal number of vessels to contain coils	3	0	1	0	No coil vacuum jacket required for resistive coils
22	High reliability	5	0	1	0	SC magnets once installed and commissoned successfully are very reliable
23	Low cost power supplies	3	0	0	0	SC magnet power supplies could be lower cost than resistive magnet supplies. Only 1 MPS will be required to charge all SC coils, say 10V 15kA or 8kA (with varying current) (may add additional say 25K for R&D and study if required to change current in individual coils).
24	Achievability of required mechanical tolerance / clearances	3	0	0	0	The SC magnet coils are more compact, so it will be easier to achieve the required tolerances and clearances IF the SC coils share the same vacuum as the magnet enclosure. However, if a Helium option is used, then the SC coils will require a separate vacuum chamber (perhaps a thermal shield) and MLI which will make the required clearances and tolerances as difficult to achieve as for the resistive coil option.
	Totals		0	47	26	

Figure 100: *Pugh matrix for water-cooled resistive vs. superconducting magnet technology.*

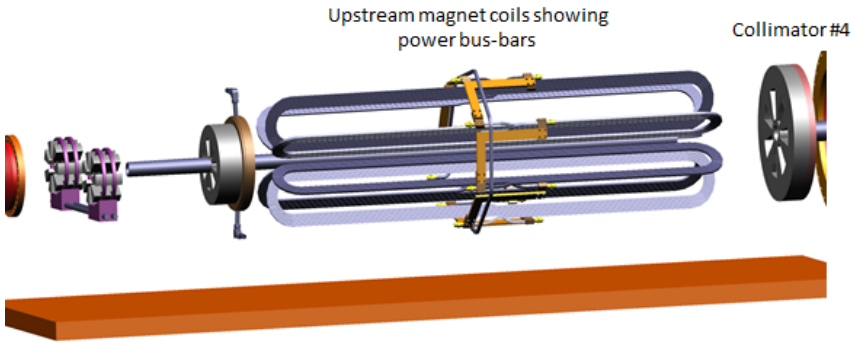

Figure 101: *Overview of the collimators. Just upstream of the upstream toroids is the acceptance-defining collimator #2. Downstream of this, just upstream of the hybrid toroids is collimator #4.*

I Alignment and Tolerances

Quantitative analysis for positioning and alignment tolerances for several subsystems has been addressed through simulations. By perturbing parameters such as target positioning, collimator apertures, and the magnetic fields, calculations of the rates and measured asymmetry provide the sensitivity on these parameters and establish tolerance limits. Due to the full azimuthal coverage and symmetry of the system, the experiment does not have particularly challenging requirements for most of these systems. The machining tolerance of the inner edge of the acceptance-defining collimator has the most stringent requirement of 200 μm.

Target Alignment The sensitivity of misalignments in the position of the target in z is studied via varying the target position along the nominal beam trajectory. The effect on the asymmetry was found to be less than 0.05% per cm.

Collimator Tolerance As the collimating system is used to define the geometric acceptance of the electrons, we have studied the positioning and machining tolerances. We consider the transverse positioning of the collimators as well as changes in the inner and outer radius of their apertures. The schematic and numbering of the collimators are given in Fig. 101 and we adopt the standard Hall A right-handed coordinate system where the z direction is nominally the beam direction and y is against gravity. Collimator 2 is of particular importance as it is designed to be the acceptance-defining collimator.

The tolerances in the transverse alignment of collimators 2 and 4 are studied by adding small positional offsets relative to their nominal positions. The offsets are introduced independently along the transverse direction to the beam propagation direction. In all cases the dependence was found to be quadratic and the linear component to be negligably small for changes on the order of 1 mm, Table 28.

Collimator Apertures The inner and outer radii of collimators 2 and 4 were varied independently within the simulation. The effects on the measured asymmetry for collimator 2 are shown in Table 29 and Fig 102. These define the machining tolerances and in particular for collimator 2, the inner radius must be machined within 200 μm for a systematic uncertainty of 0.03 ppb on the asymmetry, or 0.1%. This is the dominant systematic.

Table 28: *Parameters of the fit equation of the form* $y = a + bx + cx^2$ *of asymmetry vs collimator position offset. The first order term* b *allows for variations of* $1\ \mathrm{mm}$ *with negligable perturbations.*

	a (ppb)	b (ppb/mm)	c (ppb/mm^2)
Coll # 2, x-scan	29.9	7.34×10^{-4}	3.66×10^{-3}
Coll # 2, y-scan	29.9	4.88×10^{-4}	3.98×10^{-3}
Coll # 4, x-scan	27.0	-0.58×10^{-4}	3.84×10^{-3}
Coll # 4, x-scan	27.0	1.49×10^{-4}	3.53×10^{-3}

Table 29: *Parameters of the fit equation of the form* $y = a + bx$ *of asymmetry and fractional change in asymmetry vs inner/outer radius change of collimator 2.*

Asymmetry		
	a (ppb)	b (ppb/mm)
Inner-rad	29.95	0.14
Outer-rad	29.94	-0.06
Fractional change in asymmetry		
	a	b (1/mm)
Inner-rad	-4.19×10^{-4}	-4.74×10^{-3}
Outer-rad	-0.44×10^{-4}	2.12×10^{-3}

Magnetic Field Changes in the magnetic field can cause changes to particle trajectory and therefore the acceptance of the quartz. A study was done by modifying a single coil position and angle and then generating a modified field map and then studying the change in measured asymmetry. Variations were done for position along the beam line, radial position, and azimuthal position. In addition rotations of a single coil about its center of mass was done about three independent axes. In all cases, the change in asymmetry was less than 0.4 ppb per cm for the position dependent cases and 0.2 ppb per degree for the rotation cases.

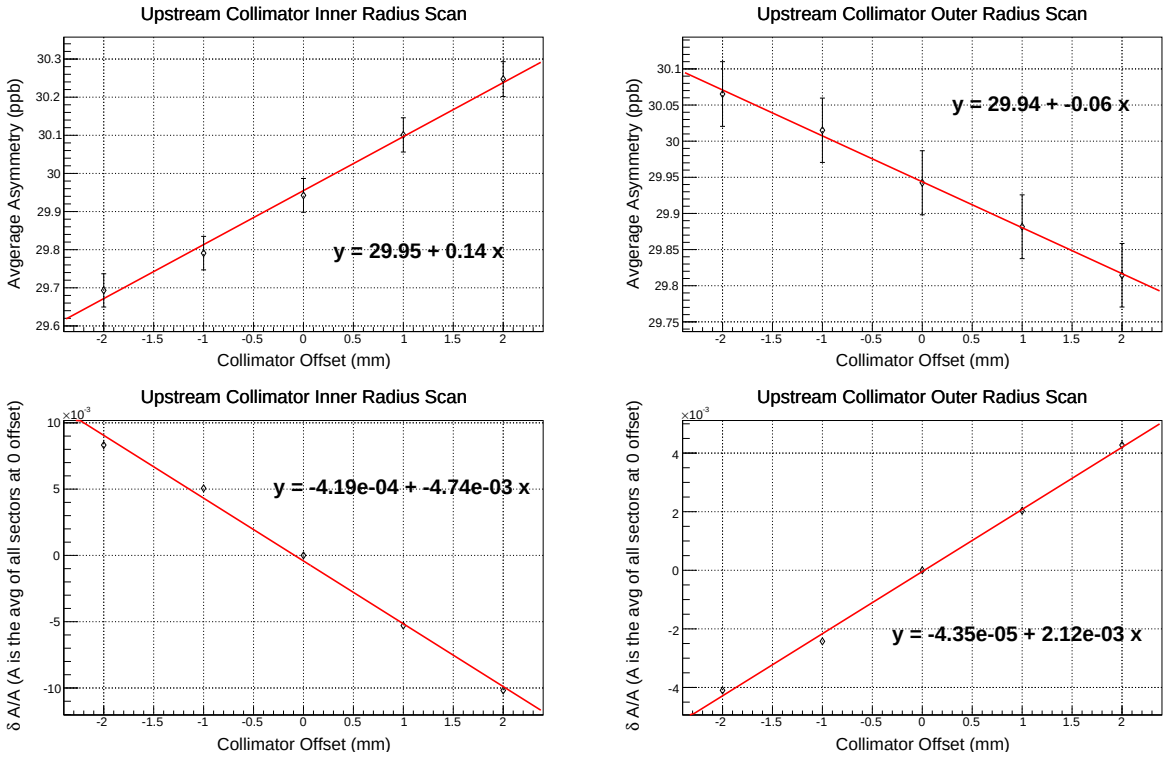

Figure 102: *Dependence of asymmetry on the inner and outer radii of Coll #2.*

J Integrating Detector Development and Test Status

The general requirements of the main integrating detectors were discussed in Sec. 8. In brief, the primary measurement of the relative flux is carried out in integrating (or current) mode; this drives various design and material choices for the detectors to confront the high signal magnitude, corresponding noise suppression, the requisite detailed understanding of the scattered flux profile, and sufficient suppression and identification of background. The latter requirements leads to the definition of auxiliary detector and the conditions and frequency of calibration runs.

The integrating detectors will consist of three major parts: the active detection volume, made from quartz, the light guide (currently envisioned to consist of an air-core light guide with walls made from a high reflectivity material), and a quartz window photomultiplier tube. In a current mode measurement, the detector noise behavior must be dominated by PMT shot noise, which is ultimately driven by event electron counting statistics and the number of photo-electrons created at the PMT photocathode per incident electron. The latter quantity is a strong function of the choice of detector material and geometry, while the maintenance of noise behavior and collection of the signal is driven by the detector electronics. The rest of this appendix will present the design and testing status of the detectors and associated geometry, the design and testing of the PMT and base assembly, and the design and testing of the front-end electronics.

J.1 Detector Module Design

Section 8.2.1 presented the overall design of the detector assembly and its constituent components, the quartz, light guide, and the PMT. Here we discuss the details of the design and detector testing. The primary concerns of the detector module design are light yield maximization and the minimization of background, both of which in turn keeps excess noise above electron counting statistics to a minimum. Both of these issues are intimately connected to the detector module geometry.

J.1.1 Light Yield

The total number of photoelectrons depends on the amount of light, due to a single electron event in the quartz, that is actually incident on the cathode, and the quantum efficiency of the cathode. After emission of the Cherenkov light from the quartz, the amount of light hitting the cathode is a strong function of the reflective properties of the light guide surfaces, as well as the length of the light guide. The orientation of the light guide with respect to the quartz and the shape of the light guide largely determine the number of reflections the Cherenkov light undergoes, before hitting the PMT cathode. Each reflection reduces the probability for detection at the cathode. The orientation of the quartz tiles and the light guides relative to each other and with respect to the scattered electrons have been optimized, such that the collection of the Cherenkov photons from each quartz piece is maximized, while the detection of light *created by events in the light guide itself* (accidentals) is minimized. Figure 103 (left) shows the design of the detector module for ring 5 (the main Møller event ring) and illustrates the concept behind the light guide and quartz geometric design. The figure on the right shows a single simulated electron event in a piece of quartz with a 45 degree cut at one end, where total internal reflection is broken to allow the light to exit into the light guide. The primary reflector in the light guide is adjusted at an angle with respect to that surface, such that the majority of the light is reflected directly toward the PMT. The rest of the light guide has a slight reduction angle toward the PMT, so that the light guide cross-section is matched to the PMT window surface area.

J.1.2 Module Design Studies

Over the past three years, significant progress has been made in the design and prototype testing of the integrating detectors. The first step was to develop a small set of viable detector configurations (geometry

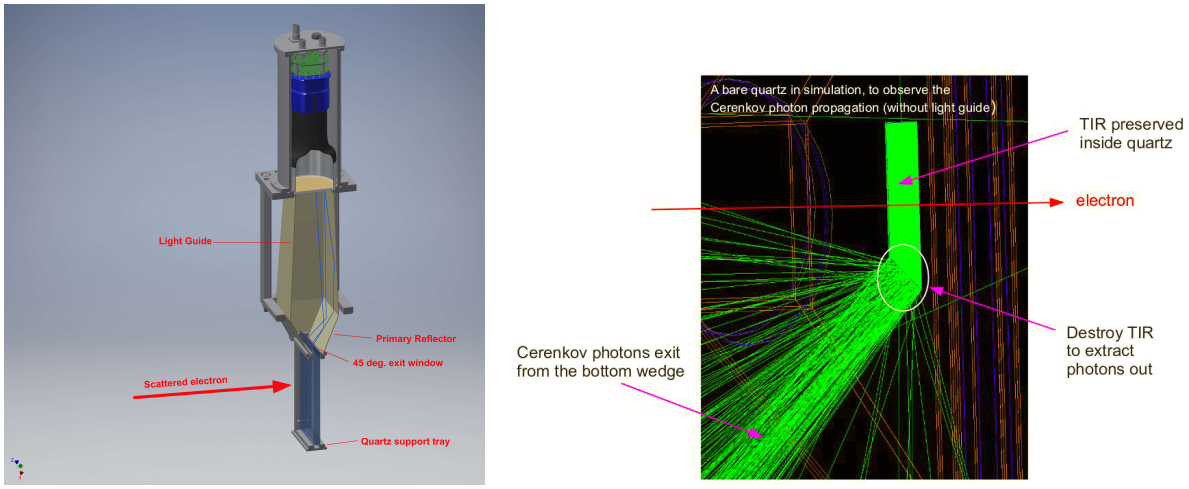

Figure 103: *Left: Ring 5 module design and illustration of quartz and light guide geometry that was chosen to facilitate the most efficient way to collect the Cherenkov light. The blue lines illustrate that the primary reflector angle and size is chosen to reflect the majority of the light that exits the quartz directly toward the PMT. Right: Simulated event in a single MOLLER main detector. The Cherenkov light produced by the passage of a minimum ionizing electron that hits the detector at normal incidence is totally internally reflected until the light hits a surface at nearly normal incidence and can escape to be detected by a photosensitive device.*

and material combinations between quartz and light guide), using detailed simulations. These were then implemented as prototype detectors and tested with minimum ionizing cosmic rays and beam electrons.

A complete detector design has been implemented in the full MOLLER simulation and many single detector simulation studies were performed to optimize geometry material and background rejection. A complete angle study was carried out, to study the effects of the quartz orientation with respect to the incident electrons and to study the effects of the light guide orientation with respect to the quartz. Simulations also included variations of quartz geometry, including trapezoidal and rectangular chapes, thickness and flat or 45 degree angle cuts along the edge that interfaces with the light guides. Light guide geometry (length, flare, size) were also studied using simulations. The primary results that were obtained for each configuration include photoelectron yield and signal RMS width. The simulations were checked against cosmic ray data, however, to get a definitive value for the number of photoelectrons, to benchmark the simulations against, and to carry out a realistic study of light yield variation as a function of reflective material properties in the light guide (which is very difficult to simulate accurately), dedicated prototype tests needed to be performed with minimum ionizing beam electrons.

Since October 2013, the detector working group has carried out many tests with prototype detectors at the MAMI facility in Mainz, using 855 MeV electrons during seven separate test beam periods. Measurements were carried out to verify the single event photoelectron yield for the simulated quartz and light guide geometries as well as for a variety of light guide reflective materials. Overall five different light guide lengths were tested (80 cm, 60 cm, 56 cm, 35 cm, and 25 cm), corresponding to the guides needed for different rings and assemblies and with different angles between the quartz and the light guide. In addition, a variety of different reflective materials for the light guides were tested. The guides were coupled to various different quartz geometries, including 1 cm, 1.5 cm, and 2.5 cm, thick quartz pieces for the Møller and super-elastic geometries. The super-elastic detector geometry is expected to have the poorest photoelectron yield, since it has the longest light guide and the least optimal quartz geometry of all the detectors. Consequently, achiev-

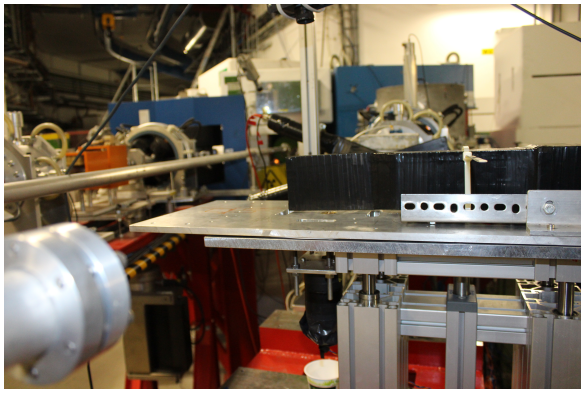

Figure 104: *Møller detector geometry prototype test setup with an 855 MeV electron beam at the MAMI facility in Mainz, Germany.*

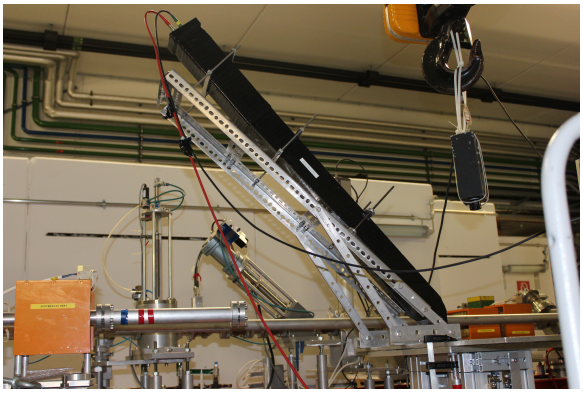

Figure 105: *Super-elastic detector geometry prototype test setup with an 855 MeV electron beam at the MAMI facility in Mainz, Germany.*

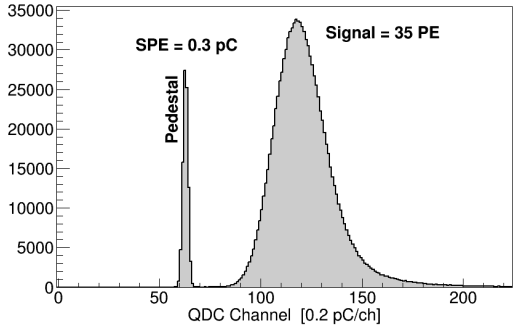

Figure 106: *Measured photoelectron yield from 855 MeV electrons incident on a 1 cm thick polished quartz attached to a 25 cm air-core light guide with Miro-Silver reflectors and a 3 inch high gain PMT.*

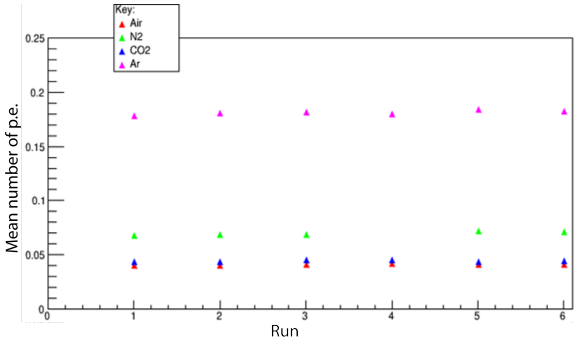

Figure 107: *Photoelectron yield from electrons traversing the light guides with various gases. The test results demonstrate that the photoelectron yield from the light guide will be very low compared to the light yield from the quartz.*

ing sufficient light yield in that detector means that we can expect the designs for the other detector rings to work as well or better. The lateral dimensions of the quartz pieces were 8.4×16 cm^2 for the Møller ring and 17.1×4 cm^2 for the super-elastic ring. The beam tests were done with 3 inch photomultipliers with quartz windows and bialkali cathodes, manufactured by Electron Tubes Inc. Figure 106 shows the result for the photoelectron spectrum for the Møller ring detector prototype.

In addition, several tests were carried out to determine the signal magnitude from events going through the light guide, to study the relative signal dilution when events traverse the light guides, as opposed to the quartz. The various results were used to benchmark our optical simulations. The most recent beam tests to verify the geometry were performed in May 2016 and included a repeat of the light yield measurements for the Møller ring and the super-elastic ring detector geometries with new light guide designs, as well as more precise tests for light yield from the light guide only, when filled with a variety of gases (aside from air). The results of the light guide study are shown in Fig. 107. Two of the prototypes tested at the MAMI facility are shown in Figs. 104 and 105. The results from the beam tests show the important result of the relative signal yield (in photo-electrons) produced by MIP electrons in the quartz and in the light guides [120]. These results can now be folded into our simulations to verify our assumption, that the background, caused by electrons traversing the light guide, is negligible. Table 30 summarizes the main tests that were done up to

now, and the general results obtained. Additional beam tests were carried out in December 2016, May 2017, and October 2018. The last beam test in 2018 was carried out with a tagged photon beam, at the MAMI A2 beam line, to test our assumptions made about the detector signal yield for incident photons. We were able to take data for photons between $\sim 15\ \mathrm{MeV}$ and $\sim 50\ \mathrm{MeV}$. Finally, two beam tests were carried out in 2019, testing the performance and radiation hardness of the current PMT base and preamplifier designs, which are described below.

Table 30: *Most Important Prototype Tests Performed at MAMI*

	Description	**General Results**
1	Light yield from 1.0 cm thick highly polished quartz, 25 cm Miro-Silver guide)	A minimum of 35 photoelectrons per event, with 4% excess noise.
2	Light yield from 1.5 cm thick highly polished quartz, 25 cm Miro-Silver guide)	A minimum of 42 photoelectrons per event, with 5% excess noise.
4	Comparison of various common Light guide reflective materials, including UVS, Miro-Silver, Alanod, and mylar.	Data with Kapton blacked-out guide shows that majority of the light is from direct shine. We may blacken some of the guide wall surface to further reduce background. Relative light yields for the tested relfective materials are all within 90% of each other.
5	Light guide length comparison for between 60 cm and 25 cm Miro-Silver guide	60 cm, corresponding to longest guide in the design, looses 32% of the light relative to the 25 cm guide.
6	Comparison of different quartz wrapping materials: No wrapping, mylar, and white paper (e.g. millipore)	White paper produced by far the best result increasing the yield by a factor of 3 with respect to no wrapping. Mylar increased the yield by a factor of 2 with respect to no wrapping.
7	Electron event hit location position scans: Lateral position scan away from the light guide and transverse to the light guide.	Only small amounts light yield variations were were observed for either direction ($\sim 8\%$)
8	Electron events through the light guide.	Events that traverse the light guides contribute to the light yield seen in a detector at the fractional PE level(see Fig 107) and the relative rates are low (about 1 in 10 electron events in a guide produces a detectable event).

The beam tests performed at the MAMI facility in Mainz and the comparison of the results to the simulations, prove that the current detector design is viable. As listed in Table 30, test results (1) through (4) show that the light yield is high enough and the excess noise low enough to perform the measurement with the proposed detector design. The largest difference in the light yield occurs for different quartz wrapping materials, as noted in result (5). Test result (6) notes that no significant variations in light yield due to varying electron hit locations was observed. This is largely expected for small detectors like these. For most of these tests, beam was normally incident on the quartz, and the light guide was tilted 45 degrees with respect to the beam, with the PMT located upstream of the quartz. The results quoted here were taken from plots with the pedestals removed and the ADC channels converted into number of photoelectrons, using single photoelectron calibrations.

J.1.3 Results from detector background sensitivity studies

The use of quartz and air-core light guides in the module design is driven by the need to keep background to a minimum. Air-core guides produce very little scintillation or Cherenkov light from events moving through them and, at the same time, they allow the PMTs to be located outside the main scattered electron envelope.

The use of quartz and air-core light guides in the module design is driven by the need to keep background to a minimum. As discussed above, air-core guides produce very little scintillation or Cherenkov light from events moving through them and, at the same time, they allow the PMTs to be located outside the main scattered electron envelope. The next possible most important background in the detectors will be from soft-photon interactions; those with energies below $100\ \mathrm{MeV}$. Based on simulations, it is expected that there will be significant rate from these photons, so it is important to determine the sensitivity of the detectors to these photons. To that end, we performed beam tests with tagged photons at the MAMI facility in Mainz, Germany. The test setup is shown in Fig 108. Tagged photon with energies between $15\ \mathrm{MeV}$ and $56\ \mathrm{MeV}$ were incident on the quartz, with a pair of trigger scintillators and a Lyso photon calorimeter placed behind the quartz. The beam was incident on the ring 5 quartz design, but in this case with the quartz attached directly to the PMT, without a light guide. Figure 109 shows a photo of the detector test arrangement. To measure the efficiency, the ratio of the number of events that registered in the quartz to the number of events that registered in the calorimeter or the trigger scintillators was calculated. It is assumed that the scintillator Lyso combination was 100% efficient for the photons of this energy. However, if that was not the case, and there were additional events that were not detected at all, then the results obtained represent an upper limit efficiency, which is the interpretation we follow here.

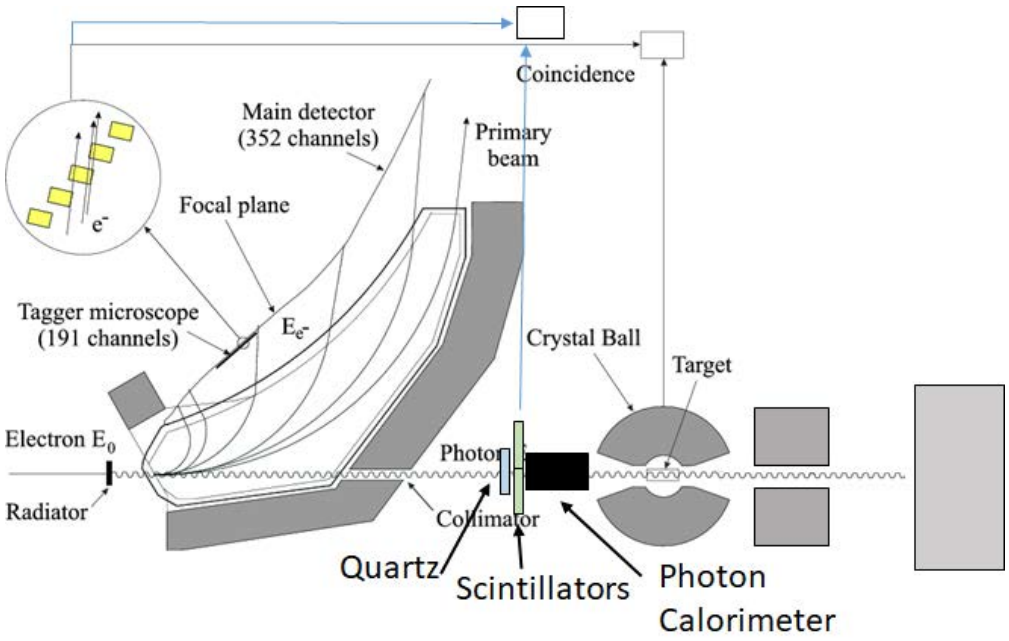

Figure 108: *Setup of the prototype detector test with tagged photons at MAMI.*

The photon calorimeter spectra for a few energies are shown in Fig. 110, clearly showing the photopeaks. Good events were counted from above the pedestal to under the photopeak for each case. The long tail in the spectra that are shown is from pile up, which was observed to decrease in runs with lower beam current. The efficiency was calculated both for the integral over the event amplitudes (the channel number of the QDC that was used), as well for channel intervals, which were converted to photoelectron number using previous calibration runs. Figures 112 and 111 show the corresponding upper limit efficiencies. The integrated

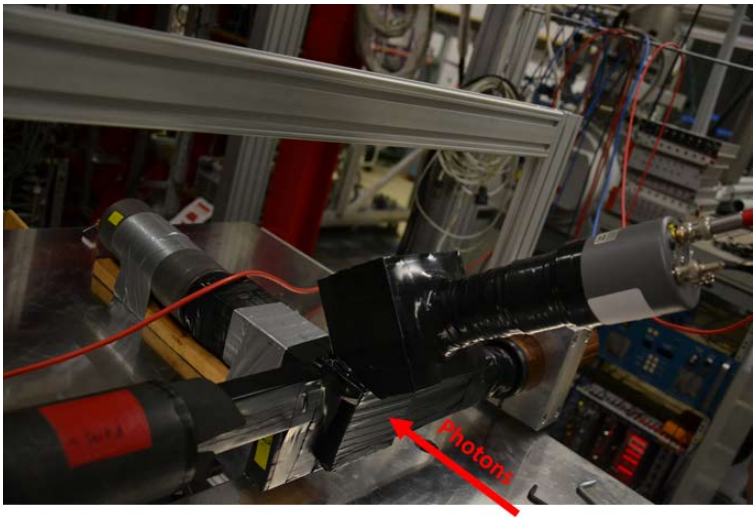

Figure 109: *Setup of the prototype quartz with the trigger scintillators and the photon calorimeter.*

efficiency (for signals the produced more than 1 photoelectron) is shown for all photon energies that were tested and is at the few % level. The efficiency as a function of photoelectron number is at the sub-percent level.

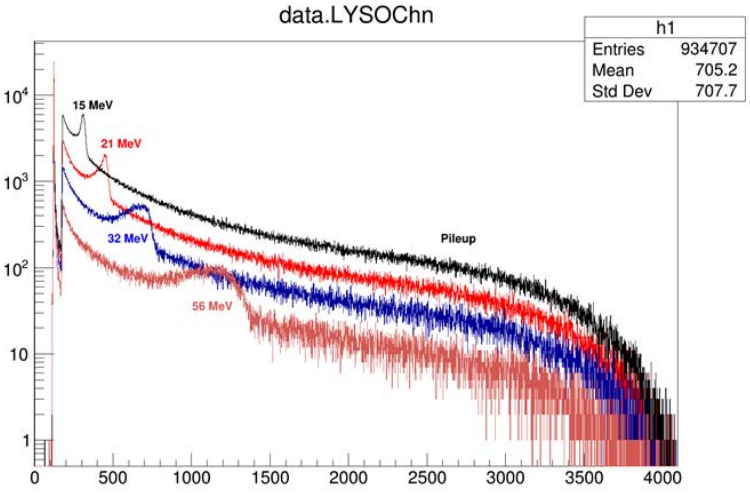

Figure 110: *Photon calorimeter signal for some of the photon energies that were measured. The photo peak is clearly visible in each case.*

J.2 Radiation Hardness and PMT Non-linearity Plans

Radiation damage is in principle a concern, since Cherenkov light production occurs predominantly in the UV, which is exactly where loss in light transmission first shows up. For example, the familiar "yellowing" of lead-glass is due to the loss of transmitted light at the blue end of the spectrum. The dose to the artificial, fused-silica radiator material from the $e + e \rightarrow e + e$ events will be only 15 MRad by the end of the experiment. Given the average path length in the radiators of only a few cm, and our non-agressive short

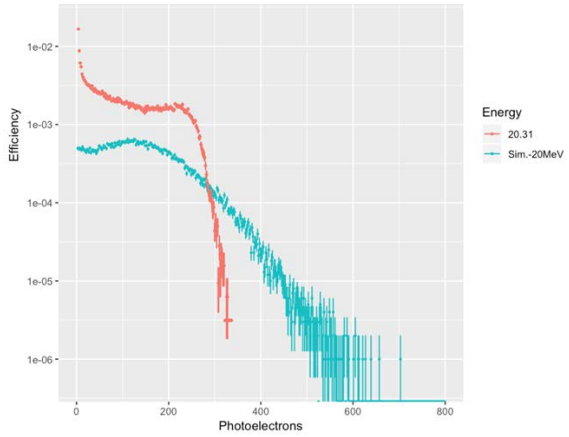

Figure 111: *Photon detection efficiency as a function of photoelectron number (amplitude of the signal produced by the photon event) for* 20 MeV *photons. The simulated distribution is also shown.*

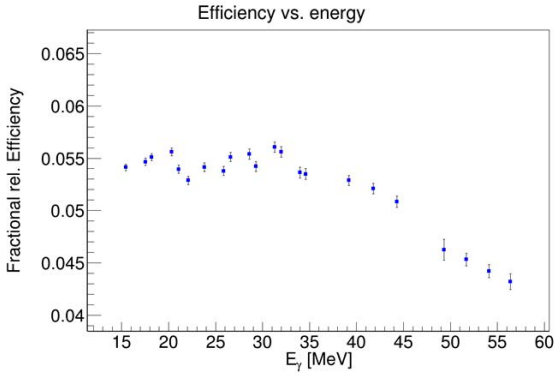

Figure 112: *Photon detection efficiency integrated over all signal amplitudes, for all photon energies that were tested.*

wavelength cutoff of 250 nm set by the UV glass of the PMT windows, no measurable loss is transmission is expected. This is ideal since it means that the photoelectron yield and any detector biases (e.g., with respect to Q^2) will be stable throughout the experiment.

All other detector construction materials in the beam envelope (such as radiator supports) must be vetted for susceptibility to damage under 15 MRad dose. Degradation by potentially elevated ozone and nitric acid levels may also be a factor in the choice of detector materials.

Preparations for quality assurance (QA) checks of the radiation hardness of MOLLER detector components are underway at the Idaho Accelerator Center (IAC). Two previous engineering test runs were performed in March 2016 and May 2018. The first test irradiated several candidate light guide materials with 8 MeV electrons at 65 mA peak current, 4 μs pulse width and 250 Hz rep-rate. The specular reflectivity at 90^o or normal incidence, for 200 - 800 nm photons, was measured periodically during the exposure to quantify any changes in reflectivity–no changes were observed. However, the dose exposures during this run were not well quantified due to saturation of the OSL dosimeters. The second engineering run did successfully calibrate dose exposures during the irradiation of a small block of Spectrosil 2000 quartz. Measurements of light transparency between 200 and 800 nm were measured after $\sim$11, 30, and 60 Mrad exposures. For this test the machine was setup for 8 MeV electrons, 50 mA peak current with 500 ns pulse width and 250 Hz rep-rate; the dose absorbed by the quartz piece was calibrated to be 215 rad/pulse. These tests as well as the light guide reflectivity study will be repeated with more refined optical measurements and with the goal of establishing a method for routine QA checks of quartz and light guide material batches. In addition, irradiation studies and QA checks will be conducted on active electronics, such as switching PMT bases and pre-amplifiers, and any other non-metal construction materials that will potentially be exposed to relatively high radiation doses, such as seals for light/gas tightness, epoxies, or 3D-printed parts.

The MOLLER collaboration (Idaho State and University of Manitoba groups) will characterize the linearity of candidate MOLLER integrating detector pmt/base combinations with the goal of achieving 0.5%$\pm$ 0.1% non-linearity. For the initial testing, the same apparatus that is used for the PREX-II/CREX PMT linearity tests will be used for MOLLER PMTs. The PREX-II flashing LED system has demonstrated the ability to routinely achieve sub 0.3% linearity measurements with up to 13 nA photo cathode currents and at 240 Hz flip frequencies. One of the main challenges with this project is the very high flip frequency proposed for MOLLER (960 Hz) and the dozen or so different light levels that are expected in the 6 thin quartz

detector rings and shower-max ring. We currently use the $Q_{\rm weak}$ integrating ADC for our measurements, but will also be using the linearity apparatus to test prototype MOLLER ADC designs.

Recent linearity studies for the PREX-II/CREX pmts seemed to show a limitation in the apparatus or measurement technique at high (480+ Hz) flip frequencies. The issue can be resolved with longer settling times (waiting longer after the LED changes state before acquiring signal), but this causes inefficiency making the 960 Hz flipping difficult or impossible to handle. The problem may be related to thermal instabilities in the flashing LED and so it has been suggested to perhaps try using a chopper-wheel to create the flashing effect while keeping the LED constantly energized. The chopper could be synchronized with the integrating DAQ readout gates (which are at 1920 Hz), or one could try to do the measurement with a phase-locked controller. This activity is about determining what low gain high voltage/base settings are required for the integrating detector ring pmts to operate with 0.5% or lower non-linearity known to a precision of 0.1%.

K Front-end Integrating Electronics Development Status

The design of the electronics is dictated by the properties of the signal and the information that needs to be extracted from it. The integrating electronics must provide the following information in the data stream:

1. For each helicity window: The sum of samples, sum of squares of samples, minimum sample value, maximum sample value, and the number of collected samples.
2. For diagnostic purposes during selected periods: Every ADC sample, up to the full sample rate of 15 Msps, across helicity window boundaries.

In addition, the electronics must maintain signal integrity from the PMT to the DAQ system, which includes maintaining the mean amplitude and the RMS width (minimizing additional noise sources) and preventing unwanted variation of the signal that is correlated with the helicity state. A concept schematic of the integrating detector electronics chain is shown in Fig. 31, in the main text. Here we give specific details about the expected signal and the processing scheme, and the design of the three main components, the PMT base, the preamplifier, and the ADC board.

K.1 Signal Structure and Sampling Scheme

K.1.1 Signal Structure

For integration mode measurements, counting statistics manifests itself in the root-mean-square (RMS) width of the shot noise at the PMT anode, which has contributions from all sources that generate an anode current, including background and dark current. To get the total RMS width in the signal, as it is sampled by the ADC, one has to add all sources of electronic noise σ_{E}^{2}, which includes resistive (Johnson) noise, as well as noise introduced by active components and filters. The total squared RMS noise density in the PMT signal can be written as

$$\sigma^2 = 2Q_{P}I_{P} + \sum_{B} 2Q_{B}I_{i_B} + 2Q_{D}I_{D} + \sigma_{E}^{2} \quad [A^2/Hz] \,. \tag{15}$$

Where the subscripts P, B, D stand for *physics*, *background*, and *dark current* contributions, to distinguish the primary signal of interest (*physics*) from the other possible contributions. Here $I_{P,B,D} = \langle I^{\pm}_{P,B,D}(t) \rangle$ is the mean anode current and $Q_{P,B,D} = \langle Q_{P,B,D}(t) \rangle$ is the mean quantum of charge at the anode. For the anode current this is simply a time average, but for the charge quantum, the assumption is, that this is the mean of a Poisson distribution and that the time integration for the current is done over a time period for which the quantum efficiency was stable. For real detector events (as opposed to electronic effects), $Q_{P,B}(t) = g_{PMT}(t) N_{P,B} \epsilon e^{-}$ is the charge present at the anode, per event, where $N_{P,B}$ the number of optical photons created per particle incident on the quartz, ϵ is the quantum efficiency of the cathode in %, and $g_{PMT}(t)$ is the unitless gain of the PMT. The mean anode current from events in the detector is given by

$$I_{P,B} = \langle I^{\pm}_{P,B}(t) \rangle = \langle R^{\pm}_{P,B}(t) Q_{P,B}(t) \rangle \quad [A] \,. \tag{16}$$

Where $R^{\pm}_{P,B}(t)$ is the instantaneous rate of electrons on a given detector. The current is converted to a voltage by an I to V amplifier with a gain of $g^{\pm}_{Amp}(t)$, in units of Ω, so that the corresponding voltage yield is

$$V^{\pm}(t) = g^{\pm}_{\mathrm{Amp}}(t) I^{\pm}(t) + V^{\pm}_{E}(t) = V^{\pm}_{P}(t) + \sum_{B} V^{\pm}_{B}(t) + V^{\pm}_{D}(t) + V^{\pm}_{E}(t) \quad [V] \,. \tag{17}$$

In all of these expressions, a possible, explicit dependence of a given parameter, on the helicity state, is indicated by the $\pm$ superscript, while general time dependence (both slow and fast), that is generally not

correlated with the helicity state is indicated by the continuous time parametrization (t). The primary concern of the electronics design, coupled with the data collection methodology (e.g. helicity reversal speed), is to suppress effects of random time variation or drifts and to remove helicity signal leakage into the electronics chain, the former being leading to a statistical degradation and the latter to a systematic false asymmetry.

Random changes and systematic drifts, both fast and slow, result from changes in beam current, target conditions (target boiling and slower density changes), electronic drifts, temperature fluctuations, and PMT aging. Almost all of these can be controlled to some degree (for example by operating the PMTs at a reasonable HV bias, in a reasonably stable temperature environment, and removed from or shielded from direct radiation exposure), but the primary way to deal with possible false asymmetries due to drifts and unwanted noise above Shot noise, due to large amplitude random drifts, is to perform each asymmetry measurement on a time scale that is short compared to the timescale of the drifts. This is achieved by running the experiments with a fast helicity reversal rate. The faster the helicity reversal rate, the more the signal variation with respect to time is well approximated as constant on the time scale of an asymmetry calculation:

$$A_{\text{raw}} = \frac{V^+(t_+) - V^-(t_-)}{V^+(t_+) + V^-(t_-)} \rightarrow \frac{V^+ - V^-}{V^+ + V^-}$$

Random variations that are faster than the helicity reversal rate are dealt with and used to advantage in the electronics chain, as described in detail below. The choice of helicity reversal rate influences or determines almost every detail of the electronics design.

Helicity correlated changes in beam conditions result in explicit changes of the rate seen in the detectors, even in the absence of any asymmetry that results from the interaction of the primary beam in the target or the rest of the experiment. Continuous time dependence in the detector signal is primarily due to variations in the beam current, target conditions, electronic drifts, temperature fluctuations, and PMT aging. A great deal of effort has gone into the overall experimental design and analysis methods to remove or mitigate the dependencies on these unwanted experimental factors and many of the solutions are explicitly related to or influence the design of the integrating electronics, such as the required bandwidth and sampling speed, the avoidance of ground loops, and the usage of optical fiber connections for the helicity gate connections to the electronics crates.

Helicity correlated changes in the beam (current, energy, position, and angle) are unavoidable, but they can be minimized to some degree (for example through feedback on the source itself,in the case of current, and other mechanism) and they can be measured using charge and position monitors. The detector electronics has been design to allow direct measurement of the sensitivity of the detectors to these beam changes. The sensitivity measurements are made by measuring the correlation between the changes measured with the beam monitors to those measured with the detectors, which requires that the electronics chain used to process the measurements from the beam monitors is identical to that of the integrating detectors. This is particularly important in the case of the beam current monitors, since the integrating detector signal is normalized to (divided by) the current monitor signal to remove random drifts, fast fluctuations, and helicity correlated changes, in the beam current.

Figure 113 shows a 2 minute period of the raw and beam current normalized signals for one of the $\mathrm{Q_{weak}}$ integrating detectors. This data corresponds to an integration with an equivalent bandwidth of half the helicity reversal rate (480 Hz), since the data for each helicity window is averaged to one value per helicity window, in the FPGA, after sampling. Even after normalization, drifts can be seen at time scales down to seconds, along with much longer drifts, and large non-gaussian drops in yield, due to target boiling, can be seen at much shorter time scales (around 30 ms). A high helicity reversal rate prevents these types of drifts from producing false asymmetries and reduces the contribution to the RMS width in the asymmetry signal, due these effects.

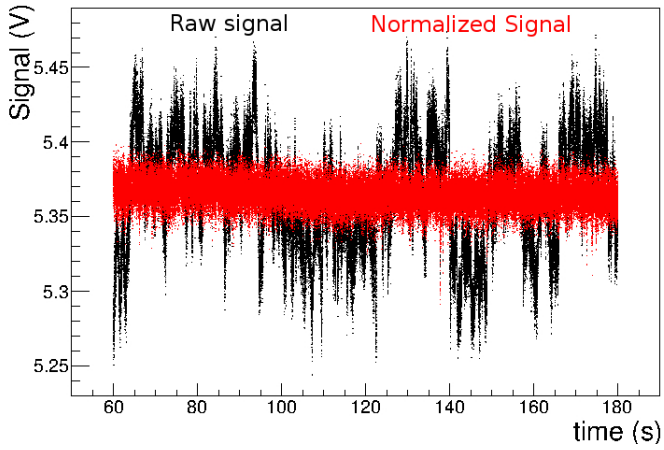

Figure 113: *Example period of a signal from one of the* $\mathrm{Q_{weak}}$ *integrating detectors. The black data shows the raw, unnormalized yield and the red data shows the beam current normalized yield.*

K.1.2 Sampling Scheme

For a mean signal of, say, 5 V a physics asymmetry of 30×10^{-9} produces a shift in the mean of about 0.15 μV, which is much smaller than the observed RMS width of a few mV. Since the bit resolution of even the best ADCs today is not high enough to measure a signal difference at that level, in a single sample, the combination of a suitable bandwidth selection and a high rate of oversampling is used to increase the effective bit resolution of the ADC.

Figure 114 illustrates the division of the integration mode detector signal into sampling regions. The period sampled for the physics measurement must be stable, which means that the time periods corresponding to the Pockels cell settling and ADC stability are excluded. However, it is important that the electronics be designed to allow sampling during the excluded time periods, so that the settling time can be monitored and used for systematic checks. The example in fig. 114 shows the time structure used for the $\mathrm{Q_{weak}}$ experiment, with a helicity reversal rate of 960 Hz, Pockels cell settling time of 70 μS, and an ADC delay of 42.5 μS. For MOLLER, the reversal rate will be 2 kHz and the goal Pockels cell settling time is 10 μS. This means that the integrating electronics settling should be correspondingly faster and operate at a higher sampling rate. The primary goal of the integrating electronics is to match the ADC bit resolution and sampling rate with the detector signal bandwidth needed to follow the changes in the beam (related to the helicity change and otherwise).

Figure 115 illustrates the concept behind the oversampling. The right hand side of the figure shows two simulated data sets (red and blue) for which the mean value differs (e.g. as a result of an asymmetry), as a function of sample time. The left hand side shows the samples accumulated by the ADC in histogram form. In this simulated data set, the mean difference between the two data sets is 20 mV, while the bin width in the histogram, which represent the resolution of the ADC, corresponds to 25 mV. Both of these values are exaggerated for illustrative purposes, but they show the general effect. The ADC resolution is too large to resolve the difference in the signal caused by the asymmetry during a single pair of samples, but if the signal is sampled many times within each period (i.e. the helicity window), the mean difference of the two distributions is clearly visible. This only works effectively, if the RMS width in the signal is significantly larger than the resolution of the ADC ($\Delta = V_{\mathrm{ref}}/2^n$ for an n-bit ADC), which then automatically exceeds the digitization error in the ADC $\sigma_d = \Delta/\sqrt{12}$. Another benefit of the larger RMS width in the signal is that any ADC non-linearity becomes less and less significant while increasing the number of ADC channels

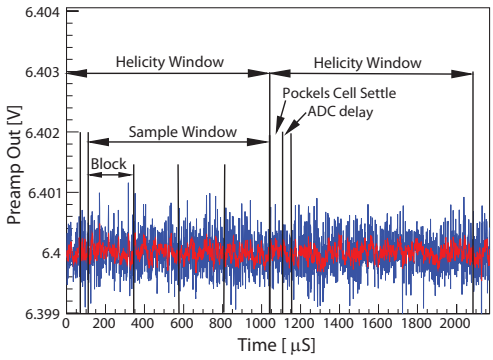

Figure 114: *Integration mode detector signal (simulated Gaussian white noise) at the preamplifier output with a* 500 kHz *bandwidth (blue) and a* 25 kHz *bandwidth(red) and how this signal is divided into helicity windows and sampling regions. A primary goal of the integrating electronics is to match the ADC bit resolution and sampling rate with the detector signal bandwidth needed to follow the changes in the beam (related to the helicity change and otherwise).*

over which the signal is spread. The experimental design and a suitable choice for the bandwidth in the preamplifiers and filters at the ADC input will ensure that this requirement is satisfied.

Specific Design Criteria The design of the integrating electronics, including the preamplifiers and ADCs is based on the criteria listed below:

1. Minimization of electronics noise contribution: $\sigma_E^2 \ll 2Q_P I_P + \sum_B 2Q_B I_B + 2Q_D I_D$
2. Minimization of drift effects and helicity correlated electronic pickup in the pedestal: $V_E^{\pm}(t) \rightarrow V_E$
3. Minimization of drift effects and helicity correlated electronic pickup in the amplifier: $g_{\mathrm{Amp}}^{\pm}(t) \rightarrow g_{\mathrm{Amp}}$
4. Bandwidth matching of all electronic components and between the various detectors that will be read out in integrating mode.
5. Optimization of ADC resolution and sampling rate with respect to a 2 kHz reversal signal and the 500 kHz input bandwidth required by the beam monitors and Pockels cell transitions. The goal is $\frac{\pi}{2} f_{3db} \geq 1$ MHz and ≥ 1 Msps.
6. Handle the large signal amplitude range across the different detectors (varying by a factor of 100), which requires significant preamp and PMT base flexibility.
7. Have good linearity (PMT, amplifier, and ADC).
8. Have good ADC amplitude resolution to spread signal RMS over many ADC bins (≥ 18 bits)

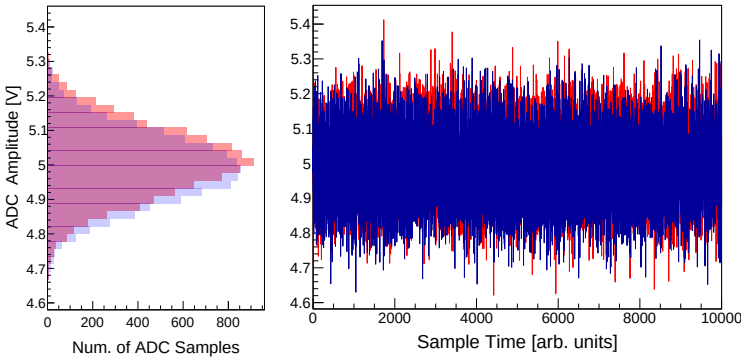

Figure 115: *Illustration of the concept behind oversampling. The right hand side of the figure shows two simulated data sets (red and blue) for which the mean value differs (e.g. as a result of an asymmetry), as a function of sample time. The left hand side shows the samples accumulated by the ADC in histogram form, where the bin width of the histogram is synonymous with the resolution of the corresponding ADC. The difference is again shown in red and blue, with the darker region being the overlap of the two distributions. The difference in the mean for the two signals is* 20 mV*, while the bin width (ADC resolution) is* 25 mV*, but the oversampling, together with the large RMS width in the signal, allows a high precision difference measurement within each helicity window.*

9. Have FPGA processing to facilitate

   Flexible accumulation and readout of various helicity window data items, including sample sums, sum of squares, min, and max, in predefined blocks.

   Streaming (readout every ADC sample)

10. Provide high data transfer bandwidth needed for streaming readout and production mode processing of all detector channels

K.2 Design Status

Based on the success of the Q_{weak} ADC and preamplifiers [64] that were designed at TRIUMF, the MOLLER design follows the Q_{weak} design, but with significant changes to the front-end (amplifier/filter/ADC) and the data readout (ADC crate system, data transfer hardware, and protocol).

K.2.1 The Photomultiplier and Base System

As discussed in Sec 8, the photomultiplier (PMT) and base system must accommodate both, integration mode and pulse mode acquisition.

PMT Type The PMT that has good properties for both acquisition modes is the 9305QKB by Electron Tubes. The quantum efficiency for the PMT, with a quartz window bi-alkali cathode, is shown in Fig. 116. This is the PMT that was used for that majority of the prototype beam tests mentioned in 8. The corresponding maximum ratings are shown in Fig 117. Figure 106 in Sec. J shows the measured photoelectron yield for this PMT, obtained with the ring 5 (Møller events) detector module design. Figure 118 shows the signal (upper, blue pulses) of the PMT with a typical high gain base design, again, using the ring 5 geometry. As

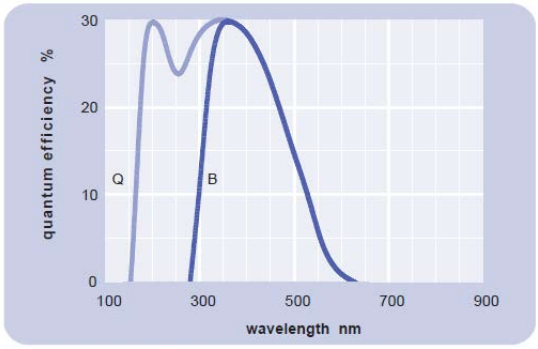

Figure 116: *Quantum efficiency of the Electron Tubes 9305QKB PMT with quartz window.*

maximum ratings:				
anode current	µA			100
cathode current	nA			200
gain	x 10^6			3
sensitivity	A/lm			200
temperature	°C	-30		60
V (k-a)[1]	V			2700
V (k-d1)	V			450
V (d-d)[2]	V			300
ambient pressure (absolute)	kPa			202

Figure 117: *Maximum ratings for the 9305QKB PMT.*

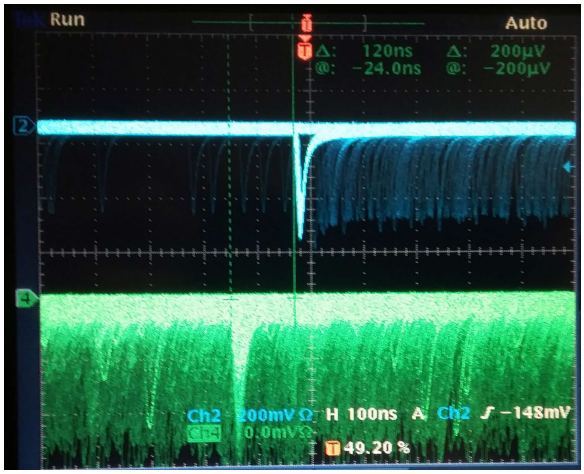

Figure 118: *The upper (blue) scope traces show pulses from the Møller (ring 5) module with the 9305QKB PMT.*

can be seen in the figure, most of the charge is collected within about 25 ns, which is more than fast enough for the MOLLER tracking requirements.

Leaving out the subscripts from above, the photoelectron rate at the PMT anode is $m = nR$, where n is mean number of photoelectrons produced at the cathode. The corresponding cathode current is simply $I_c = me^-$, while the charge at the cathode, per event, is given by $Q = ne^-$. For a Poisson distributed continuous source (integration mode) the root-mean-square shot noise at the anode is given by [113]

$$\sigma^2_{\rm shot} = 2QI_c\delta^{2k}B\frac{\delta}{\delta-1} = 2QIg^2B\left(1+\frac{\sigma_g^2}{g^2}\right)\,, \tag{18}$$

where δ is the PMT gain at each dynode, with k being the number of dynodes and δ^k the total gain of the PMT. The effective bandwidth B corresponds to half of the helicity reversal rate, or twice the integration window. The anode current is given by $I_a = I_c\delta^k$. Under ideal conditions, the relative shot noise would be equal to electron counting statistics:

$$\frac{\sigma_{\rm shot}}{I_c\delta^k} = \frac{1}{\sqrt{N}}\,, \tag{19}$$

for N detector events. However, this is modified by the factor in parenthesis, which is the noise degradation factor due to the gain in the PMT. It depends on the number of stages used in the PMT base. Due to the large rate in the detectors in integration mode, we will need to operate the PMT at a relatively low gain of around 1000, which will require the usage of a small number of dynodes, to prevent the voltage drop across each stage to get too small and to reduce the noise degradation. For example, using 5 stages in the base, at a gain of 1000, gives $\delta \simeq 4$ and an error degradation of $\sqrt{\delta/(\delta-1)}-1 \simeq 15\%$, while using 4 stages gives $\delta \simeq 5.6$ and $\sqrt{\delta/(\delta-1)}-1 \simeq 10\%$. This also shows that the gain cannot be made arbitrarily small, unless the base is operated as a unity gain base (without the use of the dynodes).

PMT base development status Two base designs are under development: An active one, which also incorporates the preamplifier on the same set of PCBs, inside the PMT housing, and a passive design, which does not incorporate the preamplifier, anticipating that it may have to be located a short distance from the detector, behind additional shielding, to prevent radiation damage. The active base design currently also includes all of the switching electronics that allows it to be switched remotely, between integration mode and pulse mode. This design has been tested on the bench, as well as with beam, including radiation damage testing. The base is connected via network cable to a computer, from which the switching, as well as gain and offset adjustments can programmed. The basic functionality and a picture of the prototype before testing, can be seen in Fig 119. The passive PMT base design is shown in Fig. 120. This design will serve as a fall-back, in case the active base described above does not survive under the expected radiation dose, for which the tests are still ongoing. For this base design, the preamplifier forms a separate board and is physically located outside the detector housing and several feet away from the detector itself.

K.2.2 The Preamplifier

The first preamplifier prototype is shown in Fig. 123 and the corresponding schematic is shown in Fig. 121. The amplifier is designed with selectable gain to ensure that the variations in the detector signals can be accommodated. In the prototype design, a set of micro-switches can be used to set the gain between 0.1 and 1.0 MΩ. The amplifier also supports offset control and it can be powered via an external 5V source, which is connected to an isolated DC-DC converter to supply $\pm$15 V internally and to provide ground isolation. The prototype does not yet support grounding through the HV of the base, which will be implemented in the next iteration.

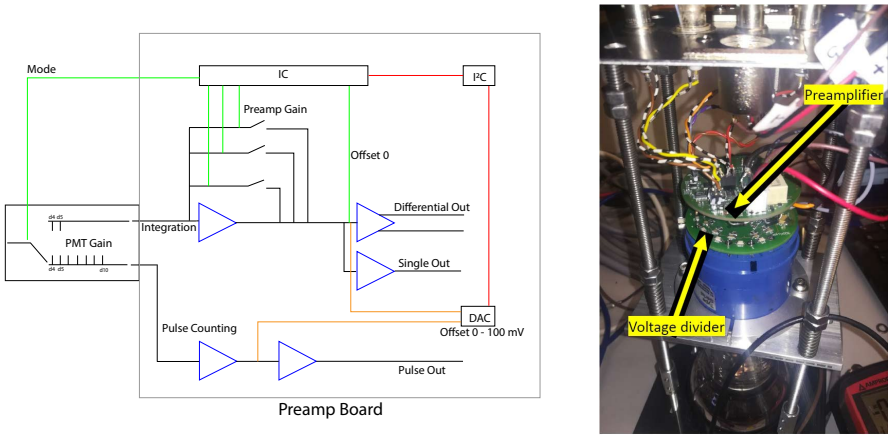

Figure 119: *Left: High level schematic that illustrates the functionality of the active base and preamplifier boards that are incorporated inside the PMT housing. The integrated circuits facilitate the switching of the base between integration mode and pulse mode, as well as the selection of the preamplifier gain, and offset adjustment. Left: Completed prototype prior to testing with beam.*

In order to extend the bandwidth to the 1 MHz goal for Møller, the OP-Amp, THS4631 from Texas Instrument [114] was selected as a good candidate, with a gain∗bandwidth product of 210 MHz. The preamplifier also incorporates a cable driver to maintain the signal over the long output cable, with large capacitance, between the amplifier and the ADC. The same OP-Amp is used for this purpose. In the prototype, Molex RF (threaded SMA) connectors are used for input and output signals, but this may not be used in the final version. The input side will be connected to PMT via a short low-capacitance cable. Because the preamplifier is powered by an isolated DC-DC converter, sufficient filtering and decoupling would be necessary to reduce ripples and switching noise (see below). Due to this drawback, the next version of the amplifier will likely incorporate a separate voltage regulator that will be connected to a ground isolated power supply and will supply all of the components on the amplifier with their needed voltage levels. After optimizing the values of some components, such as the input/feedback resistance and capacitance, the simulated bandwidth of the preamplifier was significantly increased to $\sim$ 2 MHz (see Fig. 122). To allow for relatively easy shielding and mounting close to the detector array, the PCB size is kept as small as practically possible. The dimension of the prototype board is 8 cm $\times$ 3 cm.

The prototype was tested on the bench and its performance was evaluated. Fig. 124 shows the test set up. The preamplifier board under test (middle) was shielded in a 1.5 inch diameter, cylindrical container made from aluminum tube. For testing, the current signal source was produced by a function generator (left) and a V-to-I converter. The output signal was measured by a digital oscilloscope.

It was found, that the prototype was basically functioning well under various test conditions, but further improvements will have to be made in the next version. The OP-Amp THS4631 on the prototype board uses a relatively high amount of power. The corresponding increased load for the DC-DC converter leads to relatively larger voltage ripples. In addition, as the size of our PCB board is much smaller, the interference from the power supply switching noise is larger. As mentioned above, the next version will use an isolated voltage regulator to remove the additional noise. Bandwidth tests were conducted with various configurations of trans-impedance gain, the length of input cable, and the length of output cable, to understanding about how the bandwidth is affected by the trans-impedance gain and input capacitance, and to study the capability of the cable driver. Some results of the bench tests are provided below.

Fig. 125 shows the bandwidth test results for two different gain settings, indicating that a broader band-

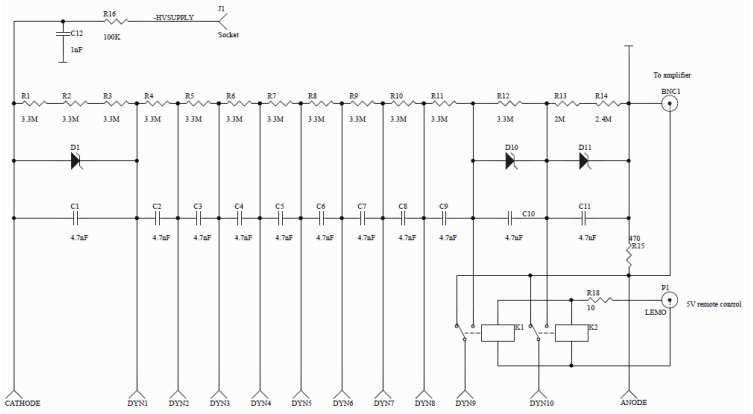

Figure 120: *Design of the passive PMT base. The base does not include active components, such as transistors, or integrated circuits. The switching is implemented via miniature reed relays.*

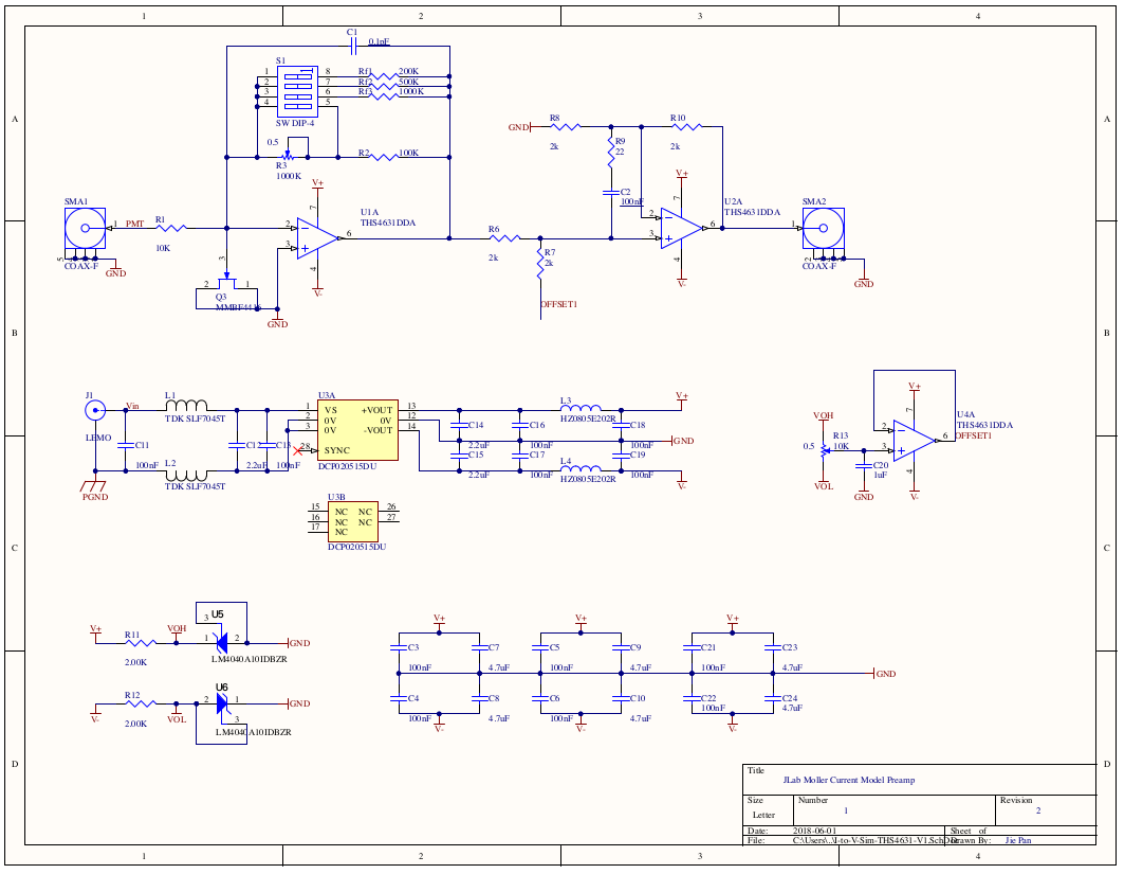

Figure 121: *The schematics for Møller preamplifier design.*

width can be obtained with a smaller gain. With a gain of 167 kΩ, the f_{3db} cutoff is $\sim$ 1.5 MHz, while for a 1 MΩ gain f_{3db} decreased to $\sim$ 180 kHz. It is therefore important to know the signal amplitude and the corresponding needed gain for each detector module in advance; most of the amplifiers for different modules need slightly different configurations.

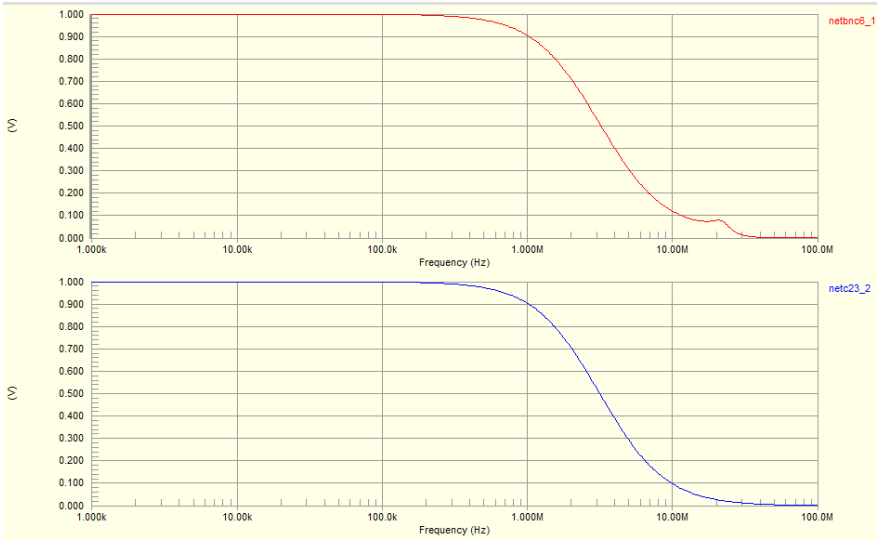

Figure 122: *The simulated Møller preamplifier frequency response at a trans-impedance gain of 1 MΩ, assuming 0 input and load capacitance. The lower blue curve show the response after I-to-V conversion stage and the upper red curve show the response after the line driver stage. About 2 MHz -3dB cutoff was obtained for both stages.*

Figure 123: *The first prototype of the Møller/P2 preamplifier.*

The frequency response was also measured under various input/output cable length conditions. The results are summarized in Table 31. RG-58 cables ($\sim$1 pF/cm) were used in the tests. From the preliminary results, shorter input cable (or smaller input capacitance) leads to a larger bandwidth. Bench tests also showed that the cable driver in the current design also has very good driving capability. Increasing the output cable length from 30 m to 200 m, one can see some effects on bandwidth and the relative gain, but the variation on the gain is relative small and acceptable. Transient or pulse transition response of the amplifier under various input cable lengths (capacitances) was also studied. A 4 μA current square wave pulse was used as input singal, while the output signal was measured with an oscilloscope. Output signal raise time and settle time were measured to verify that the preamplifier can follow rapid changes of the input signal, such as the PMT current changes due to various beam condition changes. Some of the results are listed in Table 32. One overall result is that the input cable length (from the PMT) must be short enough, so that the settling time of preamplifier is much less than the helicity reversal settling time ($\sim$10 μS), which requires that the cable length between PMT and preamplifier should be limited to somewhere around $\sim$ 1 m. Slightly

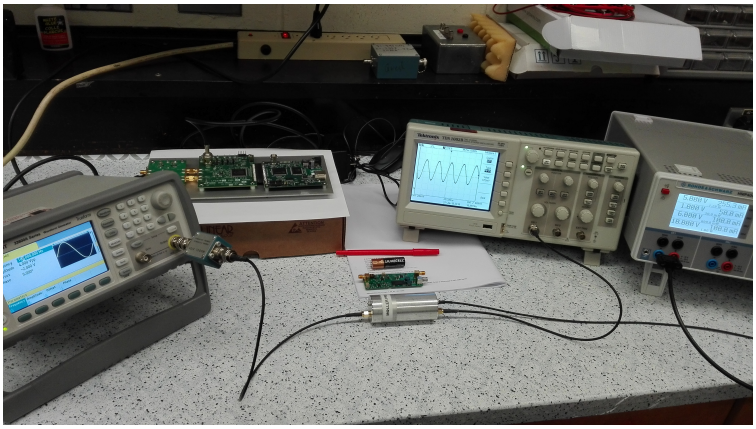

Figure 124: *Bench tests set up for the preamplifier prototype.*

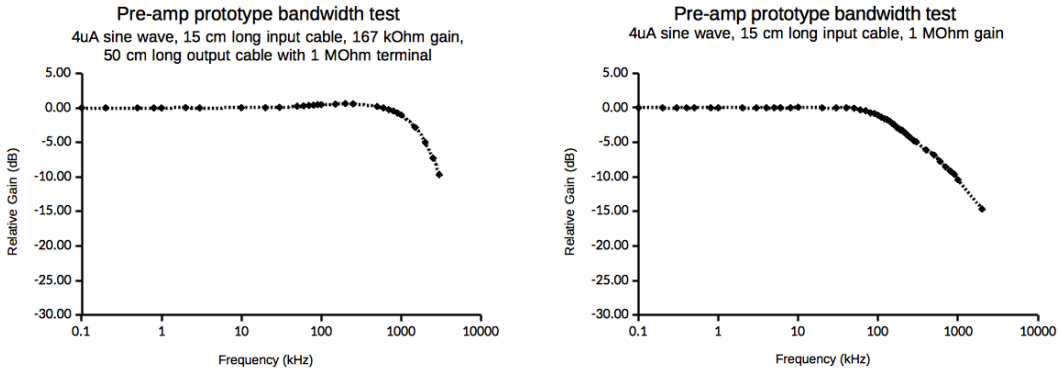

Figure 125: *The bandwidth test results with the preamplifier prototype. During this test, a 4 μA sine wave current source was used as input. The input cable is 15 cm long, and the output cable is 50 cm long with 1 MΩ terminal. Left: Frequency response at 167 kΩ trans-impedance gain. Right: Frequency response at 1 MΩ trans-impedance gain.*

longer cable lengths can be accommodated with appropriate minor design changes, but only within limits. Minimizing the preamplifier noise is one of the most critical criteria for the frontend electronics design. The input capacitor and the input protection resistor are the dominant noise sources of the preamplifier and these will be optimized in future prototypes.

K.2.3 The Integrating ADC Board

The I-to-V trans-impedance amplifier is followed by a digital integrator, which incorporates a low-pass anti-aliasing filter, an analog-to-digital converter and a FPGA to handle all aspects of sampling, initial data processing, communication with the rest of the DAQ and trigger system, and data transfer off the board. A block schematic of the board is shown in Fig 126. The first version of the board is fully designed and is currently undergoing verification and board layout preparation. A first set of prototype boards will be prepared in the first half of 2020. At the same time, improvements to the design of this board are ongoing. The current status and some details are summarized below.

Table 31: *Summary of bandwidth tests under various test conditions*

Transimpedance gain	Input cable (length)	Output cable (length and terminal)	f_{3db} cutoff
167 kΩ	15 cm	50 cm, 1 MΩ	1.5 MHz
	55 cm	50 cm, 1 MΩ	400 kHz
	32 m	30 cm, 50 Ω	7 kHz
1 MΩ	15 cm	50 cm, 1 MΩ	180 kHz
	45 cm	50 cm, 1 MΩ	160 kHz
	55 cm	50 cm, 1 MΩ	145 kHz
	150 cm	50 cm, 1 MΩ	90 kHz
	55 cm	235 cm, 1 MΩ	145 kHz
	55 cm	235 cm, 50 Ω	150 kHz
167 kΩ	55 cm	30 m, 50 Ω	330 kHz
	55 cm	100 m, 50 Ω	270 kHz
	55 cm	200 m, 50 Ω	230 kHz

Table 32: *Pulse responses of the pre-Amp to various input cable length*

Input cable length	Input capacitance	Rising time (output)	Settling time (output)
15 cm	15 pF	1.6 μS	3 μS
55 cm	55 pF	2 μS	4 μS
240 cm	240 pF	4 μS	8 μS

The Front-end Filter The filter is designed with an instrumentation amplifier at the front, which will be used as a cable receiver to reject common-mode noise coupled onto the cable from the detector and preamplifier. The cable receiver is followed by a lowpass filter designed to remove noise which would otherwise corrupt the summation data. A 5 pole filter was designed with a cutoff frequency of 500kHz to limit the bandwidth without affecting the trans-impedance amplifier response. The combination of front-end trans-impedance amplifier and anti-alias filter allows the system settling time and noise bandwidth to be controlled separately.

Fig. 127 shows the schematic for the entire front-end of the ADC board, including the differential signal receiver, the filter, and the ADC. This board is design without the FPGA and optical data transceiver parts and instead connects to an FPGA evaluation board that can be inserted into a computer PCIe slot. This is currently being used to test the front-end design. The completed board is shown in Fig. 128. All components and values were carefully selected in order to meet the bandwidth requirement. The circuit was modeled and optimized in simulations. Fig. 129 shows an example simulation result. The 1 MHz sharp cut-off frequency can be obtained with a low distortion, flat top gain response up to 500 kHz (indicated by the red solid line in the plot). The device is currently undergoing benchtop testing and will be used together with the FPGA evaluation board in a full detector-electronics chain test during beam test in the Mainz MAMI facility in 2020.

Analog-to-digital Converter The newly relased, cutting-edge technology analog-to-digital converter (ADC) chip, LTC2387-18 from Linear Technology [115], was selected as our ADC candidate. It is a low noise, high speed, 18-bit successive approximation register (SAR) ADC with excellent linearity, wide dynamic range and large signal bandwidth. It features a serial LVDS digital interface to support high speed operation

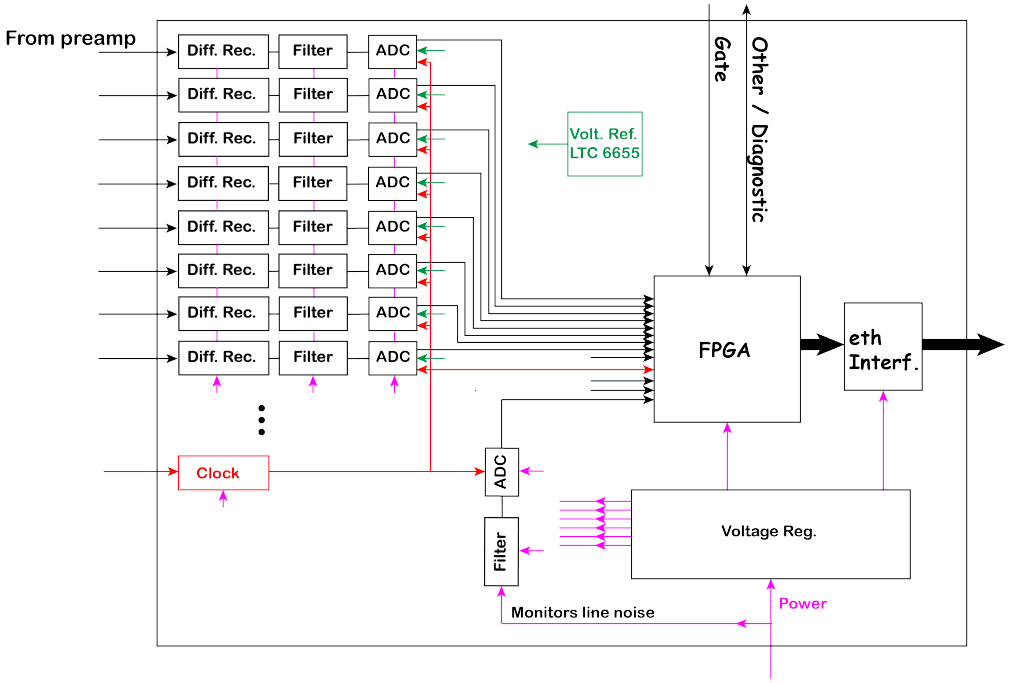

Figure 126: *The schematic diagram for the ADC board. There are 16 channels per board, each of which incorporates a differential signal receiver, an anti-aliasing filter, and the ADC chip. The on-board FPGA controls the sampling of the of ADCs and assembles the samples into helicity window data items, or facilitates the buffering and transfer of every ADC sample in streaming mode. The board also incorporates several Gbit ethernet fiber-optic transceivers to transfer the data off the board and to communicate with the rest of the DAQ and trigger system.*

while minimizing the number of data lines, allowing us to integrate multiple channels in a single board. The 18-bit ADC can operate at a selectable sampling rate up to 15 MSPS. The sample rate is several times the anti-alias filter cutoff frequency and is a multiple of 60Hz to reject power line noise.

To evaluate the actual performance of LTC2387-18, a set of evaluation boards from Linear Technology were purchased and tested, as shown in Fig. 130. The board in the middle (DC2290A) is the ADC chip evaluation board, the board on the left (DC2403) is a differential driver board, and the board on the right (DC718) is a data acquisition board with a USB controller. A data collection software, called PScope, provided by the manufacture, was used to collect, transfer and analyze the ADC data. We measured the ADC responses to DC (battery), sine wave, and square wave differential signals by varying signal amplitude and/or frequency. The ADC has a good frequency response up to a range larger than our 1 MHz bandwidth requirement, see Fig. 131 for reference.

Testing with a square wave input was used to approximate parity signals. The reconstructed waveform of the digitized square wave data showed only small distortions on the raising and fall edges. Using PScope software, the number of data samples that could be collected is limited by a maximum buffer size (32768 samples, or 2.2 ms sampling time). In order to continuously collect and save data samples for longer time for some tests, such as noise measurement and linearity a python script was developed, allowing us to take data continuously but with a small deadtime from transferring data to DAQ computer. Fig. 132 (left) shows a distribution of ADC values with small RMS as an example of a longer measurement of a constant voltage source (3.0 V DC). Another, longer, time measurement with square wave input (100 mV_{pp}, $\mathrm{V}_{\mathrm{offset}}$ = 2.048 V) was also performed. The waveform was reconstructed from ADC values and is shown in Fig. 132 (right).

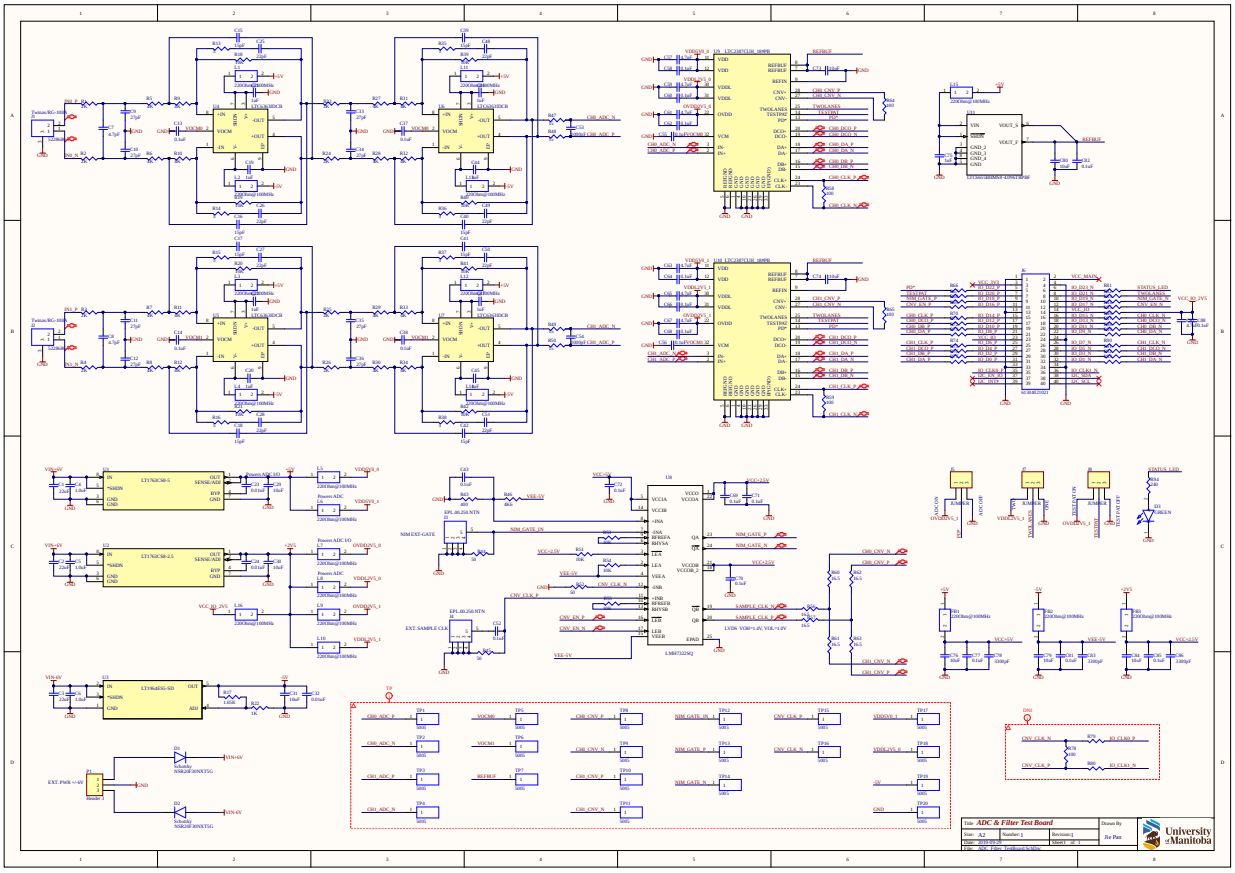

Figure 127: *The schematic diagram for the front-end of the ADC board, including the fully differential receiver, anti-alias filter, and ADC. This design is separated from the overall board and interface with an FPGA evaluation board. allowing testing of the front-end without the full implementation of the ADC board with the FPGA and data transceivers.*

Other tests results also mostly agreed with the specifications claimed by the manufacturer, except that the measured signal-to-noise ratio (SNR= 75 dB at $f_{in} = 1$ MHz) was slightly worse than the specification (SNR= 96 dB at $f_{in} = 1$ MHz). However, this can also be attributed to our test environment. For example, so far, the tests were conducted without any shielding on the boards, so that electromagnetic interference may contribute to the noise. Additional, more careful, noise tests and linearity tests are being carried out. One requirement for the ADC is, that we can use it to study the transitions during helicity reversal periods and precisely determine the helicity gate settle period and synchronize all detector channels accurately. The ADC tests will continue to verify this for this model.

FPGA The 18-bit ADC sampling clock is controlled by signals derived from external clock and gate signals. The output of each ADC in the module is summed over a selectable number of samples inside an FPGA and made available to the DAQ system through several Gigabit Ethernet interface per board.

The selected FPGA for the ADC board is Zynq UltraScale+ from Xilinx [116]. The FPGA will be implemented as a System-On-Module (SoM Mercury-XU8 produced by Enclustra [117]) rather than by incorporating the FPGA directly in the board, which is easier to handle during layout design and makes the FPGA replaceable if it gets damaged. The UltraScale FPGA is a complete System on Chip (SoC), featuring a quad core ARM Cortex-A53 processor system (PS), allowing embedded linux running on the FPGA.

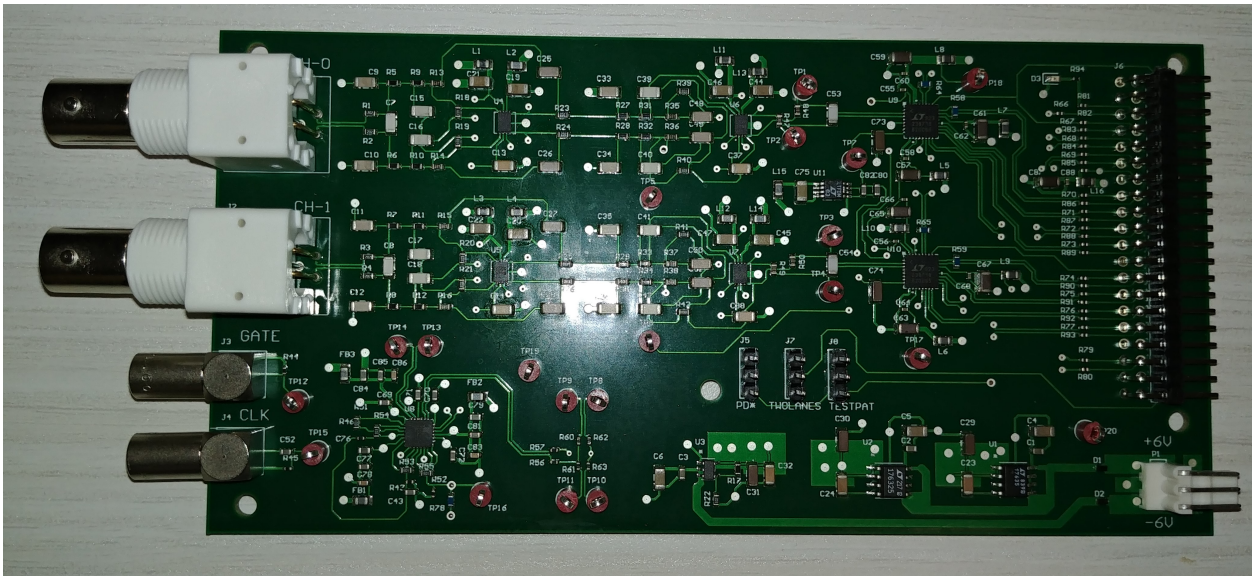

Figure 128: *The front-end of the ADC board, including the fully differential receiver, anti-alias filter, and ADC. This design is separated from the overall board and interface with an FPGA evaluation board. allowing testing of the front-end without the full implementation of the ADC board with the FPGA and data transceivers.*

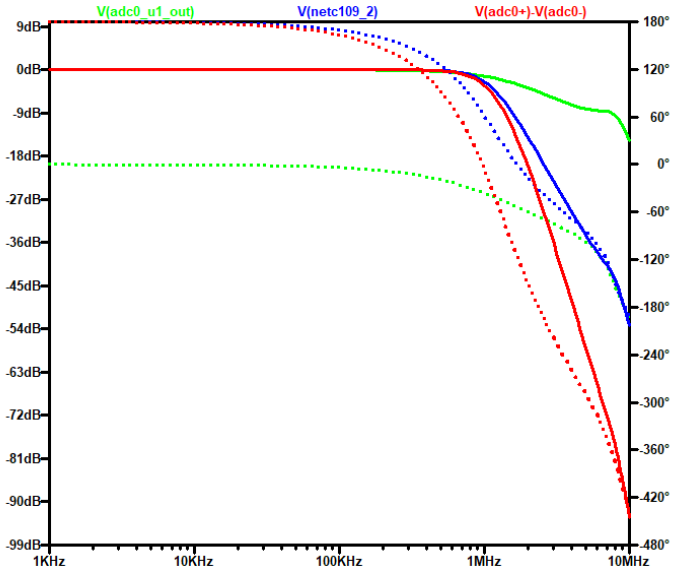

Figure 129: *Simulation result of the ADC input filter. The x-axis indicates the input signal frequency, the left y-axis indicates the relative gains represented by solid lines and the right y-axis indicates the signal phase shifts represented by dashed lines. The line colors represent the signals at different stages in the filter; green, blue and red are for the signals from output of first (AD8421), second (THS4631) and third IC (AD8139), respectively.*

The Mercury UX8 module adds several additional storage and interface modules, including DDR4 ECC SDRAM, eMMC, flash, dual Gigabit Ethernet, and dual USB 3.0. The full ADC board will be configured

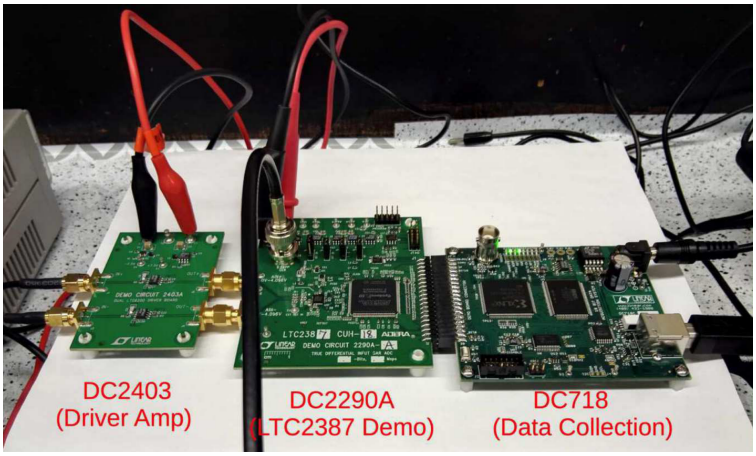

Figure 130: *Test setup for ADC evaluation board.*

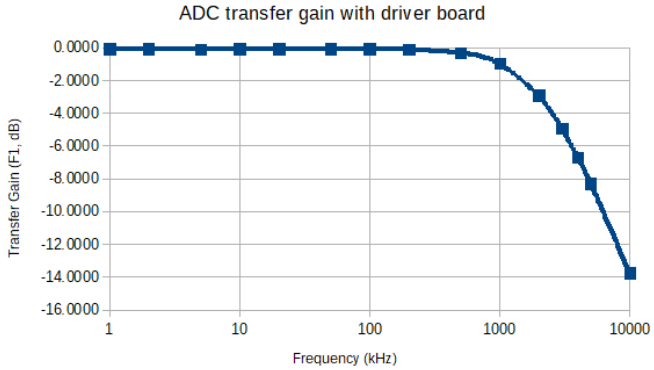

Figure 131: *Frequency response of ADC evaluation board.*

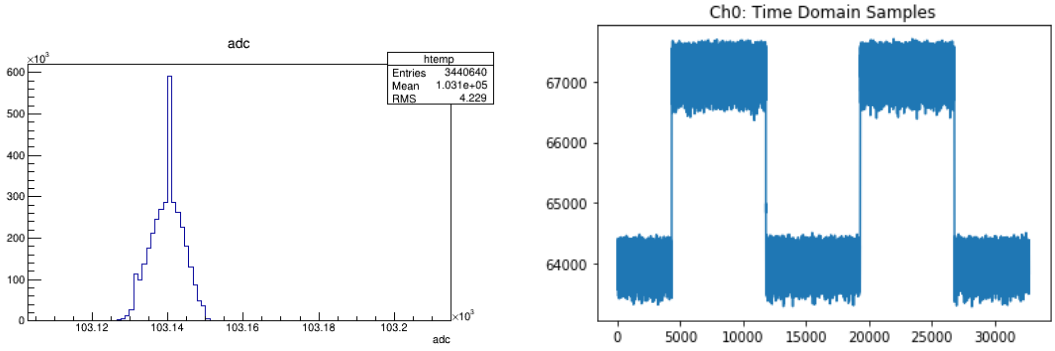

Figure 132: *Example results of continuously sampling with the evaluation board. Left: The ADC value distribution from measuring a 3 V DC constant voltage source. Right: Reconstructed waveform from measuring a square wave voltage source.*

for 10 Gigabit Ethernet transfer via several fiber-optic links, allowing full streaming mode operation of all

16 channels per board, for diagnostic purposes. The slow control of the FPGA will also be communicated via optical transceivers.

The FPGA provides 122 user pins that are available for general purpose Input/Output. For the 16 ADC channels on a single board each ADC channel can be therefore be assigned a maximum of 7 I/O pins for data transfer and control, which meets the requirements to operate the ADC in two-lane mode used for maximum data transfer rate to the FPGA. For testing purpose an evaluation board with the Mercury-XU8 SoM and a preliminary test firmware is being used.

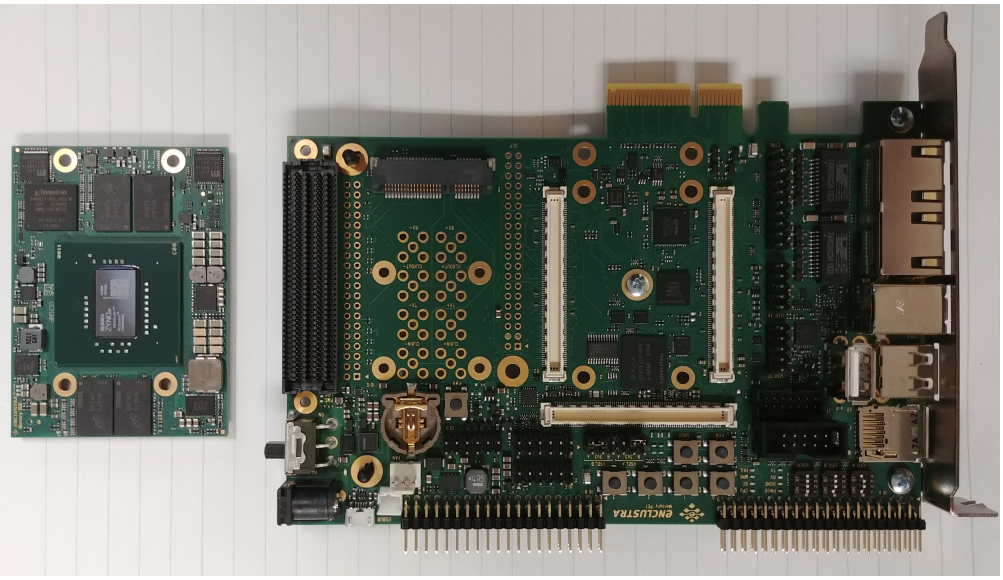

Figure 133: *The FPGA evaluation board (left) and the FPGA itself, as a system-on-module (SoM) as it will be used on the ADC board.*

L Shower-max

The shower-max baseline detector concept has an active, Cherenkov-based medium that consists of a $\sim$9.5 X_o, 4-layered "stack" or sandwich of fused silica (quartz) interleaved with high-purity tungsten. This is a sampling electromagnetic calorimeter designed to have a proportional response with better than 20% resolution for single, incident electrons with energies between 2 and 8 GeV. It uses an aluminum air-core light guide to direct Cherenkov light from the high-flux region to a shielded PMT $\sim$25 cm away. Given the high rates of intercepted scattered electrons ($\sim$8 GHz/detector for the Open region modules) over a long period of time, the radiation hardness of active detector components is a primary consideration in the basic design concept. This Appendix will cover details of the detector design and development, the simulation package used and recent testbeam results.

Development of the shower-max concept has undergone several iterative advances using a Geant4-based optical quartz Monte Carlo package (QSIM) developed by the PREX and MOLLER collaborations. The QSIM framework was developed primarily for the thin-quartz main integrating detectors for MOLLER (and PREX-II/CREX) and has been extended to include the shower-max and Small Angle Monitors. The simulation package has been extensively "benchmarked" or validated with real testbeam data, and it allows advanced design geometries to be explored with reasonable confidence in the generated pulse-height or photo-electron distribution outputs. Details of the QSIM package and its benchmarking to real testbeam data are given in the next section. The baseline design is detailed in Sec. L.2 and pre R&D and SLAC testbeam details are presented in Sec. L.3.

L.1 G4 Quartz Simulation (QSIM) package

This section focuses on the specific optical features and properties that are incorporated into the simulation framework as well as the benchmarking procedure and results. Geant4's unique capability of starting a simulation with the transport and propagation of a charged particle through matter, and completing it with the detection of generated and transported optical photons by a photo-sensitive area, all within the same event loop, make it a comprehensive and effective tool for modeling the optics of Cherenkov detectors and their associated light guides.

L.1.1 Optical Material Properties and Models

In G4, optical photons are produced in three physical processes: Cherenkov, scintillation and transition radiation. The optical transport functionality provides the possibility to set the specific optical properties for both bulk materials and surfaces. These properties include: dispersion, attenuation and surface polish for quartz tiles and quartz PMT window, and specular and diffuse reflectivity of cathode, quartz wrapping (if used), and light guide surfaces.

The refractive and attenuation indices in fused silica quartz, over the relevant wavelength range of 160 - 700 nm (1.77 - 7.75 eV), are readily available in the literature [121, 122]. The reflectivity (and absorbance and transmittance) of a typical bialkali photo-cathode is also available in the literature [123]. The values used in QSIM are displayed in Fig. 134 along with their literature references. Note that the PMT candidate for the shower-max and thin-quartz detectors is the ET Enterprises 9305KQB 70 mm diameter bialkali photocathode with fused silica window. The specular reflectivity of potential light guide materials, as a function of wavelength and angle, have been measured at Idaho State using a custom apparatus; the apparatus and measurements are briefly summarized in Figs. 135 and 136. The top three light guide material candidates are aluminized-mylar, Miro-silver 27, and Anolux UVS. All the bulk material optical properties are specified in the simulation primarily though a series of linearly-interpolated look-up tables as a function of wavelength. There is currently no lookup for reflectivity as a function of angle, but rather an average reflectivity value is

chosen based on our measurements. The final property to discuss is the quartz surface polish which is the key unknown parameter that is empirically determined through the benchmarking procedure discussed in the next subsection.

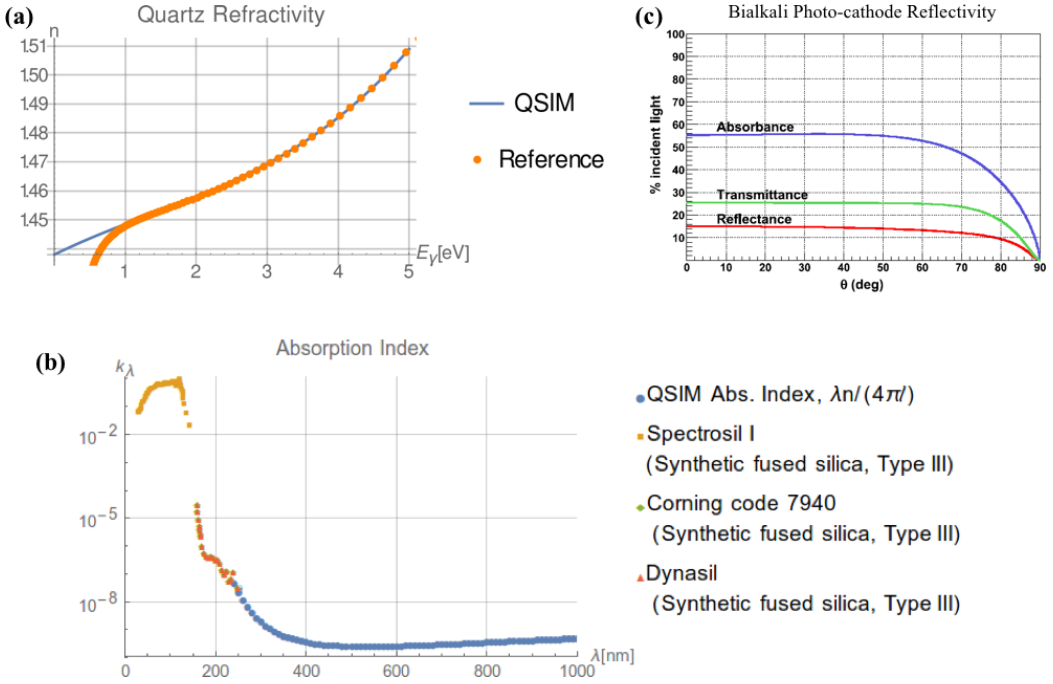

Figure 134: ***(a)*** *Quartz refractive index as a function of photon energy; disagreement in the far infrared is outside our sensitivity range; orange dots are from reference [121].* ***(b)*** *Light attenuation in high-purity fused silica. Various reference data (type III fused silica–same as Spectrosil 2000) are used for $\lambda \leq 225$ nm; for $\lambda > 225$ nm, the absorption index, k_λ, is extrapolated using an exponential decay (Beer-Lambert law).* ***(c)*** *The average photo-cathode reflectivity over all angles is approximately 12.5%.*

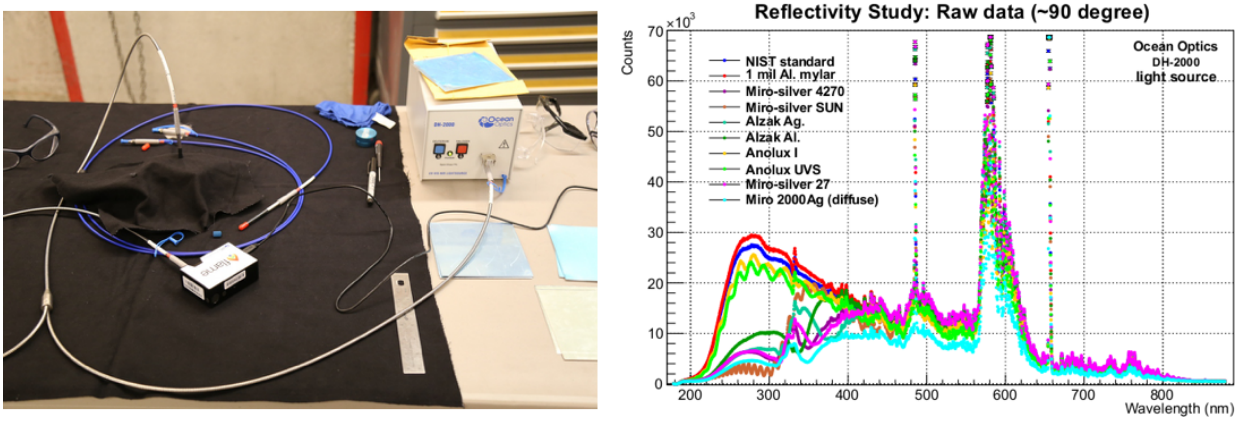

Figure 135: *(Left) Photograph of reflectivity measurement apparatus for light guide and wrapping materials. Main components are a 25 W deuterium light source (200 - 800 nm), an Ocean Optics USB Flame spectrometer, and NIST aluminum specular calibration standard. (Right) Raw data in counts per 380 pm wide bins. The primary features of the spectra come from the deuterium bulb. Several different 20 mil aluminum-sheet reflectors were tested as well as 1 mil aluminized mylar.*

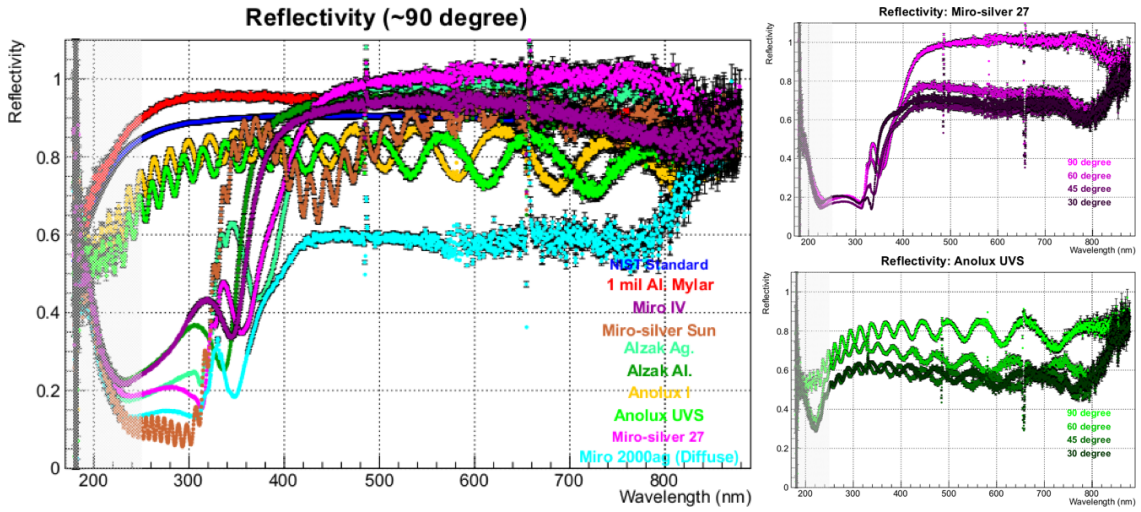

Figure 136: *(Left) Specular reflectivity measurements calibrated with traceable NIST calibration standard. Note the excellent performance of aluminized-mylar wrapping in the UV and Miro-silver 27 in the visible wavelength region; the oscillating reflectivities of Anolux I and UVS are believed to result from thin-film interference phenomenon. (Right) These two plots show the reflectivity measurements for Miro-silver 27 (top) and Anolux UVS (bottom) for 90, 60, 45, and 30* ^{o} *angles.*

G4 has two optical models for handling the surface properties of materials with respect to optical photon transport: GLISUR and UNIFIED. In QSIM, the GLISUR model is used to specify the quartz bulk surface roughness in terms of a single (ground) polish parameter; this parameter effectively dictates the probability of total internal reflection inside the quartz and thus the amount of light that exits the quartz towards the PMT; the 45^{o} bevel cut in the quartz breaks the total internal reflection and allows the light to escape. The UNIFIED model allows control of the radiant intensity of mirror surfaces and is used to model the light guides. The quartz tile's polish is specified to have a Total Indicated Reading (TIR) of 20 Angstroms or better from the manufacturer. Typical benchmarked polish parameters found for our Heraeus quartz tiles range between 0.94 and 0.98 (where 1.0 is a perfect polish).

L.1.2 QSIM Benchmarking

The benchmarking or validation of QSIM is accomplished through a multi-step process. All optical material properties (from literature) and processes (from G4) are included in the simulation along with the precise detector geometry under study. Also important here is the precise prototyping of simulated designs for testbeam studies. The basic idea of the benchmarking process is to control all known optical property inputs and then tune the quartz polish parameter to force the simulation to match real data. The big caveat here is that in order to convert measured ADC distributions to PEs (to compare real data with simulation), the PMT gain must be known. We can measure our PMT gains to $\sim$5% or better precision.

The first step in the process is to design and simulate a special version of the detector, referred to as the "benchmarking" prototype, which has no light guide complication, but instead has the PMT window within millimeters of the quartz bevel(s). Additionally, by using only a single piece of quartz (in the initial configuration of the detector) the quartz polish parameter can be determined from testbeam data. This process and result are demonstrated for the PREX-II/CREX thin quartz detector in Fig. 137, which has no light guide by design. Following the initial calibration of the quartz polish, the "benchmarking" prototype stack is assembled, one layer of tungsten and quartz at a time, and testbeam data is collected for each added layer. This data is then compared with simulation to provide a consistency check of G4's electromagnetic shower-

ing process and validate QSIM before simulating the "full-scale" shower-max prototype which includes the light guide. Results from the stack benchmarking procedure are given in Sec. L.3.

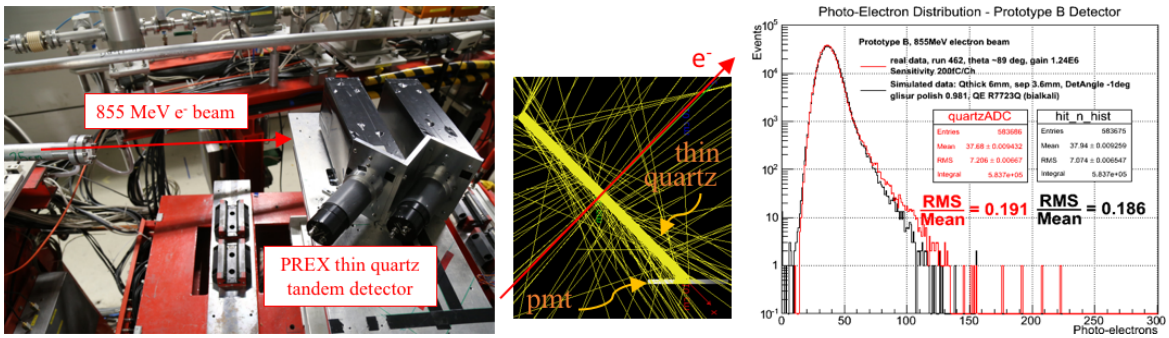

Figure 137: *2016 MAMI testbeam benchmarking of QSIM for the PREX-II/CREX thin-quartz detector. (Left) Photo of the testbeam setup at the Mainz Microtron. (Middle) G4 visualization of a single electron event; yellow lines are optical photons; this shows the importance of total internal reflection inside the quartz tile for optimizing the detector yield (and resolution). (Right) PE distribution from QSIM (black), using a polish parameter of 0.98, compared with a real data run from MAMI (red).*

An additional QSIM/G4 validation study was performed during the 2016 MAMI testbeam run that involved the use of 280, 320, and 400 nm long-pass filters installed between the quartz bevel and PMT. This was done in order to check and validate our quartz dispersion table and G4's Cherenkov process implementation in QSIM. This study used the PREX-II/CREX detector and thus had no light guide complication. A fused silica "blank" filter was also used to account for reflection losses that occur at the filter surfaces, so we could directly compare the long-pass filter results to the no-filter result. The simulated wavelength spectrum of Cherenkov light reaching the photo-cathode, for each filter setting, is shown in Fig. 138. The yellow histogram is the (blank) no-filter spectrum and the other spectra with vertical line cuts represent the corresponding long-pass filter simulations. Note that these spectra lie atop one another except for the yellow distribution which is higher due to a slight difference in the incident beam angle on quartz during the blank filter test (an unintended consequence of the testing/installation procedure). A very busy plot of the PE distributions from the testbeam filter study is given in Fig. 139 along with the corresponding simulations. Excellent agreement is seen for all filter settings giving a compelling validation of the optical material properties and processes in QSIM.

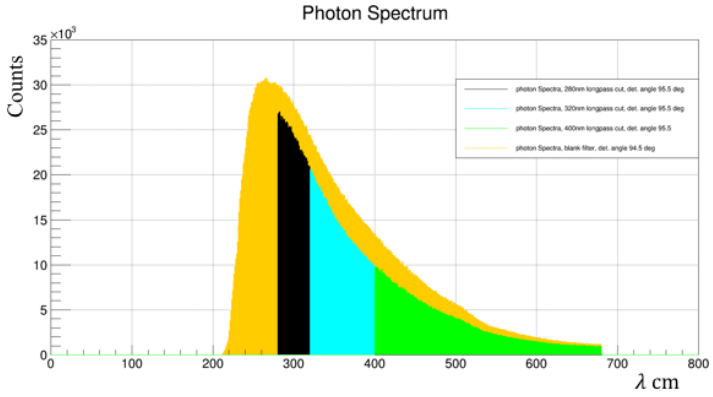

Figure 138: *Simulated Cherenkov light spectrum incident on the PMT cathode for the long-pass filter study. The yellow distribution is from a fused silica, so-called "blank" filter (should have no effect other than reflection losses), black is for the 280 nm filter, cyan is for the 320 nm filter, and green for the 400 nm filter.*

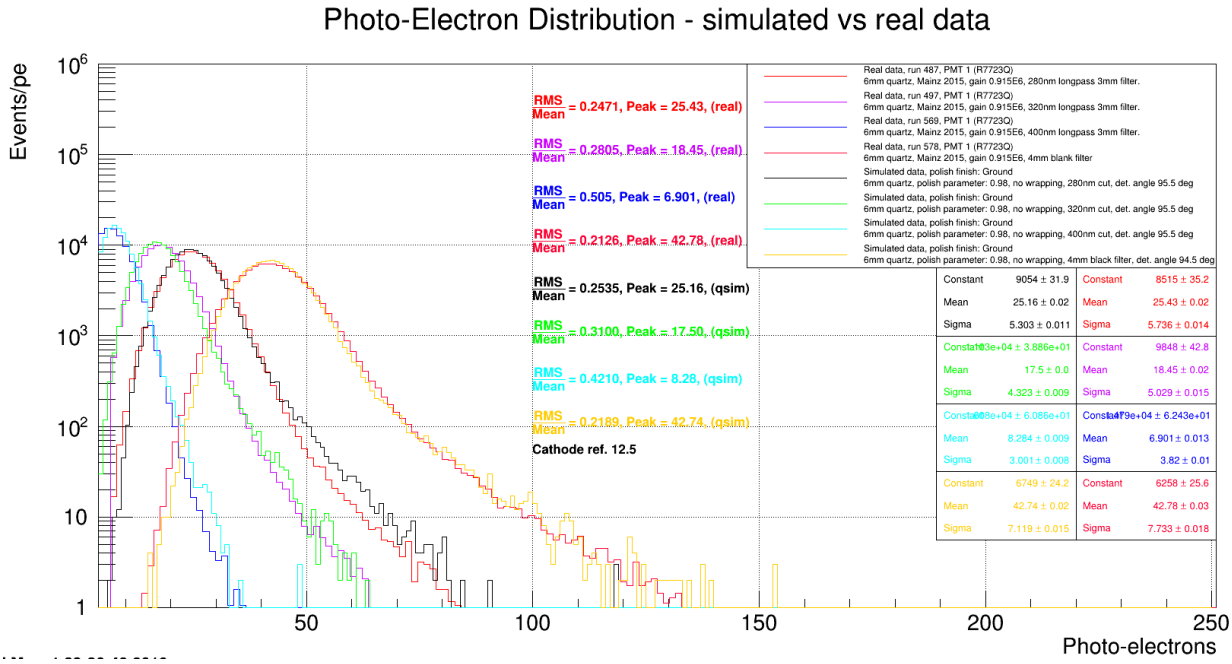

Figure 139: *Real and simulated PE distributions from the long-pass filter study for the PREX-II/CREX detector at MAMI. Real/simulated data are red/yellow ("blank" filter), red/black (280 nm filter), purple/green (320 nm filter), and blue/cyan (400 nm filter). The photon spectra for the simulated distributions are given in Fig. 138. Applying the corresponding long-pass wavelength cut in the spectra gives excellent agreement with real data. Note the green and cyan colors are swapped relative to those in Fig. 138.*

L.2 Baseline Design

Given the Cherenkov-based, sandwich calorimeter design choice, the radiation-hard detector components were chosen to be Spectrosil 2000, pure tungsten, and aluminum. Following these decisions, and our experience with thin-quartz detector designs, a series of stack geometries were studied which led to the alternating bevel and two-sided "funnel" light guide design shown in Fig. 140. These early studies also indicated no significant performance enhancement when configuring the stack with more than four layers; fewer layers means lower cost and simpler design and assembly.

L.2.1 Ring Geometry and Energy Acceptance

As with the thin-quartz "Møller ring 5" detector ring, the shower-max ring will have slightly different radial acceptances in each of the three azimuthal or ϕ-regions: Open, Transition, and Closed. The Open regions are centered between two spectrometer coils, the Closed regions are in the coil shadows, and the Transition regions are between the Open and Closed regions; all ϕ-regions have the same azimuthal extent. The situation is depicted in Fig. 141. Given the 7-coil toroid design, the 28 shower-max modules around the ring consist of seven Open, seven Closed, and fourteen Transition modules.

An important consideration in the optimization of the stack thickness is the energy acceptance of the detector. While the three ϕ-region detectors have similar geometric acceptances, they have quite different energy acceptances. Due to the phi de-focusing character of the spectrometer, lower energy scattered electrons are swept into the Transition regions and even lower energies are swept into the Closed regions, as shown by the accepted energy distributions on the left side of Fig. 142. It was determined from simulation

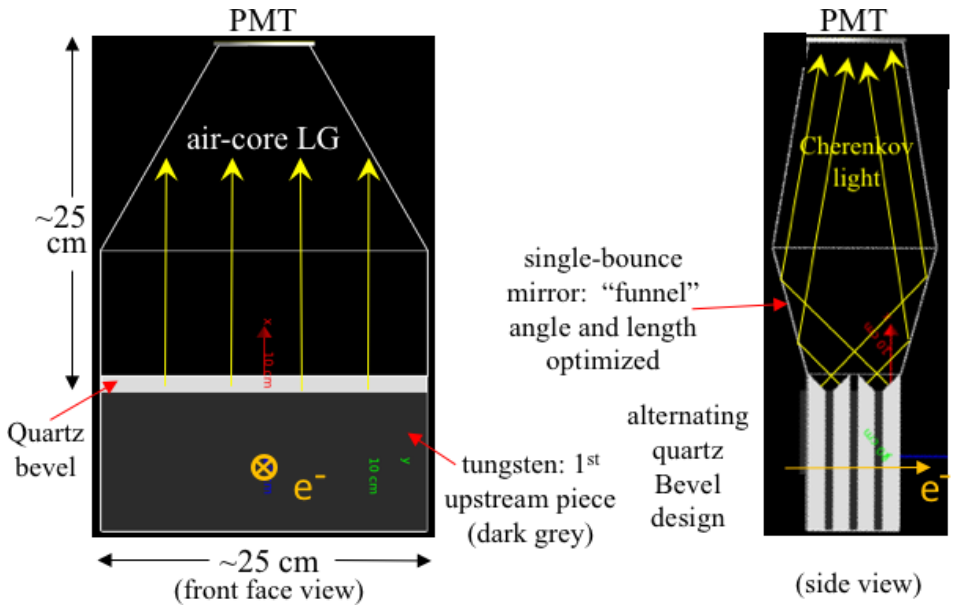

Figure 140: *Schematic of the shower-max design concept. Yellow arrows depict light rays exiting the quartz bevel. Note that the quartz (white) and tungsten (dark-grey) thicknesses are 12.5 mm and 6 mm respectively (this was a preliminary stack configuration).*

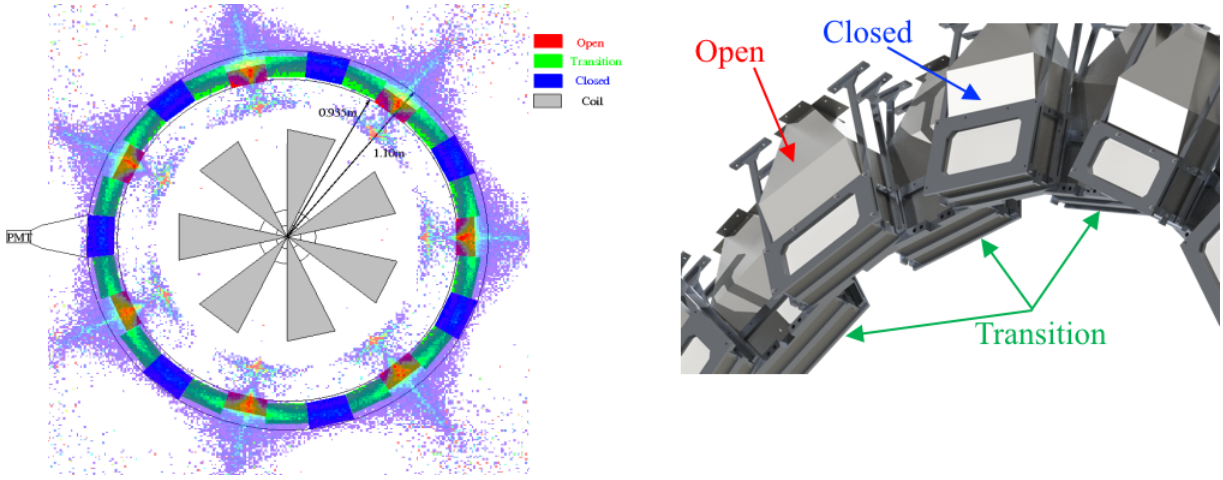

Figure 141: *(Left) Schematic cartoon (not to scale) illustrating the azimuthal or phi segmentation of the shower-max ring and the three ϕ-regions (looking downstream); overlaid is a visualization of the simulated scattered flux at the detector plane. (Right) Closeup view of the shower-max ring CAD showing the staggered detector design.*

studies that a stack thickness near 10 X_o provides better than 20% resolution for single electrons over the full range of accepted energies (∼2 - 8 GeV), as shown on the right side of Fig. 142. These single-electron detector response resolutions are critical performance parameters, but the overall finite resolution of the detector during MOLLER, which drives its excess statistical noise during the integrating measurement, is a more complicated convolution of the accepted energy distribution of each detector and its response to those energies. This is further discussed in the next section along with expected rates and yields.

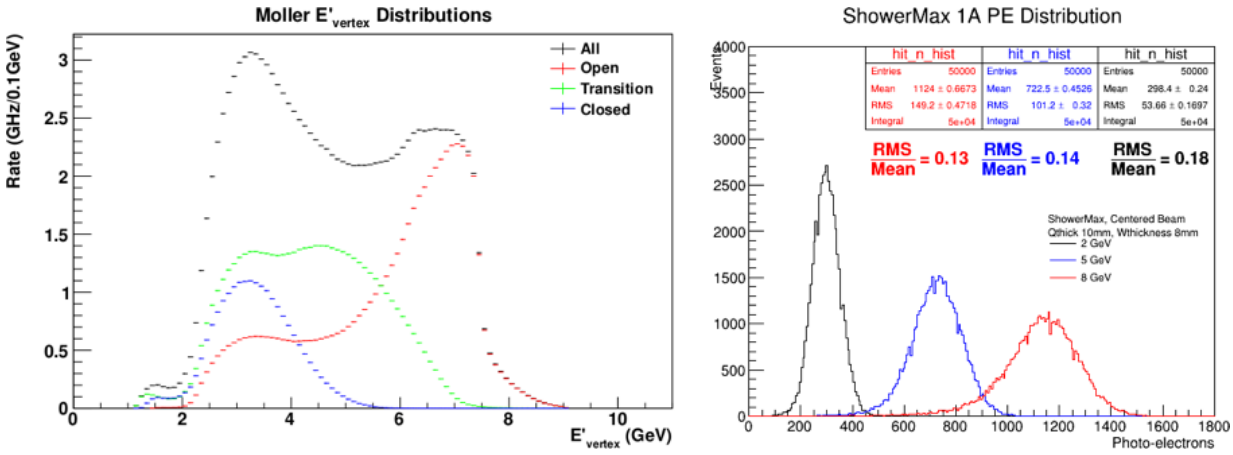

Figure 142: *(Left) Rate distribution of Møller scattered vertex energies accepted in the Open, Closed, and Transition region ring 5 and shower-max detectors. (Right) Simulated detector response for 2, 5, and 8 GeV single electrons.*

L.2.2 Resolutions and Yields

As mentioned, the overall resolution of the shower-max detector will depend on the rate distribution of accepted energies. To be more precise, it will depend on the analyzing power-weighted rate distribution of energies–which essentially enhances the importance of electrons with energies near 5 GeV. This is because the Møller A_{PV} is maximum for these $\theta_{cm} \approx 90^{\circ}$ scattered electrons which equally share the vertex beam energy. The A_{PV}-weighted rate distribution of accepted energies is shown Fig. 143 along with a plot of simulated resolutions of the shower-max single electron response as a function of energy.

To explore a perhaps conservative scenario for possible detector resolutions, the simulation is run for each ϕ-region detector using a beam energy profile that matches the red (Open), blue (Closed), and green (Transition) curves in the left plot of Fig. 143. Furthermore, the simulated beam is uniformly rastered over the entire face of the detector. The results of this study, given in Fig. 144, show PE response distributions with 25 - 30% relative widths (or resolutions) for the three ϕ-region modules. A shower-max detector with 30% overall finite resolution (per helicity window "event") leads to 4.4% error inflation in the integrating asymmetry measurement. The ring 5 thin quartz detectors will have better resolution and less excess noise than the shower-max detectors due to their energy independent response. However, while the energy-proportional response of the shower-max inherently worsens its finite resolution, it makes it much less sensitive to hadronic and low energy or soft electromagnetic backgrounds as compared to the thin-quartz detectors. Background sensitivities for the baseline shower-max design are given in the next section.

One of the key challenges to address for the practical, long-term operation of the shower-max ring during MOLLER is the very high rates of detected electrons combined with the very high PE yields per electron. Fig 145 gives the overall simulated radial rate of scatteered electrons at the MOLLER detector plane as well as the breakdown of these rates into the acceptance of each ϕ-region shower-max module. Assuming a total shower-max ring rate of 130 GHz (signal plus background), it is estimated from simulation that 56, 22, and 52 GHz are distributed within the Open, Closed, and Transition ϕ-regions of the radial acceptances. Given the 7-fold symmetry of the incident flux pattern, these total rates are divided equally among the 7 Open, 7 Closed, and 14 Transition modules leading to individual estimated flux rates per detector of 8.0, 3.1, and 3.7 GHz, respectively.

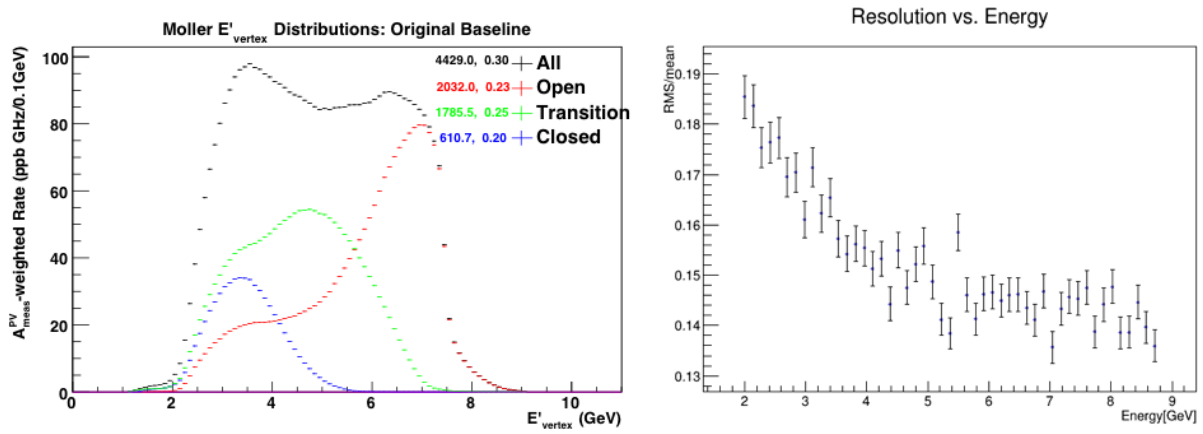

Figure 143: *(Left) Simulated A_{PV}-weighted rate distribution of Møller scattered vertex energies accepted in the Open, Closed, and Transition region ring 5 and shower-max detectors. The numbers in the legend are the integral and RMS/Mean of the distributions. (Right) QSIM shower-max resolution versus energy for single, mono-energetic electrons from a pin-point, centered beam.*

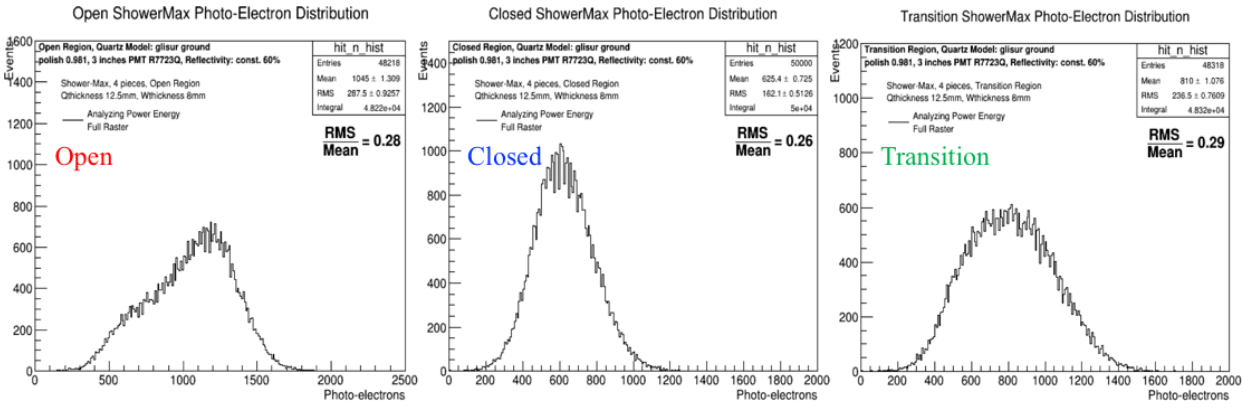

Figure 144: .
Simulated analyzing-power and energy rate weighted PE responses for the three ϕ-region shower-max modules. These results show overall resolutions in the ∼25 - 30% range.

L.2.3 Background Sensitivities

The key motivation for incorporating the shower-max ring into the main physics asymmetry measurement is its insensitivity to low energy electromagnetic backgrounds, primarily photons and soft electrons, as well as hadronic backgrounds, mainly pions. The PE response for photons with centered, normal incidence on the face of the shower-max detector is given in Fig. 146. This plot shows extremely low PE production for 100 MeV photons, relative to expected electron signal sizes, and this conclusion can be extrapolated to much higher photon energies. The shower-max will be relatively immune to any potential flux of high energy gammas resulting from interception of the primary signal flux with upstream and surrounding materials. QSIM can also be used to test the shower-max response to pion beams (as well as muons for potential cosmic-ray testing). The results of these simulation tests are given in Fig. 147. Note that the ∼50 PE peak response to pions is 10 - 20 times smaller than the typical electron response for the same energy–thus diluting the background asymmetry signal measured from pion contamination. However, this 50 PE signal is healthy enough to ”tag” pions during counting mode calibrations and aid the pion and tracking detector systems in pion identification.

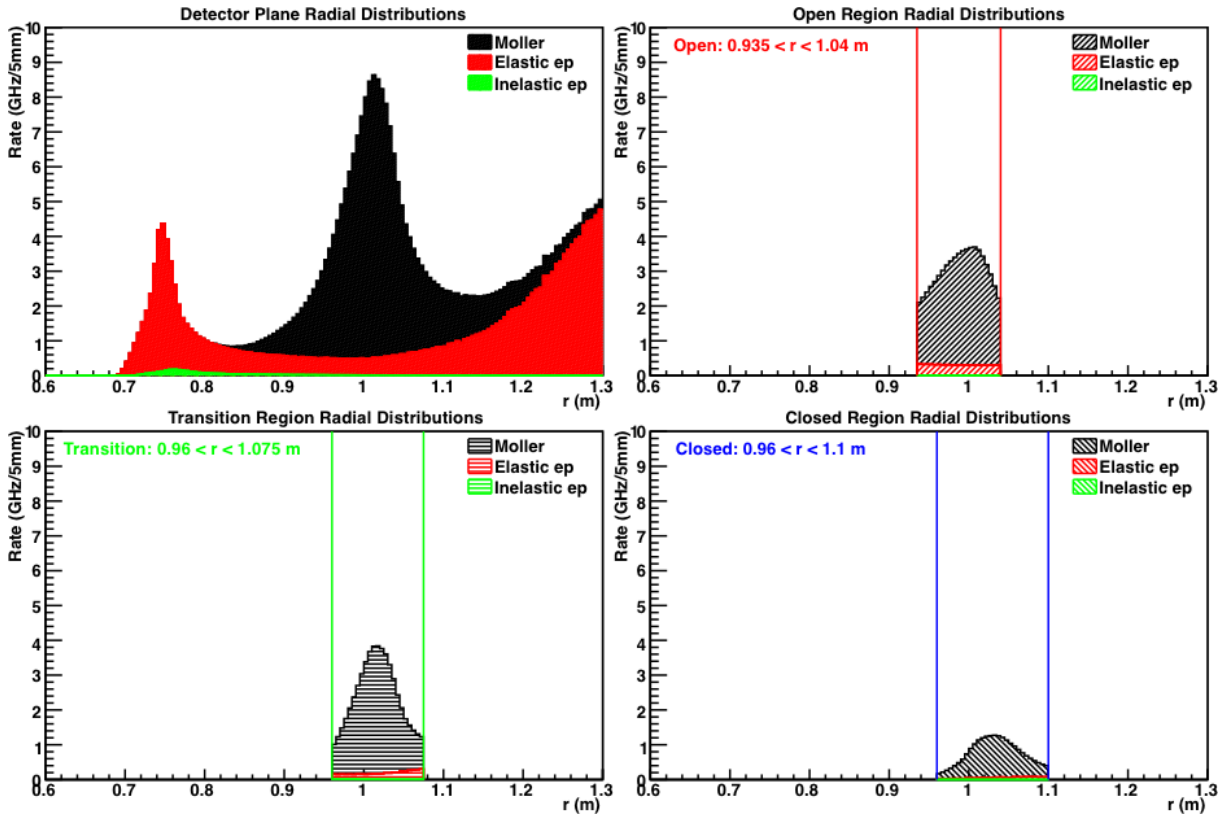

Figure 145: *Simulated radial rate distributions at the MOLLER detector plane. Upper right plot shows the entire radial distribution for signal and backgrounds, while the other plots show the distributions for the three ϕ-regions which pass the individual radial acceptance cuts (given in the plots).*

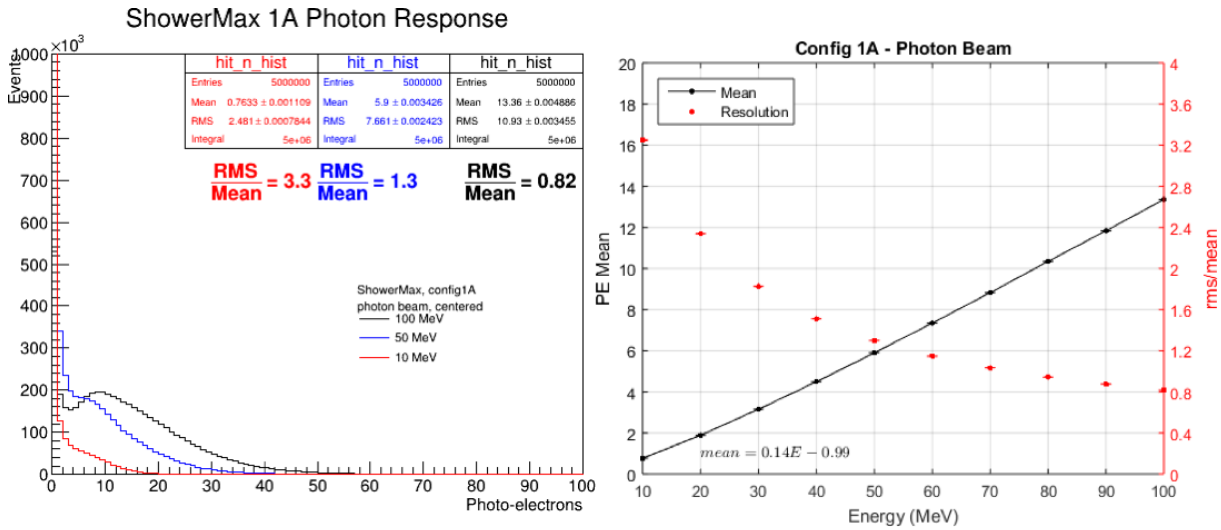

Figure 146: *Simulated PE response of the shower-max detector to photons. Left plot gives individual PE distributions for 10, 50, and 100 MeV photons, and the right plot gives the trends in the PE mean (black) and RMS/Mean (red) for the photon response.*

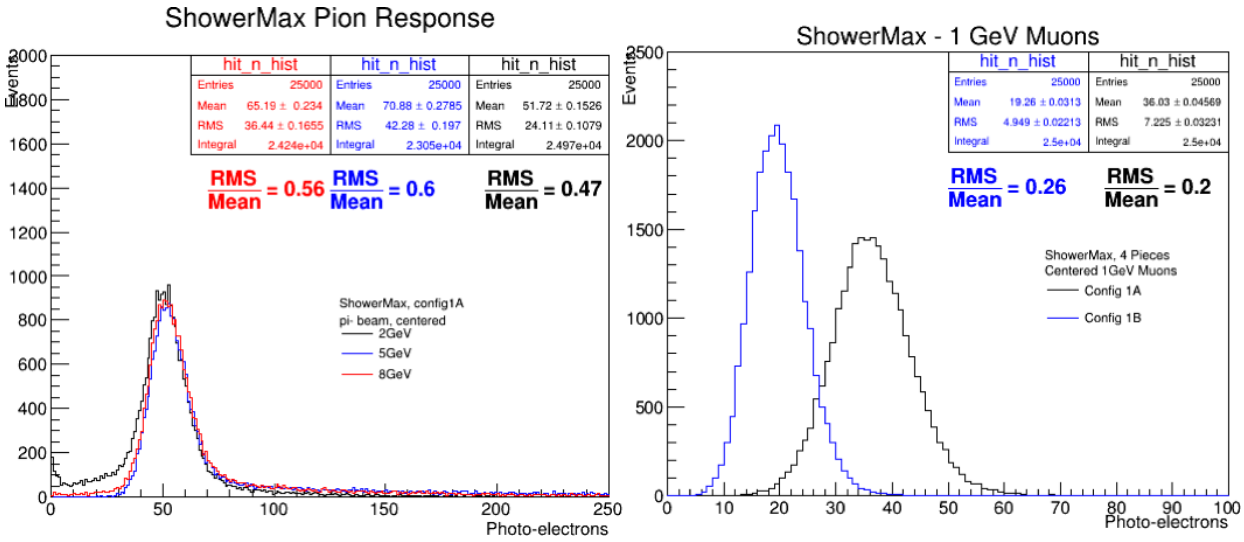

Figure 147: *Simulated PE response of the shower-max detector to pions (left plot) and muons (right plot). Config 1A uses 10 mm thick quartz and 1B uses 6 mm thick quartz; tungsten layers are always 8 mm thick.*

L.2.4 Alternative Geometries Explored

The final sub-section for describing the baseline design development covers possible alternatives to the detector geometry, and in particular, the phi segmentation. These alternatives were explored in an attempt to narrow the relative widths of the individual detector's energy acceptances–since these govern, to a large extent, the minimum finite resolutions achievable by the detectors (given their linear energy responses). Fig. 148 gives a brief introduction to some of the alternative segmentation geometries that were studied. The simulated energy rate distributions for the two alternative segmentation geometries shown in Fig. 148 are shown in Fig. 149. These results confirm that the phi-defocusing character of the spectrometer does not allow any segmentation geometry to minimize the accepted energy distribution widths, and the added complication and cost of these alternatives are not justified by any marginal gains.

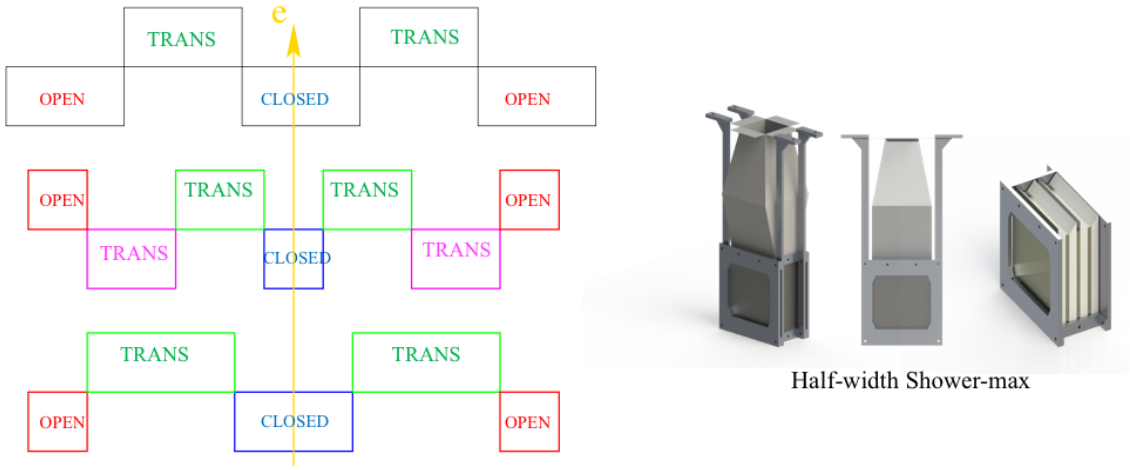

Figure 148: *The left side schematics show a radial view of various ϕ segmentation geometries; the patterns shown repeat around the ring. The baseline design segmentation is the upper-most pattern while the lower two are samples of explored alternatives. As can be seen, the azimuthal size and, in some cases, numbers of detectors changes for each variation. A sample CAD render of the "half-width" detector is also displayed .*

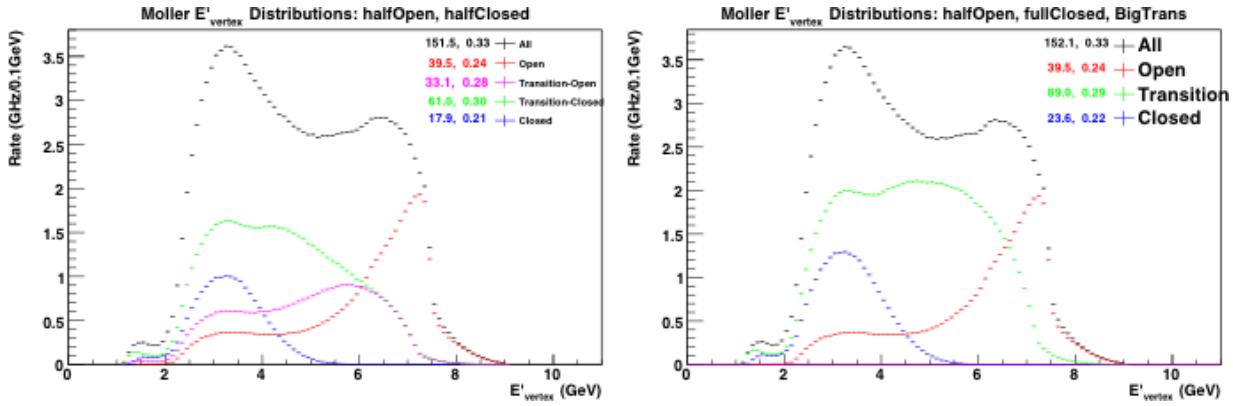

Figure 149: *Accepted energy distributions for the two alternative phi segmentations displayed in Fig. 148. There is no alternative segmentation geometry that produces narrower energy distributions than the baseline geometry.*

L.3 SLAC testbeam (pre R&D)

The shower-max SLAC testbeam run was designated T-577 and took place from Dec 6 - 12, 2018 in the End Station A Test Beam (ESTB) facility. Three different electron beam energies were used: 3, 5.5, and 8 GeV. One of the more interesting but complicating aspects of the testbeam was its electron multiplicity: the beam did not always deliver single electrons, as desired, but rather a Poisson distribution of electrons with a mean that is tunable from near 0 to 10^9. The testbeam is generated in a parasitic fashion from the 14 GeV LCLS beam and has a repetition rate of 5 Hz. While we requested a Poisson mean near 1.0, the beam pulses still often contained zero or more than one electron. This required the use of tracking detectors (GEMs) to extract only the single electron events from the data stream.

The entire shower-max testing apparatus, including DAQ and custom test-stand, were brought to SLAC and installed in the beamline tunnel at the downstream end of End Station A. The teststand provided supports and remote positioning system for the GEM chambers and detector prototype mounting platform. The GEMs and platform move together in the horizontal direction, transverse to the beamline, and the payload platform has an addition vertical degree of freedom. A CAD of the apparatus and photo taken during the testbeam are given in Fig. 150.

L.3.1 Prototype Construction

Four shower-max prototypes were constructed in 2018: two ”benchmarking” and two ”full-scale” prototypes, each version with the same stack configuration, either ”1A” or ”1B”. These configurations are both 4-layer stacks with 8 mm thick tungsten plates; 1A uses 10 mm thick quartz tiles and 1B uses 6 mm thick tiles. The full-scale prototypes use all machined aluminum framing parts, and the benchmarking prototypes parts are made from 3D-printed ABS plastic. Care was taken in the benchmarking design to ensure that all four quartz bevels of the stack were circumscribed by the 70 mm diameter PMT window. However, the lateral dimensions of the stack, relative to the beam, had to be large enough to guarantee no transverse shower leakage, which would confuse simulations. To achieve this for both the 1A and 1B configurations the benchmarking stack was chosen to be 40 mm wide by 80 mm long. The $\sim$11 mm Moliere radius for these calorimeters allows for full lateral shower containment, even if beam is not perfectly centered on the stack.

A photograph of the complete full-scale prototypes along with a collage of photos taken during assembly are given in Fig. 151. A similar set of photographs for the benchmarking prototype are shown in Fig. 152.

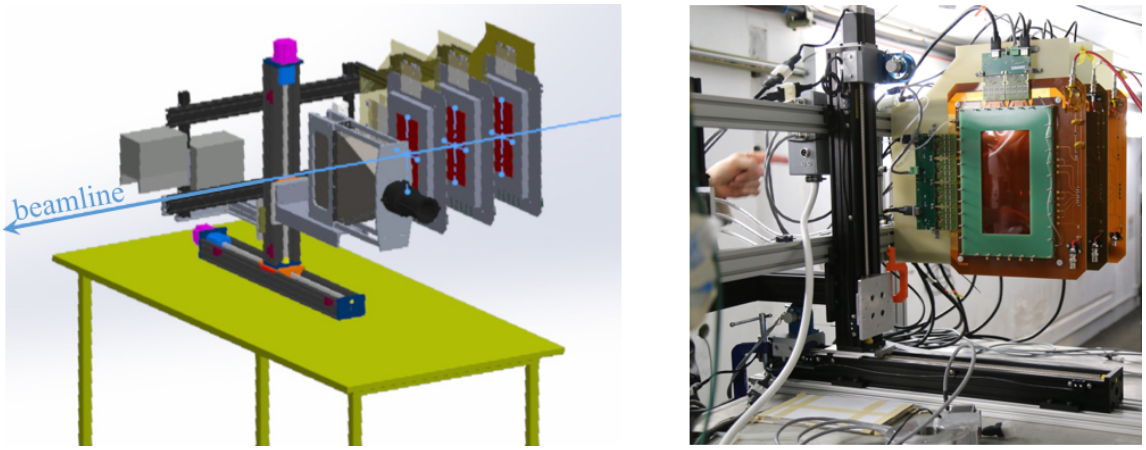

Figure 150: *(Left) CAD of the SLAC testbeam stand with full-scale prototype. (Right) Photo during installation in End Station A.*

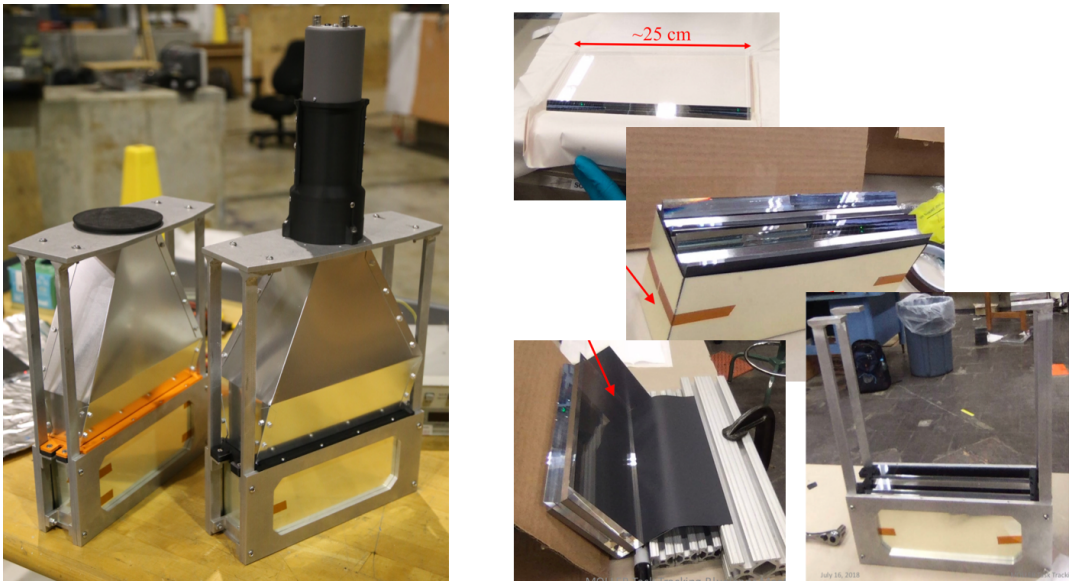

Figure 151: *Full-scale prototypes: (Left) Photograph of fully assembled 1A (with PMT) and 1B detectors. (Right) Collage of photos during assembly. Note the black Kapton wrapping is used around the tungsten plates to protect the quartz from scratches.*

L.3.2 Benchmarking Results

The results from the shower-max benchmarking prototype testbeam are presented here. As described in Sec. L.1.2, the benchmarking stacks are systematically assembled and tested one layer at a time, including a polish parameter test with only a single piece of quartz and no tungsten. The results from the single-quartz beam test for the 10 mm thick (1A) and 6 mm thick (1B) configurations are given in Fig. 153. The Poissonian nature of the beam's electron multiplicity is immediately apparent in these and all the SLAC testbeam results. For all of these and the following result plots, the real data (black) typically consists of several combined runs, each ∼15 - 20 minutes long, the fully simulated data is red, and the blue histograms represent the single-electron responses from simulation. Note that statistical precision is relatively low due to the 5 Hz beam spill rate. Also of notable interest here is that a fit to the raw detector data was performed

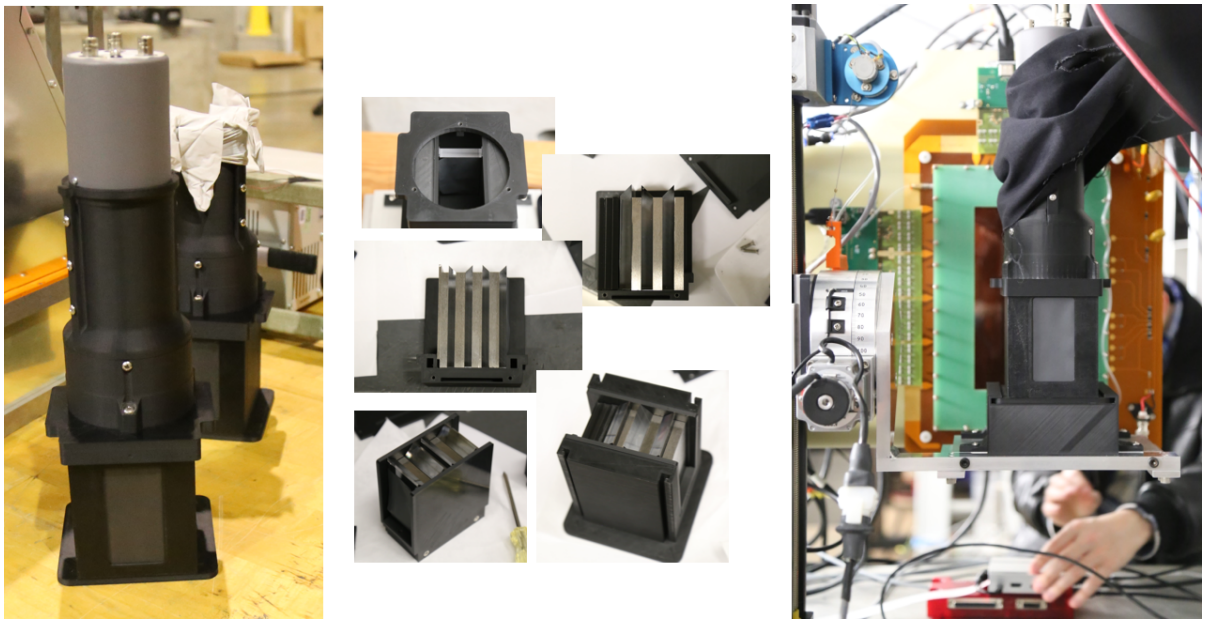

Figure 152: *Benchmarking prototypes: (Left) Fully assembled 1A and 1B detectors. (Middle) Collage of photos during the stack assembly: shows views of the single quartz (top) as well as the 3- and 4-layer stack variations. (Right) Photo of the benchmarking prototype mounted in the SLAC testbeam stand.*

to determine the precise mean of the Poissonian multiplicity of the beam, and this mean was used to define the simulated beam in QSIM.

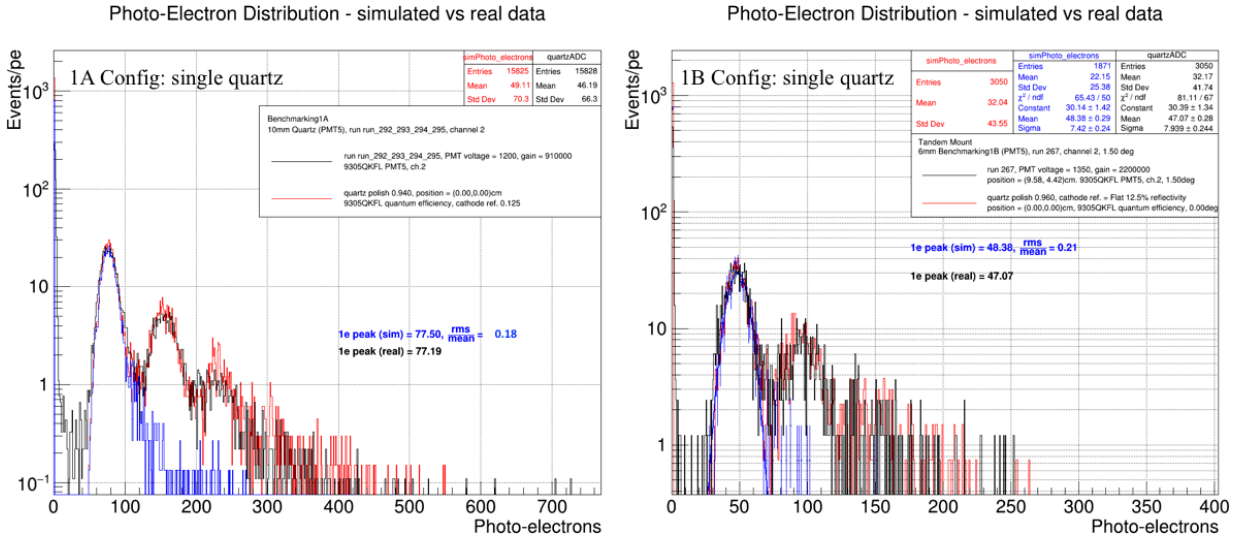

Figure 153: *Single quartz, polish parameter benchmarking data from 2018 SLAC testbeam run. (Left) 1A configuration, 10 mm thick results: 0.94 polish. (Right) 1B configuration, 6 mm thick results: 0.96 polish.*

Results from the 1A stack benchmarking procedure are presented in Fig. 154. These results are for 5.5 GeV beam energy and show excellent agreement with the simulation expectations. We see the light yield increase by a factor of $\sim$10 when adding a single tungsten pre-radiator, but the resolution is a poor 45%. As more layers are added, we see the enhancement in the yield and resolution–as the number of showering

particles increases (to near maximum), the relative fluctuation in light generation decreases. The SLAC test stand CAD and G4 visualizations for the 1B benchmarking prototype are shown in Fig. 155. Results from the 1B stack benchmarking procedure are presented in Fig. 156.

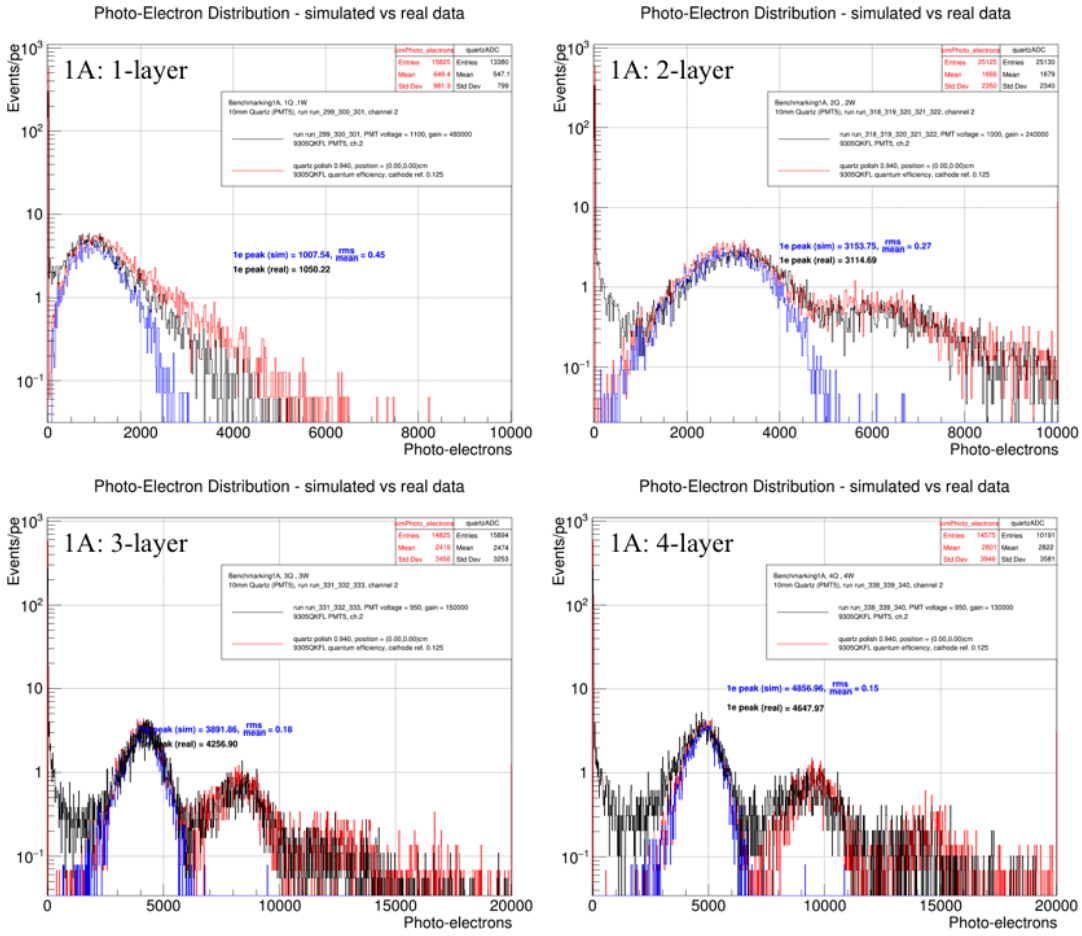

Figure 154: *Testbeam data (black), compared with simulated data (red) for 1, 2, 3, and 4 layer 1A stack configurations; quartz tiles are 10 mm thick. Blue histograms show the single-electron responses.*

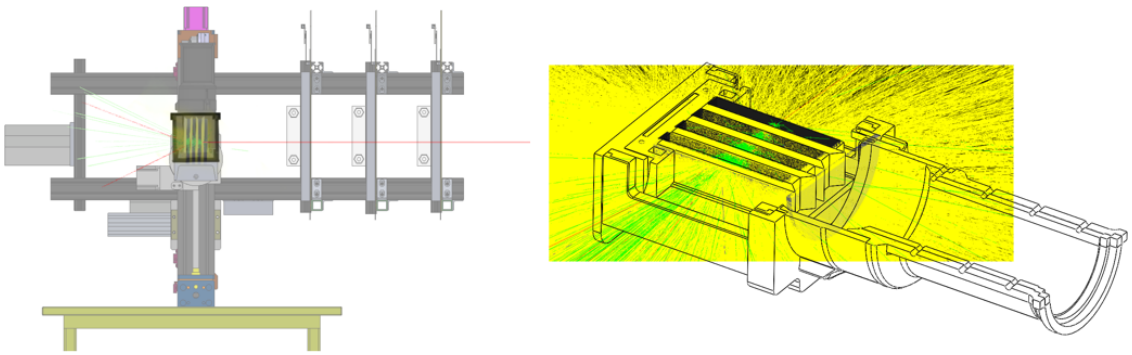

Figure 155: *CAD and QSIM visualizations of the 1B benchmarking prototype.*

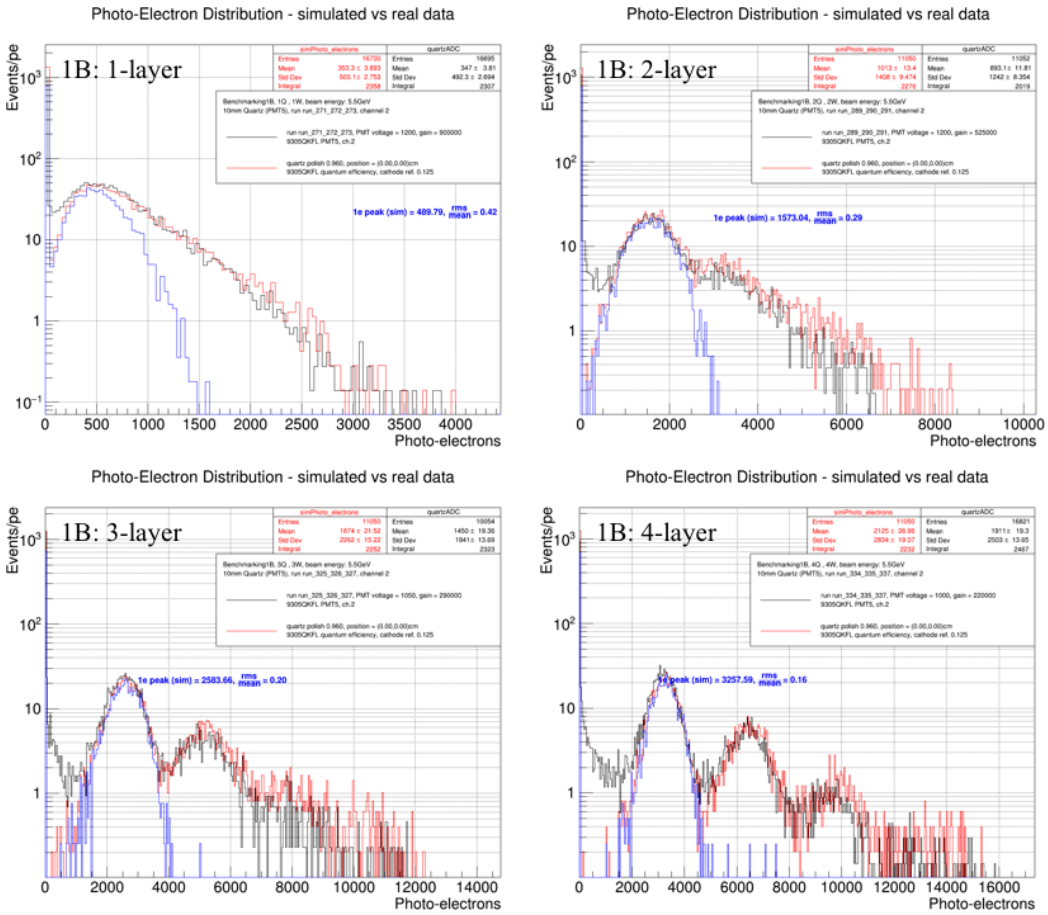

Figure 156: *Testbeam data (black), compared with simulated data (red) for 1, 2, 3, and 4 layer 1B stack configurations; quartz tiles are 6 mm thick. Blue histograms show the single-electron responses.*

L.4 Summary and Future Work

The analysis of the full-scale prototype testbeam data is still in progress. Preliminary findings indicate a factor of ∼2 - 3 lower light yields than was predicted by simulation. Given that the benchmarking prototype testbeam data had excellent agreement with simulation, our initial thoughts are that the light guide must be causing the inefficiency. While the lower light levels generated by the full-scale prototypes are not necessarily an operational concern, since the detectors are still generating 100's of PE's per electron, we nonetheless still want to fully understand why or how the generated light is lost. These surprise findings are the very reason we use testbeams and benchmark our detector simulations. While the light guide does represent the obvious culprit here, it is not 100% clear that this is the only or main problem. This is partially because the light guide has been carefully modeled and simulated with benchmarked optical properties, but also because there is another very reasonable hypothesis that could potentially explain this result (but needs to be tested). The idea is that the black Kapton wrapping, used between all the stack sub-layers to protect the quartz from scratches, is causing regions of the quartz tile surfaces to lose total internal reflection due to the smoothness of the Kapton and the sizeable mechanical pressure (and weight) within the stack as it is squeezed together during assembly. There are a few design or construction/assembly tweaks that can be pursued to test this hypothesis and possibly eliminate or greatly reduce this effect. One such obvious solution would be to not use any wrappings but instead engineer a small gap, no more than 1 mm wide, between all the stack sub-layers.

M Beam Charge Monitor Resolution Bench Studies

Section 10 summarizes the best observed performance for beam charge monitor resolution. This appendix describes the bench studies that led to some of the conclusions discussed in that section.

The MOLLER specification is 10 ppm resolution for relative beam intensity measurement for 1 kHz window pairs. Here, we report on the best values achieved to date and the work in progress by the collaboration and lab to achieve this goal. In particular, we report on the results from the recently completed $\mathrm{Q_{weak}}$ experiment. $\mathrm{Q_{weak}}$ measured beam intensity with beam charge monitors (BCM) consisting of the standard JLab hardware of resonant microwave cavities operating in the $\mathrm{TM_{010}}$ mode. The best results we obtained with an all-digital receiver electronics designed by Jefferson Lab staff member John Musson [61]. The random noise in the beam charge measurement was determined by forming the "double-difference", which is the difference between the helicity-correlated charge asymmetry for two BCMs. The RMS of this distribution determines the uncorrelated random noise of the charge measurement, referred to as the resolution. A typical measurement at the nominal $\mathrm{Q_{weak}}$ beam current of 180 μA is shown in Figure 157, with an observed value of ~ 62 ppm.

To facilitate improvements, dedicated bench tests have been set up using a $\mathrm{Q_{weak}}$ data acquisition test stand. The first goal was to show that the behavior of the $\mathrm{Q_{weak}}$ digital test receivers with beam could be reproduced with the beam signal coming from the microwave cavity monitor replaced with a radio-frequency source signal. As Figure 157 shows, the results with beam and rf source are very similar, with a similar ''noise floor" in each case. Since there is a noise floor that is independent of beam current, one hypothesis is that the noise floor in the charge measurement is limited by phase and amplitude noise in the 1.5 GHz local oscillator that is mixed with the incoming signal in the receiver electronics. To test that hypothesis, the bench study shown in Figure 158 was done. Here, a single receiver with the signal going into the two available inputs was used. Each signal's electronics path is independent with the exception of the local oscillator that is shared between the two. In this case the noise floor is reduced to ~ 18 ppm. This is consistent with the local oscillator being responsible for the 62 ppm noise floor. Further studies are in progress to confirm this and improve the situation if it is confirmed to be the cause.

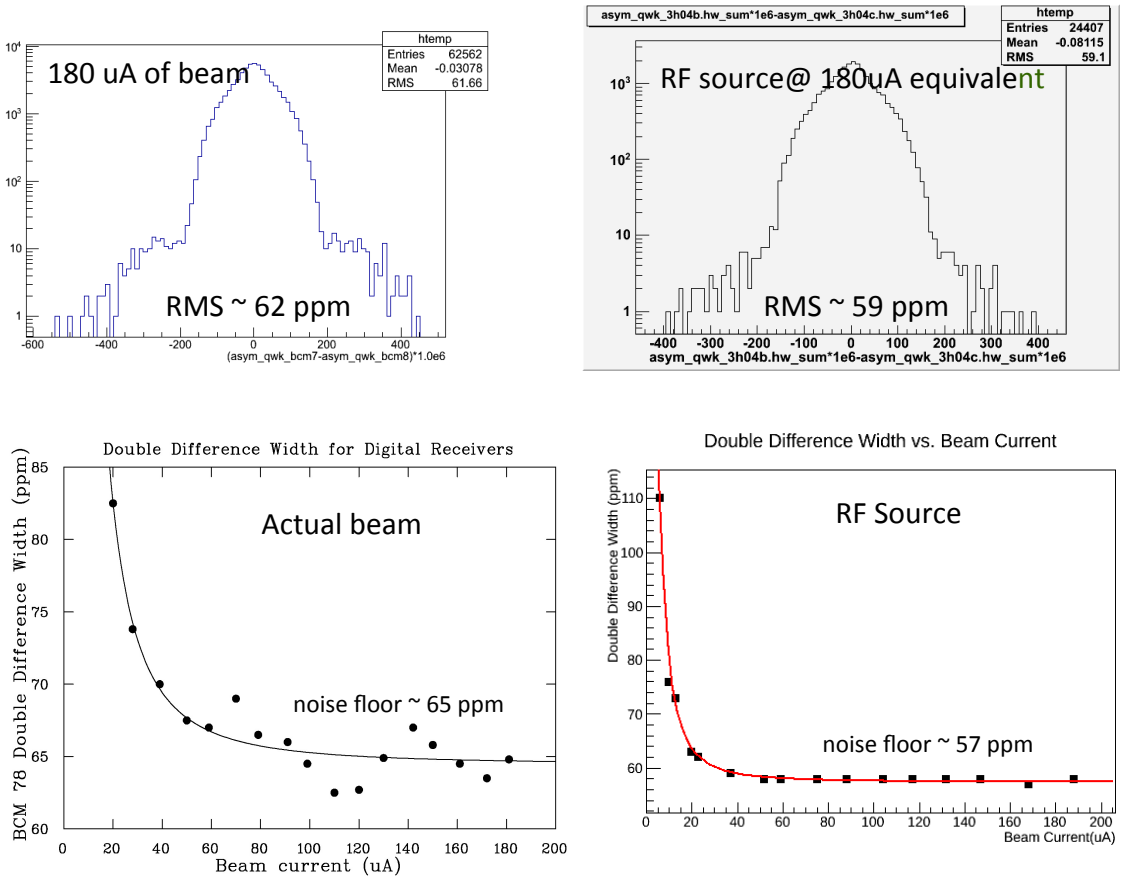

Figure 157: Q_{weak} *measurements of beam charge monitor (BCM) resolution. The left panels show the distribution of the "double-difference" between the helicity-correlated charge asymmetry of two BCMs at 180 μA and versus beam current, respectively. The right two panels show the results of bench studies with the same digital receiver electronics used during* Q_{weak}*, but the input signal is replaced with a radio-frequency source of the appropriate amplitude for that beam current.*

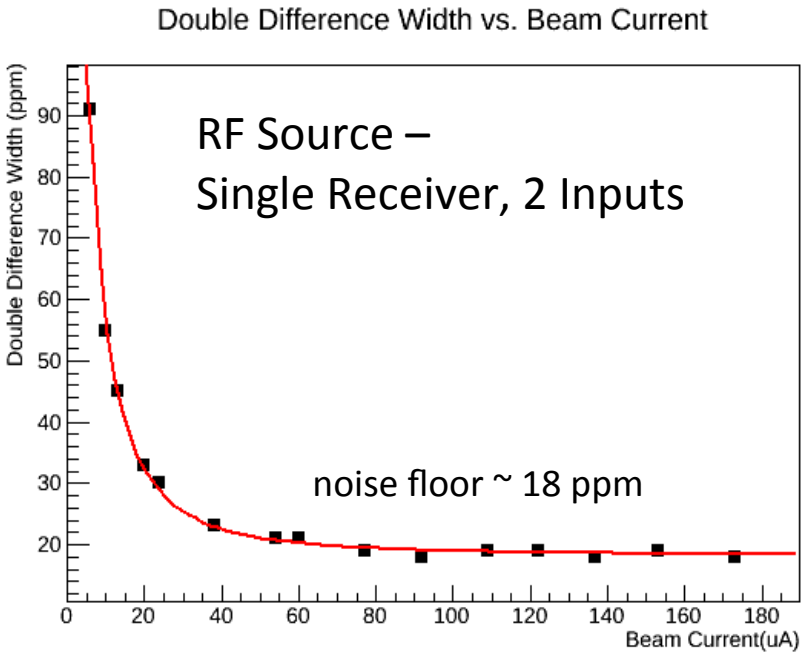

Figure 158: *BCM resolution results from a bench study with a rf source and with a single receiver with two inputs and shared local oscillator.*

N GEM Tracker

N.1 Design

The MOLLER setup requires high resolution track reconstruction under high rate conditions over a large area. A cost effective solution for such requirements is provided by the Gas Electron Multiplier (GEM) technology invented by F. Sauli [42] in 1997. The GEM is based on gas avalanche multiplication within small holes (on a scale of 100 μm), etched in a Kapton foil with a thin layer of copper on both sides. The avalanche is confined in the holes, resulting in fast (about 10 ns rise time) signals. Several GEM foils (amplification stages) can be cascaded to achieve high gain and stability in operation. The relatively small transparency of GEM foils reduces the occurrence of secondary avalanches in cascaded GEM chambers. All these properties result in very high rate capabilities of over 100 MHz per cm^2 and an excellent position resolution of approximately 70 μm. Fig. 159 illustrates the principle of operation of a triple (three foil) GEM chamber, while Fig 160 shows the zoomed in view of a X-Y type (90° angle between the two readout strip layers) 2-D readout layer used to capture the amplified electron cloud and register its position with high accuracy in both dimensions. Triple GEM chambers have been successfully used in the COMPASS experiment at CERN [43], in the PRad experiment at Jefferson Lab [44] and may other experimental setups around the world.

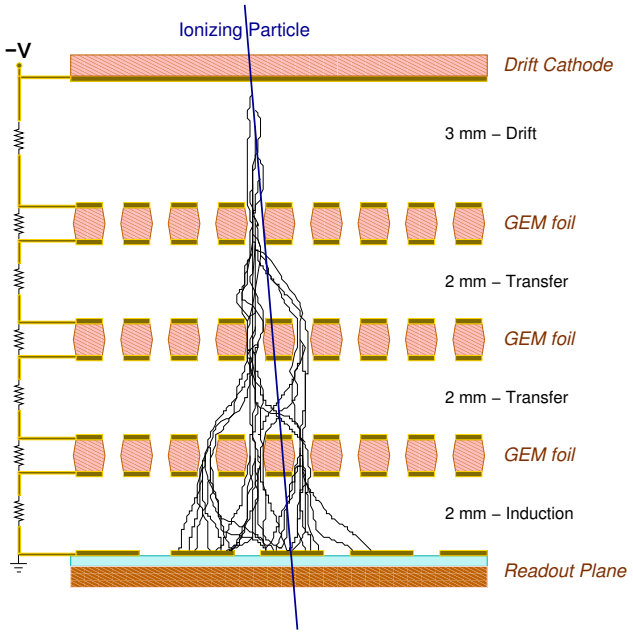

Figure 159: *Principle of triple GEM operation.*

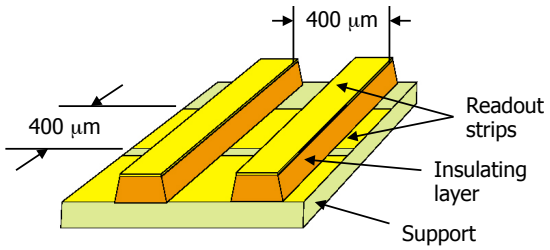

Figure 160: *The 2-D Cartesian (x-y type) readout board used in a GEM detector.*

N.2 Tracking Detector Requirements

As discussed above, our tracking system is designed to verify the spectrometer optics, to measure the appropriately weighted mean of the kinematic factor $\mathcal{A}$ that multiplies A_{PV}, and to determine backgrounds. To this end, the tracking system will consist of 4 GEM planes, located downstream of the two magnets, and upstream of the main integrating quartz detectors. The primary requirement for the acceptance is to be able to separate between events from different sieve holes when we use a staggered-hole configuration. Based on Fig. 58, this can be fulfilled with 1 mm spatial and 1 mrad angular resolution.

As discussed above, the GEM planes will be placed in two sets of pairs in rotatable wheel assemblies, as shown in Fig. 28. The GEM planes must be insertable to intercept the charge particle flux after they exit the vacuum window, but must be out of the way during the collection of production data. In order to reduce costs, we propose to cover four septants and have them attached to a remotely controlled "wheel" with the ability to rotate in the azimuth up to one septant, providing full and redundant coverage.

The present design of a GEM chamber presents less than 0.4% radiation length for electrons incident normal to the plane. Using the standard multiple scattering formula for the central 98% of the scattered distribution of ultra-relativistic particles , for the lowest momentum electrons of interest ($\sim$ 2 GeV), and $x/X_0 = 2 \times 0.4\%$ for the two upstream foils, this corresponds to $\delta\theta$ of about 0.3 mrad. This is the limiting factor on the angular resolution in the GEMs, but is still sufficient to separate the staggered peaks in the acceptance calibration.

N.3 GEM Detectors in Simulation

The design requirements of the tracking system are validated via simulation. Within the simulation, placeholder GEM detectors, each composed entirely of vacuum but capable of recording hits, is currently implemented in the GEANT 4 simulation package developed for this experiment. A total of 4 GEM detectors are represented within the simulation. The GEM detectors are located along the beam propagation axis in two sets of pairs. Each pair consists of GEM detectors separated by 1 m. The two pairs are separated by 4 m. Their nominal locations in simulation are 22.6, 23.6, 27.6 and 28.6 m respectively from the center of the target. (The quartz detectors are located at 28.7 m). The Monte Carlo hits recorded by the GEM detectors, $r_{\rm MC}$, $\phi_{\rm MC}$, $r'_{\rm MC}$ and $\phi'_{\rm MC}$, are used to generate "reconstructed" track variables, $r_{\rm rec}$, $\phi_{\rm rec}$, $r'_{\rm rec}$ and $\phi'_{\rm rec}$. This is done via χ^2-minimization of the straight line fit through coordinates defined by $r_{\rm MC}$, $\phi_{\rm MC}$, $r'_{\rm MC}$ and $\phi'_{\rm MC}$ for each track.

N.4 GEM Detector Sizes

The GEM detector sizes depend on their location along the beam propagation axis, with the detectors located further downstream requiring larger area in order to intercept the electrons in acceptance. Simulation is used to determined the GEM detector sizes. The GEM sizes necessary to intercept electrons in a given septant are determined by observing electrons that Møller scatter inside the target, and arrive at the quartz detectors. The 4 GEM detectors are located at their nominal positions of 19.25 m, 19.75 m, 21.0 m, and 21.5 m. The quartz detectors are located starting at 21.75 m.

Because the strong ϕ-defocusing of the spectrometer results in electrons being swept across the septant boundaries by the time they arrive at the quartz detectors, the electrons that arrive at a particular septant in the simulation at the nominal location of the quartz detectors are selected and tracked upstream through each of the GEM planes in order to determine the sizes of individual GEM planes. The GEM detector shapes determined from this study are trapezoidal but with the parallel sides replaced by arcs of two different radii of a concentric center.

The GEM detector sizes determined via such analysis, and incremented by 5% in r and 10% is ϕ is presented in Table 33. These are the sizes required to intercept electrons from any one particular septant. The proposed 4-septant GEM configuration is shown in Fig. 161 would allow for the full azimuthal range to be covered through only one rotation to the neighboring septant. Precise placement around the azimuth at fixed septants, shown, and also half septants would be useful to test GEM efficiency across the face. Allowing a set of GEMs to have a range of motion that it can be placed across three adjacent septants would allow full cross referencing distributions in each septant by at least two GEM sets.

As indicated above, the idealized simulated GEM module will have the parallel sides replaced by arcs of two different radii of a concentric around the beam-line. However, in reality, mechanical, structural stability

Table 33: *GEM detector sizes needed to intercept electrons incident on the quartz detector of a given septant.*

	z(m)	Inner rad(m)	Outer rad(m)	$\pm\phi$(deg)
GEM #1	19.25	0.54	1.08	31.0
GEM #2	19.75	0.56	1.10	30.5
GEM #3	21.0	0.58	1.12	28.8
GEM #4	21.5	0.59	1.13	28.8

and construction considerations make actual trapezoidal GEM modules, with straight sides, to be a much more practical choice. The drawing from the CAD model for a trapezoidal GEM module for one of the MOLLER GEM wheels, as seen from the beam's eye view, is given in Fig 162. Note that the dimensions of the trapezoidal detector are determined such that the no active acceptance area is excluded due to the straight sides.

N.5 MOLLER GEM module design

Figure 163 top-left shows the iso-metric view from the CAD design of largest size GEM module for MOLLER. The lower part of the figure shows the exploded view of this GEM module showing the details of (a) the GEM, readout and other foils, and (b) the foil holding frames which, when glued together during assembly, make up the mechanical structure and the gas enclosure of the GEM module. Starting from the right, the first red frame is the holding frame for the module. This frame anchors the module to the rotating structure. The four through-holes in the corner extensions of the frame are used for mounting. The readout support frame, made by gluing the lightweight 3 mm honeycomb layer on the yellow frame, provides structural rigidity and flatness to the module. The 2D readout plane (dark-brown) is glued on to the readout support frame. All frames are made out of Permaglass [3]. The spacers shown within the active area are for keeping the GEM foils from touching each other; these spacers are approximately 300 μm wide and contribute only about 2% reduction to the active area of the chamber. The GEM foils are mounted on the 3 blue frames, while the drift cathode is glued on the green frame. A thin Aluminized Kapton gas window is glued on the yellow frame next to the cathode foil. Input and output gas connectors are mounted on the outer-frame, shown in red and the gas flows in and out of the chamber volume through the matching holes in the gas window frame.

Figure 163 lower-right insert shows the 2D readout layer concept for MOLLER GEMs; what is shown in the picture is a micro-graph of an actual readout used for the latest prototype GEM chamber built by the UVa group as part of the EIC detector R&D program (more detail on this and other prototype GEM detectors developed by the UVa group is presented below).

The UVa group will perform the design, prototyping and fabrication of all GEM detectors for the MOLLER project. This group has extensive GEM detector design and fabrication experience and has constructed and operated several of the largest GEM detectors in the world. In 2017, the UVa group successfully completed the DOE supported large area GEM detector fabrication project for Jefferson Lab Super Bigbite Spectrometer (SBS) project, on time and on budget, by finishing the construction of 40 GEM modules, each with an active area of 60 $\times$ 50 cm^2, for the two large area GEM trackers of SBS. Since then, the group has also constructed another eight SBS GEM modules to be used as spares. All modules 48 have been tested and demonstrated to work very well meeting or exceeding the design goals of the SBS program. A DOE review panel for the SBS project noted: *"We commend the UVa group for excellent progress on chamber*

[3] Permaglass is a glass fiber material, with randomly oriented fibers, which can be machined with very high precision.

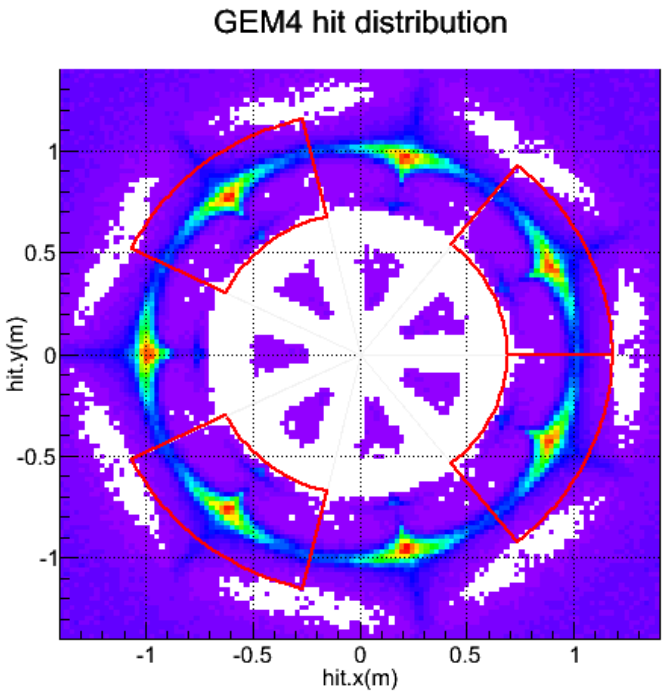

Figure 161: *The proposed GEM configuration that covers four septants. Such a configuration allows full azimuthal coverage through only one septant rotation.*

construction, and for uncovering and solving a number of sticky experimental issues through their careful analysis."

Figures 164 and 165 show results obtained during the testing of SBS GEM modules built by the UVa group. Figures 164 is the absolute efficiency, measured at several locations by using electrons from a beta source, as a function of the high voltage. An efficiency of $\approx 97\%$ was achieved. Figure 165 is the ratio of cluster charge for x and y hits. The development and prototyping details of SBS GEM modules as well as results from test runs were published in NIMA in 2015 [45].

Until a few years ago, one challenge regarding the MOLLER GEM tracker had been the large active area of the GEM modules required for MOLLER; the active area of the largest GEM modules needed will be approximately $54\times(30–54)$ cm^2. However, this is not an issue anymore: the UVa GEM group now has extensive expertise in the design, fabrication and operation of GEM detectors with even larger active area than what is needed for MOLLER. In 2015-2016 this group successfully designed and fabricated the world's largest GEM detector pair with an active area of 123 cm $\times$ 55 cm for Jefferson lab PRad experiment. The active area of these detectors were more than a factor of two larger than any other GEM chamber built before that. Both PRad GEM modules performed extremely well during the entire experiment. They yielded highly stable operation, high resolution (of approximately 70 μm as shown in Figure 167-right-top), and efficiency ($\sim 95\%$ averaged over the active area). The efficiency was stable over the duration of the whole experiment, as shown in Figure 167-right-bottom.

Figure 166 shows some of the fabrication steps of one of the PRad GEM modules in the UVa group clean room. All specialised equipment used in this process, like the large area foil stretcher and the foil high-voltage testing enclosure, were developed, designed, prototyped and built by the UVa group. Figure 167-left shows the PRad GEM detector pair installed in hall B, next to HyCal electro-magnetic calorimeter, ready for taking data during the experiment.

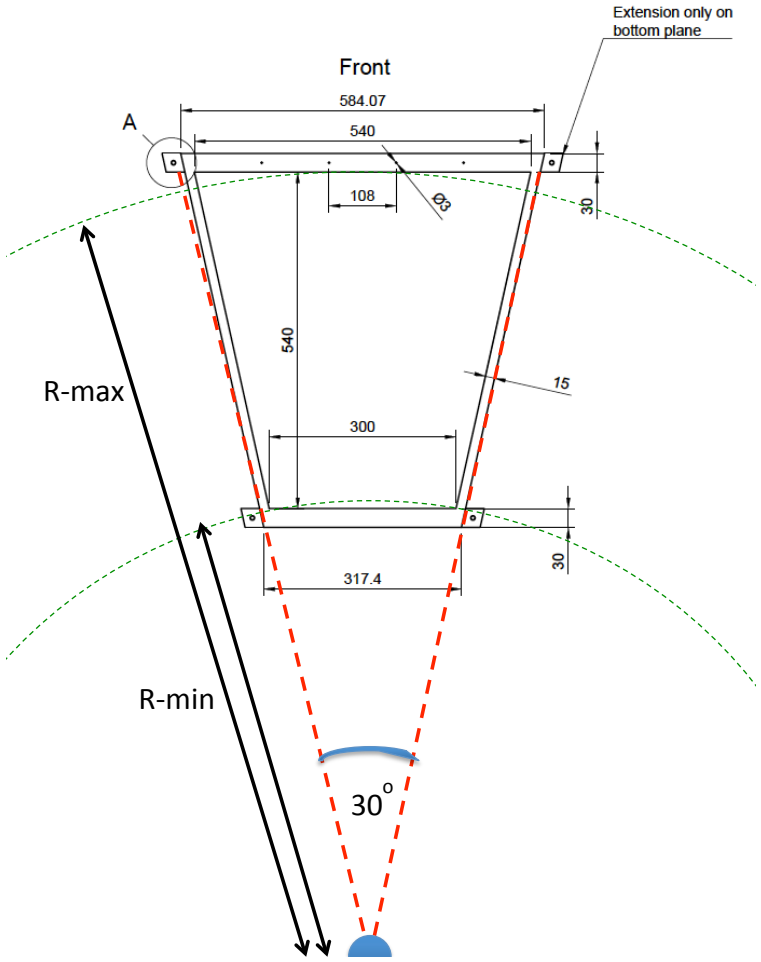

Figure 162: *The drawing for a MOLLER GEM module as seen in the beam's eye view. Note that the size of the module is determined such that the trapezoidal shape encompasses the full active area without clipping off any of the edges of the acceptance. All dimensions indicated in the CAD drawing print of the GEM are in mm.*

The PRad GEM detector project allowed the UVa group to gain expertise in the construction of large area GEMs and to demonstrate the feasibility of the GEMs with the dimensions well over what is required for MOLLER. The EIC GEM R&D program carried out by the UVa group allowed the development of several other features crucial for MOLLER as well as for SoLID and EIC GEMs. These features include U-V type 2D readout with a shallow angle between U and V strips (for MOLLER, this angle needs to be approximately 30°, as opposed to 90° in the SBS and PRad GEMs), and locating all readout electronics at the outer circumference side of the detector to avoid exposure to the high radiation levels close to the beam-line in the cylindrical geometry of MOLLER, SoLID and EIC detectors.

The first EIC prototype GEM developed by the UVa group in 2013-2014 had dimensions of 100×(22–44) cm^2, close to double the size of the largest MOLLER GEM modules, and with 12° opening angle trapezoidal shape required for MOLLER. Figure 168 shows the fabrication details for this GEM module. It was extensively tested with cosmic ray data and in a long beam test at Fermilab; the results from these tests showed that large GEM detectors of the sizes and the shape required for MOLLER are feasible and the UV

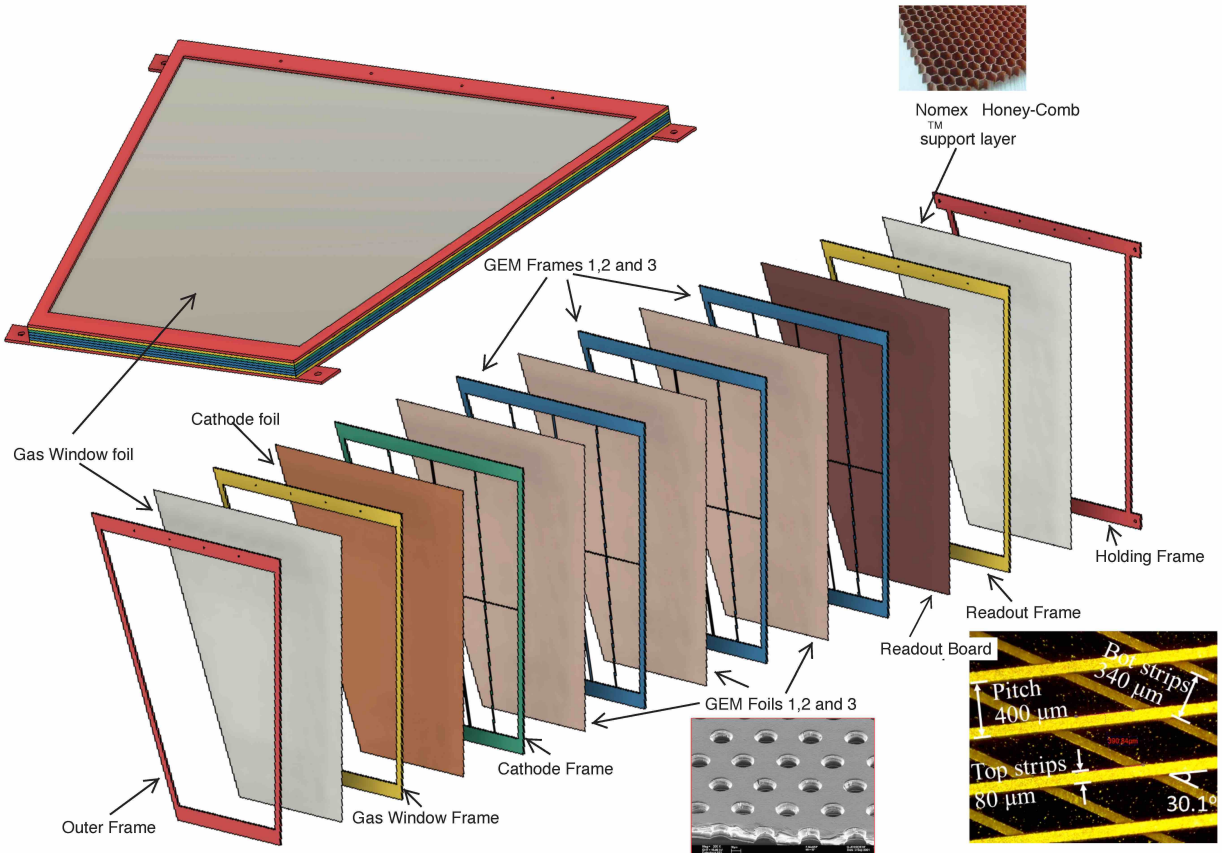

Figure 163: *Left: The CAD design for a MOLLER GEM module. Top left shows the assembled module. Please note that these prints were made from a ready-for-production CAD model similar to the CAD designs used for many other already fabricated and operated large area GEM modules at UVa. These advanced CAD models are CNC machine ready for the GEM holding frames (which are generally produced by the Resarm corporation in Belgium for the UVa group, and photolithograpy ready for the GEM, cathode and readout foils, which are produced in the GEM shop at CERN). The bottom-right insert shows a high-power micro-graph of a 2-dimensional readout board similar to what would be used for MOLLER GEMs. This is an actual micro-graph taken in the UVa GEM lab clean-room of a readout board used for the UVa-EIC-GEM-II prototype GEM detector. The MOLLER GEM readout board will be very similar to this one, except for the increased strip pitch (800 μm for MOLLER, as opposed to 400 μm shown here). The position and angular resolutions obtained from the beam tests of UVa-EIC-II prototype detector with this readout are presented later in this appendix.*

readout proposed for MOLLER delivers the required position resolution. The development and fabrication details of this prototype detector as well as results from test runs were published in NIMA in 2016 [46].

Using the lessons learned with the first prototype, a second trapezoidal (EIC and MOLLER style) prototype with new design ideas was designed, built and characterized. The the U-V strip readout includes in its design a double-sided zebra connection technique that the UVa group developed to allow the connection of all readout strips to the front-end-electronics at the outer radius side of the wedge-shaped large detector. This new connection scheme drastically minimizes the exposure of the electronics to radiation damage, eliminates the multiple scattering caused by the electronics mechanics and optimizes the dead-to-active area ratio of the detector, by moving readout electronics away from the beam-line. The prototype was successfully tested with cosmic in the Detector Lab at UVa and later with a high energy proton beam at the Fermilab

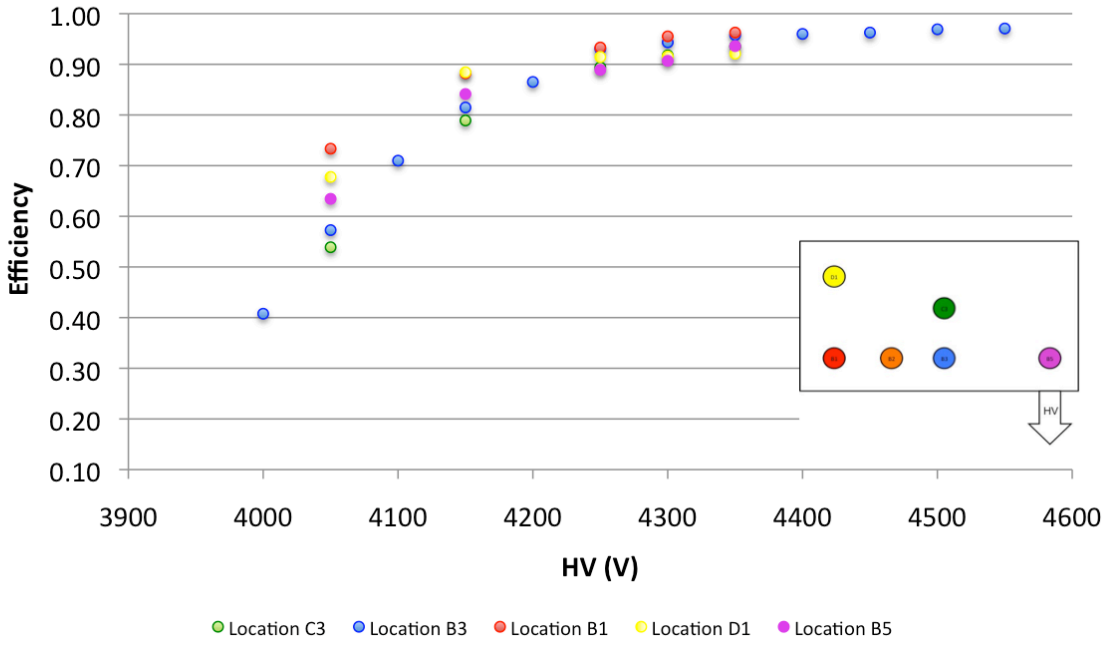

Figure 164: *Measured efficiency vs. high voltage for the 40×50 cm^2 GEM chamber*

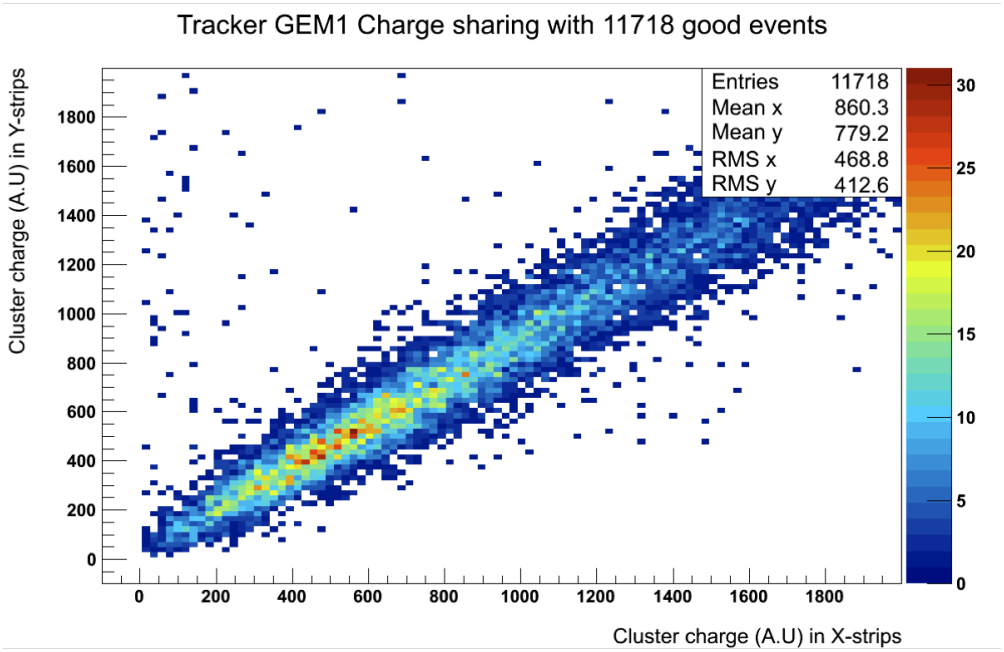

Figure 165: *The charge division between x and y stripes for the 40×50 cm^2 GEM chamber.*

Test Beam Facility (FTBF) in June and July 2018 (see Fig. 169-right). The analysis of the FTBF data is currently ongoing. The results will be published in NIMA in 2020.

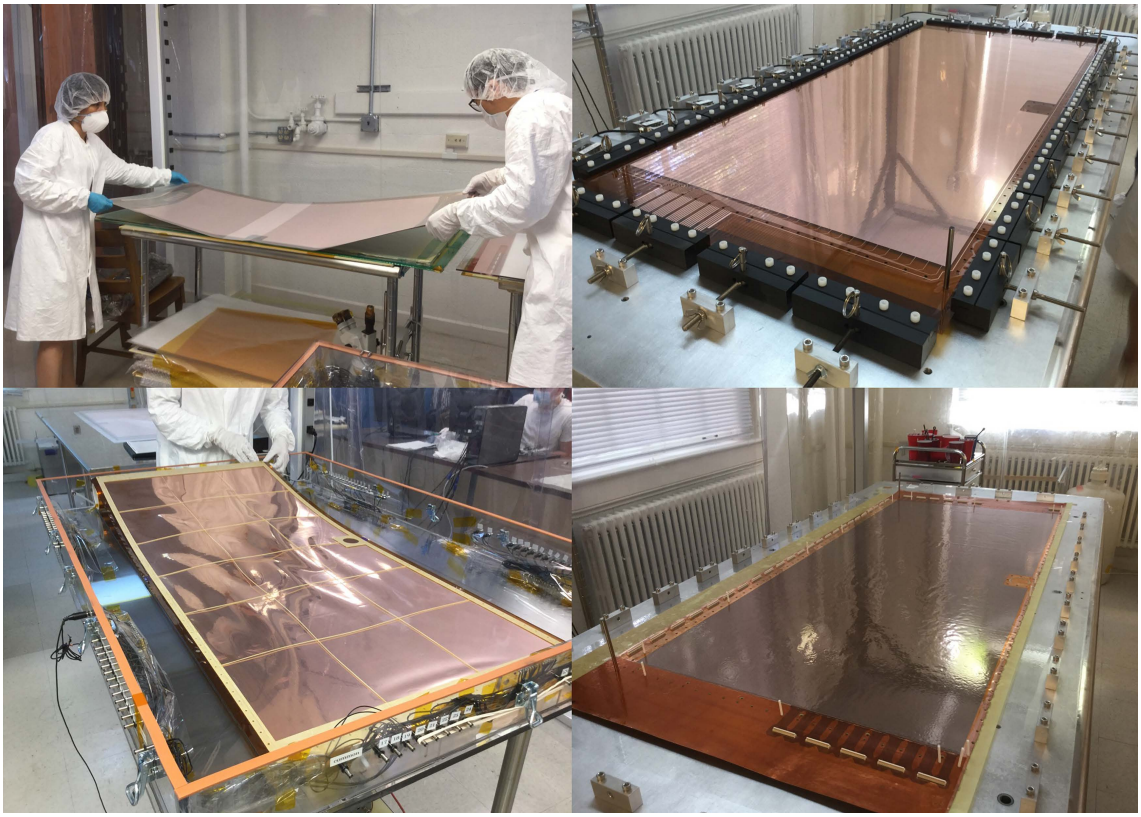

Figure 166: *Making of the world's largest GEM detector: (top left) A raw GEM foil from CERN being prepared for visual inspection. Note the the active area of the foil has been covered by a protective foil. Research scientist Dr. Huong Nguyen is the one holding the left end of the foil. She has successfully constructed close to 50 large area GEM detectors for SBS, PRad and EIC R&D projects. (top right) The GEM foil stretched on the stretcher to the required uniform tension. The left and far rows of tensioning blocks are mounted on accurate tension monitoring devices (the cables could be seen in the picture). (bottom left) A GEM foil goes through three High-voltage-testing-and-cleansing cycles (testing the GEM foil under high voltage and foil cleansing by burning any dust particles under high voltage) at the raw foil stage, after the foil is stretched and glued onto its holding frame, and after the foil has been assembled into the GEM detector. This picture shows a framed foil being installed in the large dry-nitrogen GEM foil testing box. The wrinkles seen on the foil are due the holding frame buckling under the tension on the foil. Once the framed foil is dowel-pinned on to the assembly jig and then glued together with all the other frames, the combined tension of the glued together frames prevents this type of buckling in the assembled detector. (bottom right) The 2-D x-y readout board, glued on to the base window, aligned on the assembly jig with dowel pins, waiting for the other frames to be installed over it.*

As part of SBS GEM tracker development activities, the UVa group has also carried out an aggressive R&D campaign to ensure proper readout of the GEM data and accurate track reconstruction under very high background conditions. The background hit rate in the SBS front tracker is expected to be up to 500 kHz/cm^2, several times higher than the highest hit rates expected at the location of MOLLER GEM trackers. Correctly reconstructing the particle tracks of interest in this very high background environment is achieved by using especially adapted high rate techniques at every step of the tracking process: optimizing the GEM module and tracker design at the hardware level, using high bandwidth electronics and real time Field Programmable Gate Array (FPGA) based background suppression techniques at the Data Acquisition

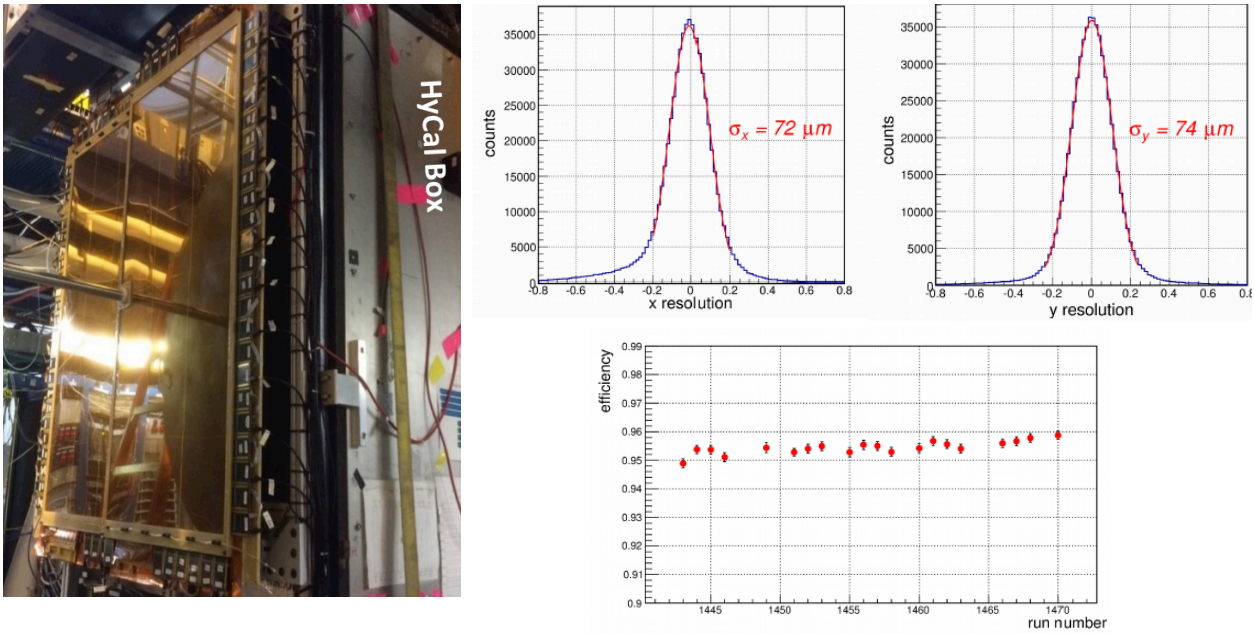

Figure 167: *(Left:) The large area GEM detector pair developed by the UVa group in PRad experiment setup next to HyCal. The beam-line can be seen passing through the especially designed through-hole in the middle of the GEM layer. (Top-right) The position resolution (approximately 72 (74) μm) for x (y) direction readout of GEM detectors achieved during PRad experiment. A previous review committee for the MOLLER project had raised the concern about a possible deterioration of the position resolution for MOLLER GEMs due to the increased capacitance of longer than 1 m readout strips. The PRad result presented here showing excellent, in-beam position resolution for PRad GEMs with 123 cm long readout strips in the x-direction (10 cm longer than the longest MOLLER readout strips) shows that this is not an issue. (Bottom-right) the GEM detection efficiency over a period of two weeks during the PRad experiment. This plot shows that the average GEM efficiency is over 95% and is stable to within 1% over long periods of time. The small periodic variations are due to gas cylinder changes which introduce very small amounts of air and humidity into the gas supply line. The small upward trend in the efficiency could be due to the long term purging of the detector, with small pockets of air and humidity trapped in the corners of the detector being cleaned out.*

(DAQ) level, and developing highly specialized tracking algorithms to pick out the signal hits from among the vast amount of background hits. As part of SBS R&D, these techniques were developed, implemented, and tested under realistic conditions. A detailed Geant4 simulation of the SBS setup was combined with a digitization package to generate the detector level pseudo-data similar to what is expected in the actual experiments. The digitization procedures were calibrated against actual GEM data from cosmic-ray runs, X-ray tests, beam test runs in experimental Hall-A, and the PRad experiment in Hall B. Then, optimized tracking algorithms were developed and implemented in an analysis program used to analyze these pseudo-data and to extract expected high-level parameters. These extracted quantities were then compared with the input parameters from the simulation to verify and determine the performance characteristics for the SBS tracker. This work has has demonstrated that the already developed techniques are adequate for the high rate operation under SBS and MOLLER conditions. A detailed description of this work could be found in [47].

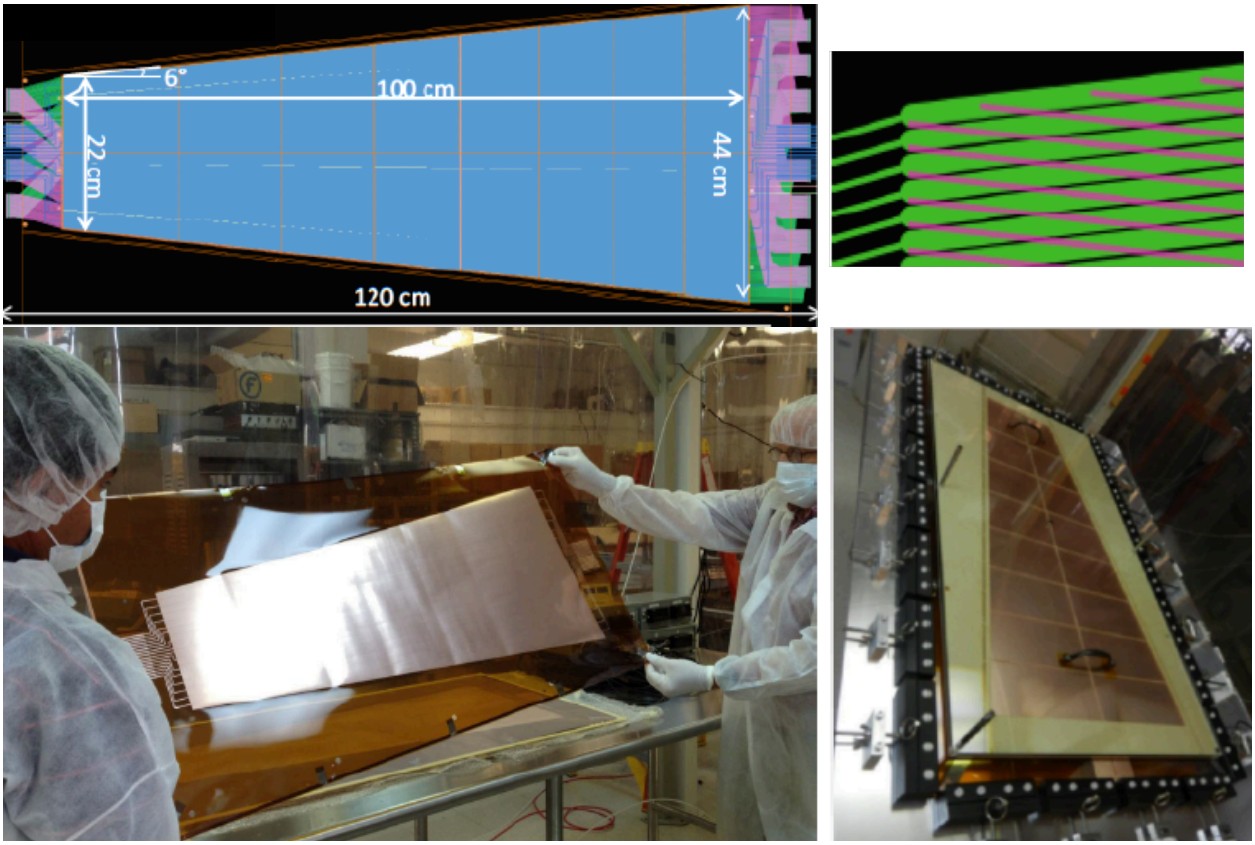

Figure 168: *(Top left:) The photolithographic design for the 2D readout board of UVa EIC GEM prototype I. As the highly zoomed-in figure on the top-right shows, the U-V readout strips in this readout structure were arranged with a 12° stereo angle between U and V, just as needed for MOLLER GEMs. The zoomed in section comes from the left-top corner of the readout board; as could be seen from the full readout board shown on the left, the purple (U) strips ending up on the top-left corner of the board are read out from the opposite edge of the detectors (away from the beam-line edge), while the green (V) strips and some of the U-strips are read out from the inner (close to the beam-line) edge of the detector in this prototype. (Bottom left:) A raw GEM foil used for UVa EIC GEM prototype-I. Note that in the case of this foil, the protective film has been removed to expose the active GEM area for visual inspection. (Bop right) A EIC prototype-I GEM foil stretched with the and the GEM holding frame glued on the foil. Some of the precision dowel pins which ensure the relative alignment between different GEM foils, holding frames and the readout could also be seen in the picture. A thick, heavy plastic "weight-plate" (the one with the black handles) has been placed the stretcher to the required uniform tension. Note the side "wings" on the trapezoidal frame; these wings are removed after the framed foil is glued into the rest of the chamber.*

N.5.1 GEM fabrication facilities at UVa

The UVa group's **UVa Micro-Pattern Gas Detector Lab** is a 15 x 15 m^2, well equipped nuclear physics detector development lab that has been used for the development, construction, and testing of many large area GEM detectors. The lab consists of a 8 x 4 m^2, level 1,000 clean room, especially set up for the GEM chamber construction. The lab contains specialized GEM construction equipment worth over $200,000, purchased mostly using capital equipment funding from the University of Virginia.

The facilities in the the lab include:

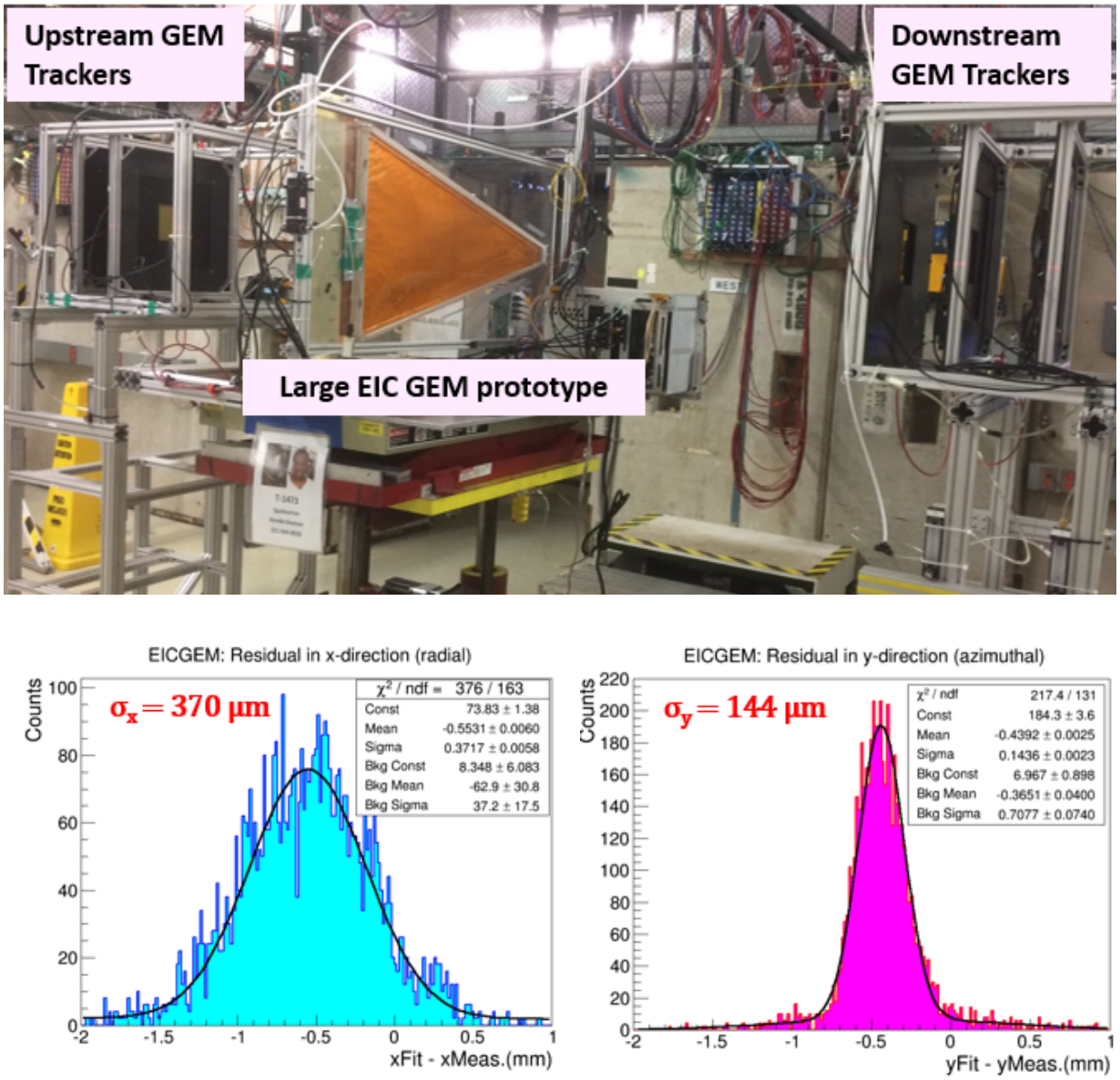

Figure 169: *(Top) EIC GEM prototype installed in test beam area at Fermilab (June-July 2018). (Bottom) Preliminary results of spatial resolution performance in both radial (x) and azimuthal (y) directions of the large GEM prototype with stereo-angle (U-V) strip readout structure. This readout is very similar to the one that will be used for MOLLER GEMs; this results clearly demonstrates adequate resolution for MOLLER*

- Equipment needed for GEM detector fabrication.
  - Mechanical Stretching systems with tension load monitoring for large area GEM foil foils.
  - High power optical microscope for GEM foil inspection.
  - Picoammeters for GEM foil testing and characterization.
  - Large volume dry N_2 boxes for GEM foil testing.
  - Large capacity ultra-sonic bath for GEM frame cleaning.

  - Laminal flow racks for GEM foil storage.
  - Particle counter for clean room monitoring.

- GEM readout system based on APV25-S1 electronics: a state of the art, 10,000 channel GEM readout system based on APV25-S1 electronics (this is the readout system used for GEM R&D activities in the lab; new separate new readout system with 127,000 channels is being set up for SBS). APV25-S1 is a fast pipeline readout chip used for COMPASS GEM trackers, CMS silicon stripe detectors, and STAR FGT GEM chambers [7]. The capacity of this system is sufficient to readout the prototype GEM trackers.

- Wiener-Iseg multi-channel High Voltage system: The UVa GEM group owns a Wiener-Iseg2 multi-channel High Voltage system that is especially suited to provide high voltage to sensitive tracking chambers. This system currently has 16 channels and can be expanded to 40 channels.

- A GEM detector testing station equipped with a high-flux x-ray tube and radioactive sources. This setup is located within a large, walk in cabinet shielded with lead.

- A cosmic ray test stand equipped with large area scintillators for trigger.

- A CODA (Jefferson lab DAQ architecture) based Data Acquisition system.

O Analysis and Data Handling

This subsystem is a dependency of the project, incorporating the software systems needed to analyze and interpret the experiment. In the analysis of an integrating parity experiment like MOLLER, the raw signals from the detectors in each helicity window are first normalized by the integrated beam current, and then they are combined with values from adjacent helicity windows to form an asymmetry in a single helicity pattern. Asymmetries are calculated on all normalized detector signals and on all beam parameters, and a correlation analysis between the detector and beam parameter asymmetries is carried out. In most of the data collection, the correlations are determined from natural fluctuation in the beam parameters, but in a small fraction of the data we "dither" the beam parameters by deliberately modifying them one-by-one. For each helicity-window, two different corrected asymmetries are computed, using the "natural" and "dither" correlations, and then these results can be accumulated either singly in output files or by averaging helicity-window asymmetries together to produce a mean and error on the asymmetry.

The parity analyzer used for the PREX-II experiment maintains an analysis rate of about 400 events per second (data throughput of about 1.5 MB/s) for the full analysis chain. Scaling for MOLLER's 4 times larger number of integration channels results in a predicted analysis rate of 100 events per second, about 20 times slower than the collected event rate. Because the data per channel from the MOLLER electronics is larger than in PREX-II, a scaling estimation based on the 130 MB/s data rate and PREX-II analyzer throughput yields an analysis rate about 80 times slower than real time. Taking the simple average of these two estimates, we expect that, using the PREX-II analysis as a baseline, a total of 50 concurrent analysis processes are needed for a full real-time analysis to stay current with the data collection. Of the set of ten workstations, two are reserved for event building and helicity-correlated feedback, leaving eight across which to distribute these 50 real-time processes.

With the data rate of 130 MB/s, each hour-long run results in a raw data volume of about 450 GB. The calculation and storage of signal averages and asymmetries for each helicity-pattern does not generally result in data reduction, and output data volume can be increased. For example, in PREX-II, an output ROOT file is about 4 times larger than the original data file. For the experiment-long accumulation, we can keep averages of these quantities at about the minute time-scale, resulting in data reduction of a factor of several thousand. However, to evaluate correlations between the beam parameters and the detector signals, and to monitor the correction process, we require keeping the results for each helicity pattern for several days. Assuming a full output file size of 1.8 TB per hour (four times the raw data size), a 100 TB staging disk allows about 2.5 days of history for this correlation/correction evaluation.

O.1 Online feedbacks and calibrations

O.1.1 Helicity correlated feedback

Helicity correlated fluctuations in beam intensity or position and angle of the beam as it impacts the target generate a "false" asymmetry in the detectors, as described in Appendix A. The correlations of the detector asymmetries with beam parameter fluctuations are determined, and corrections are applied. However, direct minimization of the helicity correlated fluctuations reduces the scale of the needed corrections, making the measured detector asymmetries more representative of the physics asymmetries. Small changes in the voltages applied to the Pockels cell can induce changes in the beam charge asymmetry, and this is used as active feedback on measurement of the charge asymmetry in the hall to minimize the charge asymmetry. Similarly, optical and electrical devices in the low-energy portion of the injector induce helciity correlations in the beam position and angle on target, and active feedback on the positions is also possible.

O.1.2 Beam parameter correlation and corrections

The coefficients α_j, introduced in Eqn. 11 to describe the correlations between detector and beam parameter fluctuations, must be continuously calibrated *simultaneously* with the collection of production data, since the numerical values depend on the details not only of the apparatus but also the accelerator beam tune and the sensitivity and location of beam monitoring devices. Various ways of accomplishing this at Jefferson Laboratory have already been implemented during the Qweak, PREX, and CREX measurements, including extensive collaboration with personnel from Accelerator Operations and careful consideration of impact on other Halls.

While α_j can be extracted from a correlation analysis of the response of the detectors and beam monitoring devices to beam fluctuations in window-pairs, proper calibration requires deliberately dithering the beam trajectory concurrent with data-taking in a quasi-continuous fashion by an amount large enough to observe all the correlations while avoiding to add a non-statistical component to $\sigma(A_i)$. More generally, the study of the detailed noise and beam response characteristics of the monitors is a critical component of understanding the systematic errors.

O.1.3 Transverse polarization minimization

As described in Appendix B, components of beam polarization which are transverse to the beam axis give rise to azimuthal variations in the asymmetries measured in the apparatus. Through averaging the azimuthal variations over the span of several days, we will be able to evaluate the transverse polarization components, and use those evaluations to make manual tweaks to the electron beam polarization launch angle in the injector to reduce the transverse components. This analysis must be done using asymmetries which are corrected for beam parameter fluctuations, which also appear as azimuthal asymmetry variations. We continue to monitor the azimuthal asymmetries to detect slow drifts which lead to increased transverse polarization components.

References

[1] MOLLER Experiment Homepage:

`https://moller.jlab.org/moller_root/`

[2] MOLLER Collaboration, J. Benesch at al, arXiv:1411.4088 [nucl-ex].

[3] P. L. Anthony *et al.* [SLAC E158 Collaboration], Phys. Rev. Lett. **95**, 081601 (2005) [arXiv:hep-ex/0504049].

[4] A. Czarnecki and W. J. Marciano, Phys. Rev. D **53**, 1066 (1996) [arXiv:hep-ph/9507420].

[5] A. Czarnecki and W. J. Marciano, Int. J. Mod. Phys. A **15**, 2365 (2000) [arXiv:hep-ph/0003049].

[6] J. Erler and M. J. Ramsey-Musolf, Phys. Rev. D **72**, 073003 (2005) [arXiv:hep-ph/0409169].

[7] E. Derman and W. J. Marciano, Annals Phys. **121**, 147 (1979).

[8] C. Amsler *et al.* [Particle Data Group], Phys. Lett. B **667**, 1 (2008).

[9] S. C. Bennett and C. E. Wieman, Phys. Rev. Lett. **82**, 2484 (1999) [Erratum-ibid. **83**, 889 (1999)] [hep-ex/9903022].

[10] V. A. Dzuba, J. C. Berengut, V. V. Flambaum and B. Roberts, Phys. Rev. Lett. **109**, 203003 (2012) [arXiv:1207.5864 [hep-ph]].

[11] D. Androi'c *et al.* [Q_{weak} Collaboration], Nature **557**, no. 7704, 207 (2018) doi:10.1038/s41586-018-0096-0 [arXiv:1905.08283 [nucl-ex]].

[12] G. P. Zeller *et al.* [NuTeV Collaboration], Phys. Rev. Lett. **88**, 091802 (2002) [Erratum-ibid. **90**, 239902 (2003)] [arXiv:hep-ex/0110059].

[13] "Uncertainties in the Theoretical Calculation of the Parity-Violating Asymmetry in Møller Scattering", MOLLER Collaboration report submitted to DOE, September 15, 2016:

`https://moller.jlab.org/DocDB/0006/000626/001/2-loopreport_final.pdf`

[14] A. Aleksejevs, S. Barkanova, Y. M. Bystritskiy, E. Kuraev and V. Zykunov, Phys. Part. Nucl. Lett. **13**, no.3, 310-317 (2016) doi:10.1134/S1547477116030031 [arXiv:1508.07853 [hep-ph]].

[15] Y. Du, A. Freitas, H. H. Patel and M. J. Ramsey-Musolf, [arXiv:1912.08220 [hep-ph]].

[16] K. S. Kumar, S. Mantry, W. J. Marciano and P. A. Souder, Ann. Rev. Nucl. Part. Sci. **63**, 237 (2013) [arXiv:1302.6263 [hep-ex]].

[17] V. Cirigliano and M. J. Ramsey-Musolf, Prog. Part. Nucl. Phys. **71**, 2 (2013) [arXiv:1304.0017 [hep-ph]].

[18] J. Erler and S. Su, Prog. Part. Nucl. Phys. **71**, 119 (2013) [arXiv:1303.5522 [hep-ph]].

[19] W. Chao, H. Li, M. J. Ramsey-Musolf, and S. Su, in preparation.

[20] V. Cirigliano, A. Kurylov, M. J. Ramsey-Musolf and P. Vogel, Phys. Rev. D **70**, 075007 (2004) [arXiv:hep-ph/0404233].

[21] P. B. Dev, M. J. Ramsey-Musolf and Y. Zhang, Phys. Rev. D **98**, no.5, 055013 (2018) doi:10.1103/PhysRevD.98.055013 [arXiv:1806.08499 [hep-ph]].

[22] H. Davoudiasl, H. -S. Lee and W. J. Marciano, Phys. Rev. D **85**, 115019 (2012) [arXiv:1203.2947 [hep-ph]].

[23] H. Davoudiasl, H. -S. Lee and W. J. Marciano, Phys. Rev. Lett. **109**, 031802 (2012) [arXiv:1205.2709 [hep-ph]].

[24] A. Kurylov, M. J. Ramsey-Musolf and S. Su, Phys. Rev. D **68**, 035008 (2003) [arXiv:hep-ph/0303026].

[25] M. J. Ramsey-Musolf and S. Su, Phys. Rept. **456**, 1 (2008) [arXiv:hep-ph/0612057].

[26] J. Erler, P. Langacker, S. Munir and E. Rojas, arXiv:1108.0685v1 [hep-ph].

[27] E. Eichten, K. D. Lane and M. E. Peskin, Phys. Rev. Lett. **50**, 811 (1983).

[28] A. Falkowski and K. Mimouni, JHEP **1602**, 086 (2016) [arXiv:1511.07434 [hep-ph]].

[29] Y. Li, F. Petriello and S. Quackenbush, Phys. Rev. D **80**, 055018 (2009) [arXiv:0906.4132 [hep-ph]].

[30] H. Davoudiasl, H. -S. Lee and W. J. Marciano, arXiv:1402.3620 [hep-ph].

[31] P. A. Souder *et al.*, Phys. Rev. Lett. **65**, 694 (1990).

[32] D. T. Spayde *et al.* [SAMPLE Collaboration], Phys. Lett. B **583**, 79 (2004) [arXiv:nucl-ex/0312016].

[33] A. Acha *et al.* [HAPPEX collaboration], Phys. Rev. Lett. **98**, 032301 (2007) [arXiv:nucl-ex/0609002].

[34] The Lead Radius Experiment PREX, E06002, K. Kumar, R. Michaels, P. Souder, G. Urciuoli spokespersons, http://hallaweb.jlab.org/parity/prex/ .

[35] S. Abrahamyan *et al.* [PREX collaboration], Phys. Rev. Lett. **108**, 112502 (2012).

[36] E. G. Brentari *et al.*, *Boiling Heat Transfer for Oxygen, Nitrogen, Hidrogen, and Helium*, National Bureau of Standards, TN 317 (1965)

[37] S. D. Covrig *et al.*, 2005, *The cryogenic target for the G0 experiment at Jefferson Lab*, Nucl. Instr. and Meth. **A 551**, 218-235

[38] J. Gao *et al.*, 2003, *A liquid hydrogen target for the precision measurement of the weak mixing angle in Møller scattering at SLAC*, Nucl. Instr. and Meth. **A 498**, 90-100

[39] A. W. Chao and M. Tigner, "Handbook of Accelerator Physics and Engineering"

[40] E. Ihloff, "Moller Coil Testing document-R1", 2018

[41] A. E. Haight and M. W. Haynes, IEEE Transactions on Applied Superconductivity, June 2017, Vol.27, doi:10.1109/TASC.2016.2643440

[42] F. Sauli, Nucl. Inst. and Meth. **A 386**, 531 (1997).

[43] B. Ketzer *et al.*, Nucl. Phys. B (Proc. Suppl.) **125**, 368 (2003).

[44] W. Xiong, *et al.*, Nature (in print) (2019).

[45] K. Gnanvo, N. Liyanage, V. Nelyubin, K. Saenboonruang, S. Sacher, and B. Wojtsekhowski, **Nucl. Inst. and Meth. in Phys. Res. A 782 (77)** (2015).

[46] K. Gnanvo, X. Bai, C. Gu, N. Liyanage, V. Nelyubin, Y. Zhao, Nucl. Inst. and Meth. in Phys. Res. A 808 (83) (2016).

[47] D. Di, PhD Thesis, University of Virginia (2019), available at `https://www.library.virginia.edu/libra/etds/`

[48] M. Villa, *et al.*, Nucl. Inst. and Meth. **A 628** 182 (2011).

[49] M. Alfonsi *et al.*, Nucl. Inst. and Meth. **A 617**, 151 (2010).

[50] D. Abbaneo *et al.*, Nucl. Inst. and Meth. **A** (2010).

[51] M.J. French *et al.*, Nucl. Instr. and Meth. **A 466** 359 (2001).

[52] F.Sauli, RD51-NOTE-2012-007 REVISED 21.09.2012.

[53] D. Abbaneo *et al.*, RD51-NOTE-2012-012 16.11.2012.

[54] William Whyte, "Cleanroom Technology: Fundamentals of Design, Testing and Operation" (2001) ISBN 978-0-470-74806-0

[55] P. Walker, V. Weber, *et al.*, Journal of Photographic Science, **18** 150 (1970).

[56] J. M. Shaw, J. D. Gelorme, *et al.*, IBM Journal of Research and Development. **41** 81 (1997) ISSN: 0018-8646

[57] Rensheng Wang, Yan Huang, Zhigang Xiao *et al.*, Nucl. Inst. and Meth. **A701** 54 (2013)

[58] R.S. Hicks *et al.* , Nucl. Inst. and Meth. **A 553** 470 (2005).

[59] T. Powers, L. Doolittle, R. Ursic, J. Wagner, "Design, commissioning, and operational results of wide dynamic range BPM switched electrode electronics", AIP Conference Proceedings, **390**, 257 (1997).

[60] B. Waidyawansa, "A 3% Measurement of the Beam Normal Single Spin Asymmetry in Forward Angle Elastic Electron-Proton Scattering using the Q_{weak} Setup", PhD thesis, Ohio University, August 2013.

[61] J. Musson, "Functional Description of Algorithms Used in Digital Receivers", JLab Technical Report No. JLAB-TN-14-028 (2014).

[62] J. Benesch, "MOLLER Beam Line", JLab Technical Report No. JLAB-TN-19-035 (2019).

[63] W. Barry, "A general analysis of thin wire pickups for high frequency beam position monitors", Nucl. Instrum. Methods. Phys. Res. **A301**, 407 (1991).

[64] T. Allison *et al.* [Q_{weak} Collaboration], "The Q_{weak} Experimental Apparatus", NIM **A781** (2015), pp 105-133.

[65] T. B. Humensky *et al.*, Nucl. Instrum. Meth. A **521**, 261 (2004) doi:10.1016/j.nima.2003.09.065 [physics/0209067].

[66] K. D. Paschke, Eur. Phys. J. A **32**, 549 (2007).

[67] Caryn Palatchi, "Laser and Electron Beam Technology for Parity Violating Electron Scattering Measurements," Doctoral Dissertation, University of Virginia, (2019).

[68] D. Androić *et al.* [Q_{weak} Collaboration], Nature **557**, no. 7704, 207 (2018) doi:10.1038/s41586-018-0096-0 [arXiv:1905.08283 [nucl-ex]].

[69] N. L. Hall, P. G. Blunden, W. Melnitchouk, A. W. Thomas and R. D. Young, Phys. Lett. B **731**, no. issue, 287 (2014) [Erratum-ibid. B **733**, 380 (2014)] [arXiv:1311.3389 [nucl-th]].

[70] D.E. Wiser, PhD thesis, University of Wisconsin-Madison, 1977.

[71] The MOLLER Collaboration, "Report on Aluminum and Inelastic Backgrounds", submitted to U.S. Department of Energy Office of Science Nuclear Physics Division, December 2, 2015:

`https://moller.jlab.org/DocDB/0006/000627/001/MOLLER_backgrounds.pdf`

[72] DOE Office of Nuclear Physics 2014 Science Review of MOLLER experiment,

`http://hallaweb.jlab.org/12GeV/Moller/scirev2014/`

[73] D. Androic *et al.* [G0 Collaboration], arXiv:1212.1637 [nucl-ex].

[74] D. Wang *et al.* [Jefferson Lab Hall A Collaboration], Phys. Rev. Lett. **111**, no. 8, 082501 (2013) [arXiv:1304.7741 [nucl-ex]].

[75] D. Wang *et al.*, Phys. Rev. C **91**, no. 4, 045506 (2015) [arXiv:1411.3200 [nucl-ex]].

[76] K. Matsui, T. Sato and T.-S. H. Lee, Phys. Rev. C **72**, 025204 (2005) [nucl-th/0504051].

[77] M. Gorchtein, C. J. Horowitz and M. J. Ramsey-Musolf, Phys. Rev. C **84**, 015502 (2011) [arXiv:1102.3910 [nucl-th]].

[78] N. L. Hall, P. G. Blunden, W. Melnitchouk, A. W. Thomas and R. D. Young, Phys. Rev. D **88**, no. 1, 013011 (2013) [arXiv:1304.7877 [nucl-th]].

[79] N. L. Hall, P. G. Blunden, W. Melnitchouk, A. W. Thomas and R. D. Young, arXiv:1504.03973 [nucl-th]. (accepted in Phys. Lett B).

[80] D. S. Armstrong *et al.*, arXiv:1202.1255 [physics.ins-det].

[81] P. E. Bosted and M. E. Christy, Phys. Rev. C P**81**:055213 (2010)

[82] C. J. Horowitz, Phys. Rev. C **89**, 045503 (2014) [arXiv:1401.6898 [nucl-th]].

[83] S. Agostinelli *et al.* [GEANT4 Collaboration], Nucl. Instrum. Meth. A **506**, 250 (2003).

[84] K. Aulenbacher, E. Chudakov, D. Gaskell, J. Grames and K. D. Paschke, Int. J. Mod. Phys. E **27**, no. 07, 1830004 (2018). doi:10.1142/S0218301318300047

[85] N. Falletto *et al*, "Compton scattering off polarized electrons with a high finesse Fabry-Perot cavity at JLab,", *"Nucl. Instrum. Meth."*, A459, 212-425, 2001.

[86] Z. Ahmed *et al.* [HAPPEX Collaboration], Phys. Rev. Lett. **108**, 102001 (2012) doi:10.1103/PhysRevLett.108.102001 [arXiv:1107.0913 [nucl-ex]].

[87] S. Abrahamyan *et al.*, Phys. Rev. Lett. **108**, 112502 (2012) doi:10.1103/PhysRevLett.108.112502 [arXiv:1201.2568 [nucl-ex]].

[88] M. Friend *et al.*, Nucl. Instrum. Meth. A **676**, 96 (2012) doi:10.1016/j.nima.2012.02.041 [arXiv:1108.3116 [physics.ins-det]].

[89] A. Narayan *et al.*, "Precision Electron-Beam Polarimetry at 1 GeV Using Diamond Microstrip Detectors," Phys. Rev. X **6**, no. 1, 011013 (2016).

[90] N. Vansteenkise, P. Vignolo, and A. Aspect, "Optical Reversibility Theorems for Polarization: Application to Remote Control of Polarization", J. Opt. Soc. Am. A, Vol. 10, No. 10, (1993) 2240.

[91] A. Denner and S. Dittmaier, "Complete $o(\alpha)$ QED cor- rections to polarized Compton scattering", Nucl. Phys. B **540** 58 (1999).

[92] M. Friend *et al*, "Upgraded photon calorimeter with integrating readout for Hall A Compton Polarimeter at Jefferson Lab", Nucl. Instrum. Methods A676, 96-105, 2012. [arXiv:1108.3116].

[93] A. V. Glamazdin, V. G. Gorbenko, L. G. Levchuk, R. I. Pomatsalyuk, A. L. Rubashkin, P. V. Sorokin, D. S. Dale and B. Doyle *et al.*, "Electron beam Møller polarimeter at JLab Hall A," Fizika B **8**, 91 (1999)

[94] E. A. Chudakov, A. V. Glamazdin, V. G. Gorbenko, L. G. Levchuk, R. I. Pomatsalyuk, P. V. Sorokin, "Electron beam Møller polarimeter at Hall A, JLab", Prob.Atom.Sci.Tech. **40**, 43 (2002)

[95] P. S. Cooper, M. J. Alguard, R. D. Ehrlich, V. W. Hughes, H. Kobayakawa, J. S. Ladish, M. S. Lubell and N. Sasao *et al.*, "Polarized electron Electron Scattering at GeV Energies," Phys. Rev. Lett. **34**, 1589 (1975).

[96] B. Wagner, H. G. Andresen, K. H. Steffens, W. Hartmann, W. Heil and E. Reichert, "A Møller polarimeter for CW and pulsed intermediate-energy electron beams," Nucl. Instrum. Meth. A **294**, 541 (1990).

[97] J. Arrington, E. J. Beise, B. W. Filippone, T. G. O'Neill, W. R. Dodge, G. W. Dodson, K. A. Dow and J. D. Zumbro, "A Variable energy Møller polarimeter at the MIT Bates Linear Accelerator Center," Nucl. Instrum. Meth. A **311**, 39 (1992).

[98] K. B. Beard, R. Madey, W. M. Zhang, D. M. Manley, B. D. Anderson, A. R. Baldwin, J. M. Cameron and C. C. Chang *et al.*, "Measurement of the polarization of a pulsed electron beam with a Møller polarimeter in the coincidence mode," Nucl. Instrum. Meth. A **361**, 46 (1995).

[99] H. R. Band, G. Mitchell, R. Prepost and T. Wright, "A Møller polarimeter for high-energy electron beams," Nucl. Instrum. Meth. A **400**, 24 (1997).

[100] P. Steiner, A. Feltham, I. Sick, M. Zeier and B. Zihlmann, "A high-rate coincidence Moller polarimeter," Nucl. Instrum. Meth. A **419**, 105 (1998).

[101] M. Hauger *et al.*, "A high-precision polarimeter," *Nucl. Instrum. Meth.*, vol. A462, pp. 382–392, 2001, nucl-ex/9910013.

[102] L. V. de Bever, J. Jourdan, M. Loppacher, S. Robinson, I. Sick and J. Zhao, "A target for precise Møller polarimetry," *Nucl. Instrum. Meth.*, vol. A400, pp. 379–386, 1997.

[103] M Loppacher, "Møller Polarimetry for CEBAF Hall C," PhD thesis, Universität Basel, April 1996.

[104] M. Hauger et al., "A high-precision polarimeter," *Nucl. Instrum. Meth.*, vol. A462, pp. 382–392, 2001, nucl-ex/9910013.

[105] G. G. Scott and H. W. Sturner, "Magnetomechanical Ratios for Fe-Co Alloys," Phys. Rev. **184**, 490 (1969).

[106] J. Crangle and G. M. Goodman, "The Magnetization of Pure Iron and Nickel," Proceedings of the Royal Society of London, Series A, **321**, 477 (1971).

[107] C. D. Graham, Jr., "Iron and Nickel as Magnetization Standards," J. Appl. Phys. **53**, 2032 (1982).

[108] G. G. Scott, "Review of gyromagnetic ratio experiments," *Rev. Mod. Phys.*, vol. 34, pp. 102–109, Jan 1962.

[109] L. G. Levchuk, "The Intraatomic motion of bound electrons as a possible source of a systematic error in electron beam polarization measurements by means of a Møller polarimeter," *Nucl. Instrum. Meth.*, vol. A345, pp. 496–499, 1994.

[110] C. Y. Prescott *et al.*, Phys. Lett. B **77**, 347 (1978).

[111] Emmanouill Kargiantoulakis, "A Precision Test of the Standard Model via Parity-Violating Electron Scattering in the Qweak Experiment," Doctoral Dissertation, University of Virginia, (2015).

[112] Rupesh Silwal, "Probing the Neutron Radius of Lead and the Strangeness Content of the Proton Using Parity-Violating Electron Scattering," Doctoral Dissertation, University of Virginia, (2012).

[113] A. G. Wright, "The Photomultiplier Handbook"

[114] Texas Instrument: THS4631, High Speed FET-Input Operational Amplifier.

[115] Linear Technology: LTC2387-18, 18-Bit, 15Msps SAR ADC.

[116] XILINX: Zynq-UltraScale SoCs.

[117] Enclustra: Mecury+XU8 SoM

[118] S-O. Flyckt and C. Marmonier, "Photomultiplier Tubes, Principles and Applications", http://www2.pv.infn.it/ debari/doc/Flyckt_Marmonier.pdf

[119] ET Enterprises, "Understanding Photomultipliers", http://et-enterprises.com/images/brochures/Understanding_Pmts.pdf

[120] S. Riordan *et al.*, "Study of light backgrounds from relativistic electrons in air light-guides", Nucl. Instr. And Meth. A, 896 (2018) 96-102

[121] I. H. Malitson. "Interspecimen Comparison of the Refractive Index of Fused Silica". In: J. Opt. Soc. Am. 55.10 (Oct. 1965), pp. 1205–1209. doi: 10.1364/JOSA.55.001205
url: http://www.osapublishing.org/abstract.cfm?URI=josa-55-10-1205

[122] Rei Kitamura, Laurent Pilon, and Miroslaw Jonasz. "Optical constants of silica glass from extreme ultraviolet to far infrared at near room temperature". In: Appl. Opt. 46.33 (Nov. 2007), pp. 8118–8133. doi: 10.1364/AO.46.008118
url: http://ao.osa.org/abstract.cfm?URI=ao-46-33-8118

[123] Daniella Motta and Stefan Schoenert. “Optical properties of bialkali photo-cathodes”. In: Nuclear Instruments and Methods in Physics Research Section A: Accelerators, Spectrometers, Detectors and Associated Equipment 539 (Sept. 2004), pp. 217–235. doi: 10.1016/j.nima.2004.10.009